Determination of the absolute luminosity at the LHC

S. White

LAL 10-154
Septembre 2010

THÈSE

présentée le 11 octobre 2010

par

Simon WHITE

pour obtenir le grade de

Docteur ès Sciences
de l'Université Paris-Sud 11

Determination of the absolute luminosity at the LHC

Soutenue devant la commission d'examen composée de :

M.	H.	Burkhardt	
M.	W.	Fischer	
Mme.	V.	Halyo	Rapporteur
M.	O.	Napoly	Rapporteur
M.	P.	Puzo	Directeur de thèse
M.	G.	Wormser	Président

Contents

Introduction

For particle colliders, the most important performance parameters are the beam energy and the luminosity. High energies allow the particle physics experiments to study and observe new effects. The luminosity describes the ability of the collider to produce the required number of useful interactions or events. It is defined as the proportionality factor between the event rate, measured by the experiments, and the cross section of the observed event which describes its probability to occur. The absolute knowledge of the luminosity therefore allows the experiments to measure the absolute cross sections.

The **L**arge **H**adron **C**ollider (LHC) was designed to produce proton proton collisions at a center of mass energy of 14 TeV. This energy would be the highest ever reached in a particle accelerator. The knowledge and understanding of particle physics at such high energy is based on simulations and theoretical predictions. As opposed to e^+ e^- colliders, for which the Bhabba scattering cross section can be accurately calculated and used for luminosity calibration, there are no processes with well known cross sections and sufficiently high production rate to be directly used for the purpose of luminosity calibration in the early operation of the LHC.

The luminosity can also be expressed as a function of the number of charges per beam and the beam sizes at the interaction point. Using this relation, the absolute luminosity can be determined from machine parameters. The determination of the absolute luminosity from machine parameters is an alternative to the cross section based calibration and provides complementary information to the fragmentation model. In the LHC, it was proposed to use the method developed by S. Van Der Meer at the ISR [1] to provide a luminosity calibration based on machine parameters to the physics experiments during the first year of operation.

The work presented in this thesis started in 2007. At the time, the LHC was expected to start operating in 2008 and to produce collisions at the design center of mass energy of 14 TeV. Some of the studies and simulations intended as a preparation for luminosity calibration were done for this original design energy. After a very successful start-up in 2008 issues were found that required a major repair and consolidation which resulted in an extended shutdown period of one year. Operation resumed in 2009 with a reduced target center of mass energy of 7 TeV and the first collisions were produced in March 2010.

This shutdown period was used to extend the scope of this thesis to more general studies such as luminosity optimization, optics studies and operation in collision. It also allowed for a collaboration with BNL. Luminosity calibration measurements were performed at the RHIC collider in 2009 as a preparation for LHC start-up. The RHIC collider is in some sense very similar to the LHC and most of the experience acquired during this collaboration could directly be applied to the LHC. Differences still exist and beam dynamics or instrumental effects have to be considered while analyzing the RHIC data which do not apply to the LHC. The work presented here therefore includes more general considerations not directly related to the calibration of the luminosity at the LHC.

Chapter 1 of this thesis is intended as an introduction to general accelerators physics concepts and definitions that will be used in the following chapters. The principles of transverse beam dynamics are explained as well as some basic notions related to beam-beam interactions. General expressions of the luminosity are derived including complications such as the presence of a crossing angle or the hourglass effect.

Chapter 2 focuses on the Van Der Meer method. The principle of the method and implications of the effects introduced in Chapter 1 are discussed. Most of these effects are small and well controllable under specific beam conditions. Initial estimates on the expected uncertainty related to luminosity calibration in the LHC are discussed.

Chapter 3 and 4 give an overview of the CERN accelerator complex focusing on the LHC and its instrumentation. Beam dynamics and optics studies related to the optimization of the collisions and more generally of the interaction regions are shown as well as tracking simulations for the LHC luminosity monitors.

Chapter 5 and 6 present the results obtained at the LHC and RHIC during luminosity calibration measurements. A detailed analysis of the systematics uncertainties associated to the measurement and proposals for future improvements are discussed.

Chapter 6 also describes more specifically the procedure and implementation of the tools for luminosity optimization and calibration at the LHC as well as the first experience with operation in collision.

Finally, in Chapter 7, an alternative method for luminosity calibration is introduced. Dedicated optics are required for this measurement. An overview of the study and performance of these optics is presented.

My personnal work can be found in some of the derivations of the luminosity presented in Chapter 1, in Chapter 2, in the second part of Chapter 3 and Chapter 4 and in the last three Chapters of this thesis. The luminosity scan software was written as part of this thesis and was used to collide and optimize the LHC beams for the first time. It is now used on a regular basis and represents my most significant contribution to LHC operation.

Chapter 1

Beam Dynamics

This Chapter aims at introducing some general concepts of beam dynamics and defining common parameters and formalism that will be used in this thesis. General equations of the motion of the particles in an accelerator will be derived as well as a definition of the beam-beam interactions. More specifically, the concept of luminosity and its calculation under various conditions will be detailed as an introduction to the following chapters.

1.1 Basics of Accelerator Physics

A charged particle with charge q, momentum $\vec{p}$ and velocity $\vec{v}$ in the electromagnetic fields $(\vec{E},\vec{B})$ experiences the Lorentz's force $\vec{F}$:

$$\vec{F} = q(\vec{E} + \vec{v} \times \vec{B}) = \frac{d\vec{p}}{dt}. \tag{1.1}$$

In an accelerator, the charged particles gain energy by their interaction with the electric field $\vec{E}$. The magnetic force $\vec{v} \times \vec{B}$ is perpendicular to both $\vec{v}$ and $\vec{B}$. The trajectory of a charged particle will be curved when it passes through a dipole magnet. At relativistic velocities an electric field E and a magnetic field B have the same effect for $E = cB$. A magnetic field of 1 T would then be the equivalent of an electric field of 3.10^8 V.m^{-1}. Producing such an electric field is far beyond technical limits for current magnet designs, as a result we always use magnetic fields to steer the beams. The physical fundamentals of beam steering and focusing are called *beam optics*.

1.1.1 Coordinate System

We can define a coordinate system shown in Figure 1.1 to describe the path of the particles in which s will describe the longitudinal direction along the reference orbit. x and y will define the transverse plane and furthermore the deviation from the reference. Locally the trajectory has a radius of curvature ρ. In a circular accelerator the elements the beam is passing through can be straight or curved, this coordinate system is therefore curvilinear. The trajectory of the reference particle $\vec{r_0}$ is the one that has null x and y coordinates for all s. The particle trajectory around the reference orbit can be expressed as:

$$\vec{r} = \vec{r_0}(s) + x\hat{x}(s) + y\hat{y}(s), \tag{1.2}$$

where $\hat{x}$ and $\hat{y}$ are the unit vectors in the transverse plane.

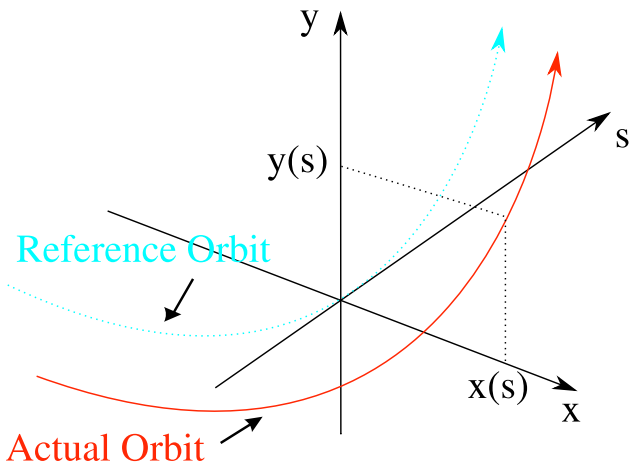

Figure 1.1: Coordinate System.

1.1.2 Magnetic Field

The magnetic field component in the s direction can be approximated to zero. The magnetic field in a magnet is then expressed as:

$$\vec{B} = B_x \hat{x} + B_y \hat{y}. \tag{1.3}$$

Using the first order Taylor expension, the field components can be expressed as function of a dipolar and quadrupolar term:

$$B_x = B_x(0,0) + \frac{\partial B_x}{\partial y} y + o(y^2),$$

$$B_y = B_y(0,0) + \frac{\partial B_y}{\partial x} x + o(x^2). \tag{1.4}$$

In an accelerator, $B_x(0,0)$ is set to 0 and $B_y(0,0)$ is required to compensate for the centrifugal force. In addition the Maxwell equation $\vec{\nabla} \times \vec{B} = 0$ imposes:

$$\frac{\partial B_x}{\partial y} = \frac{\partial B_y}{\partial x}. \tag{1.5}$$

1.1.3 Dipoles

Dipole magnets are used to guide the charged particles along the closed orbit. The bending angle θ is given by the Lorentz force law:

$$\theta = \frac{q}{p} \int_{s_1}^{s_2} B dl = \frac{1}{B\rho} \int_{s_1}^{s_2} B dl. \tag{1.6}$$

The total bending angle of a circular accelerator is 2π, and the total integrated dipole field is:

$$\oint B dl = \frac{2\pi p}{q} = 2\pi B\rho, \tag{1.7}$$

from which we derive the bending radius

$$\rho = \frac{mv}{qB} = \frac{p}{qB}, \tag{1.8}$$

where m and $p = mv$ are the *mass* and the *momentum* of the particle and $B\rho = p/q$ is the *momentum rigidity* of the beam.

1.1.4 Quadrupoles

Quadrupole magnets are used to focus or defocus the beam and therefore control the beam size. Using Equations 1.4 and 1.5, the magnetic field of an ideal quadrupole is given by:

$$\vec{B} = B_1(y\hat{x} + x\hat{y}), \tag{1.9}$$

where $B_1 = \partial B_y/\partial x$ is the field evaluated at the center of the quadrupole. For a charged particle passing through the center of a quadrupole the magnetic field and the Lorentz's force are zero. At a displacement from the center with coordinate (x,y) the Lorentz's force becomes:

$$\vec{F} = qvB_1\hat{s} \times (y\hat{x} + x\hat{y}) = -qvB_1 y\hat{y} + qvB_1 x\hat{x}, \tag{1.10}$$

with $\hat{s}$ the unit vector in the longitudinal direction. A focusing quadrupole in the horizontal plane is also defocusing in the vertical plane and vice versa. Consequently quadrupoles with opposite polarities alternate in an accelerator to provide focusing in the two transverse directions. A typical structure used in accelerators is the so-called FODO cell where F stands for focusing, O for a drift space and D for defocusing.

1.1.5 Acceleration Cavities

The electric fields used for beam acceleration are of two types: the DC acceleration column and the radio-frequency (RF) cavities. The DC acceleration column is usually used for low energy accelerators, I will therefore only cover the RF cavities.

An RF acceleration cavity generates a longitudinal electric field at an RF frequency. The energy gain / loss per passage through a cavity gap is

$$\Delta E = q\Delta V, \tag{1.11}$$

where $\Delta V = V_0 \sin(\omega_{\rm rf} t + \phi)$ is the effective gap voltage, ω_{rf} is the RF frequency, V_0 is the effective peak accelerating voltage and ϕ is the phase angle. Accelerating charged particles to high energy requires synchronization with the RF frequency.

1.2 Betatron Motion

Particle motion around the reference closed orbit is called *betatron motion*. It describes the transverse motion of the particles.

1.2.1 Transfer Matrix and Stability

The betatron equation of motion is governed by the magnetic fields applied in the ring and is therefore derived from the Lorentz force:

$$\vec{F} = q\vec{v} \times \vec{B} = \frac{d\vec{p}}{dt}. \tag{1.12}$$

$\vec{B}$ can be expended as in Equation 1.4 and its component along the s axis is null. Developing Equation 1.12 we get:

$$x'' + \left[\frac{1}{\rho^2(s)} + \frac{1}{B\rho}\frac{\partial B_y(s)}{\partial x}\right] x = 0,$$
$$y'' - \frac{1}{B\rho}\frac{\partial B_y(s)}{\partial x} y = 0, \tag{1.13}$$

which can be written in the form of Hill's equations:

$$\begin{aligned} x'' + K_x(s)\,x = 0, \qquad & K_x = 1/\rho^2 \mp K_1(s), \\ y'' + K_y(s)\,y = 0, \qquad & K_y = \mp K_1(s), \end{aligned} \tag{1.14}$$

where $K_1(s) = B_1(s)/B\rho$ is the effective focusing function which sign depends on the charge of the particle. $B_1(s) = \partial B_y/\partial x$ is evaluated at the closed orbit. The focusing functions $K_{x,y}(s)$ are periodic and because accelerator components usually have uniform or nearly uniform magnetic fields, we can assume they are also piecewise constant. The two equations differ from a term $1/\rho^2(s)$ which is related to the centripetal force in the radial direction. Let K represent either the vertical or the horizontal component with the periodic condition $K(s+L) = K(s)$. The solutions to Hill's equation with constant K are:

$$y(s) = \begin{cases} a\cos(\sqrt{K}\,s + b) & K > 0, \\ a\,s + b & K = 0, \\ a\cosh(\sqrt{-K}\,s + b) & K < 0, \end{cases} \tag{1.15}$$

where a and b are integration constants to be determined by the initial values y_0 and y'_0. Letting

$$\mathbf{y}(s) = \begin{pmatrix} y(s) \\ y'(s) \end{pmatrix}, \tag{1.16}$$

be the betatron state vector, the solution of Equation 1.14 can be expressed as:

$$\mathbf{y}(s) = M(s|s_0)\,\mathbf{y}(s_0), \tag{1.17}$$

where $M(s|s_0)$ is the betatron transfer matrix which becomes for a constant focusing function K:

$$M(s|s_0) = \begin{cases} \begin{pmatrix} \cos\sqrt{K}\,\ell & \frac{1}{\sqrt{K}}\sin\sqrt{K}\,\ell \\ -\sqrt{K}\sin\sqrt{K}\,\ell & \cos\sqrt{K}\,\ell \end{pmatrix} & K > 0 : \text{focusing quad}, \\ \begin{pmatrix} 1 & \ell \\ 0 & 1 \end{pmatrix} & K = 0 : \text{drift space}, \\ \begin{pmatrix} \cosh\sqrt{|K|}\,\ell & \frac{1}{\sqrt{|K|}}\sinh\sqrt{|K|}\,\ell \\ \sqrt{|K|}\sinh\sqrt{|K|}\,\ell & \cosh\sqrt{|K|}\,\ell \end{pmatrix} & K < 0 : \text{defocusing quad}, \end{cases} \tag{1.18}$$

where $\ell = s - s_0$. For a pure sector dipole with $K = 1/\rho^2$ and $\theta = \ell/\rho$ the transfer matrix is:

$$M(s|s_0) = \begin{pmatrix} \cos\theta & \rho\sin\theta \\ -\frac{1}{\rho}\sin\theta & \cos\theta \end{pmatrix}. \tag{1.19}$$

The transfer matrix for any intervals made up of subintervals is the product of the transfer matrices of the subintervals, for an interval of length $\ell = s_2 - s_0 = (s_2 - s_1) + (s_1 - s_0)$ we get:

$$M(s_2|s_0) = M(s_2|s_1)\,M(s_1|s_0). \tag{1.20}$$

Defining $\mathbf{M}$ as the transfer matrix for a full revolution the condition for orbit stability is:

$$|\mathrm{Trace}(\mathbf{M})| \leq 2. \tag{1.21}$$

1.2.2 Courant-Snyder Parametrization

Looking back at the solutions of Hill's equations for $K > 0$, Equation 1.15, they can be interpreted as an harmonic oscillator for which the solution is expressed as:

$$y(s) = a\cos\left(\Phi(s) - \Phi_0\right), \tag{1.22}$$

where $\Phi(s) = \sqrt{K}\,s$ and a and Φ_0 are the constants of integration. For circular accelerators, the function $K(s)$ is periodic, $K(s+L) = K(s)$ where the period L can coincide with the accelerator circumference but normally corresponds to the distance between two FODO cells. The general solution to this equation is:

$$y(s) = a\,w(s)\cos(\Phi(s) - \Phi_0), \tag{1.23}$$

where $w(s)$ is a periodic function with periodicity L. The motion has a spatially varying amplitude and a phase which does not change linearly with s. By substituting the general solution 1.23 in the Hill's equation 1.14 we get:

$$[w''(s)\,w(s)\,\Phi'^2(s) + K(s)\,w(s)]\cos(\Phi(s)+\Phi_0) - [2\,w'(s)\,\Phi'(s) + w(s)\,\Phi''(s)]\sin(\Phi(s)+\Phi_0) = 0, \tag{1.24}$$

the equation of motion should be independant from Φ_0, the sine and cosine coefficient have therefore to vanish. Multiplying the sine coefficient by $w(s)$ and setting it to zero we get:

$$2\,w(s)\,w'(s)\,\Phi'(s) + w^2(s)\,\Phi''(s) = [w^2(s)\,\Phi'(s)]' = 0, \tag{1.25}$$

which can be written as

$$\frac{\partial\Phi(s)}{\partial s} = \Phi' = \frac{k}{w^2(s)}, \tag{1.26}$$

where k is an integration constant. Equation 1.23 can be written as

$$y(s) = w(s)\,(A_1\cos\Phi + A_2\sin\Phi), \tag{1.27}$$

which results in

$$y(s) = (A_1\,w' + \frac{A_2\,k}{w})\cos\Phi + (A_2\,w' + \frac{A_1\,k}{w})\sin\Phi, \tag{1.28}$$

where the constants A_1 and A_2 are expressed as

$$A_1 = \frac{x_0}{w}, \tag{1.29}$$

$$A_2 = \frac{x_0'\,w - x_0\,w'}{k}, \tag{1.30}$$

by imposing some initial conditions x_0 and $x_0^{'}$. $w(s)$ is a periodic function with periodicity L, the tranport matrix from s_0 to s_0+L is then:

$$M(s_0+L|s_0) = \begin{pmatrix} \cos\Phi - \frac{ww'}{k}\sin\Phi & \frac{w^2}{k}\sin\Phi \\ -\frac{1+(ww'/k)^2}{w^2/k}\sin\Phi & \cos\Phi + \frac{ww'}{k}\sin\Phi \end{pmatrix}, \tag{1.31}$$

where

$$\Phi = \Phi(s) - \Phi_0 = \Phi(s_0 \rightarrow s_0+L) = \int_{s_0}^{s_0+L} \frac{k\,ds}{w^2(s)}. \tag{1.32}$$

A new set of variables is commonly defined

$$\beta(s) = \frac{w^2(s)}{k}, \tag{1.33}$$

$$\alpha(s) = -\frac{1}{2}\frac{\partial\beta(s)}{\partial s}, \tag{1.34}$$

$$\gamma(s) = \frac{1+\alpha^2(s)}{\beta(s)}, \tag{1.35}$$

from which the transfer matrix $\mathbf{M}$ can be parametrized as

$$\mathbf{M} = \begin{pmatrix} \cos\Phi + \alpha\sin\Phi & \beta\sin\Phi \\ -\gamma\sin\Phi & \cos\Phi - \alpha\sin\Phi \end{pmatrix}, \tag{1.36}$$

where α, β and γ are the *Courant-Snyder parameters* and Φ is the *betatron phase advance* defined as

$$\Phi = \int_{s_0}^{s_0+L} \frac{ds}{\beta(s)}, \tag{1.37}$$

where L is the length of the periodic beam line for which $K(s+L) = K(s)$ and $\beta(s)$ is the *betatron amplitude function*. Considering an accelerator of circumference $C = NL$ with N identical superperiods, $N\Phi$ is the phase change per revolution and we can derive characteristic quantities Q_x and Q_y for an accelerator called the *betatron tunes*

$$Q_u = \frac{N\Phi_u}{2\pi} = \frac{1}{2\pi}\int_s^{s+C} \frac{ds}{\beta_y(s)}, \tag{1.38}$$

defined as the number of betatron oscillations per turn. The betatron oscillation frequency is $Q_u f_0$, where f_0 is the revolution frequency and $u = x, y$. The general solution of Equation 1.14 in the vertical plane becomes

$$y(s) = a\sqrt{\beta_y(s)}\cos[\Phi_y(s) + \Phi_0] \qquad \text{with} \qquad \Phi_y(s) = \int_0^s \frac{ds}{\beta_y(s)}, \tag{1.39}$$

where a and Φ_0 are constants to be determined by the initial conditions. This corresponds to a pseudo-harmonic oscillation with varying amplitude $\beta_y^{1/2}(s)$. From these results we can deduce that in an accelerator structure, the motion can be reconstructed knowing the evolution of the Courant-Snyder parameters and of the phase advance along the coordinate s.

1.3 Transverse Emittance

The particles distribution is generally described by a six dimensional density function $\rho(x, p_x, y, p_y, s, E)$ in which x, y, s represent the variables that define the coordinate system shown in Figure 1.1. $p_x \approx p x'$ and $p_y \approx p y'$ are the components of the momentum $p = E v/c^2$ in such coordinates and E is the particle energy. Its deviation from the ideal particle energy $\Delta E = E - E_0$ or the relative energy deviation $\Delta E/E_0$ are often taken as the sixth dimension. For a system at constant energy the transverse momenta are often replaced by the slope of the trajectories x' and y'. In linear dynamics the tranverse and longitudinal distributions are often considered as uncorrelated, the six dimensions can therefore be factorized into three independant phase-spaces (x,x'), (y,y') and (s,E).

1.3.1 Courant-Snyder Invariant

Recalling the general solution of the equation of motion 1.39 and replacing $\Phi_y(s) + \Phi_0$ by $\theta(s)$, we can write

$$y(s) = a\sqrt{\beta(s)}\cos\theta(s), \tag{1.40}$$

and

$$y'(s) = -\frac{a}{\sqrt{\beta(s)}}[\sin\theta(s) + \alpha(s)\cos\theta(s)]. \tag{1.41}$$

We can then introduce the expressions of $y(s)$ and $y'(s)$ in the following polynomial expression to get

$$\gamma y^2 + 2\alpha y y' + \beta y'^2 = a^2 \tag{1.42}$$

in which all the variables y, y', α, β, γ and θ are functions of s. The expression is referred to as the *Courant-Snyder invariant* and remains constant along a particular particule trajectory describing an ellipse, shown in Figure 1.2, in the phase space (y,y') which parameters are determined by the lattice functions α, β and γ at the location s. a^2 is referred to as the *emittance* of a single particle following its individual trajectory:

$$\varepsilon = a^2 = \frac{\text{Ellipse area}}{\pi} \tag{1.43}$$

The ellipse in phase space can have different orientations depending on the location s around the ring but its area remains constant.

1.3.2 Beam Emittance

So far only the motion of a single particle has been considered. However a beam consists of an ensemble of particles centered around the reference orbit. For any distribution of the particles it is possible to define a region in phase space occupied by the particles.

Given a normalized distribution function $\rho(y,y')$ with $\int\int \rho(y,y')\,dy\,dy' = 1$, the moments of the beam distribution are

$$\langle y\rangle = \int\int y\,\rho(y,y')\,dy\,dy',\ \langle y'\rangle = \int\int y'\,\rho(y,y')\,dy\,dy', \tag{1.44}$$

$$\sigma_y^2 = \int\int (y - \langle y\rangle)^2\,\rho(y,y')\,dy\,dy',\ \sigma_{y'}^2 = \int\int (y' - \langle y'\rangle)^2\,\rho(y,y')\,dy\,dy' \tag{1.45}$$

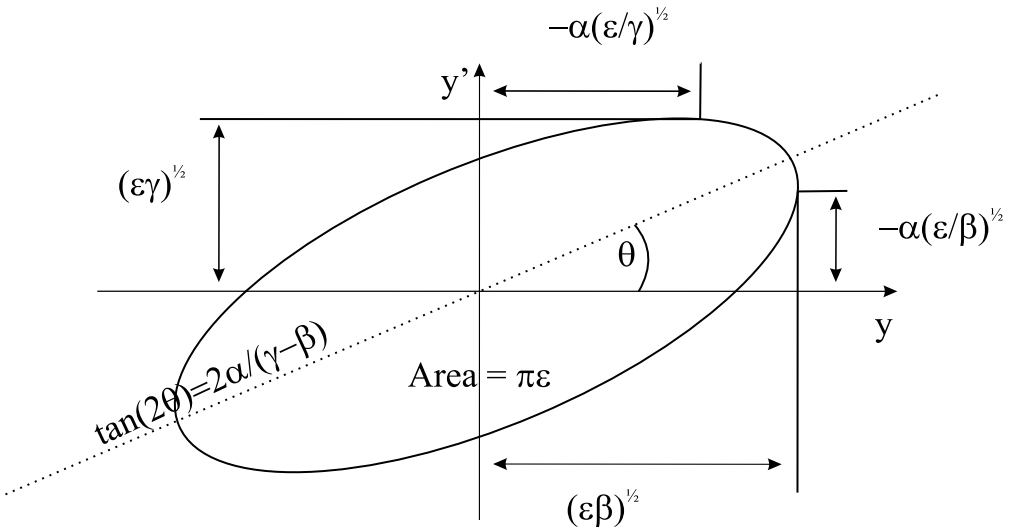

Figure 1.2: The motion of a single particle, at longitudinal location s is defining an ellipse characterized by the Courant-Snyder parameters α, β and γ.

$$\sigma_{yy'} = \int\int (y - \langle y \rangle)(y' - \langle y' \rangle)\, \rho(y,y')\, dy\, dy' = r\, \sigma_y\, \sigma_{y'}, \tag{1.46}$$

where σ_y and $\sigma_{y'}$ are the RMS beam widths, $\sigma_{yy'}$ is the correlation, and r is the correlation coefficient. The *RMS beam emittance* is then defined as:

$$\varepsilon_{\text{rms}} = \sqrt{\sigma_y^2\, \sigma_{y'}^2 - \sigma_{yy'}^2} = \sigma_y\, \sigma_{y'}\, \sqrt{1 - r^2}. \tag{1.47}$$

The RMS emittance is equal to the phase space area enclosed by the Courant-Snyder ellipse of the RMS particle. It can be shown that for a beam with RMS emittance $\pi\varepsilon$, the RMS beam width is $\sqrt{\beta\,\varepsilon}$ and the RMS beam divergence is $\sqrt{\gamma\,\varepsilon}$.

1.4 Beam-beam Interactions

This section briefly introduces the notion of beam-beam interactions. More details can be found in [2]. A particle beam is a collection of a large number of charges and represents an electromagnetic potential for other charges. It will therefore exert forces on the particles of the other beam and on itself. In the case of particle colliders these forces are experienced only when two beams cross each other. The forces are the most important for high density beams, i.e. high intensity and small beam sizes, which are the key for high luminosity. The beam-beam interactions are therefore often the limiting factor for the luminosity.

1.4.1 The Beam-beam Force

The distribution of particles producing fields can follow various possible functions, leading to different fields and forces. It is not always possible to integrate the distribution to get an analytical expression. We will therefore restrict ourself to the Gaussian beam case to derive analytical expressions. In the two-dimensional case of a Gaussian beam with density distribution $\rho(x,y) = \rho(x)\,\rho(y)$ in the transverse plane and with beam

sizes σ_x and σ_y:

$$\rho(u) = \frac{1}{\sigma_u\sqrt{2\pi}}\exp\left(-\frac{u^2}{2\sigma_u^2}\right) \quad \text{where} \quad u = x, y, \tag{1.48}$$

we can give a two dimensional potential $U(x, y, \sigma_x, \sigma_y)$ [3]:

$$U(x, y, \sigma_x, \sigma_y) = \frac{ne}{4\pi\varepsilon_0}\int_0^\infty \frac{\exp\left(-\frac{x^2}{2\sigma_x^2+q} - \frac{y^2}{2\sigma_y^2+q}\right)}{\sqrt{(2\sigma_x^2+q)(2\sigma_y^2+q)}}dq, \tag{1.49}$$

where n is the line density of particles in the beam, e is the elementary charge and ε_0 the permittivity of free space. The transverse fields $\overrightarrow{E}$ can be derived by taking $\overrightarrow{E} = -\nabla U(x, y, \sigma_x, \sigma_y)$ as demonstrated in [4]. In the case of elliptical beams and for $\sigma_x > \sigma_y$ we have:

$$E_x = \frac{ne}{2\varepsilon_0\sqrt{2\pi(\sigma_x^2-\sigma_y^2)}}\,\mathrm{Im}\left[\mathrm{erf}\left(\frac{x+iy}{\sqrt{2(\sigma_x^2-\sigma_y^2)}}\right) - \exp\left(-\frac{x^2}{2\sigma_x^2}+\frac{y^2}{2\sigma_y^2}\right)\mathrm{erf}\left(\frac{x\frac{\sigma_y}{\sigma_x}+iy\frac{\sigma_x}{\sigma_y}}{\sqrt{2(\sigma_x^2-\sigma_y^2)}}\right)\right], \tag{1.50}$$

and

$$E_y = \frac{ne}{2\varepsilon_0\sqrt{2\pi(\sigma_x^2-\sigma_y^2)}}\,\mathrm{Re}\left[\mathrm{erf}\left(\frac{x+iy}{\sqrt{2(\sigma_x^2-\sigma_y^2)}}\right) - \exp\left(-\frac{x^2}{2\sigma_x^2}+\frac{y^2}{2\sigma_y^2}\right)\mathrm{erf}\left(\frac{x\frac{\sigma_y}{\sigma_x}+iy\frac{\sigma_x}{\sigma_y}}{\sqrt{2(\sigma_x^2-\sigma_y^2)}}\right)\right]. \tag{1.51}$$

If $\sigma_y > \sigma_x$, x and y have to be inverted in the above expressions. The function $\mathrm{erf}(t)$ is the complex error function:

$$\mathrm{erf}(t) = e^{-t^2}\left[1 + \frac{2i}{\sqrt{\pi}}\int_0^t e^{z^2}dz\right]. \tag{1.52}$$

The magnetic field components follow from:

$$B_y = -\beta_r E_x/c \quad \text{and} \quad B_x = \beta_r E_x/c. \tag{1.53}$$

The Lorentz force acting on a particle with a charge q:

$$\overrightarrow{F} = q(\overrightarrow{E} + \overrightarrow{v} \times \overrightarrow{B}). \tag{1.54}$$

This expression can be simplified in the case of round beams ($\sigma_x = \sigma_y = \sigma$):

$$\overrightarrow{F} = q(E_r + \beta c B_\phi) \times \overrightarrow{r}, \tag{1.55}$$

and we get for the fields:

$$E_r = -\frac{ne}{4\pi\varepsilon_0}\frac{\partial}{\partial r}\left(\int_0^\infty \frac{\exp\left(-\frac{r^2}{2\sigma^2+q}\right)}{2\sigma^2+q}dq\right), \tag{1.56}$$

and

$$B_\phi = -\frac{ne\beta c\mu_0}{4\pi}\frac{\partial}{\partial r}\left(\int_0^\infty \frac{\exp\left(-\frac{r^2}{2\sigma^2+q}\right)}{2\sigma^2+q}dq\right). \tag{1.57}$$

We can now express the radial force as a function of the offset $r^2 = x^2 + y^2$:

$$F_r(r) = -\frac{ne^2(1+\beta^2)}{2\pi\varepsilon_0}\frac{1}{r}\left[1-\exp\left(-\frac{r^2}{2\sigma^2}\right)\right]. \tag{1.58}$$

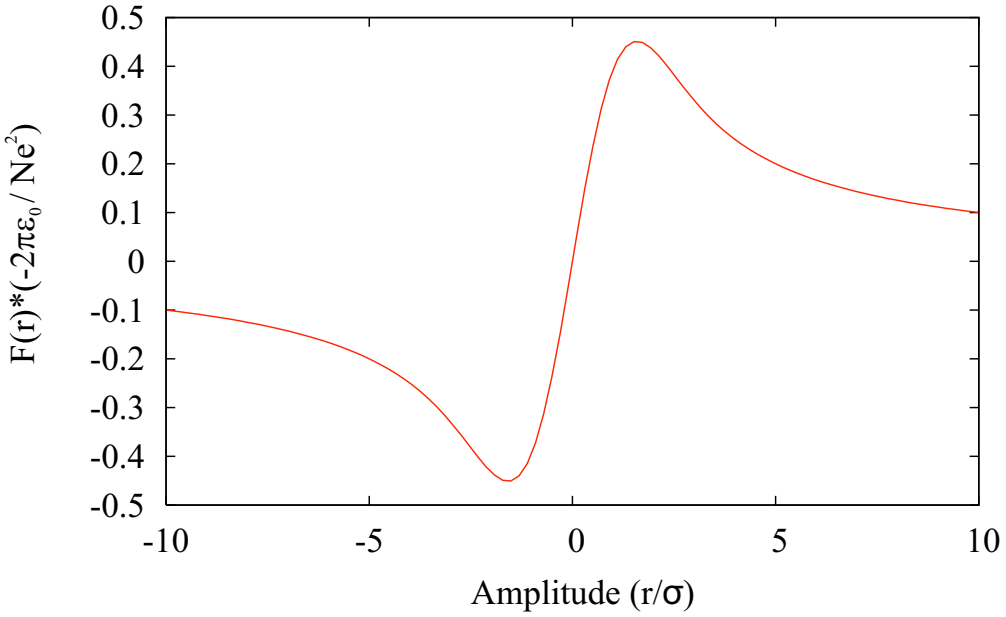

Figure 1.3: Beam-beam force for round beams. Force in arbitrary units and amplitude in units of RMS beam size.

Figure 1.3 shows the shape of the force as a function of the amplitude. For small amplitude it is approximately linear and will result in a change of the tune like in a quadrupole. This quadrupole will be defocusing when the beams have charges of the same sign and focusing when they have opposite signs. At larger amplitudes the force becomes strongly non-linear and the tune change is dependent on the amplitude. From this analytical form we can see that the beam-beam force includes higher multipoles and becomes non-linear at large amplitudes. We can therefore expect that a large number of resonances can be excited by the beam-beam force and that we will get all effects that are known from resonance and non-linear theory such as unstable motion and beam blow-up or bad lifetime.

1.4.2 Beam-beam Parameter

The linear beam-beam parameter represents the tune shift due to the beam-beam force at small amplitude. Starting from the two-dimensional force, multiplying it by the longitudinal distribution which depends on s and t and assuming the longitudinal shape is a Gaussian with width σ_s, we get for the force:

$$F_r(r,s,t) = -\frac{Ne^2(1+\beta^2)}{\sqrt{(2\pi)^3}\varepsilon_0\sigma_s}\frac{1}{r}\left[1-\exp\left(-\frac{r^2}{2\sigma^2}\right)\right]\left[\exp\left(-\frac{(s+vt)^2}{2\sigma_s^2}\right)\right], \tag{1.59}$$

where N is the total number of particle. The radial deflection can then be expressed as:

$$\Delta r' = \frac{1}{mc\beta\gamma}\int_{-\infty}^{+\infty} F_r(r,s,t)\,dt. \tag{1.60}$$

The radial kick $\Delta r'$ received by a particle with a radial distance r from the opposite beam center is then:

$$\Delta r' = -\frac{2Nr_0}{\gamma}\frac{1}{r}\left[1-\exp\left(-\frac{r^2}{2\sigma^2}\right)\right], \tag{1.61}$$

where γ is the relativistic Lorentz factor and r_0 is the classical particle radius

$$r_0 = \frac{e^2}{4\pi\varepsilon_0 mc^2}, \tag{1.62}$$

where m is the mass of the particle. For small amplitudes r we can derive the asymptotic limit:

$$\Delta r'|_{r\to 0} = -\frac{Nr_0 r}{\gamma\sigma^2}. \tag{1.63}$$

This limit is the slope of the force at $r = 0$. From the proportionality factor which represents a focal length we can derive a quantity ξ which is known as the *linear beam-beam parameter*:

$$\xi = \frac{Nr_0\beta^*}{4\pi\gamma\sigma^2}, \tag{1.64}$$

where β^* is the β-function at the interaction point. The beam-beam parameter can be generalized to the case of non-round beams [3]:

$$\xi_{x,y} = \frac{Nr_0\beta^*_{x,y}}{2\pi\gamma\sigma^2_{x,y}(\sigma_x+\sigma_y)}. \tag{1.65}$$

The beam-beam parameter is often used to quantify the strength of the beam-beam interactions, however it only reflects the linear part of the force.

1.4.3 Long-range Interactions

So far only the case with two bunches interacting head-on was considered. In the LHC, the beams consist of trains of bunches with up to 2808 bunches per beam. In order to avoid collisions away from the interaction point the beams cross with an angle which allows for collisions at the interaction point and separates them in other places. The details of the crossing angle are presented in more details in Chapter 3. Close to the interaction point, where they travel in a common beam pipe, the bunches will feel the electromagnetic forces from the bunches of the opposing beam as illustrated Figure 1.4. These are called *long-range interactions*.

Although the long-range interactions distort the beams much less than a head-on interaction, their large number (30 for IP1 and IP5 with nominal filling scheme) implies non-negligible effects. Figure 1.5 illustrates the effect of the long-range interactions on the tune footprint. We can see that the particles at large amplitude are more affected by the long-range interactions while at small amplitude the effect of the head-on interactions dominates. In addition, not all the bunches experience the same number of head-on collisions and long-range interactions. In the LHC the bunches will therefore travel on different closed orbits and with different tunes depending on their collision pattern.

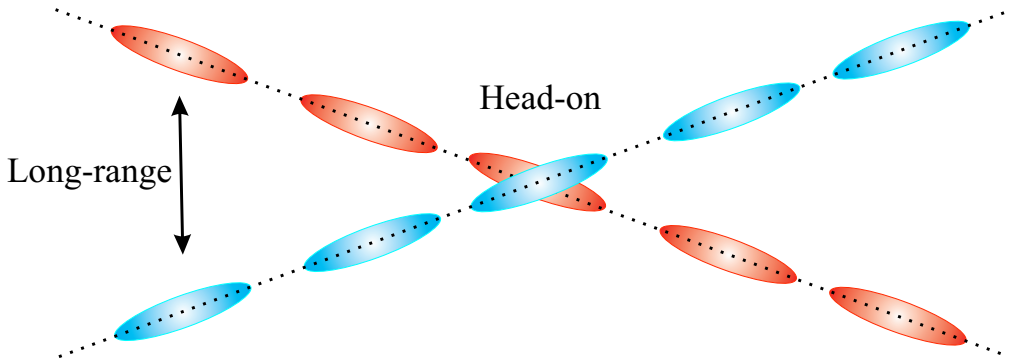

Figure 1.4: Head-on and long-range interactions in an LHC interaction point.

1.5 Luminosity

In a particle collider, the most important performance parameters are the beam energy and the luminosity. The energy available for the production of new effects is the most important parameter. The required large center of mass energy can only be provided with colliding beams. Besides the energy the other important parameter is the rate of useful interactions, usually called *events*. The quantity that defines the ability of a collider to produce events is called the *luminosity* $\mathcal{L}$ and is the proportionality factor between the event rate $\dot{N}$ and the cross section of the observed event σ:

$$\dot{N} = \mathcal{L}\sigma. \tag{1.66}$$

The unit used for the luminosity is therefore $\mathrm{cm}^{-2}\mathrm{s}^{-1}$. In this section generalized equations will be derived. Additional effects such as crossing angle, offset collisions and hourglass effect as well as their consequences on the luminosity will be described and different methods for absolute luminosity determination will be presented. Only the case of bunched beams, as relevant for the LHC will be considered. The calculation for unbunched beams is presented in [5]. A discussion of the general the concept and operational aspects can be found in [6].

1.5.1 Head-on Collisions

In order to compute the luminosity for two colliding bunched beams several parameters have to be taken into account. The density distribution of each beam in the transverse and longitudinal planes are obviously very important. In addition, the two beams are moving towards and through each other. The longitudinal position and therefore the time as they cross each other has also to be considered. To integrate the luminosity we use the distance to the central collision point $s_0 = vt$ where the velocity of the bunch is $v = \beta c$. In the relativistic case we get $s_0 = ct$ which we use as the time-dependant integration variable. Hence, the general equation for luminosity, represents a convolution of the 3-D time dependant distribution functions of the two beams as described in [3].

In principle the two beams have different distribution functions and number of particles as shown Figure 1.6. The overlap integral of the distribution functions is proportional to the luminosity and can be written as:

$$\mathcal{L} = N_1 N_2 f N_b K \int\int\int\int_{-\infty}^{+\infty} \rho_1(x,y,s,-s_0)\,\rho_2(x,y,s,s_0)\,dx\,dy\,ds\,ds_0, \tag{1.67}$$

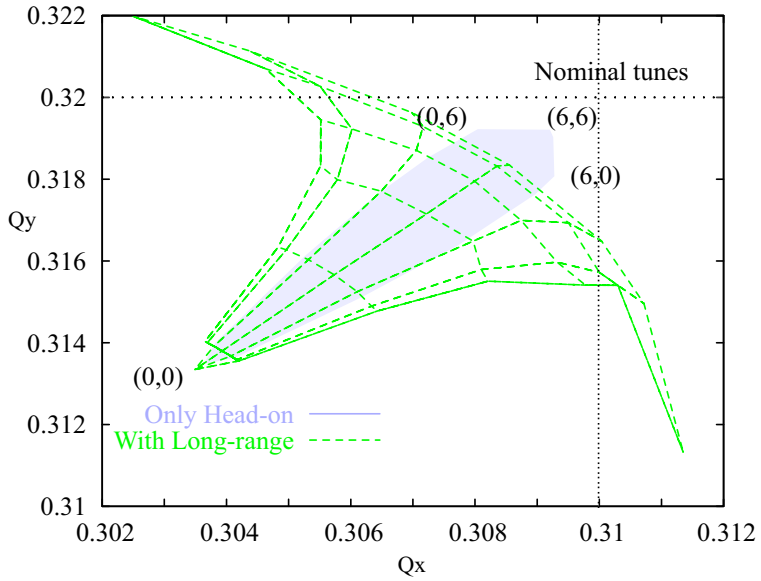

Figure 1.5: Tune footprint with and without long-range interactions. Nominal tunes are 0.31 and 0.32. The coordinates represent the particle amplitude in x and y expressed in units of RMS beam size. The maximum tune shift is observed at (0,0).

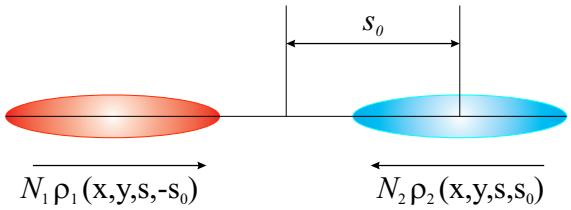

Figure 1.6: Schematic view of two colliding bunches where N_i is the number of particles per bunch (intensity) and ρ_i is the density function. s_0 is the distance from the central collision point.

where ρ_1 and ρ_2 are the time dependant distribution functions of the two beams, N_1 and N_2 are the bunch intensities, f is the revolution frequency and N_b is the number of colliding bunches. Assuming the beams are colliding at $s_0 = 0$ and because they move against each other, the kinematic factor K is defined as [7]:

$$K = \sqrt{(\overrightarrow{v_1} - \overrightarrow{v_2})^2 - (\overrightarrow{v_1} \times \overrightarrow{v_2})^2/c^2}. \tag{1.68}$$

In the case of head on collisions where $\overrightarrow{v_1} = -\overrightarrow{v_2}$ and in the ultra-relativistic approximation the kinematic factor $K = 2$. Assuming all densities are uncorrelated in all planes we can factorize the distribution functions and the luminosity becomes:

$$\mathcal{L} = 2 N_1 N_2 f N_b \int\int\int\int_{-\infty}^{+\infty} \rho_{1x}(x)\,\rho_{1y}(y)\,\rho_{1s}(s-s_0)\,\rho_{2x}(x)\,\rho_{2y}(y)\,\rho_{2s}(s+s_0)\,dx\,dy\,ds\,ds_0, \tag{1.69}$$

In order to evaluate this integral all distributions should be known. In general, the beam profile can be evaluated as a Gaussian distribution and the integral calculated analytically. The profiles in all dimensions

for a Gaussian beam are expressed as:

$$\rho_{iu}(u) = \frac{1}{\sigma_{iu}\sqrt{2\pi}} \exp\left(-\frac{u^2}{2\sigma_{iu}^2}\right) \quad \text{where } i = 1,2 \text{ and } u = x,y, \tag{1.70}$$

$$\rho_{is}(s \pm s_0) = \frac{1}{\sigma_{is}\sqrt{2\pi}} \exp\left(-\frac{(s \pm s_0)^2}{2\sigma_{is}^2}\right) \quad \text{where } i = 1,2. \tag{1.71}$$

Using these expressions in equation 1.69 the overlap integral becomes:

$$\begin{aligned} \mathcal{L} &= \frac{2N_1 N_2 f N_b}{(\sqrt{2\pi})^6 \sigma_{1x}^2 \sigma_{2x}^2 \sigma_{1y}^2 \sigma_{2y}^2 \sigma_{1s}^2 \sigma_{2s}^2} \cdot \\ &\int\int\int\int_{-\infty}^{+\infty} e^{-x^2\left(\frac{1}{2\sigma_{1x}^2}+\frac{1}{2\sigma_{2x}^2}\right)-y^2\left(\frac{1}{2\sigma_{1y}^2}+\frac{1}{2\sigma_{2y}^2}\right)-\frac{(s-s_0)^2}{2\sigma_{1s}^2}-\frac{(s+s_0)^2}{2\sigma_{2s}^2}} dx dy ds ds_0. \end{aligned} \tag{1.72}$$

The equation can be integrated using the formulae for an arbitrary Gaussian [8]:

$$\int_{-\infty}^{+\infty} e^{-(ax^2+2bx+c)}\, dx = \sqrt{\frac{\pi}{a}} \exp\left[\frac{b^2 - ac}{a}\right]. \tag{1.73}$$

A detailed calculation is presented in [9]. After integration the general expression of the luminosity for unequal Gaussian bunched beams colliding head-on is:

$$\mathcal{L} = \frac{N_1 N_2 f N_b}{2\pi\sqrt{\sigma_{1x}^2 + \sigma_{2x}^2}\sqrt{\sigma_{1y}^2 + \sigma_{2y}^2}} = \mathcal{L}_0. \tag{1.74}$$

It is worth mentioning that the luminosity does not depend on the bunch length σ_s in the case of head-on collisions. This is due to the assumption that the density distributions are not correlated. This expression assumes bunches of equal intensities. If this is not the case the luminosity contribution of each bunch crossing has to be properly summed in order to obtain the total luminosity. This expression is the maximum luminosity one can achieve for perfect head-on collisions. In practice we have to include additional effects which reduce the maximum achievable luminosity.

1.5.2 Offset Collisions

The two counter rotating beams do not always collide head-on and the beam distributions can be shifted in the horizontal and vertical directions by arbitrary amounts x_i and y_i where $i = 1,2$. The transverse profile is then expressed as:

$$\rho_{iu}(u) = \frac{1}{\sigma_{iu}\sqrt{2\pi}} \exp\left(-\frac{(u-u_i)^2}{2\sigma_{iu}^2}\right) \quad \text{where } i = 1,2 \text{ and } u = x,y. \tag{1.75}$$

The velocities of the beams are still collinear and the kinematic factor is unchanged. We can carry out the integration of the luminosity and obtain

$$\mathcal{L} = \mathcal{L}_0 \exp\left[-\frac{\delta x^2}{2(\sigma_{1x}^2 + \sigma_{2x}^2)} - \frac{\delta y^2}{2(\sigma_{1y}^2 + \sigma_{2y}^2)}\right], \tag{1.76}$$

where $\delta x = x_1 - x_2$ and $\delta y = y_1 - y_2$ indicate the relative displacements of the centroids of the two beams in the transverse plane. The dependence of the luminosity on the transverse offset is a Gaussian

function. The RMS of this Gaussian function is directly related to the transverse sizes of the two beams. Using this property one can optimize the luminosity and measure the transverse beam sizes, hence calibrate the absolute luminosity, by scanning the transverse planes. This method for luminosity optimization and calibration is called the Van Der Meer scan method and was first used in the ISR [1].

1.5.3 Crossing Angle

When the bunch spacing becomes small, it is necessary to introduce a crossing angle at the interaction point in order to avoid unwanted interactions. When the LHC reaches its nominal performance each beam will consist of almost 3000 closely spaced bunches and will collide with an angle of about 300 μrad. In the following calculation the crossing angle will be in the horizontal plane. The same results apply in the case of a vertical crossing angle. The overlap integral was calculated above in the x and y coordinate system. In order to compute the effect of the crossing angle we have to transform the bunches in the proper coordinate system as previously shown in [3].

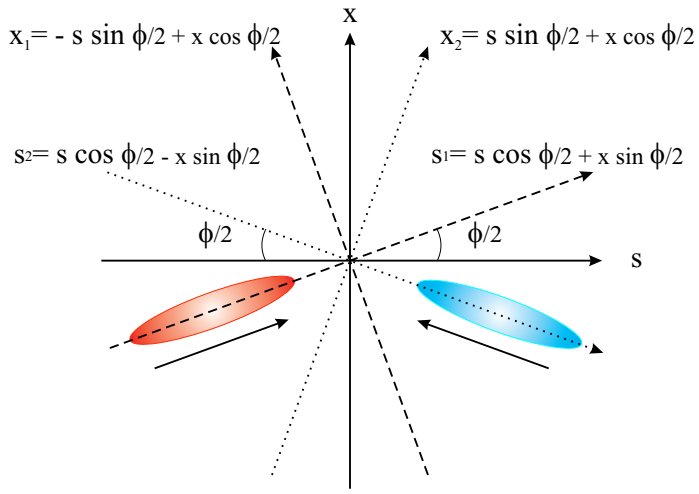

Figure 1.7: Rotated reference system for collisions with crossing angle ϕ.

We can apply a rotation corresponding to $\pm\phi/2$ for beam 1 and beam 2 respectively in order to keep the symmetry as shown Figure 1.7. x and s are now different for the two beams:

$$x_1 = x\cos\frac{\phi}{2} - s\sin\frac{\phi}{2} \quad , \qquad s_1 = s\cos\frac{\phi}{2} + x\sin\frac{\phi}{2}, \tag{1.77}$$

$$x_2 = x\cos\frac{\phi}{2} + s\sin\frac{\phi}{2} \quad , \qquad s_2 = s\cos\frac{\phi}{2} - x\sin\frac{\phi}{2}. \tag{1.78}$$

The velocities of the bunches are not collinear anymore and the kinematic factor becomes $K = 2\cos^2\frac{\phi}{2}$. The luminosity is then expressed as:

$$\mathcal{L} = \frac{2N_1N_2fN_b\cos^2\frac{\phi}{2}}{(\sqrt{2\pi})^6\sigma_{1x}^2\sigma_{2x}^2\sigma_{1y}^2\sigma_{2y}^2\sigma_{1s}^2\sigma_{2s}^2}\int\int\int\int_{-\infty}^{+\infty} e^{-y^2\left(\frac{1}{2\sigma_{1y}^2}+\frac{1}{2\sigma_{2y}^2}\right)} \cdot e^{-\frac{(s\cos\frac{\phi}{2}+x\sin\frac{\phi}{2}-s_0)^2}{2\sigma_{1s}^2}-\frac{(s\cos\frac{\phi}{2}-x\sin\frac{\phi}{2}+s_0)^2}{2\sigma_{2s}^2}-\frac{(x\cos\frac{\phi}{2}-s\sin\frac{\phi}{2})^2}{2\sigma_{1s}^2}-\frac{(x\cos\frac{\phi}{2}+s\sin\frac{\phi}{2})^2}{2\sigma_{2s}^2}} dxdyds\,ds_0, \tag{1.79}$$

and after integration:

$$\mathcal{L} = \mathcal{L}_0 \frac{1}{\sqrt{1+\frac{\sigma_{1s}^2+\sigma_{2s}^2}{\sigma_{1x}^2+\sigma_{2x}^2}\left(\tan\frac{\phi}{2}\right)^2}}. \tag{1.80}$$

Colliding beams with a crossing angle will therefore reduce the luminosity by a factor:

$$S_u = \frac{1}{\sqrt{1+\frac{\sigma_{1s}^2+\sigma_{2s}^2}{\sigma_{1u}^2+\sigma_{2u}^2}\left(\tan\frac{\phi}{2}\right)^2}}, \tag{1.81}$$

where $u = x, y$ depending on the plane where the crossing angle is applied. This can be interpreted as a correction factor to the beam size and leads to the definition of the effective beam size as seen by the luminosity:

$$\sigma_{\text{eff}} = \sigma_u \sqrt{1+\frac{\sigma_{1s}^2+\sigma_{2s}^2}{\sigma_{1u}^2+\sigma_{2u}^2}\left(\tan\frac{\phi}{2}\right)^2}. \tag{1.82}$$

This concept of effective beam size also applies to the calculation of beam-beam effects in the presence of a crossing angle [3].

This formula can be generalized to the case where a crossing angle is seen in the horizontal and vertical plane. To characterize the system we first have to define a certain number of parameters:

- $\frac{\phi_x}{2}$ is the angle between the projection of the trajectory on the (x,s) plane and the s-axis.
- $\frac{\phi_y}{2}$ is the angle between the projection of the trajectory on the (y,s) plane and the s-axis.
- $\frac{\phi'_x}{2}$ is the angle between the trajectory and the (y,s) plane.
- $\frac{\phi'_y}{2}$ is the angle between the trajectory and the (x,s) plane.
- $\frac{\phi}{2}$ is the angle between the trajectory and the s-axis. ϕ is the total effective crossing angle.

The values of all these angles are of opposite signs for beam 1 and beam 2 such that the system is symmetric about the central collision point. The various angles relate to each other as follows:

$$\begin{cases} \tan\frac{\phi'_x}{2} = \tan\frac{\phi_x}{2}\cos\frac{\phi_y}{2}, \\ \tan\frac{\phi'_y}{2} = \tan\frac{\phi_y}{2}\cos\frac{\phi_x}{2}, \\ \tan^2\frac{\phi}{2} = \tan^2\frac{\phi_x}{2} + \tan^2\frac{\phi_y}{2}. \end{cases} \tag{1.83}$$

The transformation of the bunches into the proper coordinate system will then consist of two consecutive rotations of ϕ_x and ϕ'_y or ϕ_y and ϕ'_x for beam 1 and $-\phi_x$ and $-\phi'_y$ or $-\phi_y$ and $-\phi'_x$ for beam 2. Assuming we first rotate about the x-axis by ϕ_y and then about the new y-axis by ϕ'_x this leads to:

$$\begin{cases} x_1 = x\cos\frac{\phi_y}{2} + s\sin\frac{\phi_y}{2}, \\ x_2 = x\cos\frac{\phi_y}{2} - s\sin\frac{\phi_y}{2}, \\ y_1 = y\cos\frac{\phi'_x}{2} + s\cos\frac{\phi_y}{2}\sin\frac{\phi'_x}{2} - x\sin\frac{\phi_y}{2}\sin\frac{\phi'_x}{2}, \\ y_2 = y\cos\frac{\phi'_x}{2} - s\cos\frac{\phi_y}{2}\sin\frac{\phi'_x}{2} - x\sin\frac{\phi_y}{2}\sin\frac{\phi'_x}{2}, \\ s_1 = s\cos\frac{\phi'_x}{2}\cos\frac{\phi_y}{2} - y\sin\frac{\phi'_x}{2} - x\cos\frac{\phi'_x}{2}\sin\frac{\phi_y}{2} - s_0, \\ s_2 = s\cos\frac{\phi'_x}{2}\cos\frac{\phi_y}{2} + y\sin\frac{\phi'_x}{2} + x\cos\frac{\phi'_x}{2}\sin\frac{\phi_y}{2} + s_0. \end{cases} \tag{1.84}$$

In this case the kinematic factor becomes $K = 2\cos^2\frac{\phi'_x}{2}\cos^2\frac{\phi_y}{2}$. Using these expressions to carry out the integration we get

$$\mathcal{L} = \mathcal{L}_0 \frac{1}{\sqrt{1+\frac{\sigma_{1s}^2+\sigma_{2s}^2}{\sigma_{1y}^2+\sigma_{2y}^2}\left(\tan\frac{\phi_y}{2}\right)^2+\frac{\sigma_{1s}^2+\sigma_{2s}^2}{\sigma_{1x}^2+\sigma_{2x}^2}\left(\frac{\tan\frac{\phi'_x}{2}}{\cos\frac{\phi_y}{2}}\right)^2}}. \tag{1.85}$$

Replacing $\tan\frac{\phi'_x}{2}$ by $\tan\frac{\phi_x}{2}\cos\frac{\phi_y}{2}$ we are left with

$$\mathcal{L} = \mathcal{L}_0 \frac{1}{\sqrt{1+\frac{\sigma_{1s}^2+\sigma_{2s}^2}{\sigma_{1y}^2+\sigma_{2y}^2}\left(\tan\frac{\phi_y}{2}\right)^2+\frac{\sigma_{1s}^2+\sigma_{2s}^2}{\sigma_{1x}^2+\sigma_{2x}^2}\left(\tan\frac{\phi_x}{2}\right)^2}}. \tag{1.86}$$

Rotating first about the y-axis by ϕ_x and then about the new x-axis by ϕ'_y gives the same result. The generalized reduction factor for collisions with crossing angle is then:

$$S = \frac{1}{\sqrt{1+\frac{\sigma_{1s}^2+\sigma_{2s}^2}{\sigma_{1y}^2+\sigma_{2y}^2}\left(\tan\frac{\phi_y}{2}\right)^2+\frac{\sigma_{1s}^2+\sigma_{2s}^2}{\sigma_{1x}^2+\sigma_{2x}^2}\left(\tan\frac{\phi_x}{2}\right)^2}}. \tag{1.87}$$

1.5.4 Crossing Angle and Offset Beams

In real machines, misalignments and magnetic imperfections are the source of orbit distortions which lead to a combination of these two effects. Figure 1.8 shows a schematic view of two bunches colliding with offsets and crossing angle in the horizontal plane.

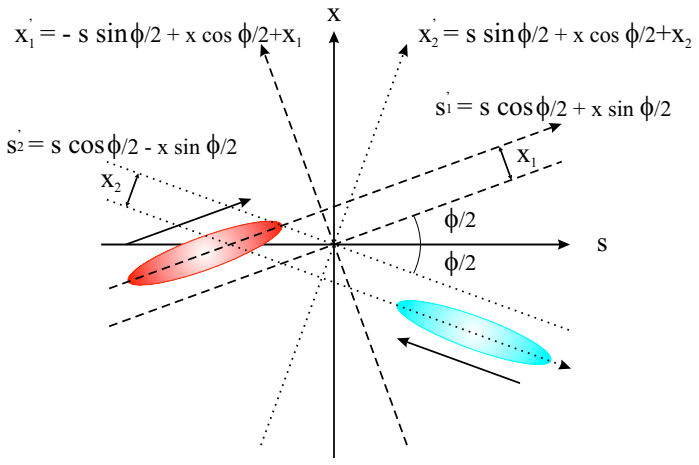

Figure 1.8: Transformed system for collisions with crossing angle ϕ and offsets x_1 and x_2 in the horizontal plane.

The transformed coordinates for the two beams are now:

$$\begin{aligned} x'_1 &= x_1 + x_{01}, \quad & y'_1 &= y_1 + y_{01}, \quad & s'_1 &= s_1, \\ x'_2 &= x_2 + x_{02}, \quad & y'_1 &= y_1 + y_{01}, \quad & s'_1 &= s_1. \end{aligned} \tag{1.88}$$

Following the previous integration strategy, we can rewrite the luminosity with three correction factors:

$$\mathcal{L} = \mathcal{L}_0 \cdot S \cdot T \cdot U, \tag{1.89}$$

where

$$S = \frac{1}{\sqrt{1 + \frac{\sigma_{1s}^2+\sigma_{2s}^2}{\sigma_{1y}^2+\sigma_{2y}^2}\left(\tan\frac{\phi_y}{2}\right)^2 + \frac{\sigma_{1s}^2+\sigma_{2s}^2}{\sigma_{1x}^2+\sigma_{2x}^2}\left(\tan\frac{\phi_x}{2}\right)^2}}, \tag{1.90}$$

and

$$T = \exp\left[-\frac{\delta x^2}{2\left(\sigma_{1x}^2+\sigma_{2x}^2\right)} - \frac{\delta y^2}{2\left(\sigma_{1y}^2+\sigma_{2y}^2\right)}\right], \tag{1.91}$$

and

$$U = \exp\left[S^2\,\frac{\sigma_{1s}^2+\sigma_{2s}^2}{2}\left(\frac{\delta x\tan\frac{\phi_x}{2}}{\sigma_{1x}^2+\sigma_{2x}^2} + \frac{\delta y\tan\frac{\phi_y}{2}}{\sigma_{1y}^2+\sigma_{2y}^2}\right)^2\right]. \tag{1.92}$$

The factorization enlightens the different contributions. T and S are the already calculated reduction factors from the crossing angle and offset and U is only present when we have both effects simultaneously.

1.5.5 Hourglass Effect

In the previous calculations we assumed that the beam density functions are uncorrelated in the transverse and longitudinal planes and that the beam sizes were constant over the whole collision region. In reality, and in particular for low-β^* insertions, this is not always a good approximation. The β-function in a drift space varies with the distance to the minimum like:

$$\beta(s) = \beta^*\left(1 + \frac{s^2}{\beta^{*2}}\right), \tag{1.93}$$

and therefore the beam size $\sigma = \sqrt{\beta(s)\,\varepsilon}$

$$\sigma(s) = \sigma^*\sqrt{1 + \frac{s^2}{\beta^{*2}}}. \tag{1.94}$$

Figure 1.9 displays the evolution of the β-function and the beam size as a function of the distance from the interaction point for two different values of β^* (11 m and 0.55 m). The name hourglass effect comes from the shape of $\beta(s)$. The hourglass effect is then larger as the β^* gets smaller and becomes important when β^* is equal or smaller than the bunch length σ_s. In this case not all particles collide at the minimum of the transverse beam sizes and the luminosity is reduced. In order to take into account this effect we have to replace in the luminosity formulae σ by $\sigma(s)$. The luminosity for head-on collision before integration over s is expressed as:

$$\mathcal{L} = \frac{N_1 N_2 f N_b}{\sqrt{2}\pi^{3/2}\sqrt{\sigma_{1s}^2+\sigma_{2s}^2}}\int_{-\infty}^{+\infty}\frac{\exp\left[\frac{2s^2}{\sigma_{1s}^2+\sigma_{2s}^2}\right]}{(\sigma_{1x}^2(s)+\sigma_{2x}^2(s))(\sigma_{1y}^2(s)+\sigma_{2y}^2(s))}\,ds. \tag{1.95}$$

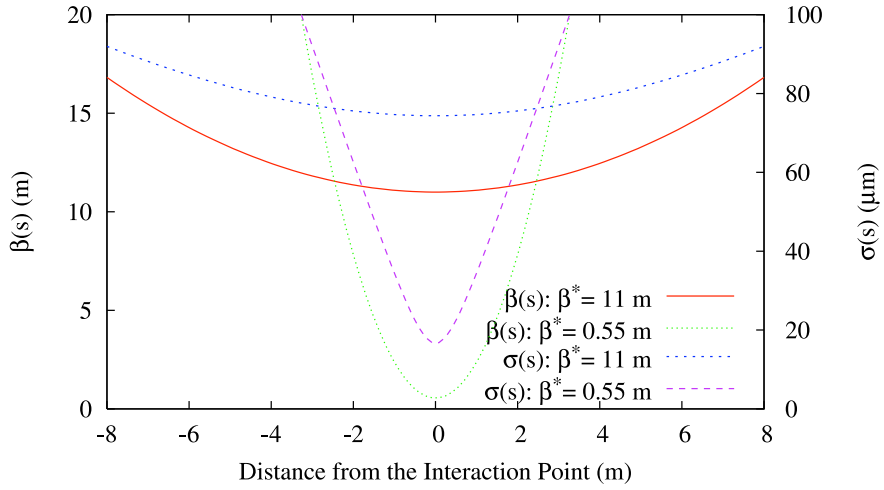

Figure 1.9: β-function and beam size at 7 TeV in a drift space as a function of the distance from the IP.

After changing the integration variable to $t = \frac{\sqrt{2}s}{\sqrt{\sigma_{1s}^2+\sigma_{2s}^2}}$ and having defined the variable

$$t_u^2 = \frac{2\,(\sigma_{1u}^{*2}+\sigma_{2u}^{*2})}{(\sigma_{1s}^2+\sigma_{2s}^2)(\sigma_{1u}^{*2}/\beta_{1u}^{*2}+\sigma_{1u}^{*2}/\beta_{1u}^{*2})}, \quad \text{where} \quad u = x, y, \tag{1.96}$$

we can derive a new expression for the luminosity:

$$\mathcal{L} = \mathcal{L}_0 \int_{-\infty}^{+\infty} \frac{1}{\sqrt{\pi}} \frac{e^{-t^2}}{\sqrt{(1+t^2/t_x^2)(1+t^2/t_y^2)}}\, dt, \tag{1.97}$$

where

$$\mathcal{L}_0 = \frac{N_1 N_2 f N_b}{2\pi\sqrt{\sigma_{1x}^{*2}+\sigma_{2x}^{*2}}\sqrt{\sigma_{1y}^{*2}+\sigma_{2y}^{*2}}}, \tag{1.98}$$

as previously demonstrated in [10]. $\mathcal{L}_0$ is equivalent to the one computed for head-on collisions for which we made the hypothesis of constant beam sizes over the collision region ($\sigma(s) = \sigma^*$). When $\sigma_s \gg \sigma_{x,y}$ we have $t_x, t_y \to \infty$ and therefore $\mathcal{L} \to \mathcal{L}_0$ as expected. For the LHC the lattice is designed such that $\beta_{1x}^* = \beta_{2x}^* = \beta_{1y}^* = \beta_{2y}^* = \beta^*$. Assuming the machine is fully corrected we get

$$t_x^2 = t_y^2 = t_r^2 = \frac{2\beta^{*2}}{\sigma_{1s}^2+\sigma_{2s}^2}, \tag{1.99}$$

and

$$\mathcal{L} = \mathcal{L}_0 \int_{-\infty}^{+\infty} \frac{1}{\sqrt{\pi}} \frac{e^{-t^2}}{(1+t^2/t_r^2)}\, dt = \mathcal{L}_0\, \sqrt{\pi} t_r\, e^{t_r^2}\, \mathrm{erfc}(\mathrm{t_r}), \tag{1.100}$$

where erfc(z) is the complementary error function

$$\mathrm{erfc(z)} = \int_{\mathrm{z}}^{+\infty} \mathrm{e}^{-\mathrm{t}^2}\,\mathrm{dt}. \tag{1.101}$$

Including the effect of the crossing angle we get:

$$\mathcal{L} = \mathcal{L}_0 \frac{\sqrt{K}}{\sqrt{\pi}\sqrt{\sigma_{1s}^2+\sigma_{2s}^2}} \int_{-\infty}^{+\infty} \frac{e^{-s^2 \frac{K}{(\sigma_{1s}^2+\sigma_{2s}^2)S^2(s)}}}{1+\frac{s^2}{\beta^{*2}}} ds, \tag{1.102}$$

which can be simplified with the following change of variables:

$$t_r^2 = \frac{K\beta^{*2}}{\sigma_{1s}^2+\sigma_{2s}^2}, \tag{1.103}$$

and

$$t^2 = \frac{Ks^2}{\sigma_{1s}^2+\sigma_{2s}^2}, \tag{1.104}$$

as

$$\mathcal{L} = \mathcal{L}_0 \frac{1}{\sqrt{\pi}} \int_{-\infty}^{+\infty} \frac{e^{-\frac{t^2}{S^2(t)}}}{1+\frac{t^2}{t_r^2}} dt, \tag{1.105}$$

where K is the kinematic factor and S is reduction factor due to the crossing angle replacing σ by $\sigma(t)$. This last integral is difficult to compute analytically and is generally estimated numerically.

1.5.6 Linear Coupling

In the presence of coupled lattices the beam ellipse in the (x,y) plane can be tilted by an angle ϕ. Moreover in asymmetric colliders the tilt angles can be different for each beam and will result in a reduction of luminosity as demonstrated in [11]. The coupling angle calculation is detailed in Appendix B.

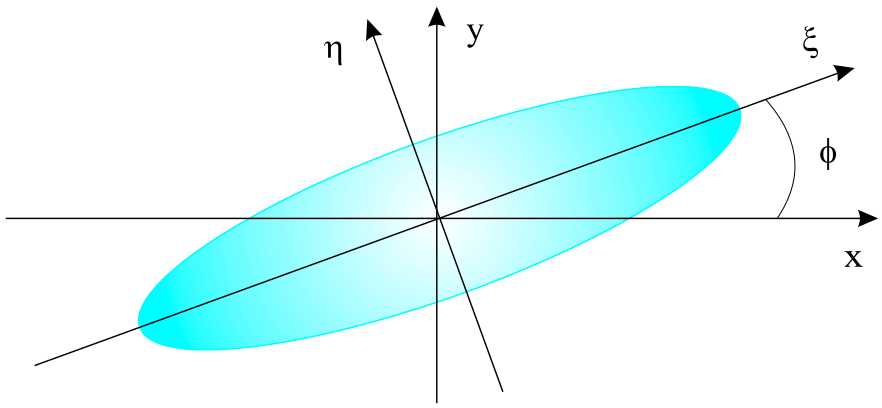

Figure 1.10: Titled Beam ellipse. ϕ is the tilt angle, (ξ,η) is the rotated coordinate system in which the σ-matrix is diagonalized.

The 2D normalized density function in case of a Gaussian beam can be expressed as:

$$\rho(x,y) = \frac{\sqrt{\det\Sigma^{-1}}}{2\pi} \exp\left(-\frac{1}{2} z^T \cdot \Sigma^{-1} \cdot z\right), \tag{1.106}$$

where z is the vector describing the beam coordinates:

$$z = \begin{pmatrix} x \\ y \end{pmatrix}, \tag{1.107}$$

and Σ^{-1} is the inverse of the sigma matrix

$$\Sigma = \begin{pmatrix} \sigma_{xx} & \sigma_{xy} \\ \sigma_{xy} & \sigma_{yy}, \end{pmatrix} \tag{1.108}$$

where σ_{xx}, σ_{yy} and σ_{xy} are the moments defined in Equations 1.45 and 1.46 for the (x,y) plane. The matrix Σ^{-1} can be diagonalized by a simple rotation as illustrated Figure 1.10:

$$\begin{pmatrix} \xi \\ \eta \end{pmatrix} = \begin{pmatrix} \cos\phi & \sin\phi \\ -\sin\phi & \cos\phi \end{pmatrix} = \begin{pmatrix} x \\ y \end{pmatrix}, \tag{1.109}$$

where ϕ is the tilt angle. The elements of Σ^{-1} in this rotated coordinate system become:

$$\begin{cases} \Sigma_{xx}^{-1} = \left(\frac{\cos^2\phi}{\sigma_\xi^2} + \frac{\sin^2\phi}{\sigma_\eta^2} \right), \\ \Sigma_{yy}^{-1} = \left(\frac{\sin^2\phi}{\sigma_\xi^2} + \frac{\cos^2\phi}{\sigma_\eta^2} \right), \\ \Sigma_{xy}^{-1} = \left(\frac{1}{\sigma_\xi^2} - \frac{1}{\sigma_\eta^2} \right) \sin\phi\cos\phi, \end{cases} \tag{1.110}$$

where σ_ξ and σ_η are the beam sizes along the ξ and η axis. The condition on the tilt angle for the matrix to be diagonal is:

$$\tan 2\phi = \frac{2\Sigma_{xy}^{-1}}{\Sigma_{xx}^{-1} - \Sigma_{yy}^{-1}},$$

and the beam sizes along the rotated axes are:

$$\begin{aligned} \frac{1}{\sigma_\xi^2} &= \frac{1}{2}\left[\Sigma_{xx}^{-1} + \Sigma_{yy}^{-1} + \frac{\Sigma_{xx}^{-1} - \Sigma_{yy}^{-1}}{\cos 2\phi} \right], \\ \frac{1}{\sigma_\eta^2} &= \frac{1}{2}\left[\Sigma_{xx}^{-1} + \Sigma_{yy}^{-1} - \frac{\Sigma_{xx}^{-1} - \Sigma_{yy}^{-1}}{\cos 2\phi} \right]. \end{aligned} \tag{1.111}$$

We can now integrate the overlap integral in the transverse plane

$$\mathcal{L} = N_1 N_2 f N_b \int\int_{-\infty}^{+\infty} \rho_1(x,y)\,\rho_2(x,y)\,dx\,dy = N_1 N_2 f N_b \frac{\sqrt{\det\Sigma_1^{-1}\det\Sigma_2^{-1}}}{2\pi\sqrt{\det\left(\Sigma_1^{-1} + \Sigma_2^{-1}\right)}}. \tag{1.112}$$

This leads to

$$\mathcal{L} == \mathcal{L}_0 \frac{1}{\sqrt{1 + \frac{(\sigma_{1\xi}^2 - \sigma_{1\eta}^2)(\sigma_{2\xi}^2 - \sigma_{2\eta}^2)}{(\sigma_{1\xi}^2 + \sigma_{2\xi}^2)(\sigma_{1\eta}^2 + \sigma_{2\eta}^2)} \sin^2(\phi_2 - \phi_1)}}, \tag{1.113}$$

where

$$\mathcal{L}_0 = \frac{N_1 N_2 f N_b}{2\pi\sqrt{\sigma_{1\xi}^2+\sigma_{2\xi}^2}\sqrt{\sigma_{1\eta}^2+\sigma_{2\eta}^2}}. \tag{1.114}$$

It is seen that the reduction factor vanishes in the case of round beams or when $\phi_1 = \phi_2$. In the LHC, the beams are round by design and the residual coupling is small such that this effect is usually considered as negligible.

1.5.7 Integrated Luminosity

All the luminosity formulae derived above only consider the instantaneous number of interactions per second. The relevant figure of merit describing the number of events collected over the lifetime of a machine is the so-called *integrated luminosity*:

$$\mathcal{L}_{\text{int}} = \int_0^T \mathcal{L}(t')\,dt'. \tag{1.115}$$

This integral is taken over the time the machine is filled or in other words excluding dead time. A common model for the decay of the luminosity with time is an exponential behaviour with a given lifetime τ:

$$\mathcal{L}(t) \rightarrow \mathcal{L}_0 \exp\left[\frac{-t}{\tau}\right]. \tag{1.116}$$

Various sources contribute to this lifetime such as the decay of beam intensity, emittance growth and increase of the bunch length. Considering an exponential decay has the advantage that the contribution from the different effects can easily be added. In these conditions, when its decay is fast, the luminosity should be optimized as soon as possible during the fill when the reachable maximum luminosity and the decay are the largest in order to improve the performance of the machine.

1.5.8 Methods for Luminosity Calibration

The cross section observed by the experiments is essential to absolutely normalize the experimental data. If the cross section for a process is known, the relation between the cross section and the luminosity can be used to calibrate the luminosity. In e^+e^- colliders, the theoretically well known Bhabha scattering is generally used for this purpose. For hadron colliders as no corresponding process with a well-known cross section can be used in a direct way other methods have to be investigated.

Calibration from the Standard Model

In proton-proton interactions there are electromagnetic processes such as muon pairs production via two photons exchange that can be calculated to better than 1 % but the rates are extremely low and the experimental acceptance and efficiency are difficult to estimate accurately. Another process that can be well suited for luminosity determination is the production rate of W and Z. At the moment the uncertainty in the calculation of the cross section is in the 5-10 % range. More details can be found in [12]. These normalizations rely on the fragmentation model and it is desirable to cross check the theoretical expectations with an independent measurement.

Determination via the Optical Theorem

This technique has been used since ISR in a number of machines such as UA4 [13] at CERN, the Tevatron [14], RHIC [15] and in HERA [16] and consists of determining the luminosity via an extrapolation to zero scaterring angles in combination with a measurement of the total inelastic rate using the optical theorem:

$$\frac{1}{\mathcal{L}} = \frac{1}{16\pi}\frac{\sigma_{tot}^2\,(1+\rho^2)}{dR_{el}/dt|_{t=0}}, \tag{1.117}$$

where

$$\rho = \left.\frac{Re\, f_{el}(t)}{Im\, f_{el}(t)}\right|_{t=0}. \tag{1.118}$$

R_{tot} is the total interaction rate and R_{el} the elastic rate and f_{el} is the scattering amplitude. This approach is taken by TOTEM [17] but requires special optics with very high β^* of several kilometers which are not suited for early LHC operation. This method and the implementation of these special optics will be covered in more details in Chapter 7.

From Machine parameters

The luminosity can also be determined directly from machine parameters. The basic idea is to measure the absolute luminosity under specific and controlled beam conditions which would allow for a calibration of the luminosity monitor of the machine or the experiments. Let us recall the basic formulae of the luminosity in the most simple case of Gaussian beams without crossing angle or hourglass effect:

$$\mathcal{L}_0 = \frac{N_1 N_2 f N_b}{2\pi\sqrt{\sigma_{1x}^2+\sigma_{2x}^2}\sqrt{\sigma_{1y}^2+\sigma_{2y}^2}}. \tag{1.119}$$

N_1, N_2 are the bunch intensities which are generally measured with a good accuracy, f and N_b are the revolution frequency and the number of bunches which are very well known. A measurement of the effective beam sizes at the interaction point would therefore give a calibration of the luminosity. Several methods can be used to absolutely calibrate the beam sizes at the IP using basic beam dynamics principle. The so-called beam-beam deflection scans rely on the expression of the beam-beam deflection angle as a function of the transverse offset as presented Equation 1.61:

$$\Delta r' = -\frac{2Nr_0}{\gamma}\frac{1}{r}\left[1-\exp\left(-\frac{r^2}{2\sigma^2}\right)\right], \tag{1.120}$$

in the case of round Gaussian beams. The deflection angle $\Delta r'$ directly depends on the transverse offset r and the IP beam size σ. The transverse offset is measured using beam position monitors with about a μm precision and the beam size can be derived via a fit. This effect is observable only for high bunch intensity N and is therefore not suited for early LHC operation. In addition, Equation 1.120 assumes Gaussian beams which is usually not the case in real machines as will be presented in Chapters 6 and 5. The second method was pioneered by S. Van Der Meer at the ISR [1] and uses the dependency of the luminosity on a transverse offsets:

$$\mathcal{L} = \mathcal{L}_0 \exp\left[-\frac{\delta x^2}{2(\sigma_{1x}^2+\sigma_{2x}^2)} - \frac{\delta y^2}{2(\sigma_{1y}^2+\sigma_{2y}^2)}\right]. \tag{1.121}$$

Similarly to the beam-beam deflection scans measuring the transverse displacement together with the collision rates it is possible to compute the effective beam size at the IP. This method can be used at lower

intensity as the observable is the event rate which measurement precision is only limited by statistics. This method is therefore very well suited for early LHC operation [18] and was used to give a first calibration of the luminosity at the LHC. A detailed description of this method and further analytical approach and systematics from the various parameters will be given in Chapter 2. The experimental results for RHIC and the LHC are presented in Chapters 5 and 6. To be noted that these two methods are also well suited for luminosity optimization in the transverse plane as the beam-beam force goes to zero and the luminosity reaches a maximum for head-on collisions.

More recently LHCb proposed a measurement of the individual beam sizes using the vertex reconstruction from beam gas events from which they plan to calibrate the luminosity [19].

Chapter 2

Absolute Luminosity From Machine Parameters

The importance of the calibration and measurement of the luminosity was briefly covered in Chapter 1. This chapter aims at giving a more detailed description of the method of measuring the luminosity from machine parameters. Let us recall the basic definition of the luminosity $\mathcal{L}$. For any given process of cross section σ, the event rate $\dot{N}$ is expressed as:

$$\dot{N} = \mathcal{L}\sigma. \tag{2.1}$$

Historically the luminosity in hadron colliders is determined using the optical theorem but this measurement requires dedicated beam conditions and optics which are very demanding and difficult to commission as presented in the last chapter. In this chapter the alternative of measuring the absolute luminosity from machine parameters will be presented as it is very well suited to give a first luminosity calibration during the LHC commissioning phase [18].

The aim of this chapter is to present the method and detail how certain beam conditions can affect the precision of the measurement. Most of the effects presented here are considered small and can be well determined. It is however necessary to understand and characterize all these effects in order to perform the measurement in the best possible conditions and make sure all the necessary information for a complete and detailed analysis are acquired during the calibration measurement. A discussion of the expected uncertainty will also be presented.

2.1 The Van Der Meer Method

The Van Der Meer scan method for luminosity determination was pioneered by S. Van Der Meer at the ISR in 1968 [1]. This section will review the fundamental principles set by S. Van Der Meer and detail this approach in the presence of additional effects such as non-Gaussian beams, hourglass effect or crossing angles.

2.1.1 Concept of Luminosity

The concept and derivation of the luminosity was already presented in details chapter 1. For the purpose of describing the Van Der Meer method I will recall some basic ideas. Luminosity is a general concept that can be interpreted from geometry and flux of particles per unit of time.

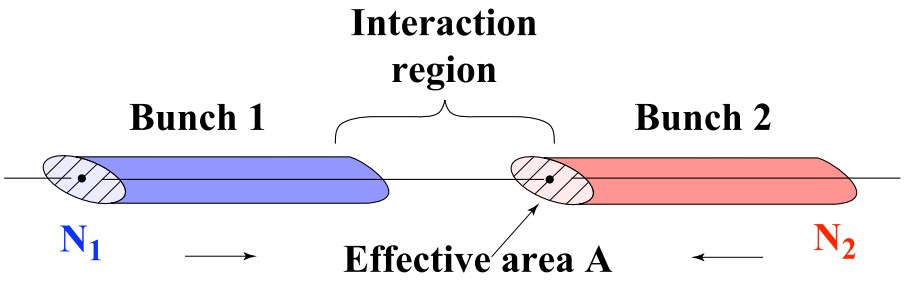

Figure 2.1: Luminosity from particles flux and geometry.

We consider two bunches of N_1 and N_2 particles colliding in an interaction region as shown in Figure 2.1. For bunches crossing at a frequency f (revolution frequency in the case of a circular collider) the luminosity is expressed as:

$$\mathcal{L} = \frac{N_1 N_2 f}{A_{\text{eff}}}, \tag{2.2}$$

where A_{eff} is the effective transverse area in which the collisions take place. The revolution frequency in a collider is accurately known and the number of particles or beam intensity is continuously measured with beam current transformers with a certain accuracy as will be described in Chapter 4. The only unknown parameter that needs to be measured is the effective transverse area. This can be be done with the Van Der Meer method.

2.1.2 Principle

S. Van Der Meer started with the statement that the effective beam height h_{eff} is equal to:

$$h_{\text{eff}} = \frac{\int \rho_1(u)\,du \int \rho_2(u)\,du}{\int \rho_1(u)\,\rho_2(u)\,du}, \tag{2.3}$$

where ρ_1 and ρ_2 are the density functions of the two beams as a function of the transverse coordinate u. If we now consider that one beam is displaced transversally with respect to the other beam by a quantity δu we can express the counting rate $\dot{N}$ (number of events per second) as:

$$\dot{N} = A \int \rho_1(u)\,\rho_2(u-\delta u)\,du, \tag{2.4}$$

where A is an unknown constant. From there we can define the following equality:

$$\frac{\int [A \int \rho_1(u)\,\rho_2(u-\delta u)\,du]\,d\delta u}{A \int \rho_1(u)\,\rho_2(u)\,du} = \frac{\int [\rho_1(u) \int \rho_2(u-\delta u)\,d\delta u]\,du}{\int \rho_1(u)\,\rho_2(u)\,du}. \tag{2.5}$$

Since the integrals are taken over the entire region where the integrands are not zero we have:

$$\int \rho_2(u-\delta u)\,d\delta u = \int \rho_2(u)\,du, \tag{2.6}$$

and therefore

$$\frac{\int [\rho_1(u) \int \rho_2(u-\delta u)\,d\delta u]\,du}{\int \rho_1(u)\,\rho_2(u)\,du} = \frac{\int [\rho_1(u) \int \rho_2(u)\,du]\,du}{\int \rho_1(u)\,\rho_2(u)\,du} = \frac{\int \rho_1(u)\,du \int \rho_2(u)\,du}{\int \rho_1(u)\,\rho_2(u)\,du} = h_{\text{eff}}. \tag{2.7}$$

Expressing this equality in terms of rates we get:

$$h_{\text{eff}} = \frac{\int R(\delta u)\, d\delta u}{R(0)} \tag{2.8}$$

This is the initial definition from S. Van Der Meer as presented in 1968 [1] in which he states that regardless of the beam shape, h_{eff} is equal to the area under the curve defined by the evolution of the rates divided by its ordinate for zero transverse displacement. The underlying assumption of this method is that the beams density functions are uncorrelated such that it is possible to factorize the 2D transverse density function into two independant functions of x and y. Performing this measurement in the two transverse planes would then give a direct measurement of the two transverse effective beam sizes and therefore the effective area expressed as:

$$A_{\text{eff}} = \frac{\int R_x(\delta x)\, d\delta x}{R_x(0)} \frac{\int R_y(\delta y)\, d\delta y}{R_y(0)} \tag{2.9}$$

where $R(\delta x, \delta y) = R_x(\delta x) R_y(\delta y)$ if the horizontal and vertical density functions are uncorrelated.

2.1.3 Formalism

The formulation given by Van Der Meer gives a general approach as a function of the density functions. In order to remain consistent with the notation used in this thesis I will reformulate a couple of terms and definitions. In chapter 1, I defined the luminosity for Gaussian beams colliding perfectly head-on, Equation 1.74

$$\mathcal{L}_0 = \frac{N_1 N_2 f N_b}{2\pi \sqrt{\sigma_{1x}^2 + \sigma_{2x}^2} \sqrt{\sigma_{1y}^2 + \sigma_{2y}^2}}, \tag{2.10}$$

for which the effective beam sizes $\sigma_{x\text{eff}}$ and $\sigma_{y\text{eff}}$ are usually defined as $\sqrt{\sigma_{1x}^2 + \sigma_{2x}^2}$ and $\sqrt{\sigma_{1y}^2 + \sigma_{2y}^2}$ respectively. $\mathcal{L}_0$ and A_{eff} can be reformulated as

$$\mathcal{L}_0 = \frac{N_1 N_2 f N_b}{2\pi \sigma_{x\text{eff}} \sigma_{y\text{eff}}}, \tag{2.11}$$

and

$$A_{\text{eff}} = 2\pi \sigma_{x\text{eff}} \sigma_{y\text{eff}}. \tag{2.12}$$

The factor 2π comes from the integration of a Gaussian. When applying a transverse offset between the beams we can define a function F which describes the evolution of the luminosity as a function of the separation

$$\mathcal{L}(\delta x, \delta y) = \mathcal{L}_0 F(\delta x, \delta y). \tag{2.13}$$

If the transverse density distributions are uncorrelated it is possible to express $F(\delta x, \delta y)$ as a product of two functions $F_x(\delta x)$ and $F_y(\delta y)$ in which case we can apply the above principle

$$A_{\text{eff}} = \frac{\int F_x(\delta x)\, d\delta x}{F_x(0)} \frac{\int F_y(\delta y)\, d\delta y}{F_y(0)}, \tag{2.14}$$

and

$$\sigma_{u\text{eff}} = \frac{1}{\sqrt{2\pi}} \frac{\int F_u(\delta u)\, d\delta u}{F_u(0)}. \tag{2.15}$$

2.1.4 Gaussian Beams

In the most simple case, the evolution of the luminosity for Gaussian beams as a function of the separation, Equation 1.76, is expressed as

$$\mathcal{L} = \mathcal{L}_0 \exp\left[-\frac{\delta x^2}{2(\sigma_{1x}^2+\sigma_{2x}^2)} - \frac{\delta y^2}{2(\sigma_{1y}^2+\sigma_{2y}^2)}\right]. \tag{2.16}$$

The function F_u is then equal to

$$F_u(\delta u) = A \exp\left[-\frac{\delta u^2}{2(\sigma_{1u}^2+\sigma_{2u}^2)}\right], \tag{2.17}$$

where A is an arbitrary constant and $u = x, y$. The effective beam size can therefore be calculated:

$$\sigma_{u\text{eff}} = \frac{1}{\sqrt{2\pi}} \frac{\int F_u(\delta u)\, d\delta u}{F_u(0)} = \sqrt{\sigma_{1u}^2+\sigma_{2u}^2}, \tag{2.18}$$

which is consistent with the expression of $\mathcal{L}_0$ quoted before.

2.1.5 Double Gaussian Beams

In hadron machines, the beams are not always fully Gaussian because of slow diffusion processes that are not damped by synchrotron radiations as in the case of lepton machines. This effect was observed in the LHC, RHIC and HERA [20] as will be presented in Chapters 5 and 6. The non-Gaussian components of the beam still contribute to the luminosity and have to be taken into account while computing the effective beam size. The core of the beam, which generally remains Gaussian is the main contributor to the luminosity. A convenient way to include the tails in the model is to fit the profile with a Gaussian, to model the core, plus another function to fit the tails. The double Gaussian (a and b) function proved to give excellent results in the presence of non-Gaussian tails. In this case the function F_u is equal to

$$F_u(\delta u) = A_{au} \exp\left[-\frac{\delta u^2}{2\sigma_{au}^2}\right] + A_{bu} \exp\left[-\frac{\delta u^2}{2\sigma_{bu}^2}\right], \tag{2.19}$$

where A_{au} and A_{bu} are arbitrary constants. This leads to

$$\sigma_{u\text{eff}} = \frac{A_{au}\sigma_{au} + A_{bu}\sigma_{bu}}{A_{au}+A_{bu}}. \tag{2.20}$$

Other models could be used to fit the tails such as a flat phase space component (results in a parabola when projected in one plane), which could be well suited for extended halo modelling. So far the double Gaussian gave the best results for the data presented in this thesis.

2.1.6 Crossing Angle

When the beams collide with an angle a reduction factor applies to the luminosity, Equation 1.80, which is then expressed as

$$\mathcal{L} = \mathcal{L}_0 \frac{1}{\sqrt{1+\frac{\sigma_{1s}^2+\sigma_{2s}^2}{\sigma_{1u}^2+\sigma_{2u}^2}\left(\tan\frac{\phi}{2}\right)^2}}, \tag{2.21}$$

where $u = x, y$. If a transverse offset is applied in the crossing angle plane, Equation 1.89, the luminosity becomes

$$\mathcal{L} = \mathcal{L}_0 \cdot S \cdot T \cdot U, \tag{2.22}$$

where S is the reduction factor from the crossing angle, T is the one from the offset and U is the crossing term that can be simplified to

$$U = \exp\left[S^2 \frac{\delta u^2}{2\left(\sigma_{1u}^2 + \sigma_{2u}^2\right)} \frac{\sigma_{1s}^2 + \sigma_{2s}^2}{\sigma_{1u}^2 + \sigma_{2u}^2} \left(\tan\frac{\phi}{2}\right)^2 \right]. \tag{2.23}$$

The function $F_u(\delta u)$ is then

$$F_u(\delta u) = T \cdot U = \exp\left[S^2 \frac{\delta u^2}{2\left(\sigma_{1u}^2 + \sigma_{2u}^2\right)} \frac{\sigma_{1s}^2 + \sigma_{2s}^2}{\sigma_{1u}^2 + \sigma_{2u}^2} \left(\tan\frac{\phi}{2}\right)^2 - \frac{\delta u^2}{2\left(\sigma_{1u}^2 + \sigma_{2u}^2\right)} \right]. \tag{2.24}$$

After some algebra it can be reduced to

$$F_u(\delta u) = \exp\left[-S^2 \frac{\delta u^2}{2(\sigma_{1u}^2 + \sigma_{2u}^2)} \right]. \tag{2.25}$$

We can now easily derive the effective beam size

$$\sigma_{u\text{eff}} = \frac{\sqrt{\sigma_{1u}^2 + \sigma_{2u}^2}}{S}. \tag{2.26}$$

The effective beam size measured by the Van Der Meer method will therefore include the reduction factor from the crossing angle if the scan is performed in the crossing angle plane. This is a very important property as it allows for a direct measurement of the absolute luminosity without additional measurement of the crossing angle. If we now consider the case where an angular component is present in both planes, the luminosity for head-on collisions, Equation 1.86, is expressed as:

$$\mathcal{L} = \mathcal{L}_0 \frac{1}{\sqrt{1 + \frac{\sigma_{1s}^2 + \sigma_{2s}^2}{\sigma_{1y}^2 + \sigma_{2y}^2} \left(\tan\frac{\phi_y}{2}\right)^2 + \frac{\sigma_{1s}^2 + \sigma_{2s}^2}{\sigma_{1x}^2 + \sigma_{2x}^2} \left(\tan\frac{\phi_x}{2}\right)^2}}, \tag{2.27}$$

where ϕ_x and ϕ_y are the projected angles in the horizontal and vertical planes respectively. Applying an offset in the two transverse planes we get an expression similar to the 1D case:

$$\mathcal{L} = \mathcal{L}_0 \cdot S \cdot T \cdot U, \tag{2.28}$$

where

$$S = \frac{1}{\sqrt{1 + \frac{\sigma_{1s}^2 + \sigma_{2s}^2}{\sigma_{1y}^2 + \sigma_{2y}^2} \left(\tan\frac{\phi_y}{2}\right)^2 + \frac{\sigma_{1s}^2 + \sigma_{2s}^2}{\sigma_{1x}^2 + \sigma_{2x}^2} \left(\tan\frac{\phi_x}{2}\right)^2}}, \tag{2.29}$$

and

$$T = \exp\left[-\frac{\delta x^2}{2\left(\sigma_{1x}^2 + \sigma_{2x}^2\right)} - \frac{\delta y^2}{2\left(\sigma_{1y}^2 + \sigma_{2y}^2\right)} \right], \tag{2.30}$$

and

$$U = \exp\left[S^2\,\frac{\sigma_{1s}^2+\sigma_{2s}^2}{2}\left(\frac{\delta x\tan\frac{\phi_x}{2}}{\sigma_{1x}^2+\sigma_{2x}^2}-\frac{\delta y\tan\frac{\phi_y}{2}}{\sigma_{1y}^2+\sigma_{2y}^2}\right)^2\right]. \tag{2.31}$$

As seen in this formula is it not possible to express the function $F(\delta x,\delta y)=T\cdot U$ as product of $F_x(\delta x)F_y(\delta y)$. In this case the Van Der Meer hypothesis cannot be applied. We can however reproduce the measurement by performing the following integral:

$$A_{\text{eff}} = \frac{\int F(\delta x,0)\,d\delta x}{F(0,0)}\frac{\int F(0,\delta y)\,d\delta y}{F(0,0)}, \tag{2.32}$$

we get for the measured effective beam size:

$$\sigma_{u\text{eff}} = \frac{\sqrt{\sigma_{1u}^2+\sigma_{2u}^2}}{S}S_u, \tag{2.33}$$

where

$$S_u = \frac{1}{\sqrt{1+\frac{\sigma_{1s}^2+\sigma_{2s}^2}{\sigma_{1u}^2+\sigma_{2u}^2}\left(\tan\frac{\phi_u}{2}\right)^2}}. \tag{2.34}$$

The measured effective area is then

$$A_{\text{eff}} = 2\pi\sigma_{x\text{eff}}\sigma_{y\text{eff}} = 2\pi\frac{\sqrt{\sigma_{1x}^2+\sigma_{2x}^2}\sqrt{\sigma_{1y}^2+\sigma_{2y}^2}}{S^2}S_xS_y. \tag{2.35}$$

The product S_xS_y is different from S

$$S_xS_y = \frac{1}{\sqrt{1+\frac{\sigma_{1s}^2+\sigma_{2s}^2}{\sigma_{1y}^2+\sigma_{2y}^2}\left(\tan\frac{\phi_y}{2}\right)^2+\frac{\sigma_{1s}^2+\sigma_{2s}^2}{\sigma_{1x}^2+\sigma_{2x}^2}\left(\tan\frac{\phi_x}{2}\right)^2+\frac{(\sigma_{1s}^2+\sigma_{2s}^2)^2}{(\sigma_{1x}^2+\sigma_{2x}^2)(\sigma_{1y}^2+\sigma_{2y}^2)}\left(\tan\frac{\phi_x}{2}\right)^2\left(\tan\frac{\phi_y}{2}\right)^2}}. \tag{2.36}$$

The measured effective area in this case is not exactly the value determining $\mathcal{L}_0$. This is illustrated Figure 2.2 where the ratio S_xS_y/S for different configurations is shown. In the small angles approximation or when one of the angular components is much larger than the other, the computation of the luminosity using directly the measured effective beam sizes is perfectly justified. The error becomes significant when the angles are of equivalent amplitudes. The error is the largest for the LHC nominal beam parameters as the ratio σ_s/σ_u is maximum. For the actual LHC beam parameters it is much less than 1 % and could be neglected. RHIC operates with significantly longer bunches than the LHC which increases the effect of the crossing angle. However, RHIC runs by design without crossing angle as will be shown in Chapter 5.

In the presence of a crossing angle with components in the two transverse planes the Van Der Meer formalism is not an exact measurement of the effective area. This effect is very small in most cases. It can become large with some specific beam conditions and has to be taken into account when necessary.

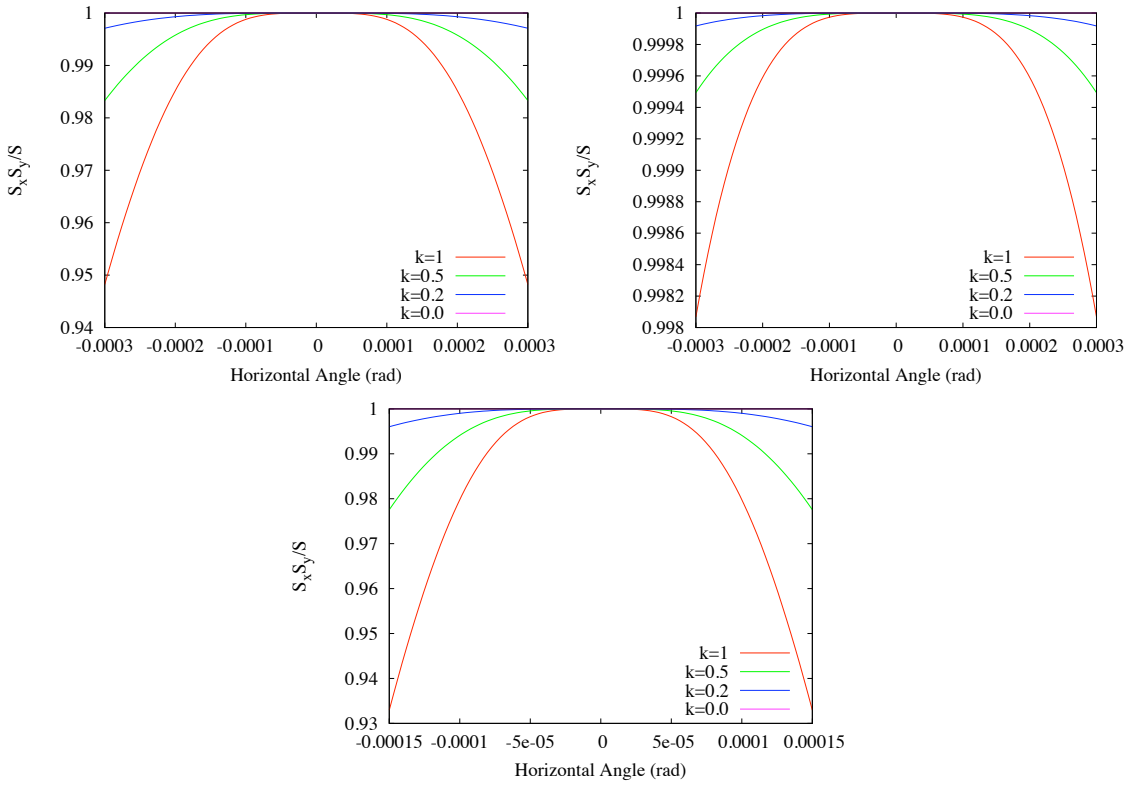

Figure 2.2: Ratio $S_x S_y/S$ for nominal LHC (top left), LHC at 3.5 TeV (top right) with $\beta^* = 2$ m and RHIC beam parameters with $\beta^* = 0.7$ m, $\sigma_s = 1$ m and an energy of 250 GeV (bottom). k represents the ratio between the projected angles, in this case ϕ_y/ϕ_x. In the actual LHC configuration the error is smaller than 1 % and can be neglected. It becomes relevant for LHC nominal parameters and RHIC.

2.1.7 Hourglass Effect

The hourglass effect describes the longitudinal dependency of the transverse beam sizes. It becomes significant when the ratio β^*/σ_s is equal or smaller than 1. Including this effect in the luminosity integration, Equation 1.97, we have

$$\mathcal{L} = \mathcal{L}_0 \int_{-\infty}^{+\infty} \frac{1}{\sqrt{\pi}} \frac{e^{-t^2}}{\sqrt{(1+t^2/t_x^2)(1+t^2/t_y^2)}} dt, \tag{2.37}$$

where

$$t_u^2 = \frac{2\,(\sigma_{1u}^{*2} + \sigma_{2u}^{*2})}{(\sigma_{1s}^2 + \sigma_{2s}^2)(\sigma_{1u}^{*2}/\beta_{1u}^{*2} + \sigma_{1u}^{*2}/\beta_{1u}^{*2})}, \quad \textit{where} \quad u = x, y, \tag{2.38}$$

and

$$t = \frac{\sqrt{2}s}{\sqrt{\sigma_{1s}^2 + \sigma_{2s}^2}}. \tag{2.39}$$

In order to treat this integral analytically we have to make the assumption that the beams are round which is usually the case in hadron colliders such as RHIC and LHC. For $\beta^*_{1x} = \beta^*_{2x} = \beta^*_{1y} = \beta^*_{2y} = \beta^*$, we can simplify these expressions to

$$t_x^2 = t_y^2 = t_r^2 = \frac{2\beta^{*2}}{\sigma_{1s}^2 + \sigma_{2s}^2}, \tag{2.40}$$

and

$$\mathcal{L} = \mathcal{L}_0 \sqrt{\pi} t_r \, e^{t_r^2} \, \mathrm{erfc}(\mathrm{t_r}). \tag{2.41}$$

where erfc is the complementary error function. Including a transverse offset the luminosity as a function of the separation is expressed as:

$$\mathcal{L}(\delta x, \delta y) = \mathcal{L}_0 \int_{-\infty}^{+\infty} \frac{1}{\sqrt{\pi}} \frac{e^{-t^2}}{1 + \frac{t^2}{t_r^2}} F(\delta x, \delta y, t) \, dt, \tag{2.42}$$

where $F(\delta x, \delta y, t) = F_x(\delta x, t) F_y(\delta y, t)$ and

$$F_u(\delta u, t) = \exp\left[-\frac{\delta u^2}{2(\sigma_{1u}^2 + \sigma_{2u}^2)} \frac{1}{1 + \frac{t^2}{t_r^2}} \right]. \tag{2.43}$$

Applying the same method as for the crossing angle the effective beam size is

$$\sigma_{u\mathrm{eff}} = \sqrt{\sigma_{1u}^2 + \sigma_{2u}^2} \frac{\frac{1}{\sqrt{\pi}} e^{\frac{t_r^2}{2}} t_r K_0\left[\frac{t_r^2}{2}\right]}{\sqrt{\pi} t_r \, e^{t_r^2} \, \mathrm{erfc}(\mathrm{t_r})}. \tag{2.44}$$

where K_0 is the modified Bessel function. A correction factor has therefore to be applied in order to compute the absolute luminosity:

$$HG_{\mathrm{corr}} = \frac{\sqrt{\pi} t_r \, e^{t_r^2} \, \mathrm{erfc}(\mathrm{t_r})}{\left(\frac{1}{\sqrt{\pi}} e^{\frac{t_r^2}{2}} t_r K_0\left[\frac{t_r^2}{2}\right] \right)^2}, \tag{2.45}$$

which results in a decrease with respect to the luminosity without correction. Figure 2.3 illustrates the evolution of this correction factor as a function of the ratio $r = \beta^*/\sigma_s$. The two cases considered are the 2009 250 GeV protons RHIC parameters ($\beta^* = 0.7$ m and $\sigma_s = 1$ m) $r = 0.7$ and the nominal LHC parameters ($\beta^* = 0.55$ m and $\sigma_s = 0.075$ m) $r = 7.3$. The correction factor is very small for the LHC and represents a few percents in the case of RHIC.

2.1.8 Hourglass and Crossing Angle

It was shown Equation 1.105, that when these two effects are combined they have to be treated together. The luminosity in this case is expressed as:

$$\mathcal{L} = \mathcal{L}_0 \frac{1}{\sqrt{\pi}} \int_{-\infty}^{+\infty} \frac{e^{-\frac{t^2}{S^2(t)}}}{1 + \frac{t^2}{t_r^2}} \, dt, \tag{2.46}$$

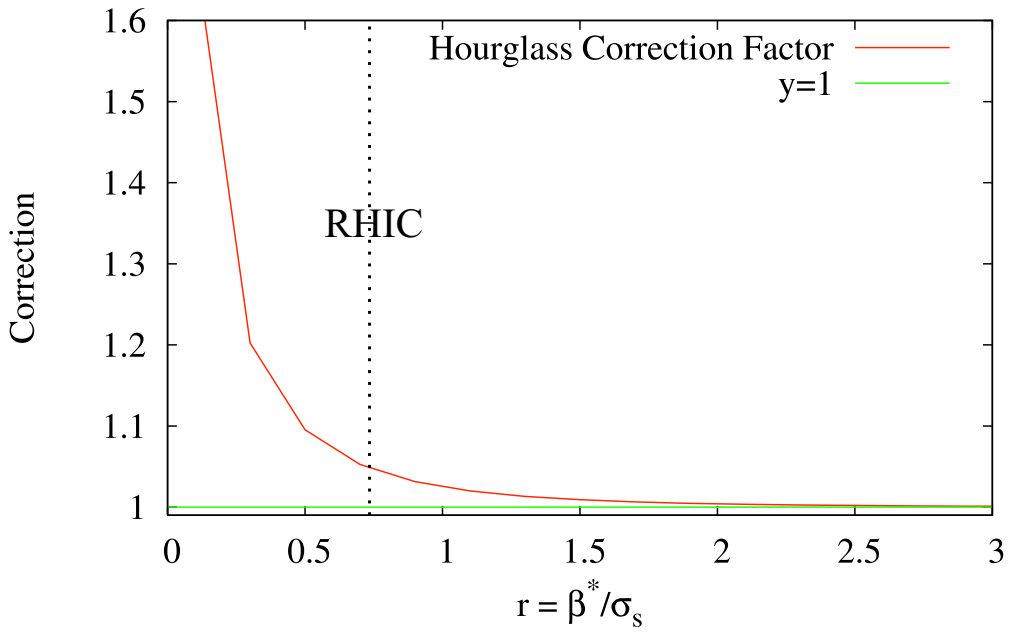

Figure 2.3: Hourglass correction factor as function of $r = \beta^*/\sigma_s$. RHIC corresponds to $r = 0.7$ and the LHC to $r = 7.3$.

where

$$t_r^2 = \frac{K\beta^{*2}}{\sigma_{1s}^2 + \sigma_{2s}^2}, \tag{2.47}$$

and

$$t^2 = \frac{K s^2}{\sigma_{1s}^2 + \sigma_{2s}^2}, \tag{2.48}$$

where K is the kinematic factor and S is the reduction factor due to the crossing angle replacing σ by $\sigma(s)$. With a transverse offset this formulae becomes:

$$\mathcal{L} = \mathcal{L}_0 \frac{1}{\sqrt{\pi}} \int_{-\infty}^{+\infty} \frac{e^{-\frac{t^2}{S^2(t)}}}{1+\frac{t^2}{t_r^2}} F(\delta x, \delta y, t)\, dt, \tag{2.49}$$

where $F(\delta x, \delta y, t) = F_x(\delta x, t) F_y(\delta y, t)$ and

$$F_y(\delta y, t) = \exp\left[-\frac{\delta y^2}{2(\sigma_{1y}^2 + \sigma_{2y}^2)} \frac{1}{1+\frac{t^2}{t_r^2}} \right], \tag{2.50}$$

and

$$F_x(\delta x, t) = \exp\left[-\frac{\delta x^2 + 2\sqrt{2}\,\delta x t \tan\frac{\phi}{2} \sqrt{\sigma_{1s}^2 + \sigma_{2s}^2}}{2\,(\sigma_{1x}^2 + \sigma_{2x}^2)\,(1+\frac{t^2}{t_r^2})} \right], \tag{2.51}$$

when the crossing angle is in the horizontal plane. Again we perform the same analysis to obtain:

$$\sigma_{y\text{eff}} = \sqrt{\sigma_{1y}^2 + \sigma_{2y}^2}\,\frac{B}{A}, \quad \sigma_{x\text{eff}} = \sqrt{\sigma_{1x}^2 + \sigma_{2x}^2}\,\frac{C}{A}, \tag{2.52}$$

where

$$A = \int_{-\infty}^{+\infty} \frac{e^{-\frac{t^2}{S^2(t)}}}{1+\frac{t^2}{t_r^2}}\,dt, \quad B = \int_{-\infty}^{+\infty} \frac{e^{-\frac{t^2}{S^2(t)}}}{\sqrt{1+\frac{t^2}{t_r^2}}}\,dt, \quad C = e^{\frac{t_r^2}{2}}\,t_r K_0\left[\frac{t_r^2}{2}\right]. \tag{2.53}$$

The correction factor becomes:

$$HGX_{\text{corr}} = \frac{A^2}{BC}. \tag{2.54}$$

One way of determining the crossing angle is to use the BPM signals. The precision of this measurement therefore depends on the accuracy of the calibration and sensitivity of the BPMs in the interaction region. Since a precise measurement of the crossing angle is not always possible, it is interesting to look at the error we would make assuming zero crossing angle when applying the hourglass effect correction factor.

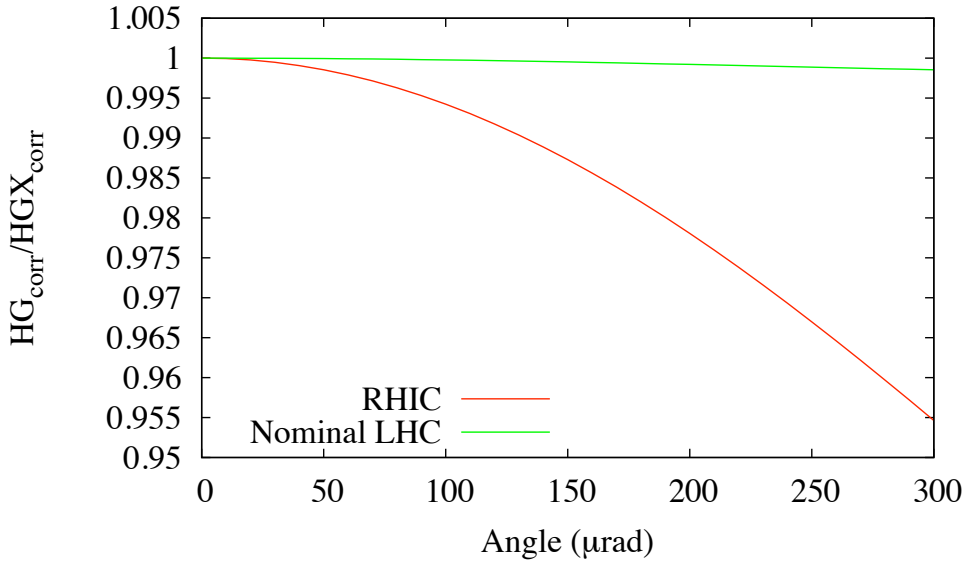

Figure 2.4: Ratio of the correction factors with and without crossing angle for the RHIC and nominal LHC beam parameters.

As expected the error is very small for the LHC as the hourglass effect is very weak. For the RHIC beam parameters the effect becomes non-negligible, as shown in Figure 2.4. It will have to be taken into account if the crossing angle cannot be measured precisely.

2.1.9 Linear Coupling

As shown in Equation 1.113 the linear coupling can also reduce the maximum luminosity as follows:

$$\mathcal{L} = \mathcal{L}_0 \frac{1}{\sqrt{1 + \frac{(\sigma_{1\xi}^2 - \sigma_{1\eta}^2)(\sigma_{2\xi}^2 - \sigma_{2\eta}^2)}{(\sigma_{1\xi}^2 + \sigma_{2\xi}^2)(\sigma_{1\eta}^2 + \sigma_{2\eta}^2)} \sin^2(\phi_2 - \phi_1)}} = \mathcal{L}_{0C}, \tag{2.55}$$

where

$$\mathcal{L}_0 = \frac{N_1 N_2 f N_b}{2\pi \sqrt{\sigma_{1\xi}^2 + \sigma_{2\xi}^2} \sqrt{\sigma_{1\eta}^2 + \sigma_{2\eta}^2}}. \tag{2.56}$$

where $\sigma_{i\xi}$ and $\sigma_{i\eta}$ are the beam sizes along the rotated axes ξ and η, shown Figure 1.10, and ϕ_1 and ϕ_2 are the tilt angles. The coupling angle calculation is detailed in Appendix B. In order to study the impact on the measured effective beam sizes we have to calculate the overlap integral with offsets in the transverse planes:

$$\mathcal{L} = N_1 N_2 f N_b \int\int_{-\infty}^{+\infty} \rho_1(x - \delta x, y - \delta y)\, \rho_2(x, y)\, dx dy = \mathcal{L}_{0C} \exp\left(-\frac{1}{2} \delta z^T \cdot M \cdot \delta z\right) \tag{2.57}$$

where $\mathcal{L}_{0C}$ is the luminosity in the presence of linear coupling without offset and δz is the vector describing the transverse offsets:

$$\delta z = \begin{pmatrix} \delta x \\ \delta y \end{pmatrix}, \tag{2.58}$$

M is a 2×2 symmetric matrix with the following elements:

$$\begin{cases} M_{xx} = \frac{1}{D}(a_1 \Sigma_{1xx}^{-1} + a_2 \Sigma_{2xx}^{-1}), \\ M_{yy} = \frac{1}{D}(a_1 \Sigma_{1yy}^{-1} + a_2 \Sigma_{2yy}^{-1}), \\ M_{xy} = \frac{1}{D}(a_1 \Sigma_{1xy}^{-1} + a_2 \Sigma_{2xy}^{-1}), \end{cases} \tag{2.59}$$

where Σ_i^{-1} is the diagonalized σ-matrix for beam 1 or beam 2 defined Equation 1.110 and $a_i = \sigma_{i\xi}\sigma_{i\eta}$.

$$D = (\sigma_{1\xi}^2 + \sigma_{2\xi}^2)(\sigma_{1\eta}^2 + \sigma_{2\eta}^2) \left(1 + \frac{(\sigma_{1\xi}^2 - \sigma_{1\eta}^2)(\sigma_{2\xi}^2 - \sigma_{2\eta}^2)}{(\sigma_{1\xi}^2 + \sigma_{2\xi}^2)(\sigma_{1\eta}^2 + \sigma_{2\eta}^2)} \sin^2(\phi_1 - \phi_2)\right) \tag{2.60}$$

Similarly to the single beam profile we can diagonalize the M-matrix with a rotation Φ:

$$\begin{cases} \tan 2\Phi = \frac{2M_{xy}}{M_{xx} - M_{yy}}, \\ \frac{1}{\sigma_{\text{eff}\xi}^2} = \frac{1}{2}\left[(M_{xx} + M_{yy}) + \frac{M_{xx} - M_{yy}}{\cos 2\Phi}\right], \\ \frac{1}{\sigma_{\text{eff}\eta}^2} = \frac{1}{2}\left[(M_{xx} + M_{yy}) - \frac{M_{xx} - M_{yy}}{\cos 2\Phi}\right]. \end{cases} \tag{2.61}$$

where $\sigma_{\text{eff}\xi}$ and $\sigma_{\text{eff}\eta}$ are the effective overlap beam sizes along the rotated principal axes. The overlap area is therefore defined as a 2D Gaussian distribution with beam sizes $\sigma_{\text{eff}\xi}$ and $\sigma_{\text{eff}\eta}$ and a tilt angle Φ. Using the following expression:

$$\cos(\arctan x) = \frac{1}{\sqrt{1 + x^2}} \tag{2.62}$$

we get for the effective beam sizes:

$$\begin{cases} \frac{1}{\sigma^2_{\text{eff}\xi}} = \frac{1}{2}\left[M_{xx} + M_{xx}\sqrt{1+\frac{4M_{xy}^2}{(M_{xx}-M_{yy})^2}} + M_{yy} - M_{yy}\sqrt{1+\frac{4M_{xy}^2}{(M_{xx}-M_{yy})^2}}\right], \\ \frac{1}{\sigma^2_{\text{eff}\eta}} = \frac{1}{2}\left[M_{xx} - M_{xx}\sqrt{1+\frac{4M_{xy}^2}{(M_{xx}-M_{yy})^2}} + M_{yy} + M_{yy}\sqrt{1+\frac{4M_{xy}^2}{(M_{xx}-M_{yy})^2}}\right]. \end{cases} \tag{2.63}$$

and for the product, replacing M_{xx}, M_{yy} and M_{xy} by their expressions as a function of ϕ_i, $\sigma_{1\xi}$ and $\sigma_{1\eta}$:

$$\begin{aligned} \frac{1}{\sigma^2_{\text{eff}\xi}\,\sigma^2_{\text{eff}\eta}} &= M_{xx}M_{yy} - M_{xy}^2 \\ &= \frac{1}{\sqrt{\sigma^2_{1\xi}+\sigma^2_{2\xi}}\sqrt{\sigma^2_{1\eta}+\sigma^2_{2\eta}}} \frac{1}{\sqrt{1+\frac{(\sigma^2_{1\xi}-\sigma^2_{1\eta})(\sigma^2_{2\xi}-\sigma^2_{2\eta})}{(\sigma^2_{1\xi}+\sigma^2_{2\xi})(\sigma^2_{1\eta}+\sigma^2_{2\eta})}\sin^2(\phi_2-\phi_1)}}, \end{aligned} \tag{2.64}$$

which corresponds to the effective area found in Equation 1.113. If the coupling is significant a 2D Gauss fit on a raster scan would therefore fully determine the overlap area expressed as:

$$A_{\text{eff}} = 2\pi\,\sigma_{\text{eff}\xi}\,\sigma_{\text{eff}\eta}. \tag{2.65}$$

A raster scan is a very lengthy measurement as it requires to cover the full (x,y) plane. When performing the Van Der Meer scan in the horizontal and vertical planes we measure the effective overlap beam sizes at $\Phi = 0$ which gives:

$$\frac{1}{\sigma^2_{\text{eff}x}} = M_{xx} \text{ and } \frac{1}{\sigma^2_{\text{eff}y}} = M_{yy}. \tag{2.66}$$

From these expressions we can estimate the error induced by coupling as a function of the tilt angle and the aspect ratio of the beams. As shown in Appendix B, the tilt angle depends on the coupling the β^* and the emittances. For simplicity we will asume equal beams and the same emittance growth in the horizontal plane for both beams. Figure 2.5 shows the evolution of the tilt angle and the uncertainty as a function of the ratio of the emittances. For almost round beams the angle will tend to 45^o and rapidely decrease as the aspect ratio increases. In the limit case of round beams, coupling has no effect on luminosity and is therefore not relevant for this study. To get an uncertainty of 1 % we need a factor 4 between the horizontal an vertical emittances. In the LHC, the beams are round by design, a difference between the horizontal and vertical plane is however possible. Well controlled emittances are therefore required to minimize this error. In Chapter 6, estimates of the tilt angle based on optics and emittances measurements will show that the uncertainty is of a few 0.1 % during the first calibration scans in the LHC.

2.1.10 Discussion

This section covered the various aspects of the Van Der Meer method and how the beam parameters can affect the precision of the measurement. It was shown that an additional uncertainty can be introduced by the crossing angle or the hourglass effect which can significantly be reduced by placing ourself in conditions where these effects become small with respect to other systematic errors. The precision of the measurement is then constrained by the intensity and the statistical error on the rates. This assumption is true as far as the beam conditions remain constant during the measurement, which in practice is not quite the case as will be seen in the LHC data. Other effects such as coupling are in general very small in the case of RHIC or LHC. At high intensity the beam-beam force which evolves non-linearly as function of the separation will also affect the measurement. When the beam conditions are adequate, the Van Der Meer scan method is a

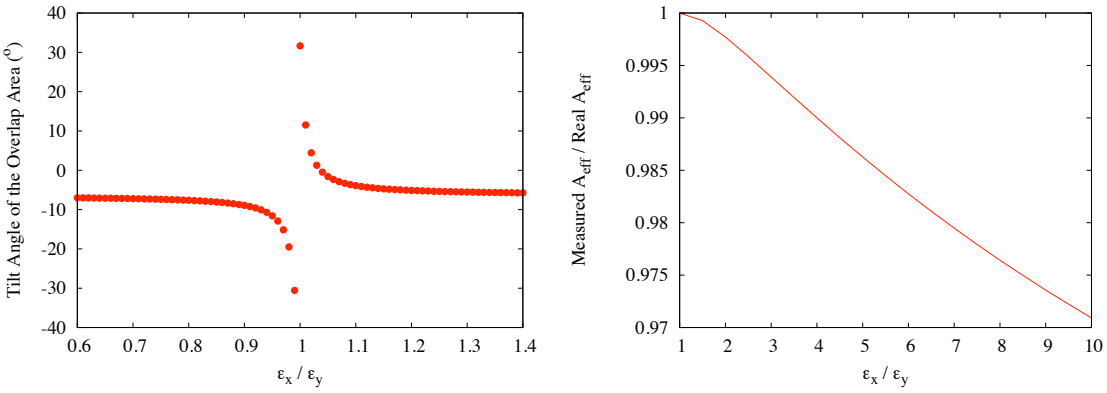

Figure 2.5: Analytical estimates of the coupling error on the measurement of the effective area and tilt angle of the overlap area. The calculation was done using a β^* of 2 m and equal beams. The coupling parameters were derived using measurements perfomed at IP8.

very powerful measurement for luminosity calibration, especially at low intensity when the beam dynamics remains more or less linear. It is then possible to define optimum beam parameters for the luminosity calibration measurements in the LHC:

- $\beta^* = 2 - 11$ m in order to minimize hourglass.
- Moderate intensity: lower than $5.0\,10^{10}$ p/bunch, the resulting beam-beam parameter is $\xi = 0.00016$ for nominal emittance and no crossing angle.
- No crossing angle (up to 156 bunches per beam).
- Optics fully corrected such that coupling is minimized.

These parameters should allow for enough statistics to keep the duration of a scan reasonable and are fully compatible with early LHC beam parameters. In the future, if luminosity calibration from machine parameters is still desired, it might be necessary to plan dedicated beam time for this measurement.

2.2 Discussion of the Uncertainty

The precision of the measurement relies on the knowledge of machine parameters and instruments which have their own uncertainties. This section will review potential sources of uncertainty related to the calibration scans and ways to estimate and minimize these effects. Most of them are very small and some are directly measurable. Initial estimates were presented in [21].

2.2.1 Statistical Accuracy

The statistical accuracy of the fit results is determined by the time spent on each point and the number of points. These parameters can be estimated from numerical simulations. The number of collisions for given beam conditions follows a Poisson distribution:

$$f(n,\lambda) = \frac{\lambda^n e^{-\lambda}}{n!}, \tag{2.67}$$

where n is the number of occurrences of the event and λ is the expected number of occurrences which is in this case given by $\mathcal{L}/\sigma$. The standard error is $\sqrt{n}$. The simulation consisted of generating a Gaussian distribution parametrized by the Poisson distribution where n is randomly generated for each separation. The two parameters to be scanned are t, the time spent at each point, and the number of points in the scan. The final results give an estimate of the statistical error due to the fit and the scan parameters:

$$\frac{\Delta\sigma}{\sigma} = \sqrt{\left(\frac{\sigma_{stat}}{\sigma}\right)^2 + \left(\frac{\mu_{stat}}{\sigma}\right)^2}, \tag{2.68}$$

were σ_{stat} and μ_{stat} are the average and standard deviation over all the seeds. The same analysis can be performed on the peak and mean. All the fits were performed using the MINUIT minimization package [22] which was used for the scans analysis. For each case 500 seeds were used which should in principle be sufficient to derive meaningful values for the average and standard deviation.

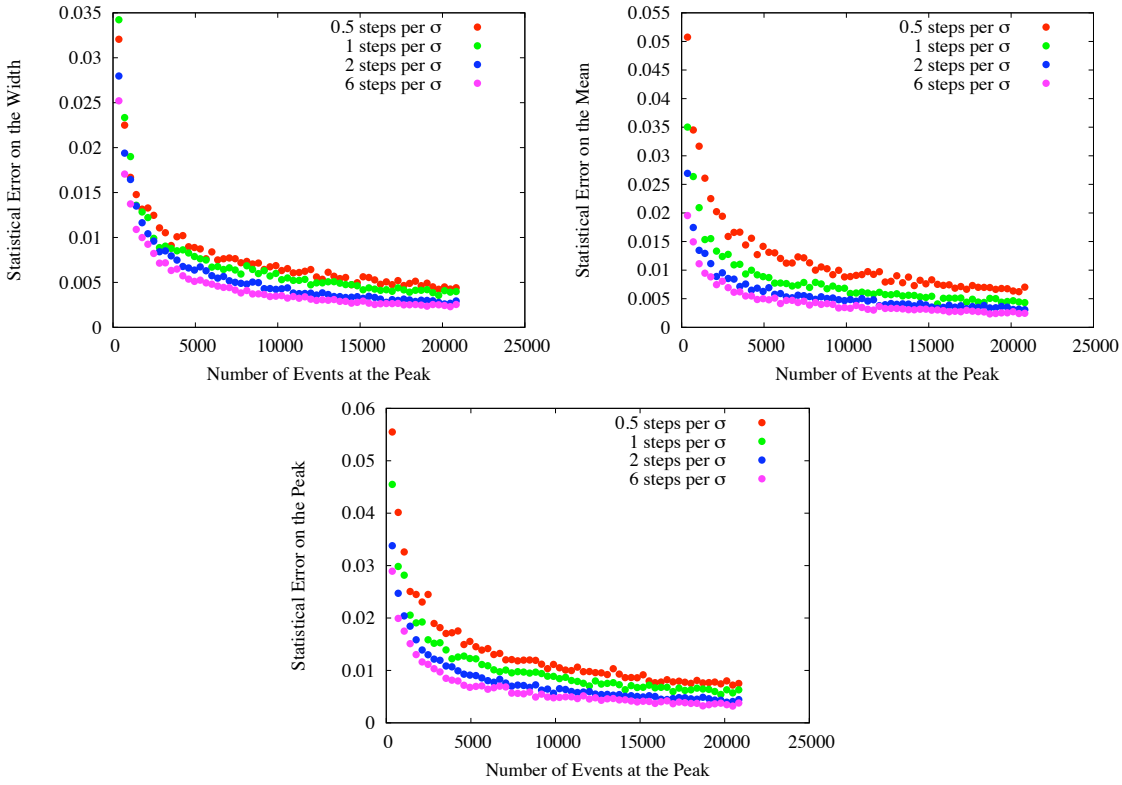

Figure 2.6: Results of the numerical simulations for various step sizes. The width is shown on upper left plot, the mean on the upper right and the peak at the bottom. A clear dependency of the statistical accuracy on the input scan parameters is observed.

The simulation results show a clear dependency of the statistical accuracy of the fitted parameters on the number of steps per σ and the number of events at the peak. The precision reaches a saturation around 10000 (1 % standard error) events at the peak and no clear improvement of the uncertainty is seen for more than 2 steps per σ. It is also seen that the statistical error is dominated by the point-to-point error on the rate i.e. accumulating sufficient statistics at each point would help reducing the number of steps which is a non-negligible gain in time. For all fit parameters the statistical error drops below 1 % for a standard error at the peak of about 1 %. This was chosen as a criterium to determine the scan parameters.

Table 2.1: Single bunch luminosity at 3.5 TeV assuming a nominal emittance of 3.75 μm and an effective cross section of 10 mb.

β^* (m)	σ^* (μm)	N_p p/bunch	$\mathcal{L}$ (cm^{-2}s^{-1})	$\dot{N}$ (Hz)	t_{step} (s)
11	105	2×10^{10}	3.58×10^{27}	36	277
2	45	2×10^{10}	1.76×10^{28}	176	56
3.5	60	1.15×10^{11}	3.29×10^{29}	3290	4

Table 2.1 lists the expected number of events per bunch for different operation scenarios. Total rates and luminosities are increased by the number of colliding bunches. An effective cross section of 10 mb is very conservative as is was derived from the efficiency of the BRAN ionization chambers calculated in Chapter 4. The efficiency of the experiments luminosity monitors is expected to be much higher. Even in early operation (second case), a few seconds are sufficient to reach a 1% statistical accuracy at the peak, the statistical error can therefore easily be reduced to a negligible level with respect to other sources of uncertainties while keeping the duration of the measurement within reasonable limits.

2.2.2 Beam Displacement

The knowledge of the absolute beam displacement is essential for the measurement of the beam size, any uncertainty or error on the scale factor will directly translate in an error on the beam size. In order to displace the beams at the interaction point the orbit is modified with a four magnet closed orbit bump which allows to establish an orbit deformation with well defined position and slope at any given position m. The position m is then located between the second and the third magnet. Considering four orbit correctors $c1, c2, c3, c4$ the requirements for the bump are:

$$x_m = A \quad \text{and} \quad x_m^{'} = A^{'}, \tag{2.69}$$

and the conditions for the bump to be closed i.e. unchanged orbit at the first and last corrector are

$$x_1 = x_4 = 0 \quad \text{and} \quad x_1^{'} = x_4^{'} = 0. \tag{2.70}$$

The equation for the closed orbit at a position m and with kicks k_i is

$$x_m = \sum \frac{\sqrt{\beta_m \beta_i}}{2\sin(\pi Q)} \cos(\pi Q - |\mu_m - \mu_i|)\, k_i. \tag{2.71}$$

By taking the derivative of this expression and after some algebra we get an expression of $x_m^{'}$:

$$x_m^{'}\beta_m + \alpha_m x_m = \sum \frac{\sqrt{\beta_m \beta_i}}{2\sin(\pi Q)} \sin(\pi Q - |\mu_m - \mu_i|)\, k_i, \tag{2.72}$$

where Q is the overall tune of the machine and β, α and μ are the β and α functions and phases at the position of the observation m and the distortions i. The conditions for the closure of the bump can be written as:

$$C \sum \sqrt{\beta_i} \cos(\mu_1 - \mu_i)\, k_i = 0, \tag{2.73}$$

Table 2.2: Hysteresis effects from the calibration scans bumps orbit correctors on the beam coordinates at the IP.

	Horizontal		Vertical	
	Position (σ)	Angle (μrad)	Position (σ)	Angle (μrad)
IP1	0.04	1.5	0.06	1.3
IP2	0.04	0.4	0.05	0.3
IP5	0.04	1.3	0.05	1.5
IP8	0.05	0.3	0.03	0.4

and

$$C\sum\sqrt{\beta_i}\sin(\mu_1-\mu_i)\,k_i=0. \tag{2.74}$$

It is then possible to formulate the problem as a system of linear equations:

$$\begin{pmatrix} x_m \\ x_m^{'}\beta_m+\alpha_m x_m \\ x_1 \\ x_1^{'} \end{pmatrix} = \begin{pmatrix} A \\ A^{'}\beta_m+\alpha A \\ 0 \\ 0 \end{pmatrix} = T\cdot C \begin{pmatrix} \sqrt{\beta_1}k_1 \\ \sqrt{\beta_2}k_2 \\ \sqrt{\beta_3}k_3 \\ \sqrt{\beta_4}k_4 \end{pmatrix}, \tag{2.75}$$

where the transformation matrix T is

$$T=\begin{pmatrix} \cos(\pi Q-\mu_m+\mu_1) & \cos(\pi Q-\mu_m+\mu_2) & \cos(\pi Q+\mu_m-\mu_3) & \cos(\pi Q+\mu_m-\mu_4) \\ \sin(\pi Q-\mu_m+\mu_1) & \sin(\pi Q-\mu_m+\mu_2) & -\sin(\pi Q-\mu_m+\mu_3) & -\sin(\pi Q-\mu_m+\mu_4) \\ 1 & \cos(\mu_2-\mu_1) & \cos(\mu_3-\mu_1) & \cos(\mu_4-\mu_1) \\ 0 & \sin(\mu_2-\mu_1) & \sin(\mu_3-\mu_1) & \sin(\mu_4-\mu_1) \end{pmatrix}, \tag{2.76}$$

and the constant C

$$C=\frac{\sqrt{\beta_m}}{2\sin(\pi Q)}. \tag{2.77}$$

For the specific case of the separation scans we displace the beam at the IP where α, the slope of the β-function, is equal to zero and we want only a parallel separation so that $x_m^{'}$ is also set to zero. This formalism demonstrates that lattice imperfections or field errors affect the closure of the bump which therefore has to be measured and calibrated. Magnetic measurements and simulations were performed for the magnets used to generate these bumps in order to estimate the effect of the hysteresis [23] which is a source of field errors. A detailed description of this study is presented in Chapter 3 and results are summarized Table 2.2.

These results represent the peak-to-peak error on the IP beam coordinates due to the hysteresis. This was done for the nominal optics at 7 TeV which proved to be the worst case scenario. We can see that the error is a fraction of a beam σ in all IPs for the position and a few μrad for the angle. This represents a change in rate of the order of about 0.1% in terms of rates which is not considered to be an issue for reproducibility.

In order to minimize the hysteresis effect during the scan, the sweep is performed always in the same direction. This should avoid any jump from one hysteresis branch to the other during a scan. In addition, for each scan an acquisition at zero separation is performed at the beginning, middle and the end of the scan. The middle point is on a different hysteresis branch as the two other points, assuming the beam conditions do not vary during a scan (emittance, intensity) this would also give an indication on the hysteresis effects.

A bump non-closure would result in a scale factor error on the beam displacement which would directly modify the measured beam size. The origin of the non-closure is the combined effect of the hysteresis

and lattice imperfections. The closure of the bump can easily be measured using orbit data, and the IP displacement calibrated using the luminous region reconstruction. The latter method was also used at SLAC [24] where a resolution of 5 μm or better on the determination of the beam position was achieved. This would represent an error of 1-2% on the length scale for a β^* of 2 m and would considerably reduce the uncertainty on the effective beam size measurement.

2.2.3 Beam Current Transformers (BCT)

The BCTs installed in the LHC are capable of integrating the charge of each LHC bunch. The precision of these measurements for the nominal LHC beams is expected to be of the order of 1% [25]. An additional uncertainty could come from the longitudinal bunch distribution; unbunched particles or non colliding bunches would be counted in the average beam intensity while not fully contributing to the luminosity. A careful bunch by bunch analysis combined with a calibration at the end of the ramp where there is no unbunched components should provide a good understanding of this uncertainty.

2.2.4 Beam-beam Effects

Beam-beam effects are relevant at high intensities. Ideally all the calibration scans should be performed at low intensity to minimize this effect. However, the LHC will be running at high intensities and it could be interesting to perform scans at nominal beam conditions. In this case, the beam-beam force will introduce a non-linear behavior as a function of the separation which can affect the orbit or emittance and will couple the transverse distributions. These effects are expected to be small. They still require a good understanding based on observations and analysis of experimental data to confirm these expectations. As a first estimate and for the purpose of this discussion we will start assuming a 1 % systematic error to account for the beam-beam effects at nominal bunch intensity.

2.2.5 Pile-up

At high luminosity the probability that one single bunch crossing produces several independent events is non-negligible, these are called *pile-up events*.

Table 2.3: Pile-up at 3.5 TeV assuming a nominal emittance of 3.75 μm and a total pp cross section of 72 mb.

β^* (m)	σ^* (μm)	N_p p/bunch	$\mathcal{L}$ ($cm^{-2}s^{-1}$)	N / bunch crossing (Hz)
11	105	2×10^{10}	3.58×10^{27}	0.023
2	45	2×10^{10}	1.76×10^{28}	0.113
3.5	60	1.15×10^{11}	3.29×10^{29}	2.106

This could potentially affect the readings of the luminosity detectors and has to be corrected for. In principle this effect is well known and can be corrected. For the purpose of a calibration of the luminosity it is however preferable to avoid it.

2.2.6 Summary

The list of expected sources of systematic uncertainties quoted above is non-exhaustive and covers only the main known sources. Other effects might contribute such as coupling which will displace the beam in one plane while scanning the other plane. Table 2.4 summarizes the identified sources of systematic errors.

Table 2.4: Expected uncertainties for nominal LHC running conditions and conditions used for calibration.

	Nominal	Calibration
Crossing Angle	2%	negligible
Beam-beam effects	1%	negligible
Beam current	1%	1-2 %
Hysteresis effects	negligible	negligible
Length scale	1-2%	1-2%

The total uncertainty resulting from this list results in an overall 4 % systematic uncertainty which has to be added to the statistical error. This assumes perfectly stable beam conditions and that the instrumentation is fully understood and calibrated. Ultimately, the precision of the measurement can therefore be expected to be of the order of 5 %, for which the two main contributors will be the intensity measurement and the determination of the beam displacement. The LHC is a very complex machine and it will require some time before it reaches its nominal performance. A resonable aim for an initial calibration of the luminosity during the first months of operation of the LHC would then be about 10 % [21]. This was already achieved at RHIC [26] with strong hourglass and beam-beam effects.

Chapter 3

From Injection to Collision at High Energy

Before they are brought into collision at high energy, the LHC beams pass through several accelerators where they are accelerated in stages to reach their final energy in the LHC. Each of these stages is essential and will determine the quality of the beams that will provide data to the experiments. This chapter will give a brief overview of the CERN accelerators complex and then focus on how the LHC beams are brought into collision.

3.1 The LHC Injectors

The acceleration of the LHC protons is performed in stages as they go through the different accelerators along the injector chain as shown Figure 3.1. The protons are generated by a duoplasmatron source from which they are extracted with an energy of 100 keV and injected into LINAC2. LINAC2 is an 80 m long linear accelerator with an extraction energy of 50 MeV. During the acceleration process in the LINAC the proton beam is also bunched using RF cavities. Once extracted from the LINAC the protons are injected into the **P**roton **S**ynchrotron **B**ooster (PSB), a 157 m circular accelerator complex capable of accelerating protons up to 1.4 GeV, which consists of a stack of four separate rings. From the PSB the particles are injected into the **P**roton **S**ynchrotron (PS), a 628 m ring where they are accelerated up to an energy of 26 GeV. All these machines are installed at ground level. A this point the beam is sent in an underground machine, the **S**uper **P**roton **S**ynchrotron (SPS), which is a 6.9 km long circular accelerator lying 50 m underground. They are then accelerated to 450 GeV, the LHC injection energy. The injection of the LHC beams from the SPS is done in IR2 for beam 1, going clockwise, and IR8 for beam 2, going anti clockwise. All these accelerators are linked through transfer lines which allow for the particles to travel from one machine to the other.

The LHC was also designed to collide heavy ions which follow a slightly different path, they first go through the LINAC3 and then LEIR (**L**ow **E**nergy **I**on **R**ing) before continuing on the same path as the protons from the PS.

3.2 The Large Hadron Collider

The LHC (**L**arge **H**adron **C**ollider) is a 27 km long circular collider which lies about 100 m underground, in France and Switzerland near Geneva in the former LEP tunnel. The two proton beams have to be deflected by opposite magnet dipole fields. The LHC was designed as two eight fold symmetry rings with separate magnet fields and beam chambers and with common sections in the experimental regions where the beams collide. There is not enough space to have two separate rings in the LEP tunnel. Therefore, the LHC uses twin magnets which consist of two sets of coils and beam channels within the same mechanical structure and cryostat as illustrated Figure 3.2. This design also reduced the overall cost of the machine. The LHC

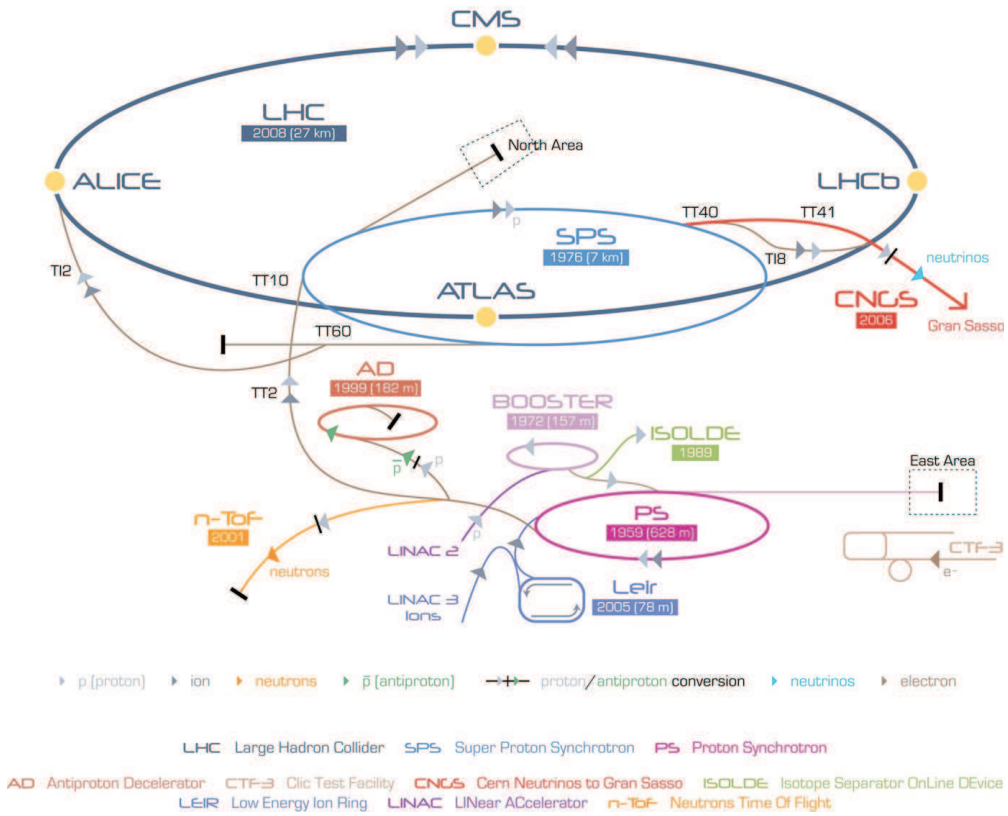

Figure 3.1: The CERN accelerators complex. The protons follow the gray arrows.

consists of a total of 9593 superconducting magnets of which 1232 are main dipoles of about 15 m long (each of the eight LHC arcs contains 154 main dipoles) and 392 are main quadrupoles.

The LHC beams collide in four interaction points, where the proton-proton collisions are observed by four large experiments, ATLAS [27] (IP1), ALICE [28] (IP2), CMS [29] (IP5) and LHCb [30] (IP8), and two smaller experiments, LHCf [31] (IP1) and TOTEM [17] (IP5). ATLAS and CMS are general purpose detectors. One goal of these large detectors is the search for the Higgs boson. ALICE was mostly designed for heavy ions collisions and will study the quark-gluon plasma, LHCb is specialized in the physics of the B-meson, TOTEM is a forward detector aiming at measuring the proton-proton cross section and studying diffractive processes and LHCf uses the LHC as a source to study processes relevant for cosmic rays in laboratory conditions.

The LHC was designed to provide a peak luminosity of $10^{34}\,\mathrm{cm}^{-2}\mathrm{s}^{-1}$ for CMS and ATLAS. The corresponding design parameters are listed Table 3.1. These parameters reflect the numbers from the initial LHC Technical Design Report [32].

The other insertion regions host the RF (IR4) which accelerates the beams and keeps them bunched, the beam dump (IR6) used for extraction from the LHC and cleaning devices (IR3 and IR7) which are critical for machine protection.

In order to provide collisions and quality data to the experiments with the desired rates, the beam parameters have to be precisely controlled. The interaction regions (IR) where the experiments are located have all very similar designs. They all consist of 13 main quadrupoles left and right of the IP out of which 3 on each side, the triplets, are situated in the common region and are used for the final focusing. The triplets will therefore affect both beams where the other quadrupoles will act on the beams independently. These quadrupoles are used to tune and control the optical functions in the insertion regions.

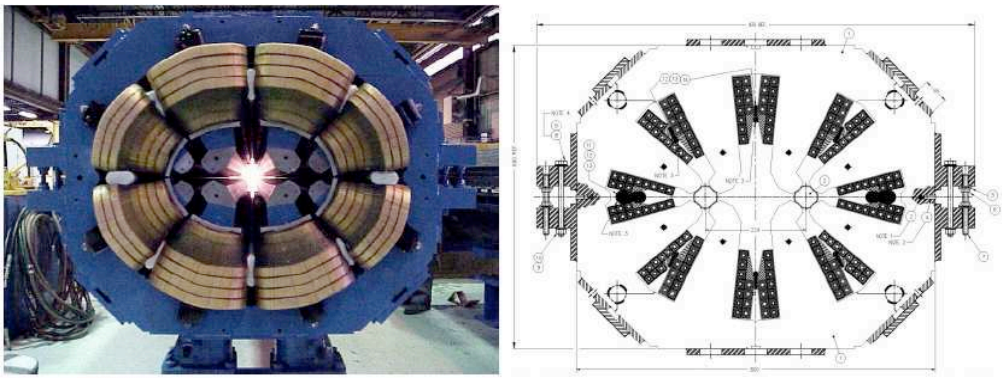

Figure 3.2: Cross section view of an LHC warm quadrupole. Illustrates the twin aperture.

Table 3.1: Nominal LHC beam parameters. The crossing angle reduction factor applies to the luminosity.

	Injection	Collision
Energy [GeV]	450	7000
Intensity [10^{11} p/bunch]	1.15	
Number of bunches	2808	
Transverse Emittance [μm]	3.5	3.75
RMS bunch length [cm]	11.24	7.55
β^* (IP1/IP5) [m]	11	0.55
β^* (IP2/IP8) [m]	10	10
RMS Beam Size (IP1/IP5) [μm]	283	16.6
RMS Beam Size (IP2/IP8) [μm]	270	70.9
Crossing Angle Reduction Factor (IP1/IP5)	-	0.836
Peak Luminosity (IP1/IP5) [$\mathrm{cm}^{-2}\mathrm{s}^{-1}$]	-	1.0×10^{34}

Figure 3.3 shows a schematic view of the final focusing region in IR5. The beams share the same beam chamber up to the D1 dipole where they are deflected and sent into two independent beam pipes. Other devices such as orbit correctors are present in order to allow adjustments of the various beam parameters around the ring.

3.3 LHC Commissioning and Operation

The LHC beams are injected at a β^* of 11 m in IP1 and IP5 and 10 m in IP2 and IP8. After this, the beams are *ramped* to high energy and then *squeezed* to smaller β^* at the interaction points to increase luminosity. During this process, the beams are kept separated at the interaction points.

Figure 3.4 shows the evolution of some key parameters through the different operation stages. The peak luminosity depends on both the energy and the β^* as illustrated by the increase during the ramp and the squeeze. In operation, the beams are kept separated until the end of the squeeze. The luminosity is therefore only shown to illustrate this dependency. During the 2010 LHC run the ramp and the squeeze took about 30 minutes, extra time is required for correction of various beam parameters in between each step of the procedure.

The first proton beam was injected in the LHC on the 10^{th} of September 2008. Excellent progress with beams were made before an issue was found that required an extended shutdown. About 50 main dipoles had to be removed for inspection and some had to be replaced. A major upgrade of some systems was

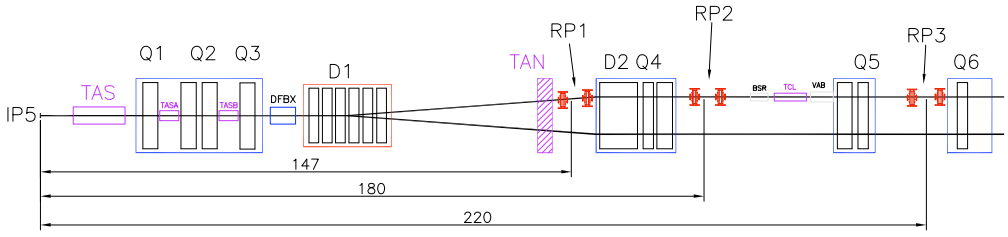

Figure 3.3: Final focusing of IR5. The beams share the same beam chamber up to D1 where they are deflected and sent into two independent beam pipes.

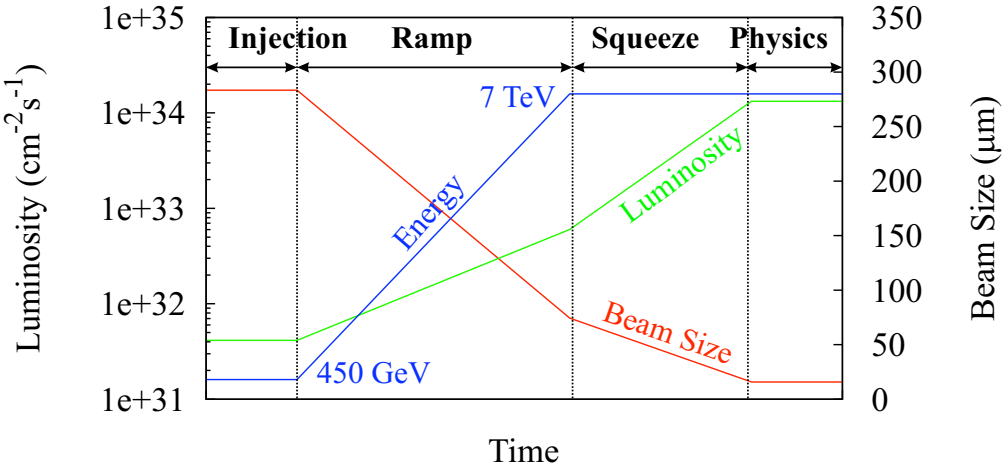

Figure 3.4: Evolution of the beam parameters through the different operation stages. The luminosity represents the maximum achievable luminosity if the beams were to collide at that point using the IP1 nominal beam parameters.

necessary to avoid another incident and it took about a year to recover and resume operation with a reduced energy of 3.5 TeV per beam.

The LHC restarted on the 23$^{\text{rd}}$ of October 2009 and saw its first ion beam on the 7$^{\text{th}}$ of Novembre 2009. With the actual set-up of the machine and because of the reduced energy the β^* is limited to 2 m without crossing angle and 3.5 m with crossing angle.

Table 3.2: Single bunch luminosity at 3.5 TeV assuming a nominal emittance of 3.75 μm.

β^* (m)	σ^* (μm)	N_p p/bunch	$\mathcal{L}$ (cm^{-2}s^{-1})
11	105	2×10^{10}	3.58×10^{27}
2	45	2×10^{10}	1.76×10^{28}
3.5	60	1.15×10^{11}	3.29×10^{29}

Table 3.2 lists some parameters during the initial steps of LHC commissioning. Most of the LHC systems have now been successfully commissioned and the effort is directed towards increased intensity to reach a target luminosity of about $1.0\times10^{32}\,\text{cm}^{-2}\text{s}^{-1}$ for the 2010-2011 LHC run.

3.4 The LHC Crossing Scheme

The crossing scheme is commonly defined as the way the beams cross each other at the interaction points. The LHC crossing schemes were designed [33, 34] using a crossing angle in one plane and a parallel separation in the other transverse plane. This section will present the design and purpose of such a configuration.

3.4.1 Design

The design of the crossing scheme is similar in all interaction points. As an example, the crossing scheme of IP1 is presented in Fig. 3.5 in the horizontal and vertical plane.

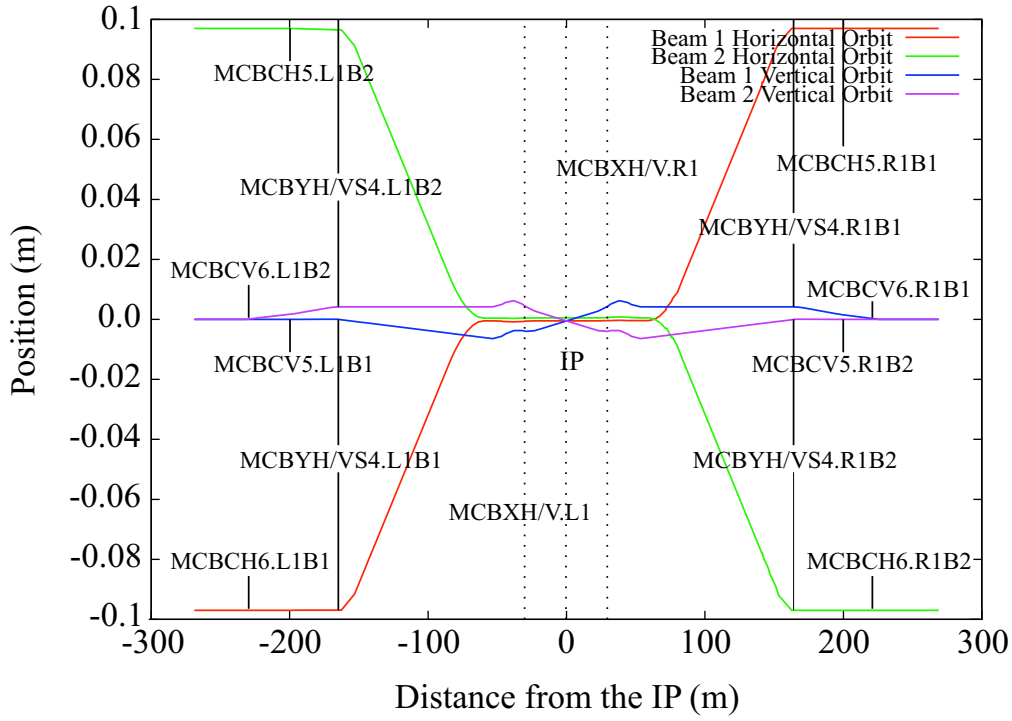

Figure 3.5: Crossing scheme in both planes at IP1. In this case the parallel separation is in the horizontal plane and the crossing angle is in the vertical plane. Six orbit correctors are used for these closed orbit bumps consisting of three families of magnets: the MCBC and MCBY which control the beams independently and the MCBX, located in the common region, which drive both beams together.

It is realized using six dipole corrector magnets per plane and beam and involves three different hardware types, called MCBC, MCBY and MCBX [32]. The MCBC and MCBY are far away from the IP and will control the beams independently where the MCBX are common for both beams. In addition the MCBX magnets are special nested magnets which control the horizontal and vertical planes, one MCBX will then be used to generate the crossing angle and separation for both beams. This design was chosen in order to gain some space in the triplet region but will result in cross talk in between planes and beams.

3.4.2 Separation Bumps

During the ramp and the squeeze the beams are kept separated using parallel closed orbit bumps, shown in Figure 3.6,in order to avoid unwanted collisions. This mode of operation becomes even more relevant when

running at high intensity as collisions might add some non-linear effects to the already delicate process of ramping and squeezing the beams.

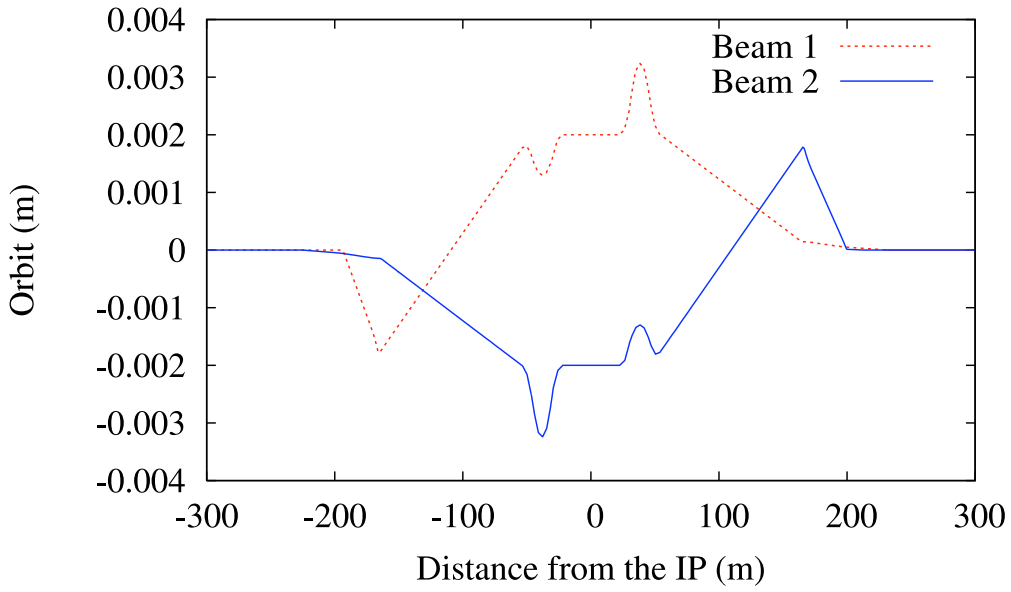

Figure 3.6: Parallel separation bumps at IP5. Vertical plane.

The separation has to be large enough to reduce the long range beam-beam effects to a tolerable level. The nominal safe margin was set to 14 σ. The separation is kept constant in millimeters all through the ramp, and in principle reduced before starting the squeeze. When the machine is stable at high-energy the bumps are ramped down to zero to produce collisions.

3.4.3 Crossing Angle

While it is rather evident why the beams are kept separated when collisions are not wanted, the use of a crossing angle requires some explanations. For nominal conditions, each LHC beam consists of 2808 bunches of protons injected in trains in the LHC. Each train consists of 72 bunches separated by 25 ns, each of these trains is separated from the next one by at least 200 ns. The gaps between trains and bunches are imposed by the capabilities of the injectors and beam dynamics considerations [35].

The D1 dipole is situated at $\ell_{\mathrm{D1}} = 58$ m from the IP. From this we can calculate the number of parasitic collisions that will occur on each side of the IP:

$$n_{\mathrm{parasitic}} = \frac{2\,\ell_{\mathrm{D1}}}{b_s\,c} \approx 15 \tag{3.1}$$

where b_s is the bunch spacing, ℓ_{D1} is the distance between the IP and the Dx dipole and c is the speed of light. Without any extra separation the beams would experience about 15 collisions on each side of the IP. These collisions are not useful to the experiments and could be critical for machine operation as some of them are located inside the triplets. To avoid these parasitic collisions an angle, shown in Figure 3.7 is added in the crossing scheme which separates the beams at the location of these parasistic collisions. A schematic view of the bunch crossing with an angle was shown Figure 1.4.

Differently from the parallel separation bumps the crossing angle has to remain on as the beams collide and moreover its value should remain constant.

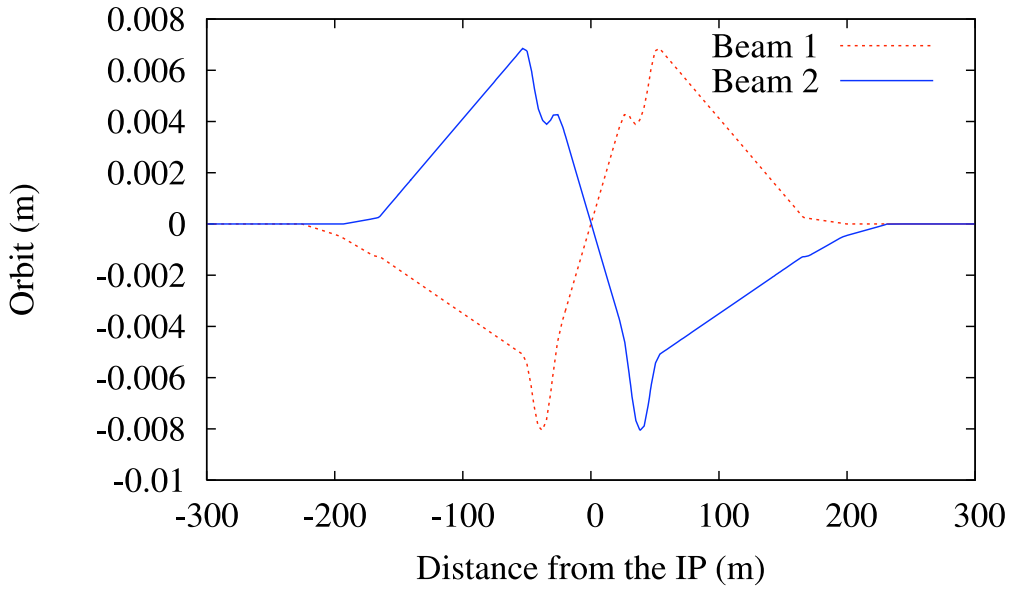

Figure 3.7: Crossing angle bumps at IP5. Horizontal plane.

3.4.4 Hysteresis Effects

As shown Figure 3.5 the crossing scheme is generated using three families of magnets, the MCBC, MBCY and MCBX. All these magnets are superconducting and subject to persistent current effects and hysteresis. Hysteresis affects the instantaneous value of the field generated by a corrector and it makes it dependent on the powering history. Field errors due to hysteresis in the orbit correctors are expected to affect the orbit position at the IP as well as the crossing angle which should in principle remain constant. These magnets will also be used for orbit correction and optimization of the IP beam coordinates. It is therefore important to know how big this effect will be in order to control the magnets appropriately. More details on the model are presented in [23, 36].

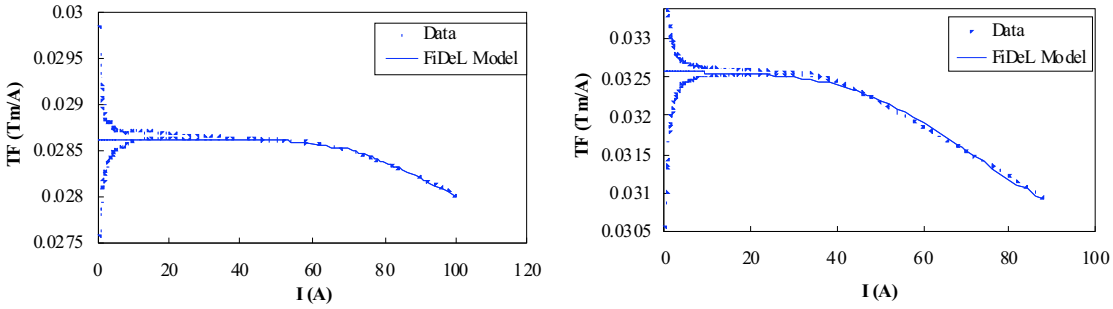

Figure 3.8: Hysteresis measurements and transfer function (TF) of the MCBC (left) and MCBY (right). The model takes into account the saturation but not the hysteresis loop, an error is therefore expected at low currents.

Figure 3.8 shows the measurements and modelling, FiDel [37], of the transfer function (TF) for the MCBC and MCBY magnets. We can see that the hysteresis loop was not modelled for these magnets, field errors and effects on the orbit are therefore expected at low currents. The errors are similar for these two magnets and were treated together. Simulations were performed in order to assess the effects on the orbit by

Table 3.3: Hysteresis effects on the IP beam coordinates from the MCBC and MCBY.

	Horizontal		Vertical	
	Position (σ)	Angle (μrad)	Position (σ)	Angle (μrad)
IP1	0.04	1.5	0.06	1.3
IP2	0.04	0.4	0.05	0.3
IP5	0.04	1.3	0.05	1.5
IP8	0.05	0.3	0.03	0.4

generating random errors for each of these magnets.

Table 3.3 summarizes the simulation results. The error quoted is the peak to peak error over all the seeds used for the simulation and illustrates the orbit distortions at the interaction point. These results are the ones for the LHC nominal optics at 7 TeV. The error in position is a fraction of a beam σ whilst the angle is affected by a few μrad. These values are very small and well within the errors originating from beam-beam effects the latter being about 0.1 to 0.2 σ offset and an angle of about 5 μrad [38]. The difference between the IPs is due to the differences in the optics layout and powering scheme.

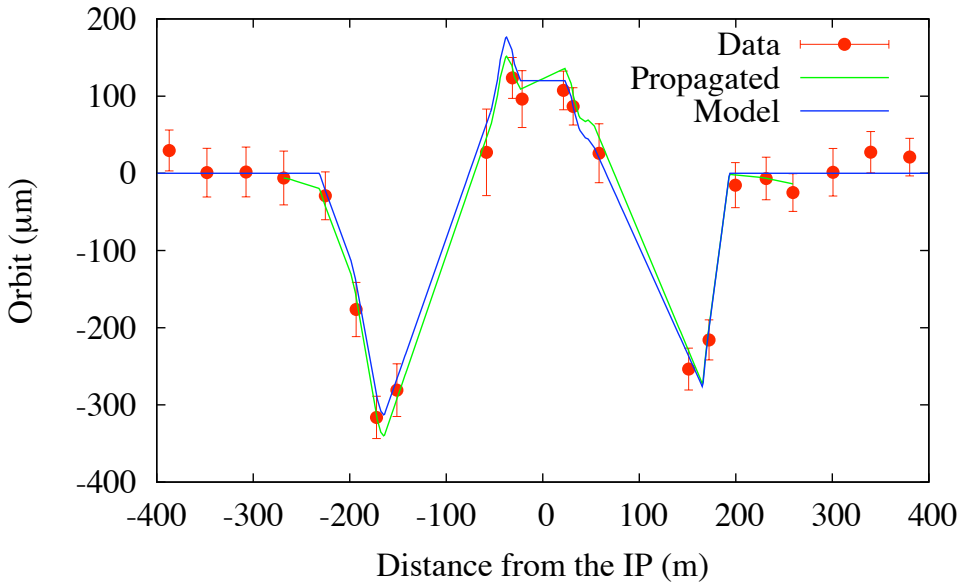

Figure 3.9: Example of bump measurement in IP1 without MCBX. The data are consistent with the model within the error bars.

Figure 3.9 shows a bump measurement in IP1 without MCBX. The data represent the difference orbit between a reference taken without the bump and one with the bump on. The model uses the design lattice and closed orbit and the propagated data, using the design lattice and inital measured conditions, would show a disagreement with the data if a field error is present within the bump. All three data sets agree very well. The data are consistent with the model within the error bars. This measurement was performed without any additional corrections on the bump that would compensate for eventual non closure and proves that the magnetic model of these magnets behaves as predicted by the simulations.

As described before, the MCBX are nested magnets consisting of an inner and an outer coil that will respectively generate horizontal and vertical deflections at the same time. Figure 3.10 represents hysteresis measurements of the inner coil of several MCBX magnets. The hysteresis is wider for these magnets. In addition, a field error in the MCBX will affect both beams. The same simulations as for the MCBC and

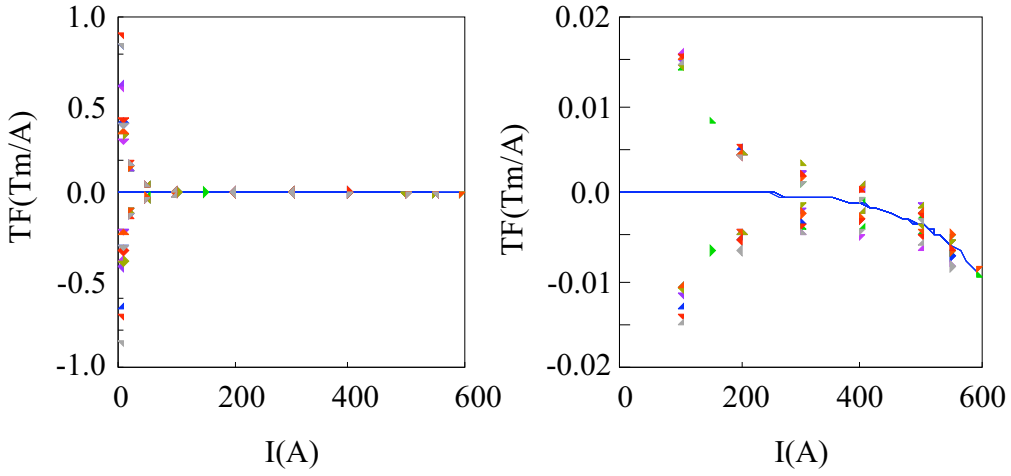

Figure 3.10: Hysteresis measurements and model for the MCBX inner coil. The left plot is a zoom of the right one around zero.

MCBY were performed using these measurements and showed that the error would result in a maximum offset of 1 σ and a maximum angle of 15 μrad at the IP for the worst case of nominal optics.

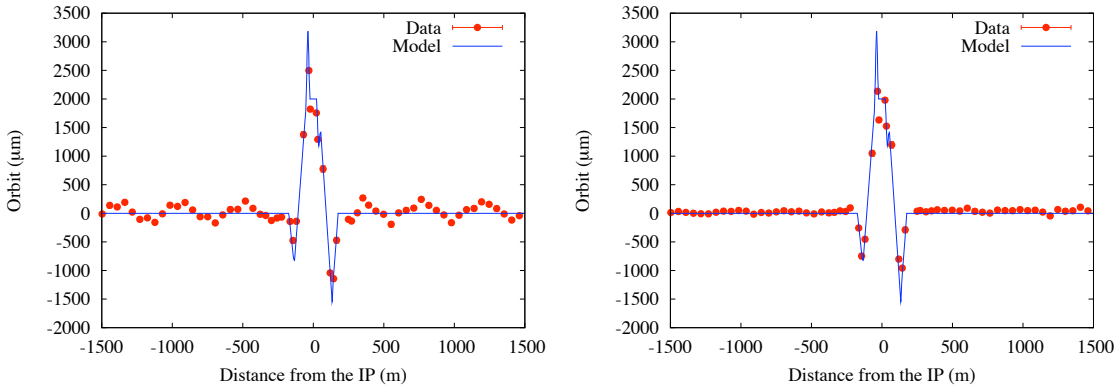

Figure 3.11: Bump measurement including MCBX magnets. Before correction (left) and after correction with only the bump correctors (right). If no correction is applied a clear non-closure is observed. Its source could be identified as a field error within the bump since it could be corrected using only the bump correctors.

Figure 3.11 shows measurements of a bump including MCBX magnets. A clear non-closure is observed and had to be corrected for. The correction could be applied using only the correctors included in the bump which confirms that the error was located inside the bump. The bump without MCBX consisted of the same orbit correctors except for the MCBX and showed no signs of large non-closure. This confirms the simulation results which showed larger effects from the MCBX. Hysteresis effects could easily be compensated for with a single orbit correction and should not affect operation of the LHC, however for the fine tuning and optimization of the IR it was decided not to use the MCBX magnets in order to keep the orbit as stable as possible.

3.5 Bringing the Beams Into Collision

During the ramp and squeeze the beams are kept separated to avoid unwanted collisions. Once the beams are stable at high energy the last step is to bring them into collision. This section will present the method and operational aspects related to this procedure.

3.5.1 Procedure

The first step towards collisions is to ramp down the separation bumps, however some residual separation can remain which will keep the beams separated. Additional corrections are then necessary. All four interaction points are equipped with directional striplines (BPMSW [32]) which give independent measurements for beam 1 and beam 2 but have independent systematic offsets and non-linearities. No optical elements are present in between those BPMs. The beam position at the IP is then calculated with a linear interpolation.

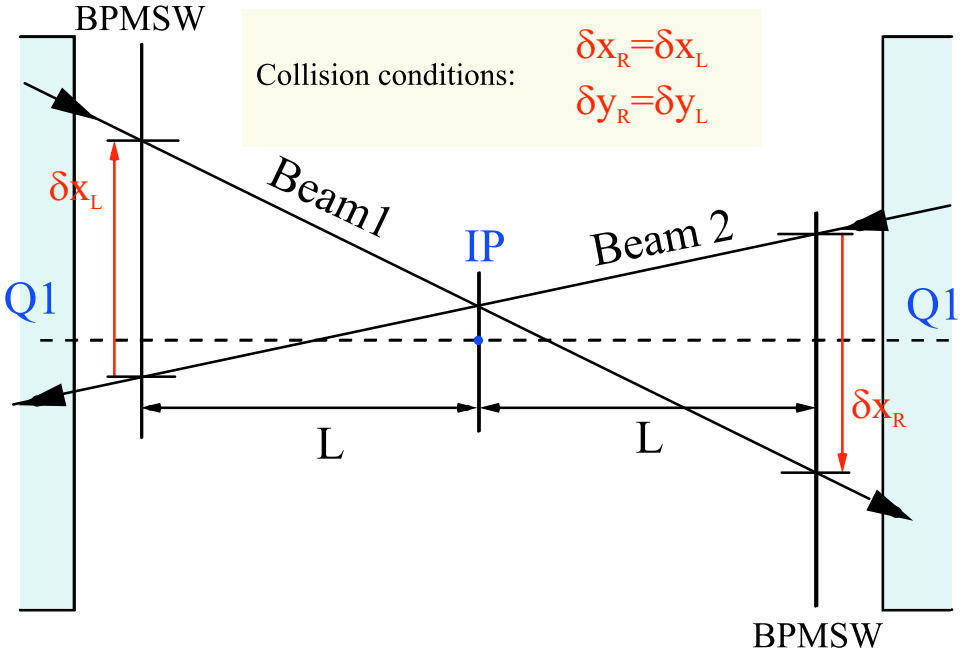

Figure 3.12: Schematic view of the interaction region. The collision point can be found by equalizing the separation on both sides of the IP. Beam Position monitors are situated left and right of the IP from which the IP beam coordinates can be derived with a linear interpolation.

As shown in Figure 3.12, the sufficient condition for the beams to collide is that the separations on both sides of the IP have equal amplitudes and opposite signs. These separations are measured with beam position monitors [39, 40], and the orbit is adjusted using closed orbit bumps. As long as the beams are large enough, the resolution of these BPMs should be sufficient to find the collision point. When the beams become smaller than the BPM resolution (200 μm at low intensity), i.e. for squeezed optics, one has to improve the method. In the case of IP1 and IP5 special button pick ups were installed that measure the two beams with the same electronics. This gives a differential measurement which considerably reduces the error on the separation. In the case of IP2 and IP8, or if the beams cannot be found even with the button pick ups, one has to scan in a methodical way to cover the transverse plane until the collision point is found. In the LHC the orbit and optics stability is rather good, using the optimal settings as a reference from fill to fill should ensure collisions without having to repeat this procedure. This was not the case for the 2 m optics, as

illustrated in Figure 6.10, where large corrections had to be applied from to fill to fill to collide the beams. Fine tuning and optimization is done using the separation scan method.

3.5.2 How Fast Can We Go Into Collision?

Assuming a perfectly corrected machine the time required to put the beams into collision is given by the collapsing time of the parallel separation bumps. As presented above, these bumps were designed using three families of magnets the MCBC, MCBY and MCBX. The ramping time of the bump is determined by the ones of these magnets.

Table 3.4: Characteristics of the orbit corrector magnets around the IP.

Magnet	Nominal I [A]	dI/dt [A/s]	d^2I/dt^2 [A/s^2]
MCBX	550	5	0.5
MCBY	72	0.67	0.25
MCBC	80	0.67	0.25

Table 3.4 shows the nominal settings of those orbit correctors. Those values were not yet achieved for all MCBX in the first hardware commissioning campaign. Collapsing the separation bumps consists of ramping all the correctors fields down to zero. In this study we will model the ramp with a parabolic-linear-parabolic approximation. The parabolic phases depend on an acceleration term and the linear phase on dI/dt. The separation at the IP is assumed to vary linearly with the currents applied to the correctors.

3.5.3 Optimizing the Collapsing Time via Optics Rematching

Many beam dynamics processes can occur while bringing the beams into collision which might degrade some critical parameters such as the emittance and the lifetime. For this reason it is interesting to study the flexibility of the current design [41]. Decreasing the ramping rate of a power converter can easily be done while the upper limit is an hardware constaint and cannot be overcome unless the power converter is upgraded. This section will then focus on this upper limit and try to give a statement on how fast the separation bumps can be ramped down. It is possible to find the minimum collapsing time by varying the strength of the MCBX magnets and closing the bump using the other correctors. This was done using the matching procedures of the MAD-X program [42].

Figure 3.13 shows the evolution of the collapsing time versus the MCBX angular kick at the four IPs for the nominal 7 TeV LHC optics (full separation at the four IPs). Given the actual hardware settings, the limitation comes from the MCBX and the collapsing time only depends on its acceleration and ramping rate. Table 3.5 summarizes the results for the nominal LHC optics. In the case of low β^*, the time is limited by the deceleration (10 s to go from the maximum dI/dt to zero for a ΔI of 25 A). At large separation the beams do not affect each other. An interesting figure of merit is the time required to ramp down the bumps from a separation of 14 σ where each beam starts to be affected by the field of the opposite beam.

During its first two years of operation the LHC will run with a limited energy of 3.5 TeV per beam with a minimum β^* of 2 m and a separation of 2 mm. The separation is twice as large as for the 7 TeV optics but the current required for the same separation will be smaller. The time required to ramp down the separation will then be equivalent and the time spent in the critical region when the beams start interacting with each other (few σ) will be shorter.

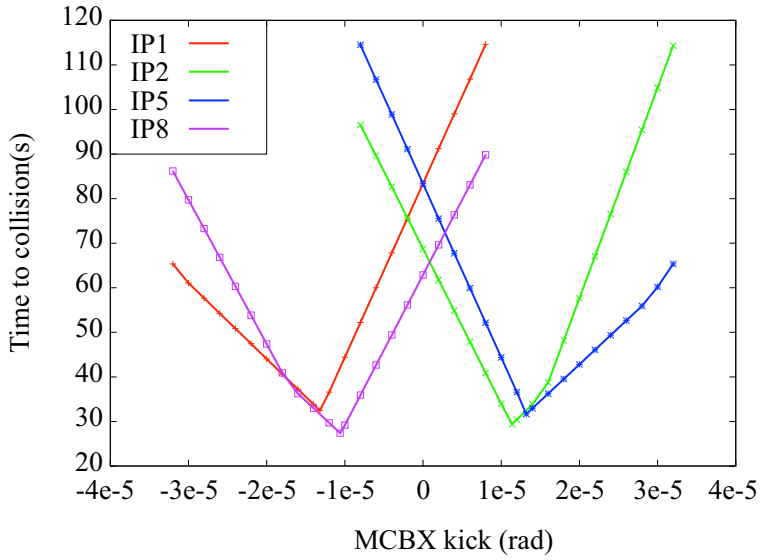

Figure 3.13: Evolution of the collapsing time with the MCBX strength. LHC version 6.503, collision optics at 7 TeV. A minimum ramping time can be found by varying the strength of the MCBX magnets.

Table 3.5: Summary table. t represents the expected collapsing time in seconds for full separation (1 mm at 7 TeV) and 14 σ separation.

	β^* [m]	t_{full} [s]	$t_{14\sigma}$ [s]
IP1	0.55	33	11
IP2	10	27	27
IP5	0.55	32	11
IP8	10	29	29

3.5.4 Beam-Beam Effects While Bringing the Beams into Collisions

In the process of collapsing the separation bumps to bring beams into collision, each beam will be influenced through the beam-beam interactions by the bunches of the counter-rotating beam. The forces depend on the actual, dynamically varying separation and beam shapes and influence the trajectories of the particles in each beam. Simulations [43] have shown a clear dependence of the emittance growth with the separation in the case of static offsets. The purpose of the simulations [41] presented in this section is to study the case of dynamic offsets to check whether unwanted effects could arise while bringing the beams into collisions.

Many detailed beam-beam simulations have been performed for the LHC for the static case with fixed offsets [43, 38]. A first study of dynamic effects was presented in [44]. Here we describe recent studies in which we dynamically change the separation between the colliding beams. We know that emittance blow up and lifetime in the presence of beam-beam may critically depend on many parameters and may substantially vary in a real machine from fill to fill. The studies presented here are mostly intended as a guidance for further work with optimization on the actual machine. For the dynamic simulations discussed here, we found it convenient to start from the object oriented program BeamTrack [45] for which simulation of beam-beam effects with programmable, time dependent separation was recently added. The beam-beam force is described in 4D. The one turn matrix is tracking the particle in 6 dimensions. The number and spatial

distribution of macroparticles in each beam can be specified separately and allows for both weak-strong and strong-strong simulation. The beam-beam kicks are calculated using the actual average beam positions and RMS beam sizes and the analytical Bassetti-Erskine [4] field calculation. Both central and parasitic (long range) collisions are simulated. In the work reported here, we allow for collisions in two interaction points, IP1 (ATLAS experiment) and IP5 (CMS). If not stated otherwise, we use nominal LHC parameters at 7 TeV. For the 25 ns nominal bunch spacing, parasitic encounters occur at multiples of 12.5 ns (3.747 m) up to about 58 m on either side of the IP. The phase advance between the interaction points and the parasitic collisions is close to 90°. This allows in good approximation to simulate the n parasitic collisions around each IP by a single, n times stronger kick.

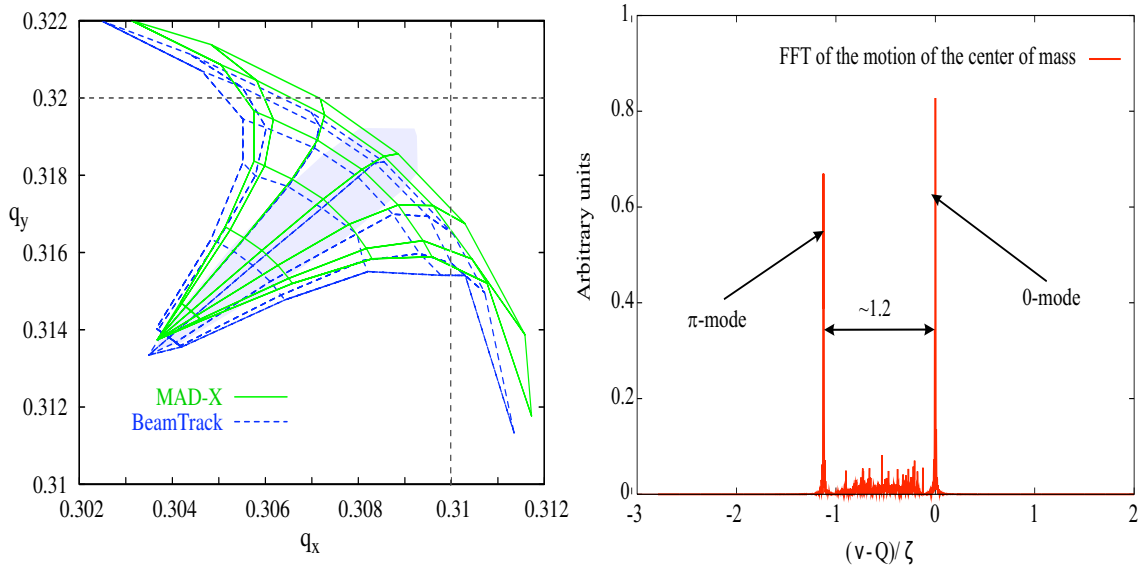

Figure 3.14: Comparison of tune footprints for 0, 1, .. 6 $\sigma_{x,y}$ obtained with detailed MAD-X simulation and our simplified model (dashed blue lines), for nominal LHC beam parameters with central and parasitic collisions in IP1&5 on the left. The shaded area shows the 0-6 σ tune fooprint from BeamTrack without parasitic collisions. Coherent beam-beam modes obtained in the simulation for a single head-on collision are shown on the right.

We checked that the tune footprint of our simulation matches quite well with the expectations of the detailed MAD-X based model, see Figure 3.14. The small discrepancies can be explained by the fact that the effect of the crossing angle was not included in the head-on collisions. The left plot in Figure 3.14 shows the coherent beam-beam modes for a single head-on as simulated by BeamTrack. Again, the results fit the expectation as the simulated Yokoya factor [46], which characterizes the distance between the dominant peaks, was found to be about 1.2.

The last check to validate our simulation code was to reproduce the studies performed in [43] which consisted of simulation of emittance blow-up due to the beam-beam interactions in the presence of a static offset for a single head-on collision. This test was done by tracking 1 000 000 particles over 500 000 turns with separations going from 0 to 4 σ with steps of 0.2 σ. The results are shown Figure 3.15 for the horizontal plane. Two peaks are clearly identified around 0.4 and 1.5 σ as previously found in studies using difference codes and approaches as shown Figure 3.16.

The early operation of the LHC will be without long range interactions, for the nominal 2808 bunches per beam, the crossing angle is required and there will be 30 long range beam-beam interactions around each interaction point. Both scenarios, no parasitic crossings (as for the early operation) and full nominal parameters with 30 parasitic crossings per IP, were studied by tracking 10^6 macro-particles for each beam.

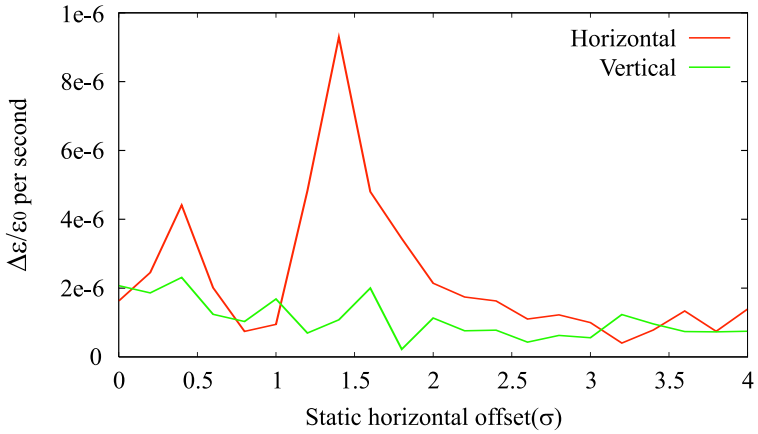

Figure 3.15: Emittance growth for different horizontal static offsets with beams colliding in one IP only and no long-range interactions.

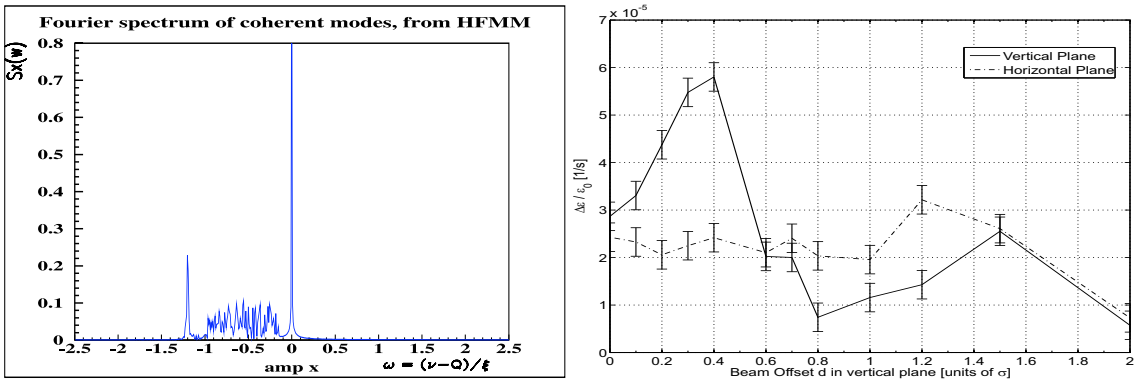

Figure 3.16: Fourier spectrum and static offset scan taken from [44] and [43]. These results are from HFMM.

The collapsing of the separation bumps was modelled by a linear function in time which underestimates by a factor two the time spent at small separation (deceleration of the magnets). All the simulations were performed with the nominal LHC intensity (1.15×10^{11} p/bunch) and collision tunes ($Q_x = 64.31$ and $Q_y = 59.32$).

The first step was to look at runs without parasitic encounters, just with head-on collisions. This is illustrated Figure 3.17. As seen on these plots a small reduction of the beam size is observed in both planes. This could be explained by the dynamic effects induced by the beam-beam force. As the beams are brought into collisions the beam-beam force evolves and pertubes the lattice as a function of the separation. In return the betatron phase advance and amplitude will be dynamically modified:

$$\frac{\beta^*}{\beta_0} = \frac{\sin\Phi_0}{\sin\Phi}, \tag{3.2}$$

where β^* is the value of the perturbed betatron amplitude function at the IP, Φ is the perturbed betatron phase advance for one turn and β_0 and Φ_0 are the unperturbed phase and amplitudes. The expected evolution of the beam size as a function of the separation is shown in green in Figure 3.17 and fits the simulated one. From these results we can deduce that the simulation showed no signs of significant beam blow-up from head-on collisions with nominal LHC parameters.

With the long-range beam-beam effects added, we started to see emittance growths for nominal param-

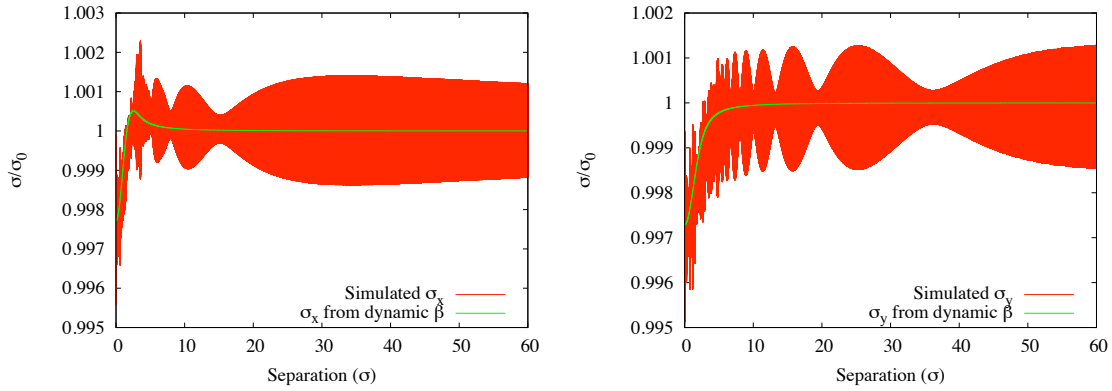

Figure 3.17: Evolution of the RMS beam size in the horizontal (left) and vertical (right) planes during a horizontal scan. The evolution of the β was calculated using nominal parameters.

eters on the level of a few percent over time scales of seconds as relevant for bringing beams into collisions. This is shown in Figure 3.18 for going into collisions in 1, 5 or 10 seconds starting from 14σ separation. Only the interval where the beams are moving is shown in this plot. The beams are stable outside this range. Scans where performed starting at 14σ. For larger separation the beam-beam force is very weak and has no effects on the beam emittance. A small emittance exchange can occur between beams and planes. We quadratically add the emittances of the two planes according to

$$\varepsilon_i = \sqrt{\frac{\varepsilon_{xi}^2 + \varepsilon_{yi}^2}{2}}, \tag{3.3}$$

to allow to refer to a single number for the emittance increase. In the example shown, beams collide in IP5 and the parallel separation is ramped down to zero in IP1. The blue curve which has the largest effect corresponds to what is actually anticipated for the collapsing time based on the parameters as given in Table 3.5.

Even with optimistic input conditions, simulations show a sizeable emittance blow-up that could be reduced by going faster into collisions. Towards smaller separation, the growth rate increases. This can be expected from the shape of the beam-beam forces which become more non-linear and is also seen in static simulations at fixed separation. One possible explanation for this emittance growth in the presence of parasitic beam-beam could come from the fact that the tune footprint is larger than the one with just head-on collisions. It would then be easier for particles to hit a resonance during the process of putting the beams into collisions. This explanation is also supported by the observation that the main contribution to this growth comes from the vertical plane, and not the separation plane as one could expect, which is the one closer to the third order resonance. Figure 3.18 indicates that going faster into collisions would reduce the emittance blow-up. This could also affect the beam lifetime during optimization of the luminosity as the beams are separated on purpose to find the optimum settings.

3.5.5 Discussion

We studied the dynamics of bringing beams into collision in the LHC. On the more practical side, we have shown that we have some flexibility to minimize the time needed to bring beams into collisions by choosing an optimal distribution of strengths between the magnets involved. These studies were complemented by beam-beam simulations. For nominal LHC beam parameters with both central and parasitic beam encounters the simulations show a sizeable emittance increase when beams are brought into collisions, which can

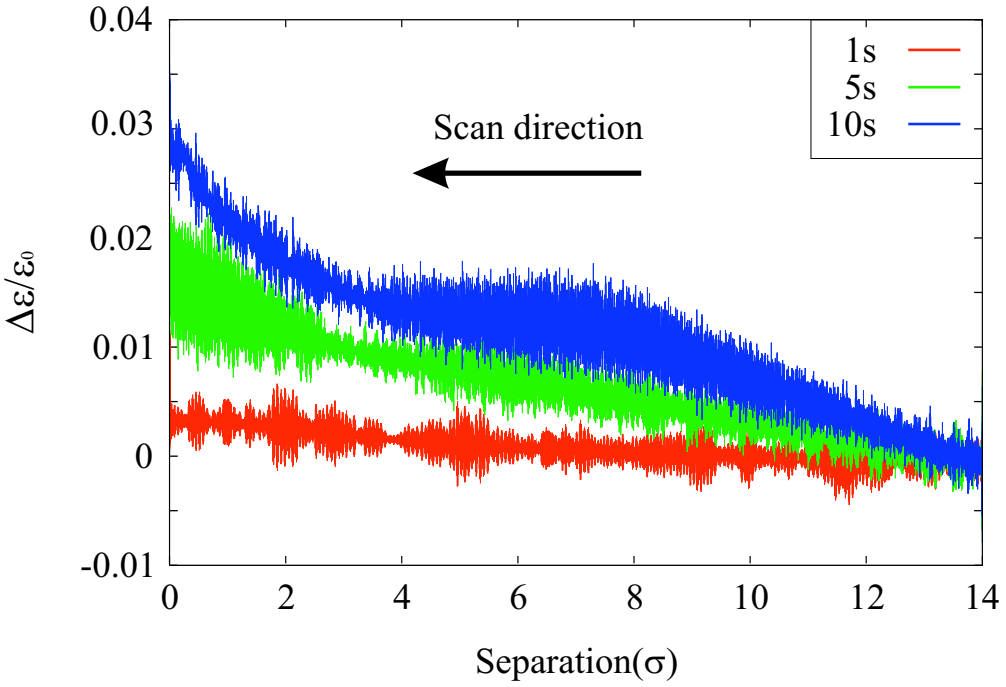

Figure 3.18: Emittance growth from simulations for different collapsing speeds in the case of two IPs with long range.

be minimized by a further reduction of the time in which beams are brought into collision. The studies presented here are mostly intended as a preparation and basis for the work with actual colliding beams in the LHC. Only a comparison with observations in the machine can tell what the amplitude of the effect will be but simulations showed that it is desirable to have more flexibility in terms of how fast we can collapse the separation bumps. In addition, we may have significant non-Gaussian tails which are hard to predict and simulate, but which may be quite important for machine protection and experimental conditions and cause machine induced backgrounds visible in the detectors.

3.6 IR Optics Optimization

The destructive effect of the beam-beam force is stronger for beams with unequal sizes as demonstrated in [47] and can result in emittance growth or bad lifetime. In addition, the luminosity for Gaussian beams in the case of head-on collisions without crossing angle is expressed as:

$$\mathcal{L}_0 = \frac{N_1 N_2 f N_b}{2\pi\sqrt{(\sigma_{1x}^2+\sigma_{2x}^2)(\sigma_{1y}^2+\sigma_{2y}^2)}} \tag{3.4}$$

where N_1 and N_2 are the bunch intensities, f the revolution frequency, N_b the number of bunches per beam and $\sigma_{ix,iy}$ the effective transverse beam sizes. Any increase of the beam sizes results in a loss of luminosity. Tools which allow for fine tuning of the beam sizes can therefore become very valuable in the LHC. The beam size at the IP where the dispersion is assumed to be equal to zero can be expressed as:

$$\sigma^* = \sqrt{\beta^* \varepsilon} \tag{3.5}$$

where σ^* and β^* are the beam size and the β-function at the IP and ε is the emittance. The only parameter

left for adjustment of the beam size is β^*. β^* adjustments are done by changing the strengths of the main insertion quadrupoles via a *knob* [48]. A knob can be represented as a matrix linking several devices, usually magnets, and allowing to drive them together trough a scale factor, the knob value. A knob can be used to change orbit or optical functions as relevant in this section. In general the variations of the parameter to be changed are linear with respect to the knob value in order to keep its implemantation and use simple.

3.6.1 Implementation

In the LHC the beams collide in four experimental regions with similar layouts [32]. The final focusing is performed with triplets which are common for the two rings. The other insertion quadrupoles (from Q4 to Q13) will drive the beams independently. For our purpose it is necessary to be able to control the beams independently, the triplets can therefore not be used. In addition, the optics changes should be as much localized as possible to the interaction region and parameters other than the β^* should remain constant. These changes were kept small by using all the insertion quadrupoles to compute the knobs.

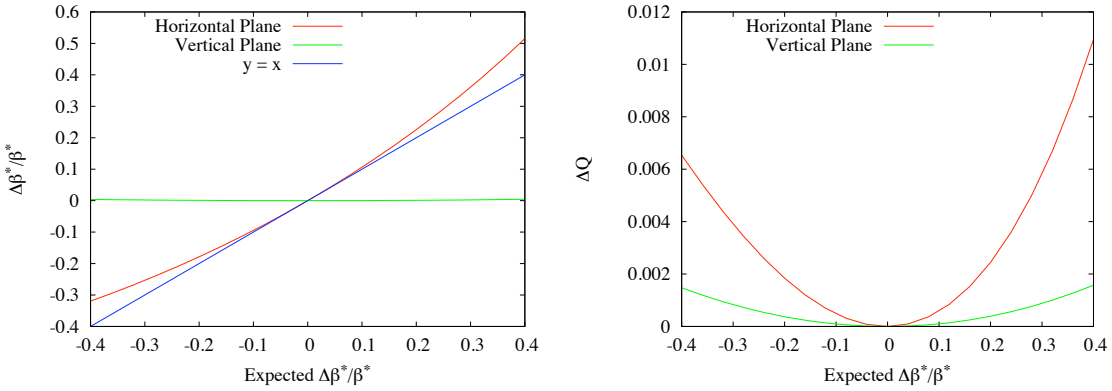

Figure 3.19: Evolution of β^* (left) and tune (right) as function of the expected change in β^*. Example of IP1 at injection optics.

The main criteria for a knob to be easily implemented and used in operation is the linearity. This is not the case when changing the strength in a quadrupole, however, if these changes remain small a linear approximation can be justified. This is illustrated in Figure 3.19 where the changes of β^* are only seen in the adjusted plane and almost linear within a range of $\pm 10\,\%$. The tune changes are of the order of a few 10^{-3} within this range.

3.6.2 β^* Measurements for Injection Optics

Table 3.6 summarizes the β^* measurements for injection optics at 3.5 TeV for which the β-beat was close to specifications (20%). The nominal values are 11 m for IP1 and IP5 and 10 m for IP2 and IP8 in both planes.

From these measurements one can estimate the loss in luminosity with respect to the nominal values using Equation 3.4. Assuming round equal beams ($\varepsilon_{ix} = \varepsilon_{iy} = \varepsilon$) to compute the losses, IP5 and IP8 are almost at nominal values while IP1 and IP2 have a loss of about 6 % and 4 % respectively, which becomes non-negligible for high luminosity operation.

The ratio of the β^* between the two beams might also become an issue for lifetime once LHC will run with high bunch intensity. As shown in Figure 3.20, the difference between beam 1 and beam 2 can go up to more than 20 % and may require corrections in the presence of strong beam-beam.

Table 3.6: β^* measurements for injection optics [49] at 3.5 TeV.

	Horizontal	
	Beam 1	Beam 2
IP1	11.54±0.20	9.89±0.27
IP2	9.21±0.12	11.54±0.15
IP5	11.85±0.27	10.74±0.21
IP8	10.20±0.69	9.45±0.15
	Vertical	
	Beam 1	Beam 2
IP1	12.74±0.45	12.70±0.15
IP2	8.92±0.30	12.04±0.07
IP5	10.73±0.47	11.15±0.40
IP8	11.35±1.24	9.19±0.05

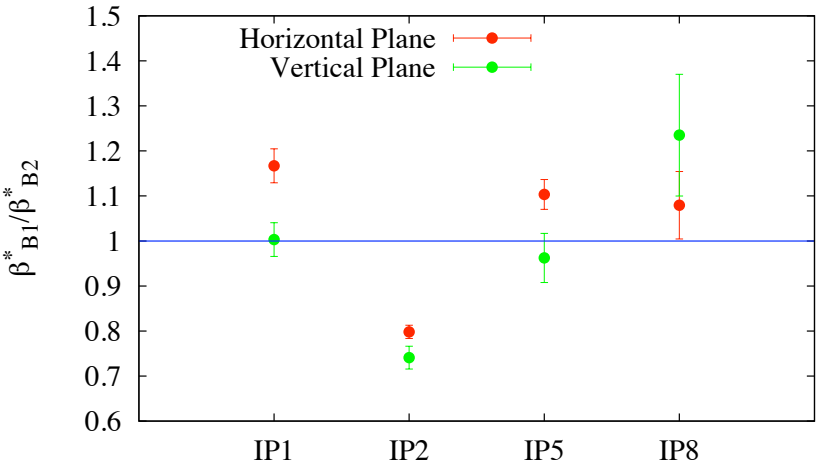

Figure 3.20: Ratio of the β^* at the four interaction points. The difference between beam 1 and beam 2 goes up to 20 % in the worst case.

3.6.3 β^* Knob Measurements

Measurements were performed at 3.5 TeV for the injection optics. The knob was tested for IP1 beam 2 horizontal. The results should be similar for the other knobs as predicted by the model. The measurement consisted of a serie of acquisitions with $\Delta\beta^*$ of 0% -20 %, -10 % and +20 % and finally back to the initial situation to check for hysteresis effects. At each point the beam was excited using the AC dipole to measure the optics.

The results for the scanned plane agree within the error bars except for the point at -10 % as shown in Figure 3.21. In the plane which is not trimmed the $\Delta\beta^*/\beta^*$ is consistent with zero for all points. It is also interesting to note that the starting point and the end point of the scan are consistent with each other which demonstrates that in these conditions the hysteresis was small enough to leave the optics unchanged.

The tune is another observable that can be measured with high precision. Figure 3.21 shows the changes in tune during the scan. The measurements show some small discrepancies with respect to the model and the initial tunes could not be recovered by going back to initial position. The differences are of the order of

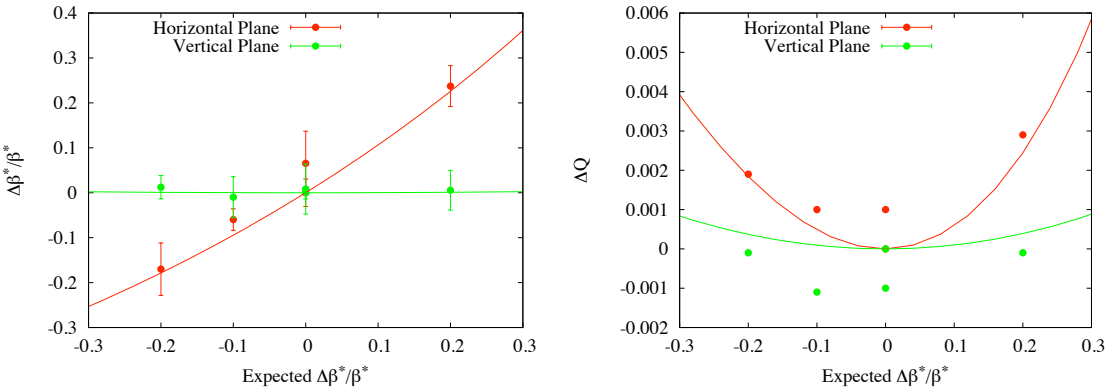

Figure 3.21: β^* scan at 3.5 TeV and injection optics. β^* is shown on the left and the tune on the right, the plain lines represent the model.

a few $\approx 10^{-3}$ which is a factor two larger than the natural tune jitter ($\approx 5 \times 10^{-4}$). This could be the sign of field errors or small hysteresis effects not seen on the less precise β-functions measurements.

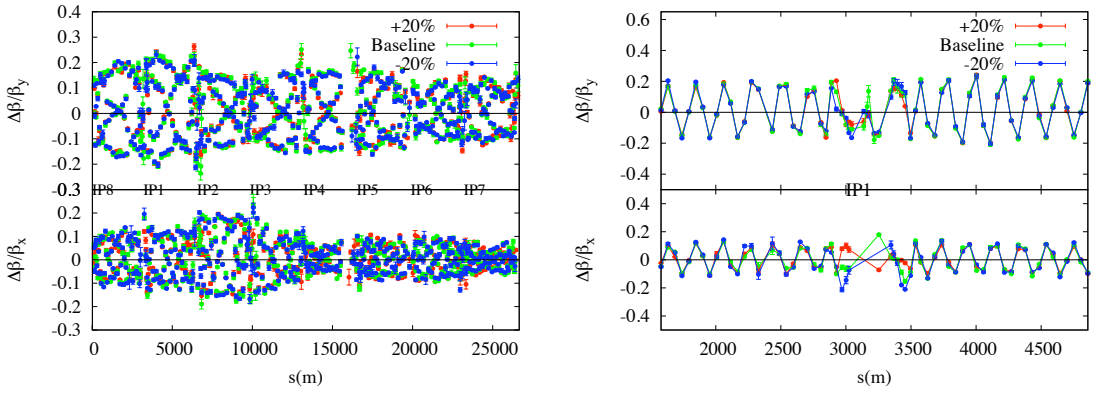

Figure 3.22: β-beat over the whole ring (beam 2) in the horizontal (bottom left) and vertical (top left) plane. The change in optics was taken into account in the model when β^* was trimmed. The right plot shows the β-beat in IR1 in the horizontal (bottom right) and vertical (top rightt) plane. In this case the β-beat was calculated with respect to the nominal optics for all cases in order to illustrate the changes in β^*.

Looking at the β-beat over the whole ring allows to check whether unwanted optics errors were induced by changing the β^*. In Figure 3.22 on the left the β-beat was calculated with respect to a model including the knob. Differences are observed with respect to the baseline optics but the overall and peak β-beat remain within the specification of 20 %. Looking closer at IR1 as illustrated in Figure 3.22 on the right, where the β-beat was calculated using the nominal optics as a reference (i.e. not including the changes from the knob), we can clearly see the changes around the IP for the different trims. The optics changes are localized to the region around the IP and the β-beat is back to the initial one in the arcs.

β^* was too small compared to nominal optics. The trim to +20 % improved the situation even if going further than the nominal β^* of 11 m. This is illustrated in Figure 3.23 where an improvement is seen in IR1 and also a slight overall improvement all around the ring.

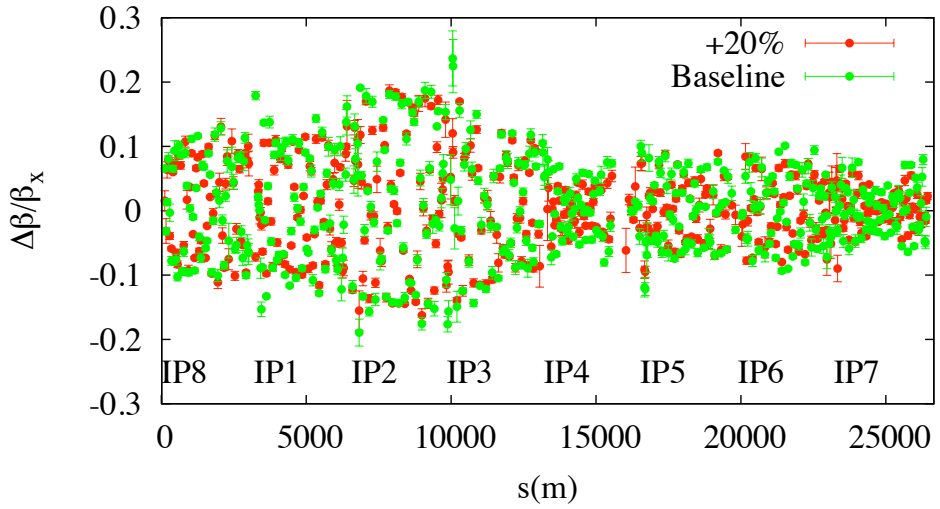

Figure 3.23: β-beat for the whole ring (beam 2) for the baseline and +20 % β^* with respect to nominal optics.

3.6.4 Outlook for Squeezed Optics and Conclusions

In order to reach the LHC nominal luminosity β^* has to be reduced down to 0.55 m. The triplet are protected by the tertiary collimators. Squeezing to lower β^* will increase the β-functions and reduce the aperture in the triplets. In order to correctly shadow the triplets the tertiary collimators aperture will also have to be reduced. One should therefore be very careful not to hit the aperture. In addition, the squeezed optics is reached by decreasing the current in the insertion quadrupoles. Operating at lower currents could lead to non-negligible hysteresis effects when trimming the β^*. For its first two years of operation the LHC will run with β^* larger or equal to 2 m. As illustrated Figure 3.24 it is more difficult for the 2 m optics to keep the β^* constant in the other plane, a change of 20 % in one plane would result in a change of about 1.5 % in the other plane. Furthermore, when trimming the β^* by -20 % the minimum $n1$ [50], which describes the aperture, is reduced by about 1.2 σ which represents a non negligible loss.

The β^* knobs were successfully implemented and tested for injection optics at 3.5 TeV. The measurements results are in good agreement with the simulations and no significant optics errors was observed. The tune measurements showed possible small hysteresis effects. In order to include these tools as part of routine operation a systematic check of all IPs separately and together needs to be performed in case these small effects add up to build larger errors. In the case of squeezed optics the situation becomes more complicated and a detailed study is required to assess the real effects and the impact on machine protection.

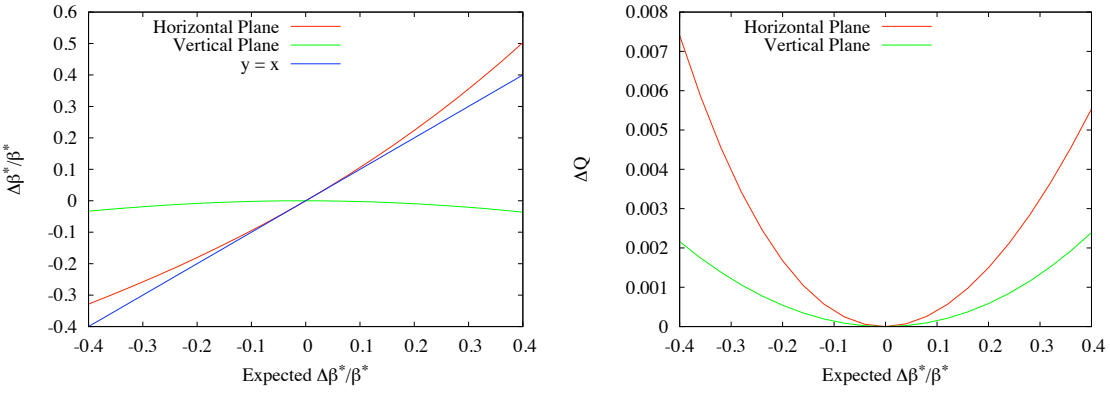

Figure 3.24: Evolution of tune and β^* as function of the expected change in β^*. Example of IP1 for 2 m optics.

Chapter 4

LHC Instrumentation

Safely operating the LHC requires to carefully diagnose the beam conditions and behavior. Most of the instruments are situated in IR4. The losses and the orbit need to be monitored in the whole machine, beam positon monitors and beam loss monitors are therefore installed all around the ring. This chapter will give an overview of the LHC beam instrumentation relevant for luminosity calibration. A more detailed description of the measurements performed during the calibration scans is presented in Chapter 6. In principle, only the intensity and relative luminosity measurements are required for luminosity calibration. Other instruments measuring the orbit or the emittance can provide useful additional information on the calibration scans. For completeness, they will also be presented as they were used for data analysis.

4.1 Beam Position Monitors (BPM)

The beam position monitors consist of two electrodes measuring the position of the center of mass of the bunches passing through these electrodes. The LHC orbit and trajectory system has been developed to fulfill the specification described in [40]. The BPM system is essential to monitor and correct the orbit in the operation of a storage ring and should therefore provide access to the following observables:

- Single pass trajectory.
- Closed orbit (average beam positions).

This information is not only essential for correction of the trajectory but its processing and analysis also gives access to other beam parameters such as the optical functions. In addition, the LHC is a superconducting machine and a small fraction of the beam can quench magnets. Operation of the LHC therefore requires an excellent monitoring and control of the orbit. A total of over 1000 BPMs were installed all around the LHC ring which are used to measure and correct the closed orbit as illustrated Figure 4.1.

4.1.1 Insertion Region BPM

Performance of the insertion region BPMs is important for operation in collision as they provide a control of the orbit in the final focusing region and a measurement of the beam coordinates at the IP. The inner triplets in all interaction regions are equipped with directional stripline couplers [32] capable of distinguishing between counter rotating beams in the same beam pipe. These BPMs are located in front of Q1, in the Q2 cryostat and after Q3. The ones situated in Q1 (BPMSW) give the IP beam coordinates by a direct linear interpolation as no optical elements are situated in between them. The BPMSW have separate readout chains for each beam and each of them will have their own systematic offsets. The expected resolution of these

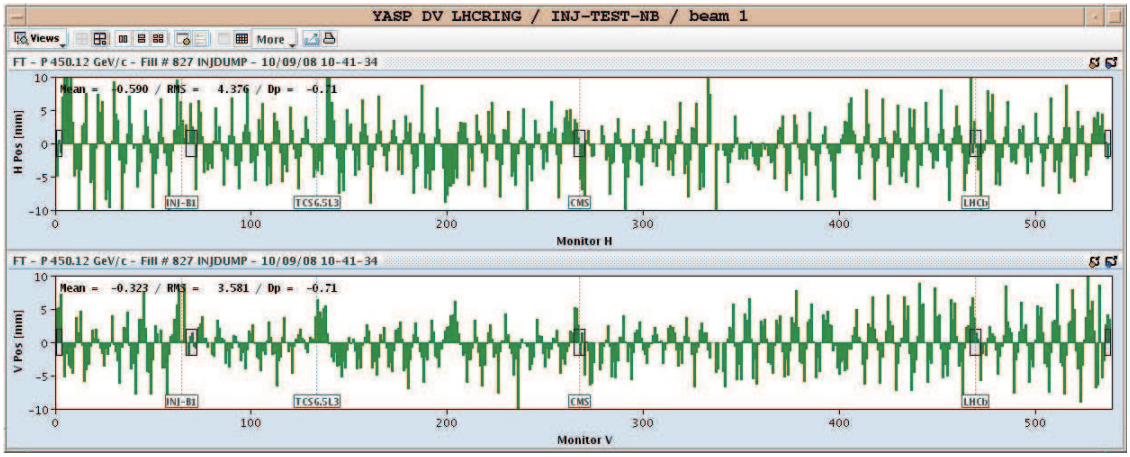

Figure 4.1: First turn in the LHC. Display used in the LHC control room to monitor and correct the orbit.

BPMs is about 100-200 μm depending on the intensity which directly corresponds to the resolution on the beam position at the IP and translates into $\approx 5-10\,\mu$rad resolution on the angle. In IP1 and IP5 additional special BPMs were installed which cannot distinguish between beams but for which both beams are acquired with the same electronics chain. All systematics except for the non-linearities therefore vanish for these BPMs as they provide a differential measurement, the purpose of these BPMs was to ensure no crossing angle is present for the high-β optics experiment, presented in Chapter 7, but they were also used in the commissioning phase of the LHC to initially find the collision point. For the calibration scan measurements the BPM data were used only the verify the linearity of the orbit displacement. The absolute displacement was calibrated using experiments data. More details on this analysis is presented in Chapter 6.

4.2 Transverse Emittance Measurements

The transverse emittance affects both the machine protection and the luminosity performance. A change in emittance during a calibration scan will introduce additional systematic uncertainties that need to be quantified. These changes were on the 1 % level over the duration of a scan.

Two classes of instruments for transverse profile measurements were developed and are considered as operational in the LHC:

- Wire scanners.
- Synchrotron radiation monitors.

Other instruments can be used to characterize the beam transverse emittance such as the ionization profile monitor [51] which are not yet operational or screen monitor [32] (BTV) which are used for non-circulating beams and injection and will not be covered in this section.

4.2.1 Wire Scanners

A wire scanner consists of a thin carbon wire crossing the beam. As the wire passes through the beam, particles collide with the wire producing secondary particles with an intensity proportional to the beam density at the wire location convoluted with the wire thickness. A photo multiplier is used to measure the intensity of the light produced by a scintillator paddle intercepting these secondary particles. These devices

are generally considered as very reliable and used to cross calibrate other profile monitors. Due to the interaction from the beam to the wire and the limit on the maximum speed the wire can be swept through the beam the wire can break for high intensity beams. Its use is then limited up to a certain intensity. In the LHC the wire scanners are intended to be used up to a tenth of the nominal intensity. A total of eight wire scanners are installed in IR4 in the LHC [39]. Each beam is equipped with two wires in the horizontal and vertical planes. An example of a wire scanner acquisition in shown in Figure 4.2.

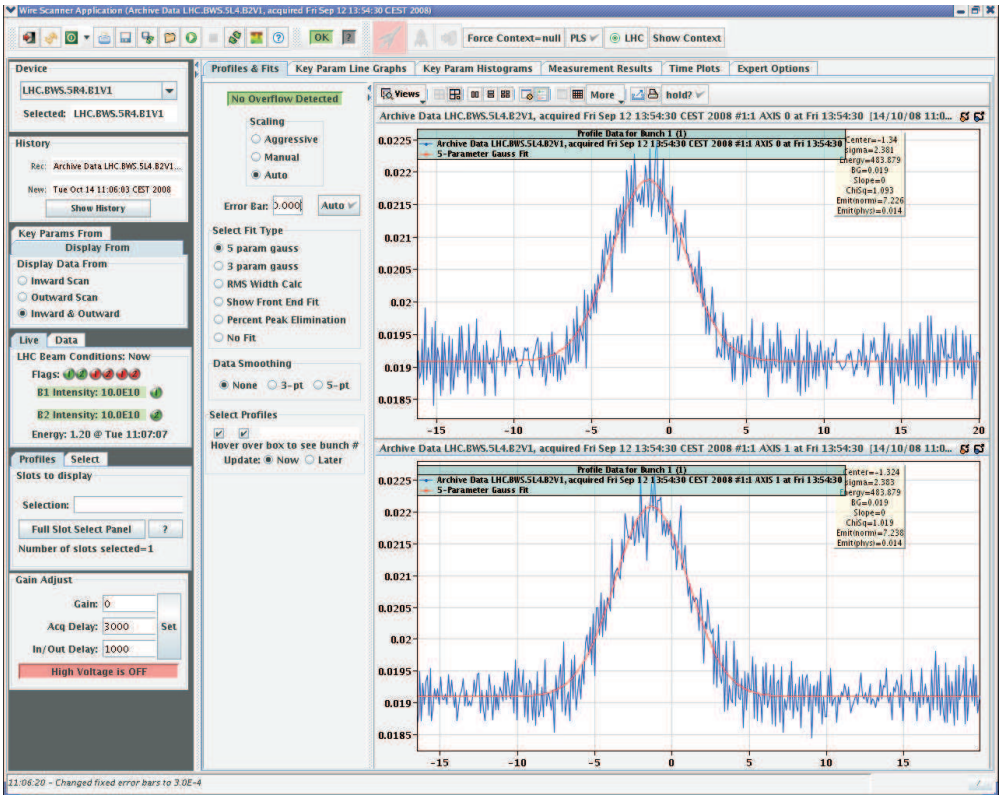

Figure 4.2: Display of the LHC wire scanner application. In and out vertical wire scans on a single circulating pilot bunch [39].

4.2.2 Synchrotron Light Monitors

The synchrotron light monitors use the radiation emitted by the accelerated particles in the bending elements. The light is transported and focused in an optical line to dedicated cameras providing an image, Figure 4.3, of the beam from which the profile is reconstructed. This method provides a continuous and non-destructive measurement of the transverse emittance which becomes particularly interesting at intensities where the wire scanners cannot be used. In the LHC each beam was equipped with one monitor in IR4 [52]. Above 1.5 TeV the light emitted in the superconducting dipoles is sufficient to image the beam. In order to be able to use these monitor at lower energies an undulator was installed.

Figure 4.3: Beam image at 450 GeV [52] as seen by the cameras.

4.3 Intensity Measurements

In accelerator physics, the term *intensity* usually defines a number of charges. Beam current transformers of two different kinds provide intensity measurements for the beams circulating in the LHC:

- DC current transformers (BCTDC) which measure the full beam intensity.
- Fast beam current transformers (FBCT) which are capable of measuring the individual bunch intensities.

Both systems are installed in sections where the vacuum chamber is at room temperature around point 4 as most of the other instruments. The specifications for these devices are detailed in [25]. The BCTDCs are based on the principle of magnetic amplifiers and measure the mean current of the circulating beam. Because of their operational importance, two independent systems are installed per ring, one for development and one for operation. These devices are designed for the nominal LHC intensity where they are supposed to reach an absolute accuracy of 1 %. For a single pilot bunch the accuracy is only of the order of 20 %. The FBCTs can measure the bunch intensities on a turn by turn basis and are insensitive to unbunched components. Similarly to the DCBCT, four systems are installed in the LHC. Each system has two channels with different bandwidths. A low bandwidth channel, independent of bunch timing, integrates over all bunches and measures the total intensity. A high bandwidth channel, requiring bunch to bunch timing, integrates over single bunches and measures the bunch intensity. During its commissioning period the LHC was running at low intensity, the low-bandwidth channel of the FBCT was used to measure the total intensity as the noise level was lower.

Figure 4.4 illustrates intensity measurements from the FBCTs and DCBCTs over the fill 1058 which consisted of two bunches of 2×10^{10} protons per beam. It is seen that the noise level on the DCBCT is much higher. The overall trend is similar for both systems, which indicates that no significant un-captured beam component built up during this fill. A negative offset is seen in the DCBCT which can easily be corrected for. The intensity measurements are essential for luminosity calibration. Special efforts were made to understand the corresponding systematic uncertainty which proved to be rather large a low intensity. A detailed description of the corrections and errors assigned to the intensity measurements during the calibration scans can be found in Chapter 6.

4.4 Luminosity Measurements

Besides the measurements provided by the experiments the LHC is equipped with luminosity monitors, the BRANs (**B**eam Collision **Ra**te of **N**eutrals) [53], at each IP. The BRANs are designed to monitor and

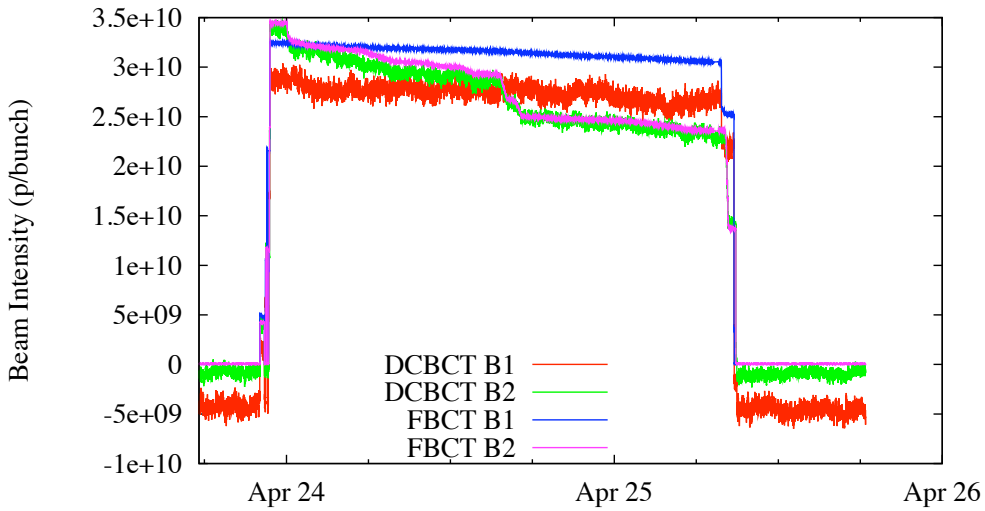

Figure 4.4: BCTs time history plot for the fill 1058 comparing the two systems. The DCCT shows high noise level, which is expected from low intensity and a negative offset that can be corrected for. The two systems agree on the relative scale.

optimize the luminosity at the four interaction points. The interaction rate is measured by monitoring the flux of small angle neutral particles produced by the collisions. Those monitors are placed on each side of the interaction points in the neutral beam absorber (TAN) at IP1 and IP5 and behind a converter in IP2 and IP8. Because of the requirements of different levels of luminosity for the different interaction points two designs have been developed to fulfill the requirements from the experiments: a fast ionization chamber for the high luminosity interaction points and a fast polycrystalline-CdTe detector for the low luminosity interaction points. The ionization chambers have low efficiency. Scintillators were therefore installed in IP1 and IP5 in order to give signals to the machine during LHC start-up i.e. at low luminosity. The scintillators are a temporary solution for low luminosity. They have a reduced lifetime as they cannot sustain high radiation levels. This section will concentrate on the two other designs.

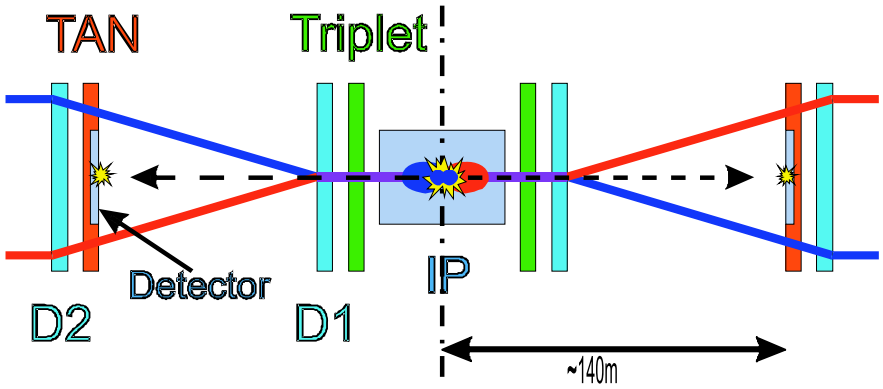

Figure 4.5: Typical layout of an experimental insertion. As the beams collide they produce a flux of neutral particles that will hit the TAN and generate electromagnetic showers detected by the BRAN.

Figure 4.5 illustrates an experimental region in the LHC. The charged particles are deflected by the D1 magnet, the flux of neutral which is not deflected, will be intercepted by the TAN in which the LHC luminosity monitors are situated. The measured signal in the detectors corresponds to the energy deposition of the showers produced by the neutral particles going through the absorber.

4.4.1 The Ionization Chambers

The ionization chambers were designed by LBNL [54] for IP1 and IP5. These detectors are situated in the high luminosity insertions and can resolve the bunch by bunch luminosity. The design was chosen in order to fulfill the requirements described in [55]:

- Dynamic luminosity range $10^{28} - 10^{34}\text{cm}^{-2}\text{s}^{-1}$.
- Bandwidth of 40 MHz to resolve the luminosity of individual bunches.
- Ability to withstand high radiation doses.

A simple detector that can meet these requirements was found to be an ionization chamber filled with a mixture of pressurized Argon and Hydrogen (6 %) at 10 bar maximum. It is composed of four independant quadrants of 4 cm^2 in order to measure the center of gravity of the neutral flux, this should in principle provide some information on the crossing angle. Each quadrant has six gaps of 1 mm connected in parallel.

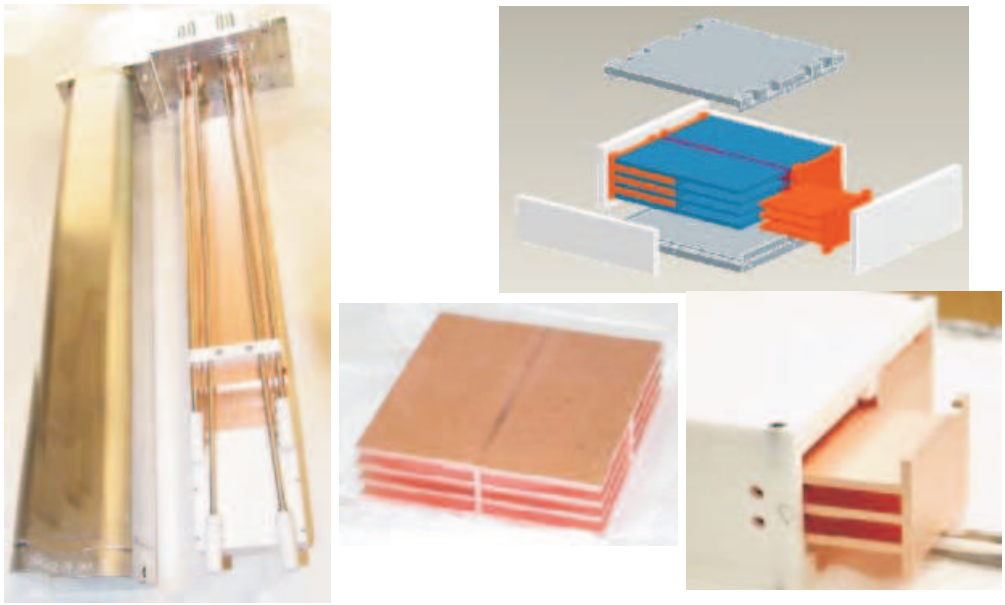

Figure 4.6: Pictures and model of the ionization chamber [53].

Figure 4.6 shows the detector. The left picture shows the ionization chamber (white rectangular object) installed on its copper filler bar and sitting next to the stainless steel pressure housing while the other pictures show the model and details of the detectors which is entirely made of copper and MACOR (glass-ceramic composit). As these detectors are installed in the high-luminosity insertions they have the ability to resolve coincidences when the number of events per bunch crossing becomes larger than one.

4.4.2 The CdTe Detectors

The Cadmium Tellurite detectors were developed in a collaboration between CERN and LETI and were designed for IP2 and IP8 as they cannot sustain the radiation dose in IP1 and IP5. The requirements are the same as for the ionization chambers except for the lower exposition to radiation. The detector consists of an aluminum housing of about 10 cm which contains 10 polycrystalline CdTe disks of 17 mm diameter and 300 μm. When a ionizing particle passes trough the disks electron/hole pairs are created and drifted to the collection electrode. The amplitude of each CdTe disk is acquired separately in order to determine the crossing angle.

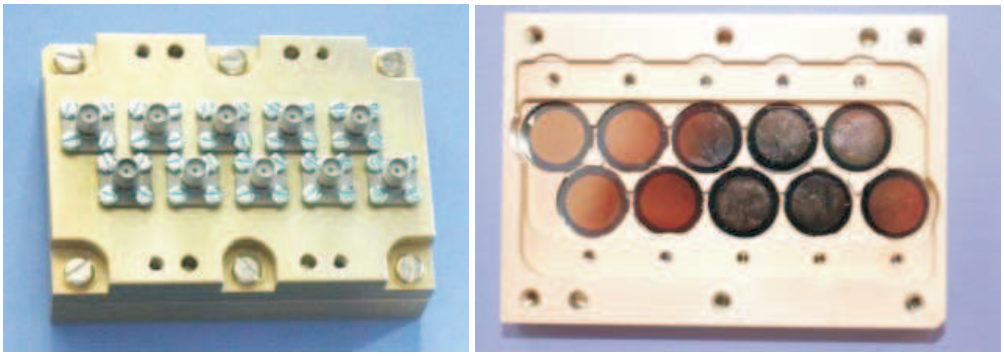

Figure 4.7: Pictures of the CdTe detectors [53].

4.4.3 Simulations

Tracking simulations of the collision products from the interaction point to the detector can provide estimates on the amplitude of the signal and the efficiency of the detectors [56]. The tracking simulations were performed using the FLUKA [57] code with initial conditions corresponding to the ones at IP5: half crossing angle of 142.5 μrad. No initial particle distribution was used, all the collisions occur exactly at the interaction point. This is not realistic for the case of the low luminosity interaction points but should be sufficiently accurate to estimate the performance of the detectors. The TAN absorber is modeled by a copper block with a length set such that the detector is placed at the maximum of the showers, approximately 15 cm as shown in Figure 4.8. For this study we tracked the product of 100 000 collisions.

The first step in the simulation was to transport the proton-proton collision products to the TAN situated at 140 m from the interaction point [58]. The TAN is installed after D1 (dipole used to separate the beams into two different beam pipes) and therefore only neutral particles are left at this point. Looking at the distributions for different energies in Figure 4.9 it is possible, with a simple Gaussian fit to compute the angle as an intermediate check.

The results are summarized in Table 4.1 and are in good agreement with the expected value of the crossing angle for the high energy neutral particles (142.5 μrad). For the intermediate energies no fit was performed because of the flat shape of the distribution. For the low energy case the peak of the distribution is outside the detector. The interactions with the beam chamber could be the source of the shape of the low energy particle distribution. The average incoming energy flux per event is of 2.6 TeV.

In all IPs the detector is placed behind a copper block with a length of 15 cm and a transverse area of 10 cm^2 in order to completely shadow the detector. The geometry of the detectors respects the dimensions of the technical drawings but was approximated for the purpose of the simulation. All the materials were modeled using the FLUKA database and the option COMPOUND for the CdTe. In the case of the ionization

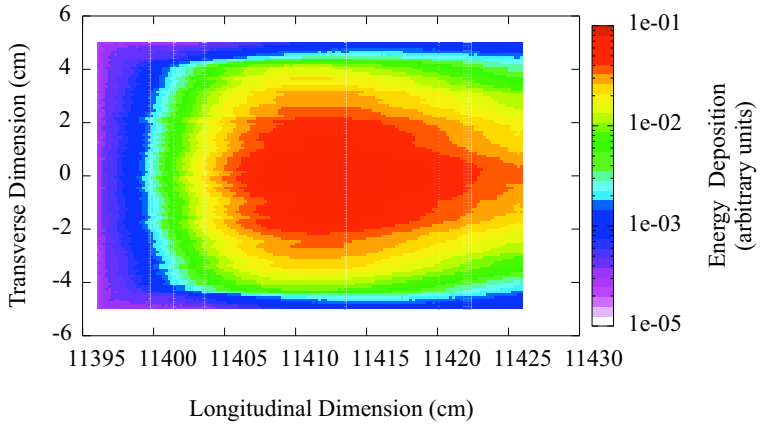

Figure 4.8: Deposited energy in 30 cm of Copper. The maximum of the showers is observed at 15 cm, this dimension was used for all the tracking simulations.

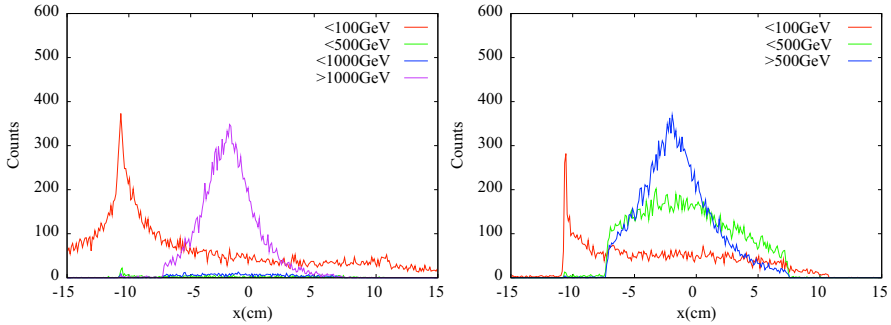

Figure 4.9: Initial neutron distributions for different energies (left) and initial photon distributions for different energies (right). A fit of these distributions gives the initial crossing angle.

chamber only the dominant gas, Argon, was considered. The pressure was set to 10 bar. All the collision products are tagged with an initial event number which is recorded during the transport. This allows to link the energy deposition in the detector with its source and to study each event separately. The energy deposition was recorded using EVENTDAT.

4.4.4 Simulation Results for the CdTe Detector (IR2 and IR8)

Each disk is giving an independent signal. In order to be as close as possible to the realistic case the ten channels where simulated and studied separately. Figure 4.10 shows the number of events detected for a given threshold energy and represents the efficiency of the detector depending on the threshold energy. The electronic noise from the detector is expected to be equivalent to 30 mV which corresponds to a deposited energy of 4.14 MeV. Applying a cut-off to compensate for this noise we would still detect $\approx 47\%$ of the events. The total energy deposited in the detector is $\approx 2.10^4$ GeV which gives an average deposited energy per proton-proton collision of 0.2 GeV.

Figure 4.11 shows the number of events detected in each channel and a Gaussian fit on this distribution. The position of the peak allows to calculate the crossing angle. The results of the Gaussian fit give -2.08$\pm$0.02 cm for the peak and a sigma of 4.11$\pm$0.04 cm. The derived crossing angle is equal to 149$\pm$2 μrad, which is comparable to the expected value of 142.5 μrad. The half crossing angles at IP8 and IP2 are of the order of 200 μrad and 150 μrad respectively and the detector is situated at 113 m from the IP in both cases.

Table 4.1: Gaussian fit results of the particle distribution at the TAN.

Photons		
Energy (GeV)	>500 GeV	>100 GeV
Pos. of the peak (cm)	-1.99 ± 0.03	-1.92 ± 0.09
Sigma (cm)	2.31 ± 0.12	5.46 ± 0.41
Crossing angle (μrad)	142 ± 2	137 ± 6
Neutrons		
Energy (GeV)	>1000 GeV	>500 GeV
Pos. of the peak (cm)	-2.01 ± 0.02	-1.86 ± 0.12
Sigma (cm)	2.39 ± 0.04	6.81 ± 0.67
Crossing angle (μrad)	144 ± 2	133 ± 9

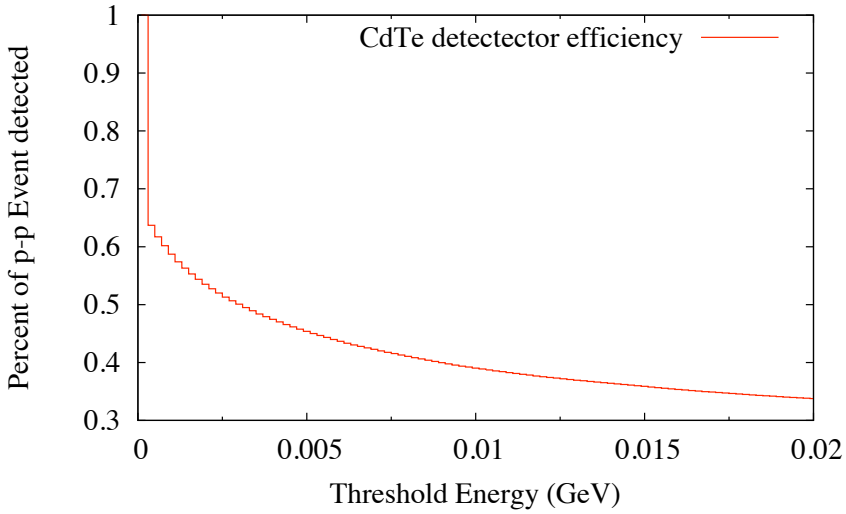

Figure 4.10: Percent of event detected versus the threshold energy in IP8. The noise level is expected to be of the order of 30 mV corresponding to a deposited energy of 4.14 MeV. This results in a efficiency of about 47 % over the noise level.

Applying a geometrical transformation we can give an estimate of what would be the position of the peaks for those IPs (-2.31 cm at IP8 and -1.75 cm at IP2). Rescaling the efficiency with the estimated peak values gives an efficiency of 45% for IP8 and 49% for IP2.

All these simulations were performed when the LHC was expected to run at 7 TeV. Later, the energy has been lowered to 3.5 TeV. This changes the incoming particles distribution and energy and large differences are expected in the simulation results. No special effort was made to perform the same simulations or generate particle distribution for IR2 or IR8 at 3.5 TeV.

4.4.5 Simulation Results for the Ionization Chamber (IR1 and IR5)

In order to simplify the geometry the detector was approximated using layers of Copper and Argon. Applying a 5 mV cut off to the efficiency curve shown in Figure 4.12 (this corresponds to a deposited energy of 0.24 MeV as calculated in the final section) we expect to detect about 45% of the proton–proton collisions. The total energy deposited in the detector is of the order of 200 GeV which gives a deposited energy per proton–proton event of 2.0 10^{-3} GeV.

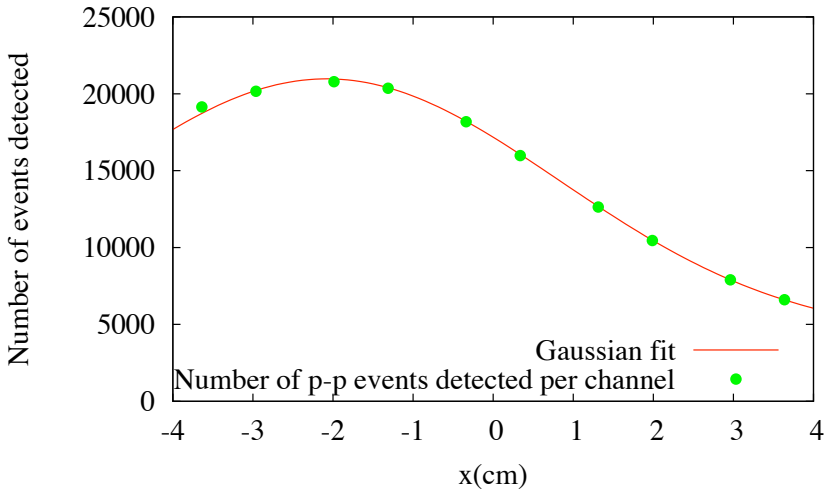

Figure 4.11: Number of events detected in each channel. A fit of this distribution gives a measurement of the crossing angle. An angle of 149±2 μrad was found which is consistent with the initial particle distribution.

More recently, additional simulations [59] at lower energies were performed using particle distributions provided by LHCf [31] which is also located inside the TAN. The energy flux for the 3.5 TeV beam was found to be one third smaller than the one a 7 TeV. The crossing angle was not included when generating this distribution.

Figure 4.13 shows the results of these simulations at 7 TeV, 5 TeV and 3.5 TeV. The efficiency at 7 TeV over the noise level of 5 mV is of about 40 % to be compared with the previous results that gave 45 %. This difference is explained by the fact that the cable attenuation was measured to be 73 % instead of the initially foreseen 96 % as presented in the next section. The geometry used was also slightly different. Taking into account these differences the results of the two simulation campaigns agree very well at 7 TeV. It is foreseen to operate the ionization chambers with a trigger level in between 20 and 40 mV. This reduces the efficiency to 25 to 30 % at 7 TeV and of the order of 5 % to 10 % at 3.5 TeV. This should be enough to observe a signal in these monitors even at lower energies.

4.4.6 Simulation and Measurements at 350 GeV

Measurements with test beam were performed in the SPS in 2007 at 350 GeV for both detectors. In this section we will describe the results and try to extrapolate the results to 7 TeV in order to give an estimate of the signal at this energy.

The four CdTe detectors have been placed behind a 15 cm thick copper block and irradiated with π^- at 350 GeV. The signal amplitude can be expressed as:

$$s = \frac{E}{I_w}\varepsilon\frac{q_e}{\tau}RG, \tag{4.1}$$

where E is the deposited energy, I_w is the energy required to create a pair (4.43 eV), ε is the collection efficiency (20%), q_e is the electron charge, τ the pulse length (5 ns), R and G are the amplifier input impedance and gain (50 Ω and 100). Simulations were made using the same geometry as for the 7 TeV case and similar beam conditions in order to reproduce the measured threshold scan. The signal was calculated from the deposited energy using Equation 4.1.

Figure 4.14 represents a comparison between the measurement and the FLUKA simulation. From this comparison between the simulations and the measurements we can deduce that the predicted and measured

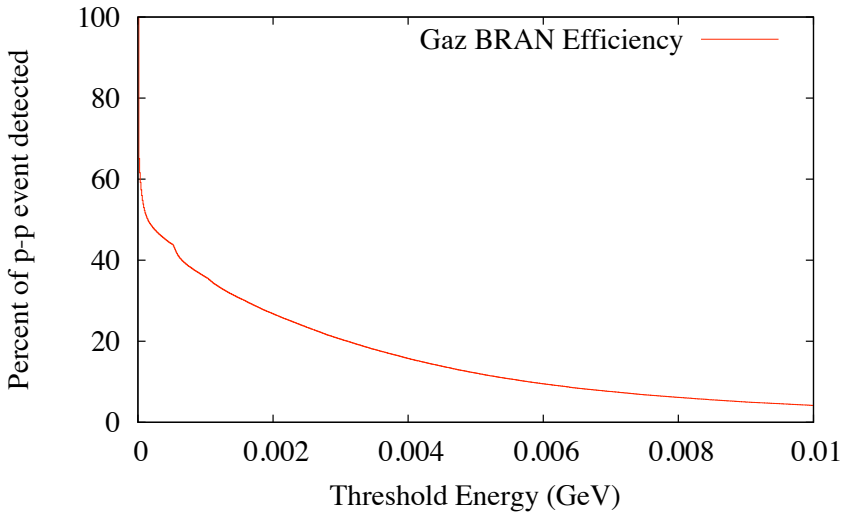

Figure 4.12: Fraction of events detected versus the threshold energy in IP5. The noise level is expected to be around 5 mV which corresponds to an energy deposition of 0.24 MeV. The resulting efficiency over the noise level is of the order of 45 %.

signals disagree by about a factor two. Applying this correction factor to the signal definition the 30 mV threshold would represent a deposited energy of 8 MeV and would reduce the efficiency of the detector to 40%. This represents a loss of about 10% and would give an average pulse height of 0.72 V per proton proton collisions.

The ionization chamber was irradiated with a 350 GeV proton beam. With a 15 cm long absorber and a gas pressure of 8 bar the measured pulse height was equal to 5 mV [60], scaling it up to 10 bar would give a pulse height of 6.2 mV. The simulations of this experiment gave an average deposited energy per incident proton of 0.3 MeV for a gas pressure of 10 bar. We can give an estimate of the simulated pulse height with the following formula [61]:

$$s = c_\varepsilon \frac{E_{deposited}}{dE/dx_{min}} F G \frac{\varepsilon}{B_d} = 6.31\,\text{mV}, \tag{4.2}$$

where c_ε the collection efficiency (0.5), F represents the number of ionization pairs created by a minimum ionizing particle (583 for 6 mm of Argon at 10 bar),G the gain ($0.32.10^{-6}$ V/e$^-$), ε the losses in the cable (0.96) and B_d the ballistic deficit (2.75 due the shaper's finite integration time). This theoretical result is in relatively good agreement with the measurements knowing that this calculation underestimates the real dE/dx. Taking the measured value as a reference and looking at the 7 TeV simulation we obtain an average pulse height per event of 41 mV.

4.4.7 First Results with Beam

Most of the simulations were performed for 7 TeV beams and are therefore difficult to compare with data. The simulations for the ionization chambers showed that an efficiency of 5-10% is expected at 3.5 TeV and the commissioning of these devices started late as the signal was too weak at low luminosity.

Figure 4.15 shows the BRANs signals at the four interaction points during a luminosity optimization. We can see that on the relative scale the resolution is sufficient to find the optimum settings for collision rates. We remind that the BRANs are designed for optimization of the luminosity as relative instantaneous rate monitors. These measurements are very encouraging and prove that BRANs signals are useful even at 3.5 TeV which is twice lower than the design energy.

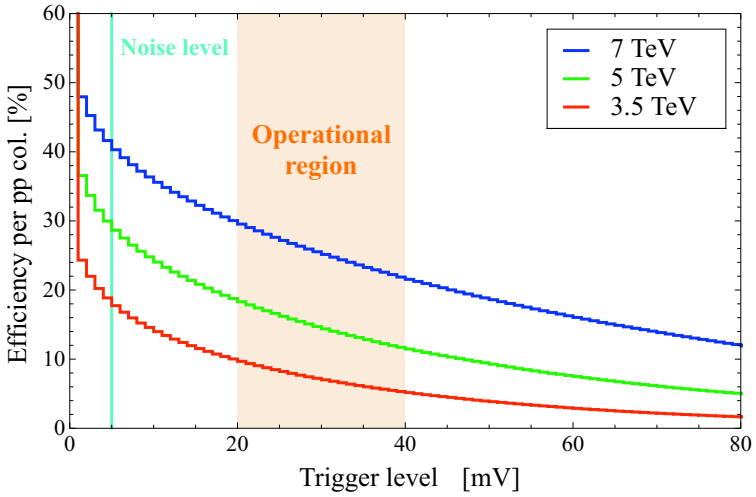

Figure 4.13: Simulated threshold scan at 3.5 TeV [59].

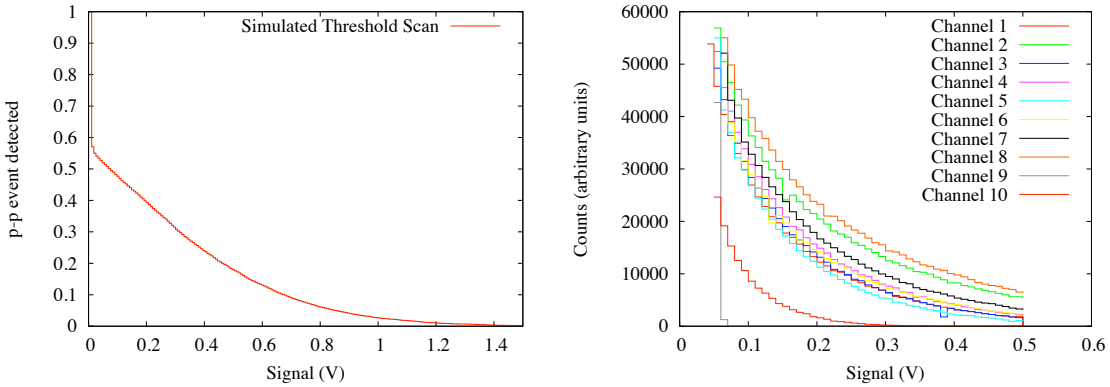

Figure 4.14: Simulated and measured threshold scan for the SPS test beam. Comparing the simulated and measured data we can see that they agree within a factor 2.

4.5 Summary

A performance note [39] summarizes the first results from the LHC beam instrumentation systems including devices that were not described in this chapter such as the BLM system or the tune measurement. The majority of the LHC beam instrumentation systems were capable of measuring beam parameters from the first injection tests. All the systems behave as expected and could be used for the commissioning of the LHC even if some work remains to be done especially on the calibration of the various measurements.

FLUKA simulations were performed for both BRAN designs. Comparison with the SPS test beam measurements and the simulations at 350 GeV are in good agreement for the ionization chamber but diverge by a factor four for the CdTe detectors. Using these results at 350 GeV as a reference we were able to estimate the performances of the BRANs at 7 TeV where both designs seem to behave as expected.

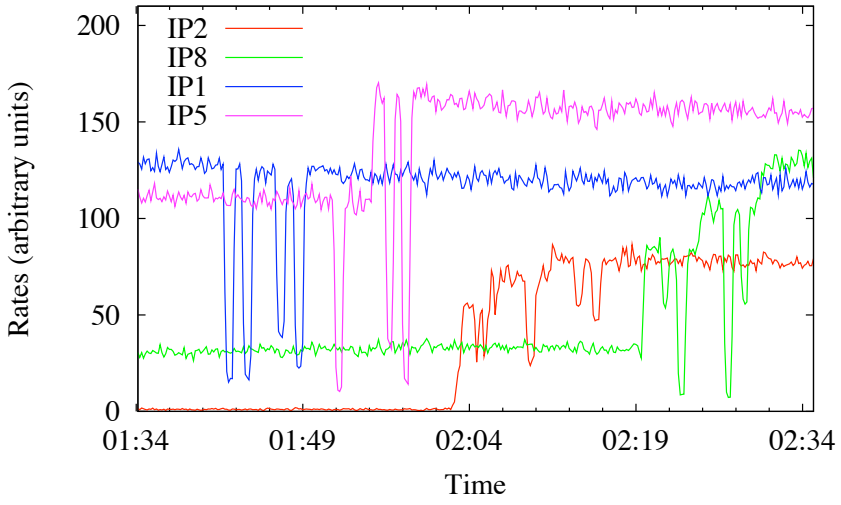

Figure 4.15: BRAN signals during a luminosity optimization at the four IPs.

Chapter 5

Experimental Results from the 2009 RHIC Proton Run

Towards the end of 2008, it became clear that there would be no collisions in the LHC in the first part of 2009. The Van Der Meer scan method is extensively used at the RHIC [26, 62] collider which offers the advantage to have a similar layout and issues as the LHC. At this time, RHIC was just preparing for its first 250 GeV proton run and a collaboration was set to gain experience and prepare for LHC start-up. This chapter summarizes the results obtained from the measurements done during the 2009 polarized proton run at RHIC.

5.1 The Relativistic Heavy Ions Collider

The **R**elativistic **H**eavy **I**ons **C**ollider (RHIC) is situated at Brookhaven National Lab in Upton, New York and was commissioned in 1999. It consists of two independent superconducting rings (referred to as the blue and yellow ring) arranged in a six-fold symmetry. Each ring consists of six arcs and six interaction regions. The collider has provided collisions in up to 5 experiments STAR, PHENIX, PHOBOS, BRAHMS and PP2PP. Currently the two large experiments, PHENIX and STAR, are in operation. The RHIC collider can operate heavy ions, such as gold, up to beam energies of 100 GeV per nucleon. The accelerator was also designed to collide lighter ions all the way down to protons. In 2009, RHIC collided polarized protons at an energy of 250 GeV per beam for the first time [63]. A schematic view of the RHIC accelerator complex is shown Figure 5.1.

RHIC has now successfully been running for 10 years and is undergoing a luminosity upgrade and planning for an electron-ion physics program [64]. This chapter will focus on the 2009 polarized proton run when the collaboration for luminosity calibration and optimization took place [65].

5.2 Beam Parameters for the 2009 Polarized Proton Run

During the 2009 polarized proton run the beams were colliding in two interaction points, at PHENIX and STAR, and where kept separated in the other IPs.

Table 5.1 summarizes the 2009 RHIC proton beam parameters and the nominal LHC beam parameters. Bunch intensities and beam-beam parameter are similar. RHIC has stronger hourglass effects which makes the analysis and model more complicated. The experience acquired at RHIC offers an excellent testbed for future LHC operation. RHIC operates by design without crossing angle.

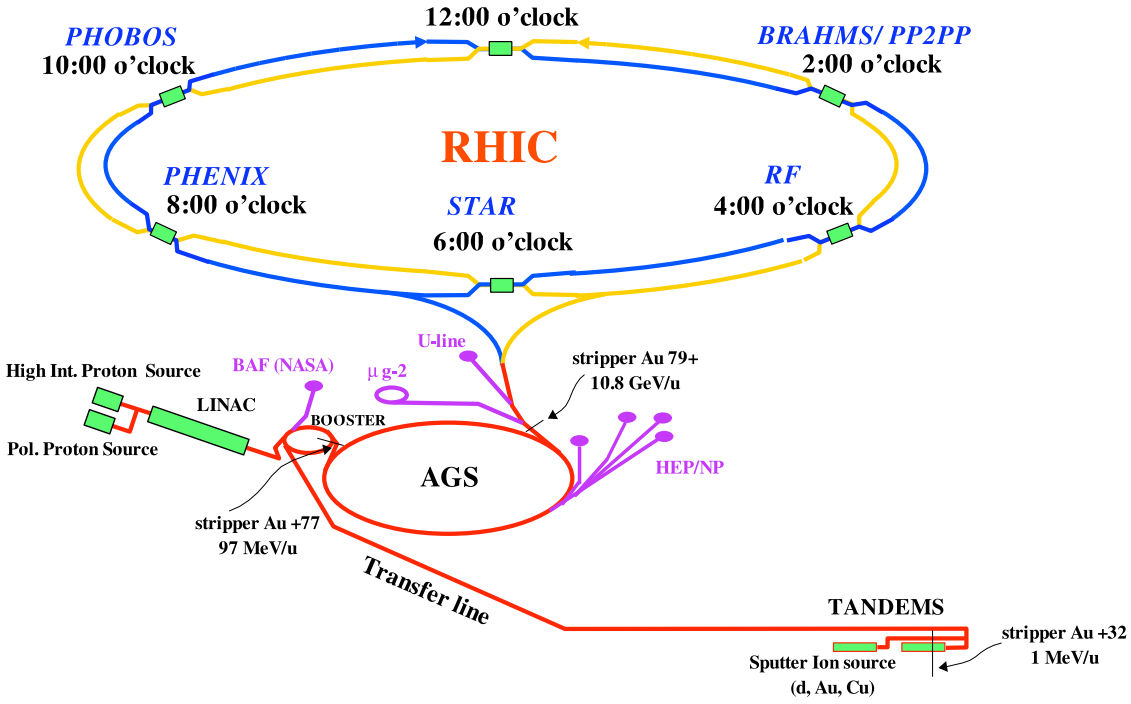

Figure 5.1: The RHIC accelerator complex. The path of the gold ions can be tracked from the TANDEMs while the polarized protons are first injected from the LINAC into the booster, AGS, and finally into RHIC.

5.3 Overview of the Measurements

Several scans were perform in both PHENIX and STAR. The collision rates are measured with the ZDCs (**Z**ero **D**egree **C**alorimeter) and, in the case of PHENIX, with BBCs (**B**eam **B**eam **C**ounter). While the two ZDCs are mostly identical in both interaction points, the BBCs are of different shape and acceptance. They provide independent measurements which can help understanding the systematic error. All the luminosity monitors consist of two identical parts on each side of the IP and provide coincidence rates. A total of 6 scans were performed at STAR and 7 at PHENIX. For each of these the ZDC and BBC data were acquired except for the first two fills where the BBC data were not available. All scans were done at $\beta^* = 0.7\,\mathrm{m}$ moving only one beam. Before each scan an optimization of the transverse position is done such that the actual calibration is performed around the peak luminosity. Calibration scans are usually performed at the end of fills when lower intensities and larger emittances result in lower beam-beam parameters than what is quoted in Table 5.1.

5.4 Data Analysis

The calibration of the luminosity using the Van Der Meer scan method at RHIC involves several devices such as BPMs (**B**eam **P**osition **M**onitor) and BCT (**B**eam **C**urrent **T**ransformer) which have their own non-linearities and systematic error to be included in the overall uncertainty. In addition, unwanted beam dynamics and physics processes such as coupling occur during the measurement which have to be corrected for. This section will summarize these effects and present how they were included in the data analysis.

Table 5.1: Beam Parameters for the 2009 RHIC Proton Run and comparison with nominal LHC.

	RHIC	LHC
Energy [GeV]	250	7000
β^*	0.7	0.55
Intensity [10^{11} p/bunch]	1.35	1.15
Number of bunches	111	2808
Emittance [μm]	3.0	3.75
σ_s [m]	1.0	0.075
β^*/σ_s	0.7	7.3
Crossing angle [μrad]	0.0	285
Beam-Beam Parameter	0.005	0.003

5.4.1 Beam Position

The measurement of the IP effective beam size requires an absolute knowledge of the displacement of the beams during the scans. The magnet settings used to generate the transverse offset give a first approximation of the separation at each scan step. The position and angle of the two beams are then measured using the DX BPMs [66]. These BPMs are situated at ± 8.3 m from the IP where the beams share the same beam pipe. No optical element is present between these two monitors except for the experimental magnets. The beam positions and angles at the IP can therefore be derived from a linear interpolation of the left and right position measurements.

Figure 5.2 illustrates a typical data set as taken during a Van Der Meer scan. On the left the moving beam is shown and on the right the idle beam. The x-axis represents the bump value and the y-axis the BPM measurements. The last row is the average of the left and right measurements shown above, which gives the beam position at the IP. A clear coupling is seen between the beams through a non-linear function of the separation. This shape is typical of the beam-beam effects as was shown Figure 1.3. Here only the scanned plane is shown. A similar (weaker) effect is seen in the other plane. A slope is also observed in the other plane. This indicates the presence of $x-y$ coupling. The source of the coupling can be an instrumental effect (titled BPM) or lattice imperfections. These displacements are very small, typically of the order of $10\,\mu$m at the peak, compared the movements due to the actual scan. Assuming an IP beam size of about $100\,\mu$m, a transverse displacement of $10\,\mu$m represents a loss of 0.25 % in luminosity for Gaussian beams.

The bottom left plot shows a linear fit of the measured IP beam position to the one calculated from the magnets settings. Some non-linearities are observed due to the beam-beam force. These non-linearities are small and the overall behavior can be considered linear. In this case the fitted slope is 1.02 instead of an expected value of 1. This difference can be explained by a miscalibration of the BPM or a bump non-closure.The strategy adopted here was to perform the scan fits using the separation from the magnets settings and add a systematic uncertainty according to the BPM measurements. This should give an upper limit on the systematic uncertainty to be assigned to the beam displacement. This method does not take into account the non-linearities due to the beam-beam force. 1 % systematic error was added to the overall uncertainty to take this into account. A list of all scans is shown in Table 5.2.

5.4.2 Intensity Measurement

Any uncertainty on the intensity measurements will directly affect to the absolute luminosity. Two independent measurements are available and can be used for cross calibration:

- The WCM which measures the bunch intensity.

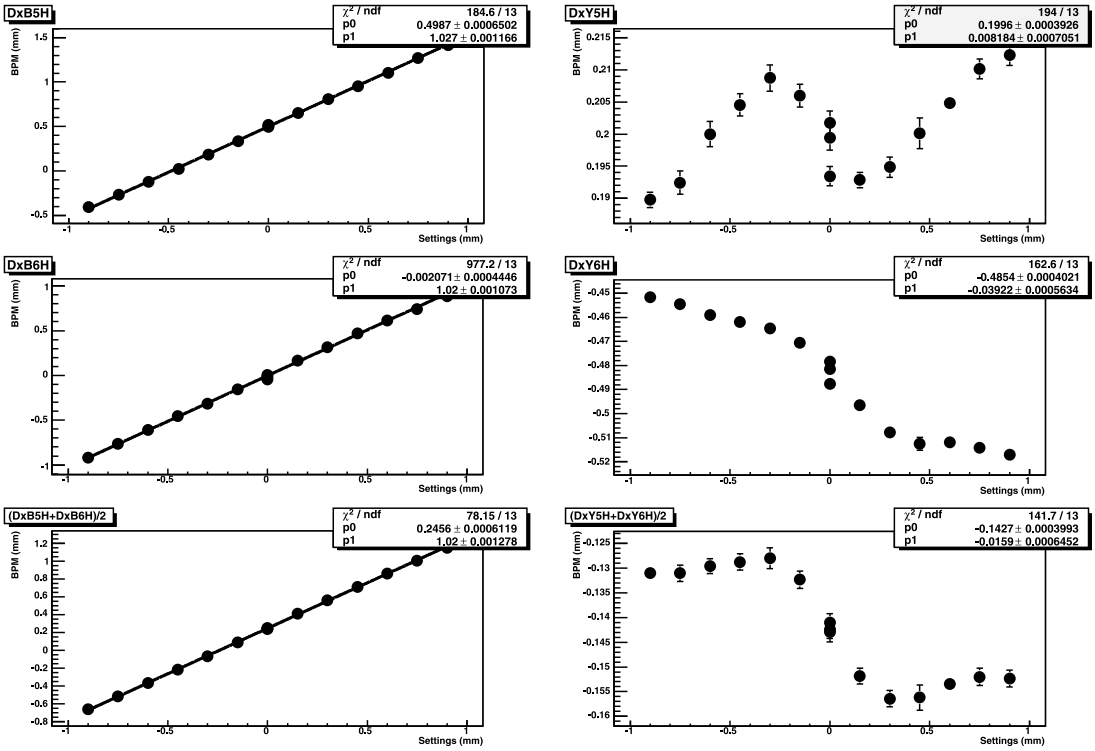

Figure 5.2: BPM data as a function of the calculated separation (bump value) acquired for a scan at STAR. On the left is the horizontal plane and on the right is the vertical plane. The first two rows represent the BPMs left and right of the IP and the last column the average (beam position at the IP). The beam was moved in the horizontal plane in which we observe a linear motion as a function of the bump value. Small movements are observed in the other plane due to coupling from lattice imperfections or beam-beam interactions.

- The DCCT which measures the full beam intensity.

The RHIC filling scheme is made such that not all bunches collide at the two IPs. One has to measure the bunch intensities of the two beams and correctly associate them to compute the product of the intensities as used in the luminosity formulae.

The effect of the filling scheme on the product of the bunch intensities is shown in Table 5.3. The last two columns show the difference between the renormalized product of the total intensities by the number of colliding bunches (assumes equal bunches) and the proper bunch pairing from the filling scheme. This reflects the effect of the filling scheme on the bunch to bunch intensity spread. The spread is larger for the 84×84 filling scheme. The correction is non negligible and proves that a careful bunch by bunch analysis is essential to precisely measure the absolute luminosity.

Experience from past years and cross calibration of the WCM with respect to the DCCT showed that an absolute error of 2 % per beam has to be assigned to the intensity measurements [62, 26]. This results in a systematic error of 3 % on the product of the intensities.

5.4.3 Crossing Angle and Hourglass Effect

The trajectories of the yellow and the blue beam interpolated from the DX BPM measurements are shown in Figure 5.3. The trajectories measured by the BPMs are not crossing exactly at the interaction point.

Table 5.2: Summary of the BPM data analysis. Results shown here are for the separation (yellow beam - blue beam). Scans were usually performed with a range of ± 1 mm.

Fill Number	Slope for Scanned plane X / Y		Slope in the other plane X / Y	
	PHENIX	STAR	PHENIX	STAR
10207	1.055 / 1.09	1.047 / 1.058	-0.001 / 0.0002	-0.0006 / 0.007
10276	0.996 / 1.031	1.031 / 1.017	0.008 / 0.003	0.01 / -0.01
10325	0.987 / 1.047		0.008 / 0.004	
10399		1.011 / 1.008		-0.01 / 0.03
10415	0.993 / 1.057	1.013 / 0.995	0.001 / 0.003	-0.002 / -0.007
10478	1.004 / 1.043		0.001 / 0.002	
10505	1.002 / 1.04		0.0002 / 0.006	
10507		1.025 / 1.008		-0.003 / -0.007
10536	1.02 / 1.037	1.037 / 1.018	0.001 / 0.004	0.01 / 0.008

Table 5.3: Effect of the filling scheme on the product of the intensities. The first two columns represent the collision pattern and the last two the difference between the average and the proper bunch sum.

Fill Nb	Filling Scheme	Nb Col. PHENIX	Nb Col. STAR	Corr. PHENIX [%]	Corr. STAR [%]
10207	54x56	54	50	0.2	-2.9
10276	56x56	56	52	-0.05	-1.2
10325	84x84	82	77	-1.9	-4.2
10399	83x83	80	75	0.1	-2.8
10415	109x108	106	101	-0.3	-1.5
10478	109x107	105	100	0.3	-1.4
10505	109x106	104	99	1.4	-1.0
10507	108x106	103	98	0.7	0.5
10536	106x106	101	96	-0.2	0.5

An optimization was systematically performed before the calibration scans to make sure the beams where colliding head-on at the IP. A BPM offset can result in a small apparent separation. An offset will also affect the crossing angle measurements. An error corresponding to the change in angle required for the beams to collide head-on at the interaction point was therefore assigned to the crossing angle measurements. Figure 5.3 illustrates this in the vertical plane for the fill 10415 in PHENIX. The corrected trajectories are represented by the dashed lines, in this case the derived uncertainty is $\Delta\phi = \Delta\phi_1 + \Delta\phi_2 = 20\,\mu$rad.

Table 5.4 summarizes the measured crossing angle values and uncertainties for each scan. From this table we can compute a maximum crossing angle of about $130\,\mu$rad in PHENIX and $137\,\mu$rad in STAR by adding the error to the measurement.

In Chapter 2, it was shown that in the presence of an angular component in the two transverse planes the Van Der Meer scan method is not an exact measurement of the effective area. From the Comparison between the measurements listed in Table 5.4 and the estimated error displayed in Figure 2.2 we can conclude that the uncertainty introduced by the crossing angle is less than 1%.

During the 2009 proton run β^* was equal to 0.7 m and σ_s was of the order of 1 m. The hourglass effect was therefore non-negligible, the effects of the crossing angle and the hourglass have therefore to be combined to derive a correction factor. It was shown in Chapter 2 that the correction factor due to the

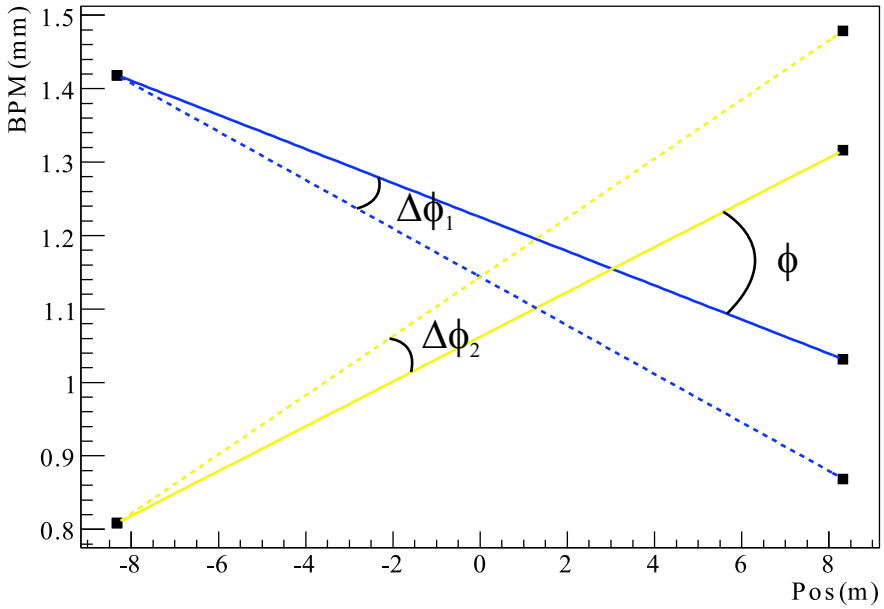

Figure 5.3: Beam trajectories at PHENIX for the fill 10415 in the vertical plane. ϕ represents the crossing angle and ϕ_1 and ϕ_2 the corrections to be applied to each beam for them to cross exactly at the IP. The dashed line represents the corrected trajectory and the solid line the measurement.

hourglass efftect to be applied to the luminosity is:

$$HG_{\text{corr}} = \frac{\sqrt{\pi} t_r e^{t_r^2} \operatorname{erfc}(\mathrm{t_r})}{\left(\frac{1}{\sqrt{\pi}} e^{\frac{t_r^2}{2}} t_r K_0 \left[\frac{t_r^2}{2} \right] \right)^2}, \tag{5.1}$$

where K_0 is the modified Bessel function, $t_r^2 = \frac{2\beta^{*2}}{\sigma_{1s}^2 + \sigma_{2s}^2}$ and $u = x, y$. The absolute luminosity is then expressed as:

$$\mathcal{L} = \frac{N_1 N_2 f N_b}{2\pi \sigma_{x\text{eff}} \sigma_{y\text{eff}}} \frac{1}{HG_{\text{corr}}}. \tag{5.2}$$

Table 5.5 summarizes the correction factor including the beam size correction and the hourglass reduction factor applied for each scan. We can see that these factors range from 3% to 5% and systematically increase the luminosity with respect to the one calculated from the apparent beam sizes as measured by the scans. This effect was already observed and measured at PEP-II [67].

The corrections shown in Table 5.5 do not include the effect of the crossing angle. Looking at the evolution of the luminosity as a function of the crossing angle in the presence of hourglass effects in Figure 5.4 it is clear that we cannot simply neglect the effect of the crossing angle for the values listed in Table 5.4.

In order to keep our model as simple as possible we can use the fact that the beams are almost round. We can therefore derive an effective crossing angle which does not depend on the transverse beam sizes:

$$\tan^2 \frac{\phi}{2} = \tan^2 \frac{\phi_x}{2} + \tan^2 \frac{\phi_y}{2}, \tag{5.3}$$

Table 5.4: Summary of the measured crossing angles and the derived errors on the luminosity.

Fill Number	Angle X / Y [mrad]		Uncertainty X / Y [mrad]	
	PHENIX	STAR	PHENIX	STAR
10207	0.040 / 0.046	0.054 / 0.004	0.043 / 0.080	0.066 / 0.043
10276	0.032 / 0.046	0.009 / 0.048	0.004 / 0.006	0.003 / 0.006
10325	0.073 / 0.057		0.002 / 0.007	
10399		0.071 / 0.006		0.0 / 0.014
10415	0.101 / 0.056	0.137 / 0.030	0.0 / 0.020	0.004 / 0.003
10478	0.050 / 0.079		0.005 / 0.030	
10505	0.020 / 0.070		0.007 / 0.030	
10507		0.070 / 0.015		0.008 / 0.002
10536	0.030 / 0.030	0.009 / 0.089	0.024 / 0.037	0.045 / 0.012

Table 5.5: Correction factor HG_{corr} due to the hourglass effect.

Fill Number	Correction Factor
10207	1.03
10276	1.05
10325	1.05
10399	1.04
10415	1.03
10478	1.04
10505	1.05
10507	1.03
10536	1.03

from which the systematic error was derived using the comparison between the correction factor with and without crossing angle as was shown in Figure 2.4. Table 5.6 lists the effective crossing angle and derived systematic errors from the model for each scan. The systematic uncertainties range from 0.2% to 1.3% in the worst case. This approach gives an upper limit to the error to be applied due to the crossing angle using the measurements available in the scans data sets. This error could be improved by analysing the orbit data and interpolating the crossing angle from BPMs further away from the IP to get independant angle measurements which could be averaged. Another method to minimize this error would be to perform a scan in angle with the same procedure as for the separation scans. This would ensure that we have zero crossing angle and further optimize the luminosity.

The PHENIX BBC is situated approximately at ± 0.75 m from the IP with a vertex cut applied at ± 0.3 m and the ZDC at ± 20 m. The ZDC will therefore see the full hourglass effect while the BBC practically measures the beam size at the IP. Comparing the two would then give a measurement of the hourglass effect.

Figure 5.5 shows the ratio of the measured beam sizes from the ZDC and BBC data. The measurements agree with the model using perfect Gaussian beams within error bars. The measured profile do not correspond to perfect Gaussian functions as will be shown in the next section. The Gaussian approximation could therefore explain the small discrepancies. The good agreement between the model and the measurements shows that the assumption of zero crossing angle is justified.

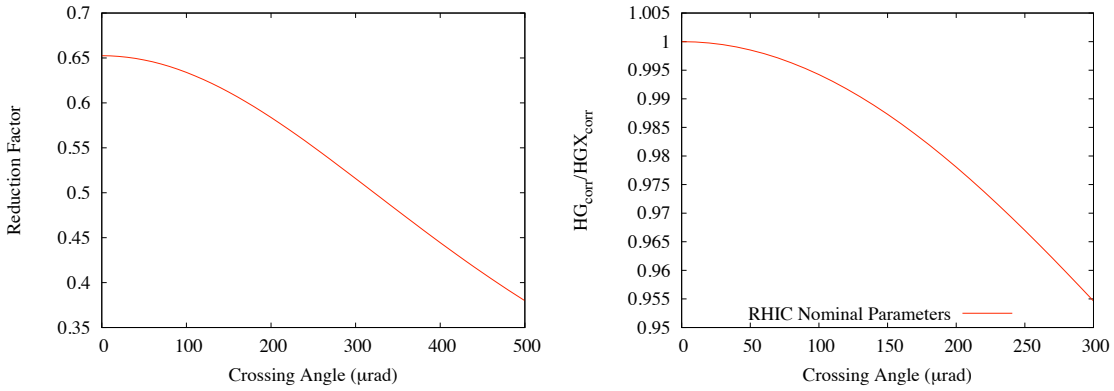

Figure 5.4: Reduction factor due to the combined effect of the crossing angle and the hourglass effect (left) and comparison between the correction factor with and without crossing angle (right) for $\sigma_s = 1\,\mathrm{m}$ and $\beta^* = 0.7\,\mathrm{m}$.

Table 5.6: Effective crossing angle and corresponding systematic errors.

Fill Number	Effective Crossing angle [mrad]		Systematics [%]	
	PHENIX	STAR	PHENIX	STAR
10207	0.150	0.129	1.3	1.0
10276	0.063	0.055	0.2	0.2
10325	0.098		0.6	
10399		0.073		0.3
10415	0.126	0.144	1.0	1.2
10478	0.122		0.9	
10505	0.103		0.6	
10507		0.080		0.4
10536	0.086	0.115	0.5	0.8

5.4.4 Beam Profile

Non Gaussian tails were observed for all scans. These non-Gaussian components of the beam still contribute to the overall luminosity and have to be taken into account while computing the overlap integral. The core of the beam, which very often remains Gaussian, is the main contributor to the luminosity. A convenient way to include the tails in the model is to fit the profile with a double Gaussian. The luminosity as function of the separation, as shown in Chapter 2 is then:

$$\mathcal{L}_0 = \frac{N_1 N_2 f N_b}{2\pi \sigma_{x\mathrm{eff}} \sigma_{y\mathrm{eff}}} \tag{5.4}$$

with

$$\sigma_{u\mathrm{eff}} = \frac{A_{au}\sigma_{au} + A_{bu}\sigma_{bu}}{A_{au} + A_{bu}} \tag{5.5}$$

Figure 5.6 shows the comparison between a Gaussian + constant fit and a double Gaussian fit. Looking at χ^2/ndf it is clear that the double Gaussian fit is more suited to the beam profile. The ZDC data proved to give very good results using the double Gauss fit method. This was not the case for the BBC data for

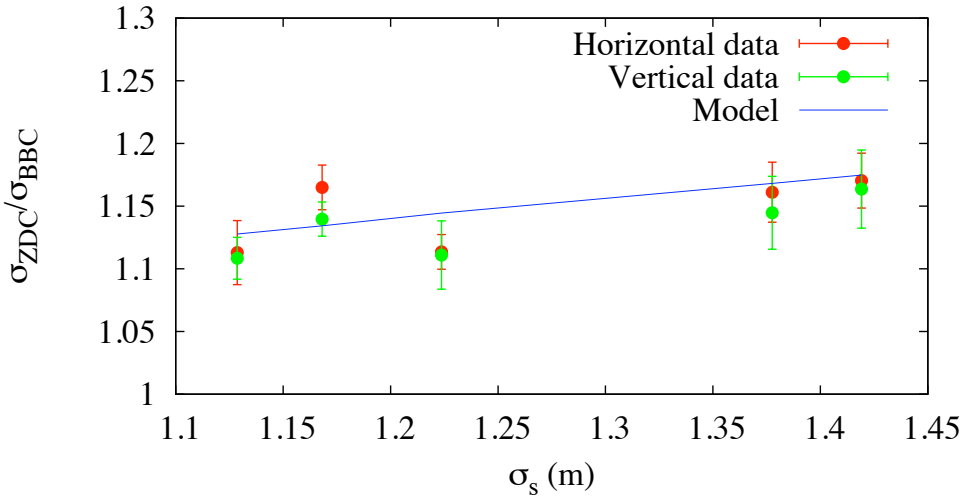

Figure 5.5: Ratio of the ZDC and BBC beam sizes as measured from the Vernier scans. σ_s represents the convoluted bunch length. The ZDC measured the full hourglass effect as the BBC measures the beam size at the IP. As expected this ratio increases with the bunch length.

which the χ^2/ndf remained poor even with this method. The effective cross section calculation and detailed analysis of the Van Der Meer scans results was therefore only performed for the ZDCs.

5.5 Results

All the systematic uncertainties from the various instruments and beam dynamics processes are summarized Table 5.7. All these errors have to be added in quadrature in order to get the overall systematic uncertainty for each scan.

Table 5.7: List of the systematic uncertainties.

Source	Uncertainty
Beam displacement	2-10 %
Crossing Angle	0.3-1.3 %
Intensity	3 %
Beam-Beam	1 %
Hysteresis	1 %

The systematic uncertainties coming from the crossing angle and the beam position are different from scan to scan. The other uncertainties coming from hysteresis, beam-beam and intensity are common to all scans. During this measurement campaign no specific effort was made to minimize these errors. The precision of the measurement could be further improved as follows:

- Scans in angle would minimize the crossing angle.
- Orbit data analysis would allow for independent measurements of the crossing angle and beam position using different pick-ups. Averaging over these measurements should improve our knowledge of

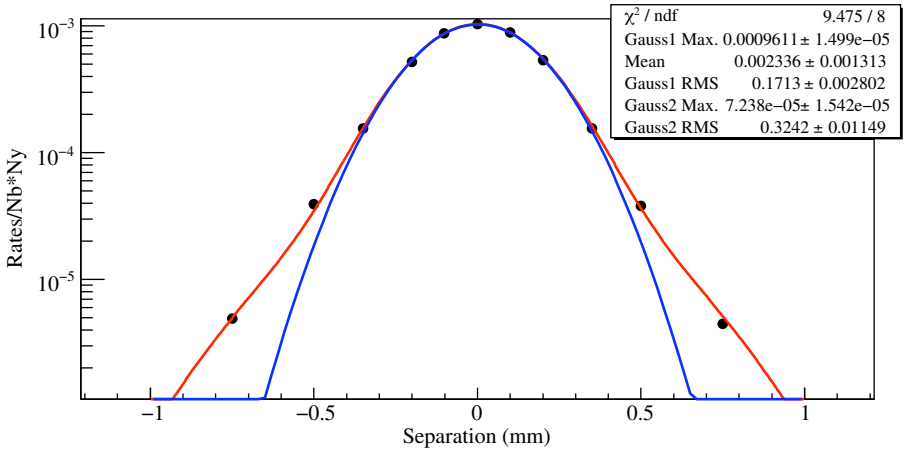

Figure 5.6: Profile as measured from the ZDC in PHENIX. A Gaussian fit is shown in blue and a double Gaussian fit with fit parameters is shown in red.

the IP beam coordinates.

- Cross calibration of the orbit bump using vertex reconstruction from the experiments. This method gave excellent results in the LHC. See Chapter 6.
- Lower intensities would reduce the beam-beam effects.
- Higher β^* would reduce the hourglass effect.

Reducing the uncertainty from the BPM data with the two methods quoted above would be compatible with normal running and the cost in physics beam time should not be too consequent for the scans in angle as the goal is only to optimize the luminosity and minimize the crossing angle (no extensive scan with a large number of points is necessary). Reducing the beam-beam and hourglass effects would require dedicated beam parameters different from the normal running conditions.

Figure 5.7 shows the fit results for the Vernier scans performed at the two IPs. Only statistical errors are shown. We can see that the cross sections are statistically consistent. Table 5.8 list the calculated effective cross section as well as the statistical and systematic uncertainty for each scan.

Considering all these measurements as independent, the ZDC effective proton proton cross section can be calculated in STAR and PHENIX by computing the weighted mean of all scans. This lead to:

- $\sigma_{\text{STAR}} = 2.18 \pm 0.13$ mb
- $\sigma_{\text{PHENIX}} = 2.30 \pm 0.15$ mb

The difference between the cross sections in STAR and PHENIX can be explained by the slightly different detector configurations in the two experiments.

5.6 Beam-beam Deflection

When two bunches cross each other the trajectories of the particles are modified by an horizontal and vertical angle $\Delta x'$ and $\Delta y'$ due to the electromagnetic field of the counter rotating bunch. In the case of equal round

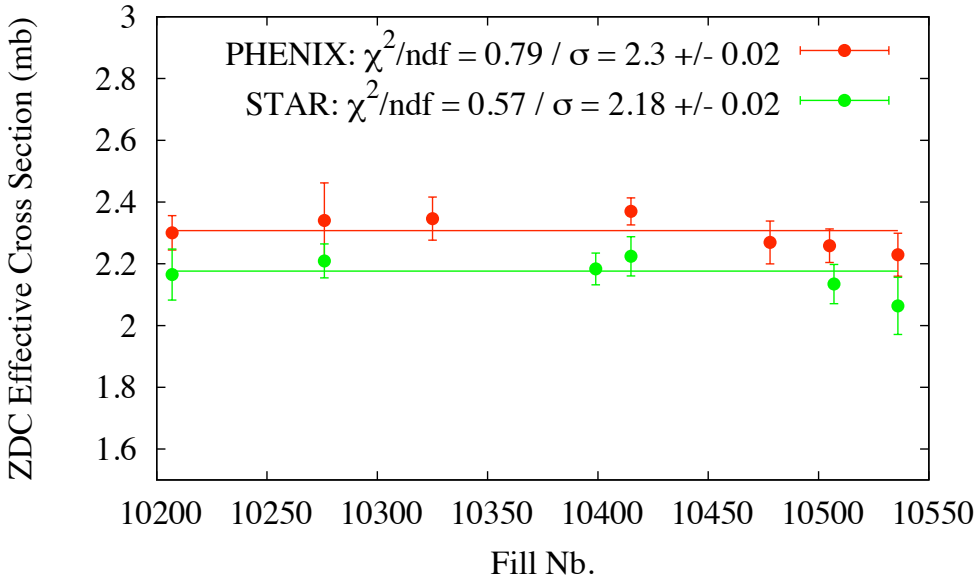

Figure 5.7: Effective cross section for the STAR and PHENIX ZDC fro all fills. Only statistical error bars are shown.

Gaussian beams the radial deflection [4] can be expressed as:

$$\Delta r' = -\frac{8\pi\xi\sigma^2}{\beta^*}\frac{1}{r}\left[1-\exp\left(-\frac{r^2}{2\sigma^2}\right)\right], \tag{5.6}$$

where $r^2 = x^2 + y^2$, β^* is β-function at the IP and ξ is the linear beam-beam parameter defined as

$$\xi = \frac{N r_0 \beta^*}{4\pi\gamma\sigma^2}. \tag{5.7}$$

.

An angular kick θ at a position s_0 can be translated into an orbit change at a given position s:

$$y(s) = \frac{\sqrt{\beta(s)\beta(s_0)}\,\theta}{2\sin\pi\nu}\cos\left(\pi\nu - |\varphi(s)-\varphi(s_0)|\right), \tag{5.8}$$

where ν is the betatron tune and φ the phase. This formula was used to compute the beam-beam deflection kick at the IP from the orbit changes at the DX BPMs left and right. Computing the beam-beam deflection angle allows for a measurement of the effective beam size and the beam-beam parameter.

Figure 5.8 shows the beam-beam deflection angle as a function of the separation. This effect was systematically observed. Most of the time the BPM resolution was not sufficient. Only the fits with reasonable χ^2 and error bars were taken into account.

Figure 5.9 compares the fitted beam-beam parameters with the ones calculated from the Vernier scan results assuming nominal β^*. It shows very good agreement between measurements and expected values. The fitted beam sizes had error bars of 10% to 20% and were generally in good agreement with what was measured from the luminosity scans as expected from the comparison of the beam-beam parameter as derived by the two methods.

In principle, this method can also be used for luminosity optimization as the deflection angle goes through zero for head-on collisions. This was done previously at LEP [68] with a beam-beam parameters

Table 5.8: ZDC effective crossing section and corresponding statistical and systematic uncertainties.

Fill Number	Cross Section [mb]	Statistical Error [mb]	Systematic Error [mb]
PHENIX			
10207	2.30	0.06	0.26
10276	2.34	0.12	0.11
10325	2.35	0.07	0.14
10415	2.37	0.04	0.16
10478	2.27	0.07	0.13
10505	2.26	0.06	0.12
10536	2.23	0.07	0.12
STAR			
10207	2.17	0.09	0.18
10276	2.21	0.06	0.11
10399	2.18	0.05	0.08
10415	2.22	0.06	0.09
10507	2.13	0.06	0.09
10536	2.06	0.06	0.11

10 times larger than in RHIC. At RHIC, the beam-beam parameter is of the order of 0.005 for nominal parameters and about a factor 2 lower at the time of the measurements (end of fills). Using only DX BPMs data to compute the deflection angles we are close to the precision limit of these instruments which resulted in large error bars. In order to improve the resolution one could try to interpolate the beam coordinates at the IP from other BPMs or average out the noise by integrating over a longer time. Originally, it was assumed that the deflection angles would be too small to be useful. The scan parameters where therefore not optimized for this measurement. The resolution on the optimum separation from the fit could be improved by changing the scan step size and range in order to add more points in the interesting region ($\pm$ 3 σ).

5.7 Summary

Van Der Meer scan were performed in both STAR and PHENIX with various beam conditions. The results in both IPs are all statistically consistent and demonstrate the reproducibility of the method. The overall uncertainty on the cross section is of the order of 7 % for which a large contribution comes from the quality of the BPM data. The precision of the measurement could be improved by looking more carefully into the orbit data and minimizing the crossing angle via scans in angle and reduce the non linearities with lower intensities and larger β^*. The hourglass effect was measured and agrees well with the model. An attempt at measuring the beam-beam deflection angle was performed and gave very encouraging results. Similarly to the Van Der Meer scans this measurement could be improved by looking at orbit data in order to increase the resolution.

The experience acquired in 2009 at the RHIC collider was very useful for future LHC operation. The LHC beam parameters are such that the hourglass effect can be neglected and as will be presented in the next chapter the Van Der Meer scans were performed at low intensity which considerably reduced the beam-beam effects. Luminosity calibration from machine parameters is foreseen as the first normalization from measurements to be used by the experiments. All the tools and procedure had therefore to be ready from the start-up. The lessons learnt from this collaboration in terms of analysis methods and software implementation were directly applied to the LHC and helped to have this measurement available from the start-up.

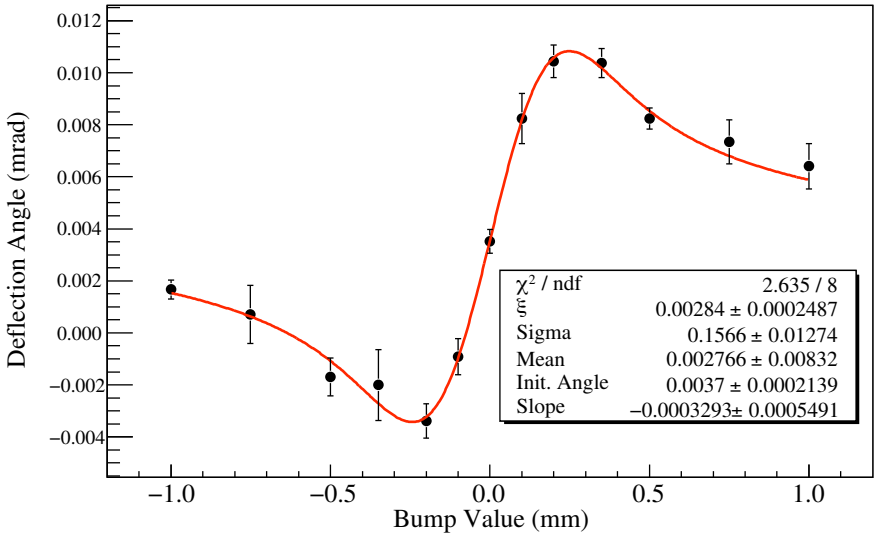

Figure 5.8: Beam-beam deflection scan in the horizontal plane observed at STAR.

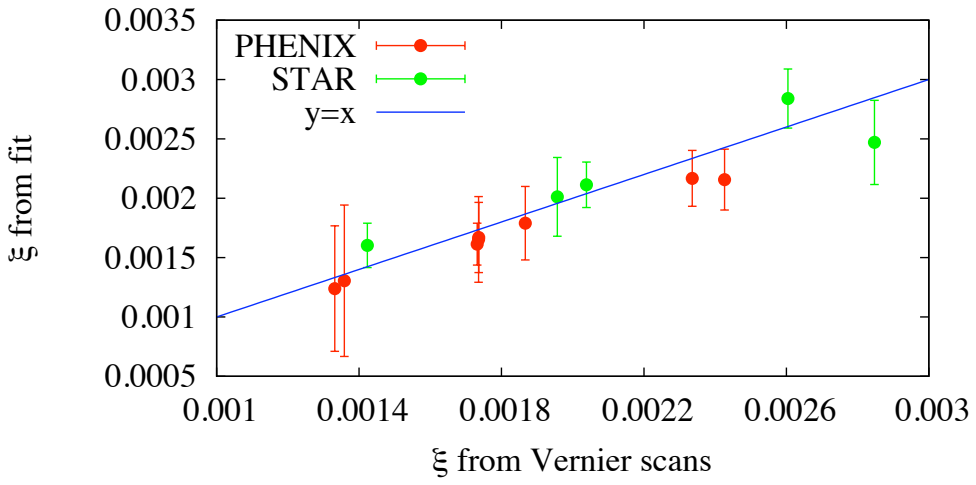

Figure 5.9: Beam-beam deflection scan results in the horizontal plane observed at STAR and PHENIX.

Chapter 6

Experimental Results from the LHC

Since October 2009, the LHC has been running without any major issues. After presenting the procedure for luminosity optimization and calibration in the LHC, this chapter will focus on how the beams were brought into collision for the first time and the results from luminosity calibration and optimization obtained during the 2010 proton run.

6.1 Implementation and Procedure for the LHC

Moving of the beam can be considered as dangerous and has to be performed in a very controlled way. The scans are done at the interaction points during physics periods when the machine status is considered stable. This adds another constraint and the obligation of communicating with the experiments. This section will describe how this measurement was planned and implemented for the LHC.

6.1.1 Procedure

In principle, the scans could be performed with a continuous linear sweep while recording the counting rates and then integrate the resulting curve. In practice, the power converters have acceleration and ramp characteristics which can result in non-linear changes of the currents in the magnets. It is therefore difficult to ensure the linearity of the displacements. It was then decided to perform the scans by moving one beam stepwise across the other one.

This method ensures the quality of each data point and allows to reduce the statistical error for each of them by accumulating data. The input parameters are the number of steps, the scan range and the integration time per step. An additional complication comes from the synchronization as we have to make sure that the acquisition is performed while the magnets are fully idle i.e. the applied current to the magnet is stable.

6.1.2 Orbit Bumps

As presented in Chapter 2 the beams are displaced at the IP via a closed orbit bump that consists of four magnets and allows to control the beams independently.

One can see in Figure 6.2 that a four magnet separation bump extends over a large fraction of the straight section around the IP. More specifically, displacing the beams at the IP will result in a change of orbit at the tertiary collimators (TCT). Given the non-negligible offset at the TCT introduced by the bumps, one has to ensure that while performing a separation scan the beams remain far enough from the aperture set by the collimators and that the displacement does not compromise the machine protection.

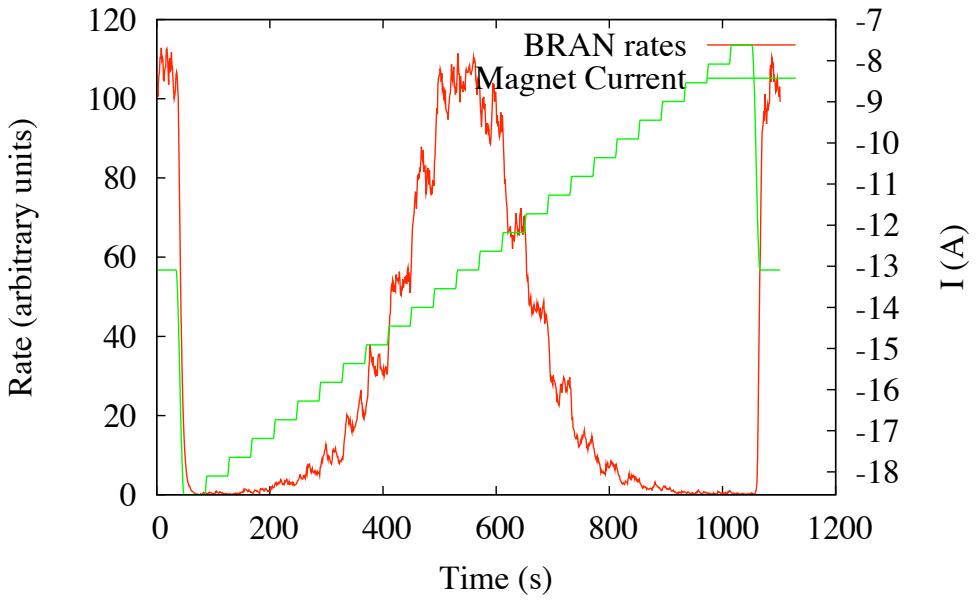

Figure 6.1: History plot of a scan showing the magnet current and the BRAN counting rates. The beams are swept stepwise through each other as illustrated by the magnet current.

6.1.3 Machine Protection

The nominal LHC beams will carry energies of about 350 MJ each which is two orders of magnitude higher than what was previously achieved at the Tevatron, the SPS or HERA. This makes the LHC beams highly destructive. In addition, the LHC is a superconducting machine and the magnets will quench if a small amount of energy is deposited in the superconducting magnet coils. The machine protection system efficiency is therefore a key parameter for the operation of the LHC. During the initial set-up the collimators are centered around the beams for a given orbit reference. The initial collimator setup-up and orbit reference represents the configuration where the machine should be protected and can be safely operated. Any deviation from this reference will reduce the protection efficiency and can be dangerous for the machine.

Figure 6.3 represents a schematic view of the collimation system for the LHC. As illustrated, the next aperture bottleneck after the beam dump protection are the tertiary collimators (TCTs), which were not designed to be hit directly by primary protons. Displacing the orbit at the TCT will reduce the distance between the beam dump envelope and the TCTs and eventually, if the orbit distortion becomes too large, the TCT aperture could drift inside the beam dump envelope which should be avoided. The margin for displacing the beams at the TCT is then set by the aperture difference between the beam dump protection and the TCTs to ensure that they are shadowed by the beam dump protection.

The available margins, summarized Table 6.1 depend on the optics and the collimators settings. In order to include uncertainties from optics, mechanical movements of the collimators or natural orbit drifts one fourth of the full margin was given for local bumps. The IP displacement corresponding to the available margin at the TCT was calculated from a four magnet bump without MCBX shown in Figure 6.2.

The purpose of the tertiary collimators is to protect the triplet from the secondary halo (particles coming from the secondary collimators). An orbit offset at the TCT will also displace the beam halo. In order to

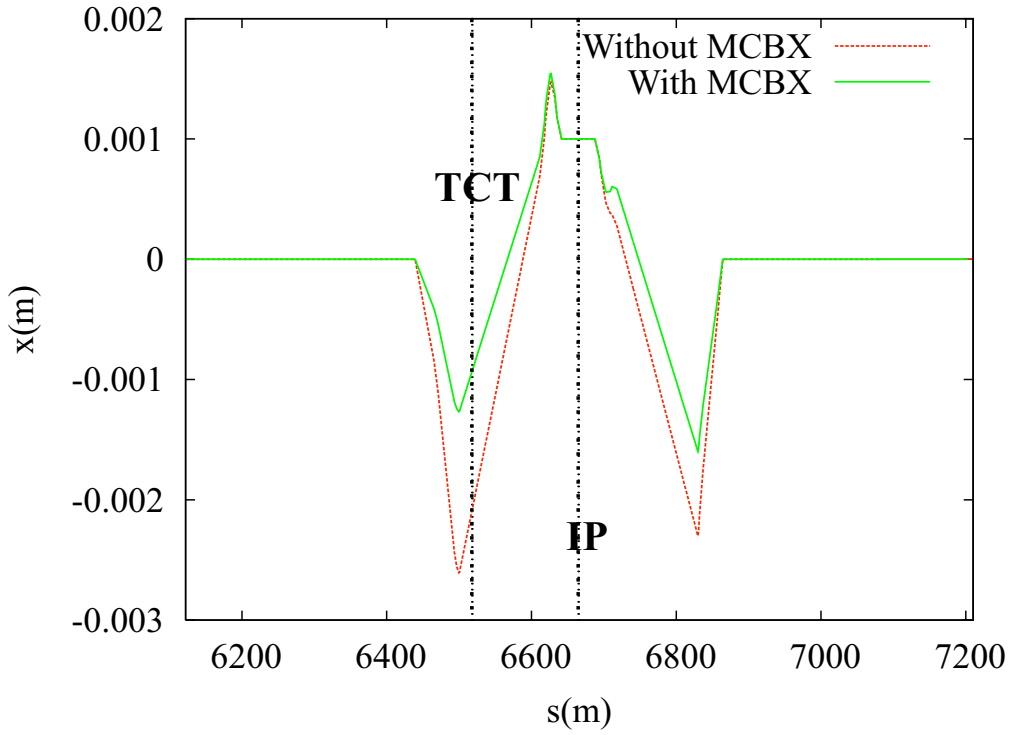

Figure 6.2: Example of closed orbit bumps. The case without MCBX is the one described above, with MCBX is a six magnet bump used for injection which reduces the orbit excursion outside the interaction region. Displacing the beam at the IP also changes the orbit at the tertiary collimator location.

keep the triplets in the shadow of the TCT the displacement should also be smaller than the difference in aperture between the TCTs and the triplets. The requirements for the TCTs to correctly shadow the triplets are:

$$|\Delta x_{\mathrm{TCT}}| < n\sigma_{\mathrm{QX}} - n\sigma_{\mathrm{TCT}} - 1\sigma \tag{6.1}$$

and

$$n1_{\mathrm{min}} < 10.5, \tag{6.2}$$

where Δx_{TCT} is the displacement at the TCT in beam σ, $n\sigma_{\mathrm{QX}}$ and $n\sigma_{\mathrm{TCT}}$ are the available apertures in number of beam σ in the triplets and the TCT respectively. $n1_{\mathrm{min}}$ is the minimum $n1$ over the insertion

Table 6.1: Orbit steering margins for different optics.

	$\beta^* = 11$ m	$\beta^* = 2$ m	$\beta^* = 0.55$ m
Primary	6 σ_{nom}	6 σ_{nom}	6 σ_{nom}
Dump Protection	10.2 σ_{nom}	10.2 σ_{nom}	7.5 σ_{nom}
Tertiary	25 σ_{nom}	12.8 σ_{nom}	8.4 σ_{nom}
Full Margin	14.8 σ_{nom}	2.6 σ_{nom}	0.9 σ_{nom}
Operation Margin	3.7 σ_{nom}	0.7 σ_{nom}	0.2 σ_{nom}
IP displacement	5 σ_{nom}	3.5 σ_{nom}	3.3 σ_{nom}

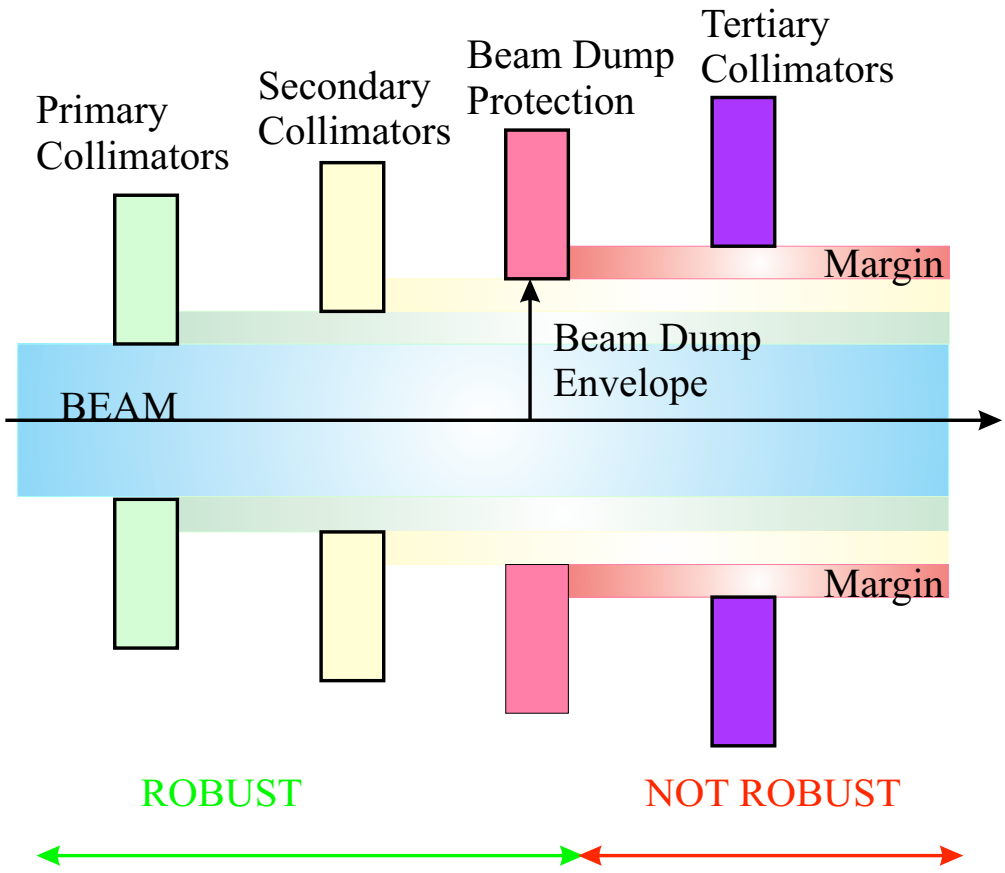

Figure 6.3: Schematic view of the collimation system and hierarchy. In order to ensure safe operation the tertiary collimators have to remain outside the beam dump envelope.

region. $n1$ is the parameter which defines the aperture in MAD-X [50]. The first condition becomes a limitation in the case of squeezed optics when the aperture in the triplets gets smaller. 1σ margin is left for collimator operation. The limitation of $n1_{\text{min}} < 10.5$ is only relevant for the intermediate collimators settings which was used in 2010. The nominal specification is $n1_{\text{min}} < 7$.

Figure 6.4 shows the evolution of the orbit at the TCT and of $n1$ as a function of the bump amplitude for the most constrained case of the 2 m squeezed optics in IP5. The margin available from the difference in aperture between the triplet and the TCTs is of $0.8\,\sigma$ which is larger than the one coming from the dump protection. This margin increases as the β^* gets larger. We can therefore take the limit from the dump protection as our condition for operating the scans safely. As shown in Table 6.1, this margin represents $\pm 3\,\sigma$ around the reference orbit. This is sufficient for luminosity optimization scans for which the interesting region is situated around the peak but not for luminosity calibration where we need to measure the full overlap profile. This range can be doubled by moving the two beams in opposite directions or including the MCBX (common correctors) in the bump as seen Figure 6.2. The MCBX magnets suffer large hysteresis effects as presented in Chapter 2 and are therefore not suited for precision measurements. The strategy adopted for the LHC was to displace the two beams opposite directions using two four magnet bumps.

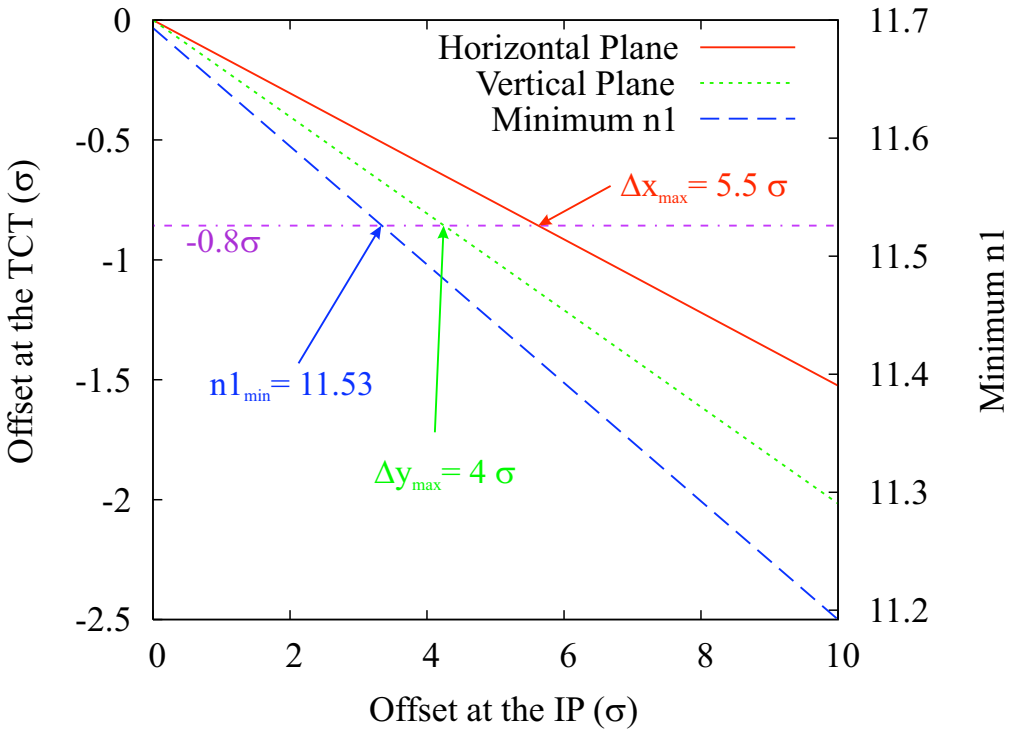

Figure 6.4: Evolution of the displacement at the TCT and $n1_{min}$ as a function of the offset at IP for a bump without MCBX in the case of the 2 m β^* optics at IP5 and for intermediate collimators settings, half gap of 12.8 σ.

6.1.4 Software

As part of this work, a dedicated control software was developed in the framework of the LHC Software Architecture (LSA) [69] allowing the operator to perform separation or angle scans manually or automatically. The main panel of the software is shown in Figure 6.5. Different features are available within the application:

- Monitoring of the relevant devices (BPM, BCT, luminosity monitor, orbit corrector).
- Creation of the separation bumps to be trimmed via LSA or the MADX online model.
- Data exchange with experiments via the Data Interchange Protocol (DIP) [70].
- Online analysis.
- Acquisition of the measurements in a database for offline analysis.
- Fast optimization (peak finder).

This application was developed such that all the tools required to perform and analyze a separation or angle scan are available in the same software.

One of the main challenges that arose while developing the software was the communication in real time and in a synchronous way of the scan progresses, i.e. status of the beams: idle or moving, to the experiments. This is done via DIP and allows the experiments to know exactly when the beams are moving and when they should acquire data. The synchronization is done using a timestamped flag.

Figure 6.6 represents a zoom of a scan step together with the flag value. If we look at the time history from left to right the status starts with the flag equal to TRUE (beams idle) and moves to FALSE when the trim is sent (in practice the status false is sent before the trim in order to ensure the consistency of the

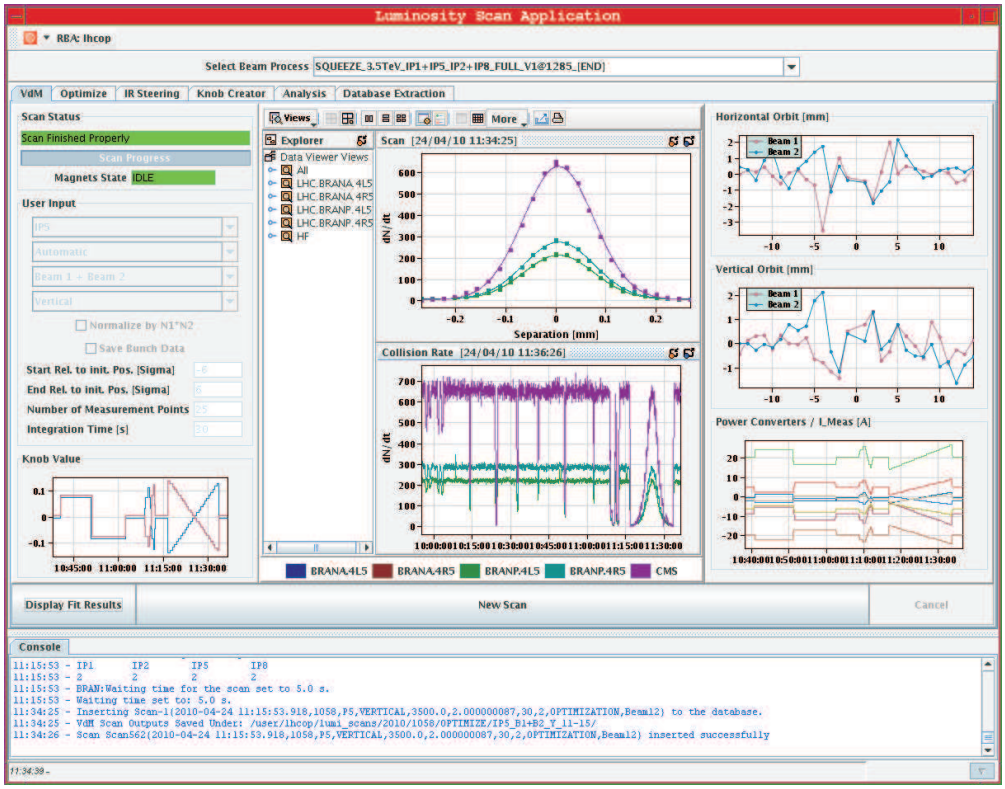

Figure 6.5: Screenshot of the software main panel where the scans can be monitored in real time. Example of a scan in IP5.

information sent over the network). When the beams have finished moving to the next step the status remains FALSE for a certain time Δt. This time is given by the experiments themselves, still over DIP, and represents the time over which the luminosity is integrated for each update of their publications. One second is added to compensate for network delays. This method ensures that both the magnets and the luminosity monitors are stable when the data are declared as valid.

During a scan the rates are recorded together with other relevant quantities such as intensity or BPM data and stored at the end of the scan in a file and in the database for offline analysis. The requirements for the software are described in a technical note [71] and were used as a basis for its implementation. The software is now fully commissioned and operational and used in routine operation as a tool for luminosity optimization. More details on the software architecture and functionalities are presented in Appendix A.

6.2 First Collisions and Optimization

The LHC saw its first proton-proton collisions on the 23rd of November 2009 at an energy of 450 GeV per beam [72]. On the 30th of March 2009 the beams were brought into collision at 3.5 TeV per beam, the highest energy ever reached by a collider.

6.2.1 450 GeV Collisions

At 450 GeV the beam size is about 300 μm. As explained in Chapter 4, each IR is equipped with directional striplines (BPMSW) which give independent measurements for beam 1 and beam 2 with a resolution of

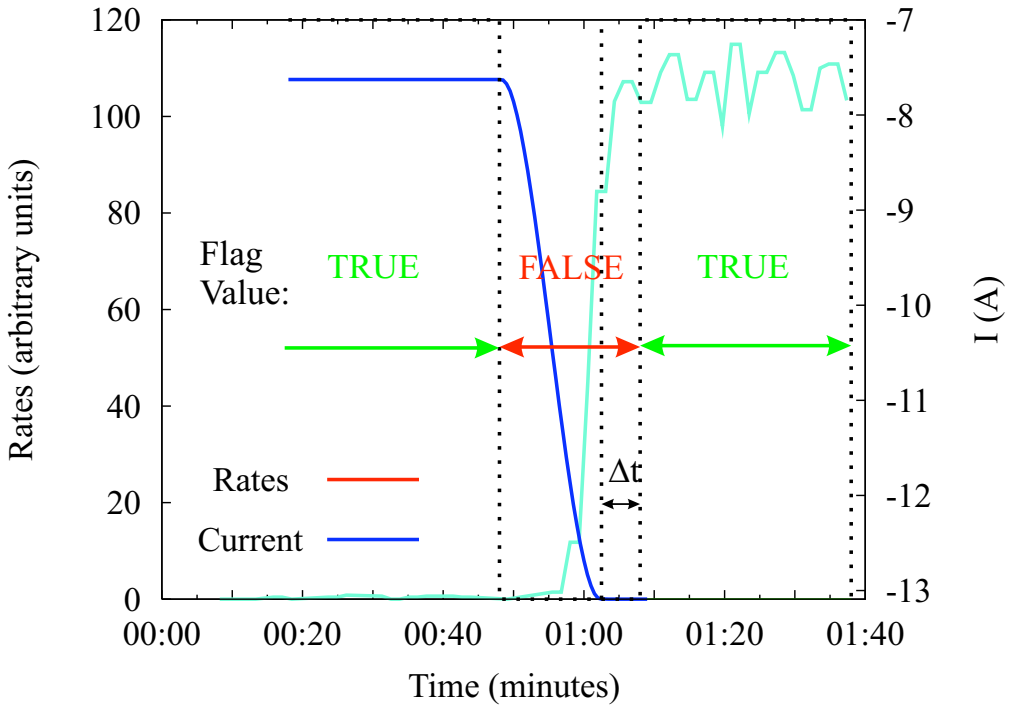

Figure 6.6: Synchronization signals over DIP. The flag is used as trigger by the experiments. When the flag is set to TRUE the beams and luminosity monitors are fully idle.

about 200 μm at low intensity. As the resolution of these BPMs is smaller than the beam size, they were used to optimize the beam positions at the IP and establish the first collisions at 450 GeV.

Table 6.2: Residual separation and IP position measured before the very first collisions in the LHC.

	Separation [mm]		IP Position [mm]	
	Horizontal	Vertical	Horizontal	Vertical
IP1	1.15	1.34	-0.40	0.47
IP2	0.50	1.20	2.40	0.79
IP5	2.35	0.85	-0.40	0.40
IP8	0.30	0.75	0.10	1.05

Table 6.2 summarizes the corrections applied to align the beams and the position of the IP in the transverse planes. Very large offsets of several millimeters had to be corrected for, however at this intensity the beams can hardly damage the machine and it was considered safe to go over the limitations coming from machine protection. The beams were brought together by moving beam 1 and beam 2 towards each other to minimize the offset at the TCT coming from the bump.

6.2.2 Luminosity Optimization at 450 GeV

Mini-scans over a limited range were performed at the four interaction points. Given the very low luminosity (about $1.0 \times 10^{26}\,\mathrm{cm}^{-2}\mathrm{s}^{-1}$) the scans were performed manually stepping through the different separations and waiting for the experiments to collect enough statistics. This was very successful and allowed to signifi-

cantly increase the luminosity in IP5 and IP8. The scans in IP1 and IP2 showed that the beams were already at optimum settings for luminosity.

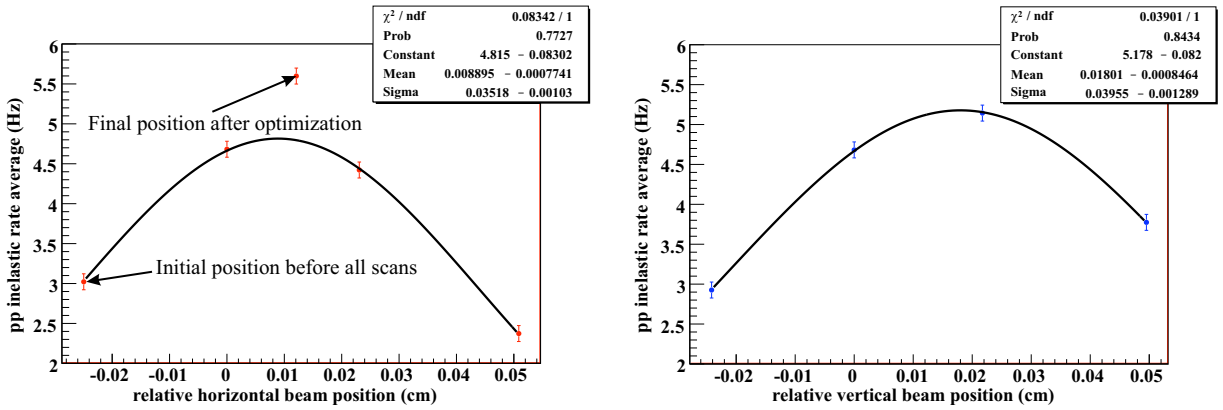

Figure 6.7: Scan done in LHCb in the horizontal (left) and the vertical (right) plane. The rates before and after optimization (left plot) show an improvement of about 80 % [73].

The software interlock system limits the changes in strength in the orbit correctors. At injection energy, the default settings were found to be too tight and had to be manually released to allow for $\pm 1\,\sigma$ scan range. This proved to be a real limitation for the two experiments that required an optimization (IP5 and IP8) and several iterations were necessary to reach the optimum settings. Figure 6.7 shows the summary of all scans in LHCb. As the scan range was limited to $\pm 1\,\sigma$ all scans consisted of three points (moving beam 2 allowed to add a fourth point when necessary) and each scan lasted about 20 minutes due to the very low rates. The 450 GeV run allowed to test the method and software for luminosity optimization which proved to be very useful and safe for machine operation.

6.2.3 3.5 TeV Collisions

The first 3.5 TeV collisions took place on the 30$^{\text{th}}$ of March 2010 [74]. This represented a major event for CERN as it was broadcasted worldwide on television. The set-up for collisions was done the night preceding the media event with longitudinally separated beams in order to avoid any collisions before the press event. At 3.5 TeV the beam size is reduced to about 100 μm, which is smaller than the BPMSWs resolution. As a result alternative methods with respect to the 450 GeV collisions were used to align the beams such that they would collide as soon as the injection separation bumps are removed:

- **IP1 and IP5**: as presented in Chapter 4, are equipped with special BPMs (BPMWF) providing a direct measurement of the separation, and therefore a much better resolution.
- **IP8**: the individual beam positions could be reconstructed by looking at beam-gas events. LHCb provided the corrections to be applied.
- **IP2**: none of these alternative methods could be used and the initial settings were computed using the BPMSW data.

Figure 6.8 illustrates the first collisions at 3.5 TeV recorded by the BRANs in all IPs. The injection separation bumps were ramped down simultaneously at the four interaction points. The collision point was found in all IPs as soon as the separation bumps were ramped down. The step in IP8, after the separation bumps were removed, corresponds to the time when the corrections measured with beam-gas reconstruction

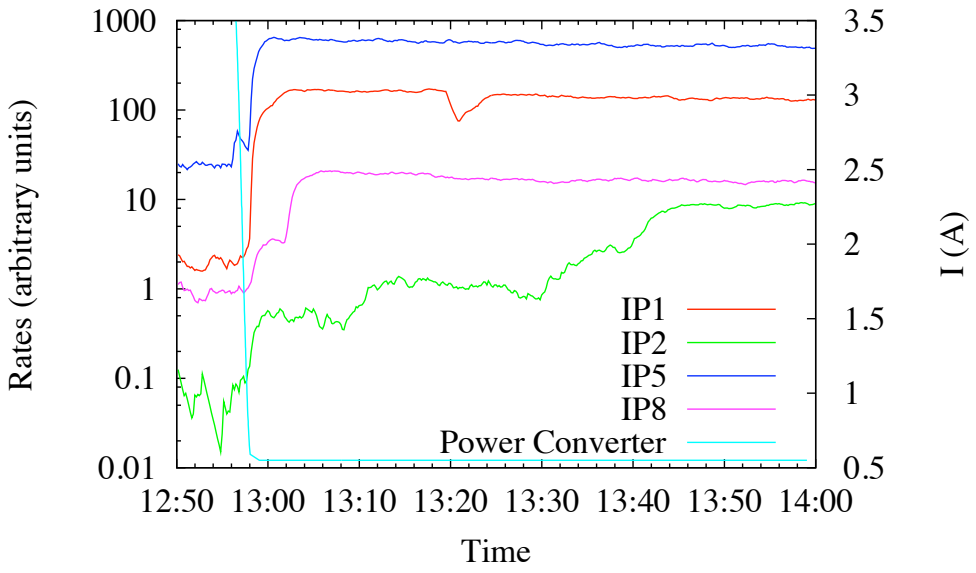

Figure 6.8: First collisions at 3.5 TeV as seen by the BRANs in all IPs. The power converter data illustrates the time when the injection separation bumps were ramped down. The BRAN data shown here are not calibrated which explains the differences between the IPs.

was applied. As expected, the luminosity in IP2 was not optimal from the beginning and was increased by scanning the transverse planes.

6.2.4 Luminosity Optimization at 3.5 TeV

Operating the LHC at 3.5 TeV results in a decrease of the beam size by about a factor 2.8 ($\sigma = \sqrt{\beta \varepsilon_N / \gamma}$) and therefore an increase of the luminosity by about a factor 8 with respect to injection energy. This allowed to use the BRANs signal for optimization and the automated procedure from the software as soon as operation resumed.

Figure 6.9 shows the optimization of all IPs in series during a squeezed optics physics fill with a luminosity of about $5\,10^{27}\mathrm{cm}^{-2}\mathrm{s}^{-1}$. The luminosity was significantly increased in all IPs except for IP1 where no correction was needed. Each scan consisted of 3 steps of 30 s with a range of $\pm 2\sigma$ for a total duration of a few minutes. The overall duration of the full procedure was 45 minutes. At low luminosity, the duration of a scan is constrained by the requirements on the statistical accuracy for each scan step. After each fill the optimum settings are saved and used as the new reference for the next fill. Luminosity optimization using the Van Der Meer scan method is now part of routine operation in the LHC and systematically performed during physics fill.

It is possible to track the orbit stability at the IP by looking at the evolution of the corrections applied to collide beams head-on. At 3.5 TeV, the LHC has mainly been running with three different optics configurations:

- Injection optics, IP1 and IP5 at 11 m β^*, IP2 and IP8 at 10 m β^*

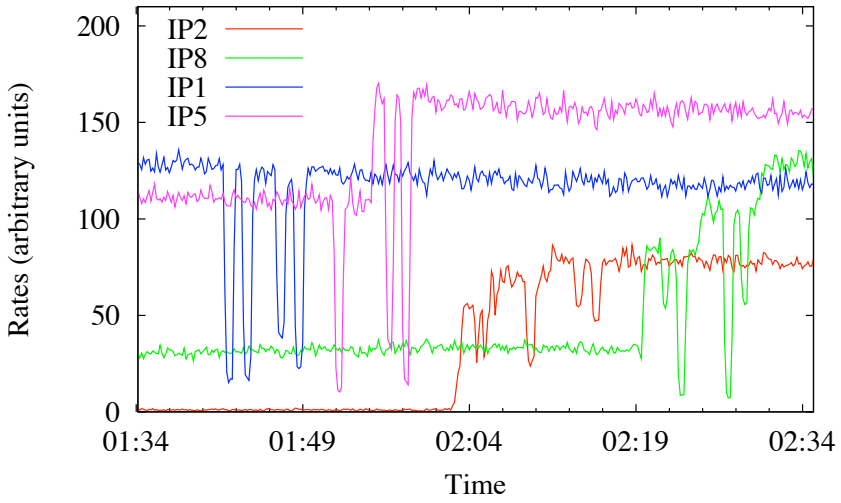

Figure 6.9: Optimization scans performed for squeezed optics in all IPs. The BRAN data shown here are not calibrated which explains the differences between the IPs.

- 2 m squeezed optics for all IPs.
- 3.5 m squeezed optics for all IPs. Crossing angle on, IP2 colliding with an offset.

Figure 6.10 represents the evolution of the corrections applied in all IPs and plane as a function of the fill number. The three cases are shown separately. The orbit at injection optics was stable to about 100 μm ($\approx 1\,\sigma$). Some features are observed such as peaks or sudden changes observed in all IPs. This could be explained by the fact that this was the first extensive physics run for LHC and the procedures for orbit corrections were not clearly defined and introduced artificial changes in the orbit. For the 2 m optics the situation is much more critical due to the complicated process of squeezing the beam and the reduced beam size. The orbit is stable within several 100 μm (several σ). This illustrates the difficulty of squeezing the beams while keeping all other parameters under control. The improvements in the squeeze procedure and experience in running the machine are seen when looking at the 3.5 m optics where the orbit is stable within 100 μm ($\approx 1\,\sigma$). A jump is observed around fill 1232 explained by a change of the reference orbit. The situation seems to stabilize again afterwards where the stability is even improved down to 50 μm. In the case of IP2 horizontal, the situation is a bit more complicated as the beams do not collide head-on and the separation is used to adjust the luminosity to the level desired by ALICE. The slope seen towards the end is therefore not so relevant in terms of stability but could become an issue for machine protection.

The nominal LHC IP beam size is of the order of 16 μm at 7 TeV. The stability range of a 50 μm might become an issue as it represents about 3 σ. More optimization will be required once we move on to smaller beam sizes.

6.2.5 First Experience with High Intensity

At high intensities the beam-beam effects become relevant and can be destructive in the presence of transverse offsets. It is therefore desirable to optimize the luminosity as fast as possible.

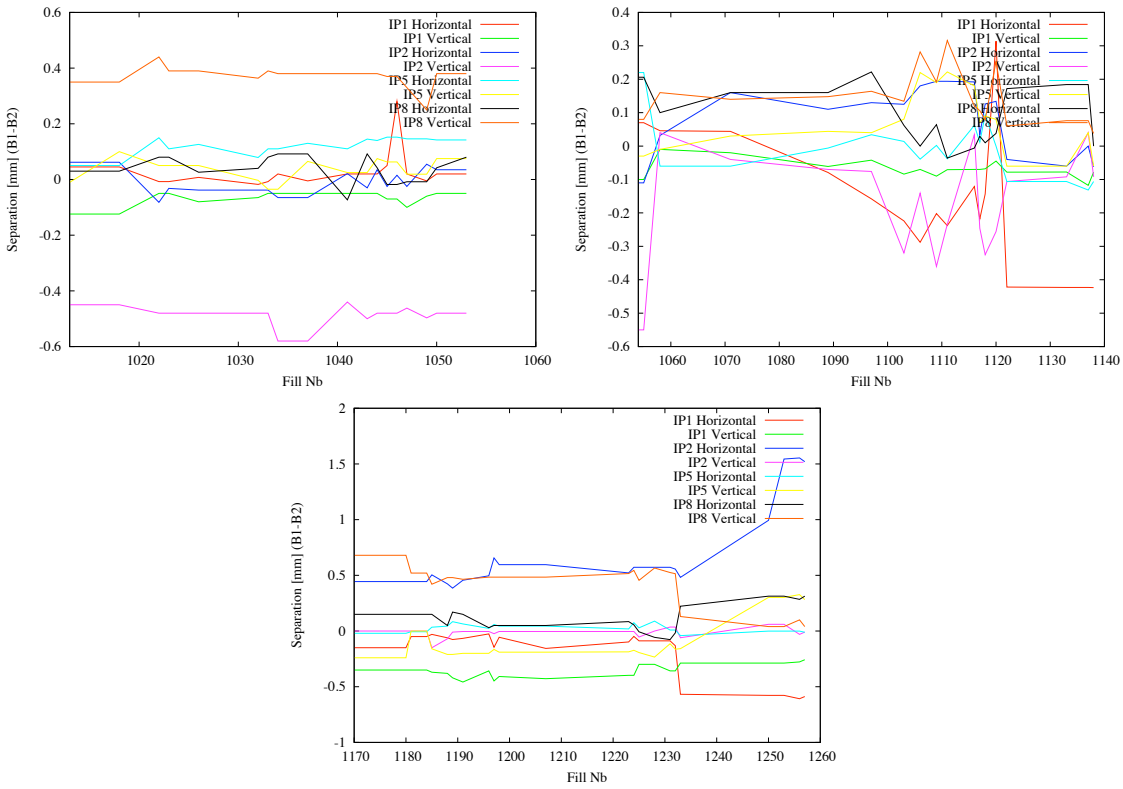

Figure 6.10: Evolution of the IP separation corrections. The top left plot is for injection optics, top right plot for 2 m optics and the bottom plot is for the 3.5 m optics.

Figure 6.11 illustrates the luminosity and intensity at the beginning of a fill with nominal bunch intensity. The intensities shown here are the total beam intensities which consisted of 25 bunches. The beam size measurement in the horizontal plane is very noisy. It still gives indications on possible losses as the vertical plane data seem to be reliable. Slow losses are observed when the beams are brought into collision which stabilize after a certain period as illustrated on the intensity and beam size plots (more for beam 2 vertical). No significant blow up or losses directly related to the scans was observed. The time spent optimizing the luminosity was reduced to 10 minutes for three interaction points with an upgrade of the software.

6.3 Luminosity Calibration

The method and anticipated systematic uncertainties related to the measurement of the absolute luminosity have been presented in Chapter 2 and 4. This section will give a detailed analysis of the first calibration scans performed in the LHC and characterize the uncertainty on the absolute luminosity determination based on experimental results. The results and conclusions reflect my personal view point of an analysis done in collaboration with the experiments. The experiments data will only be used to validate the method and no attempt at calculating the total proton-proton cross section will be made. The data will be quoted in arbitrary units in order to avoid any speculations on the cross section from this analysis. The experiments published results can be found in [75], [76] and [77].

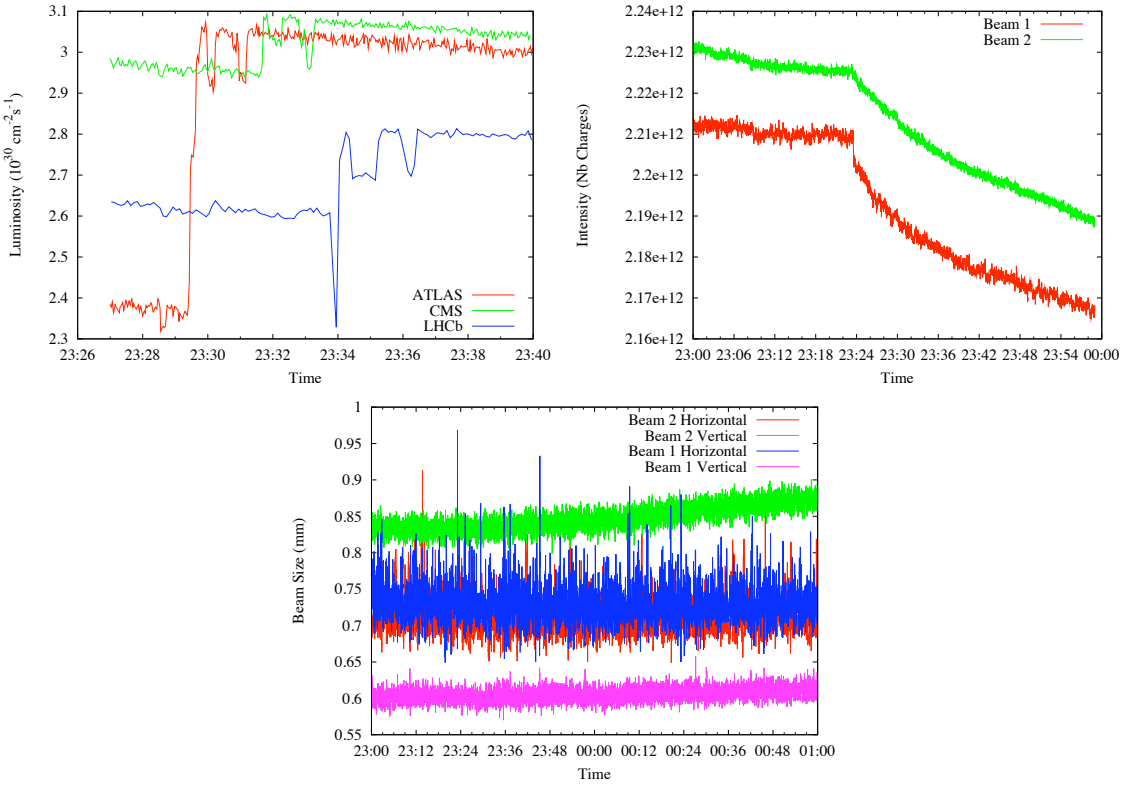

Figure 6.11: Intensity beam sizes (from the synchrotron light monitors) and luminosity at the beginning of a fill with nominal bunch intensity. We can see a change of slope in the intensity and beam size history plots when the beams are brought into collision (23:24). The time spent optimizing the luminosity was reduced to about 10 minutes for three IPs.

6.3.1 Measurements Summary

Calibration scans were performed in all IPs for squeezed optics with $\beta^* = 2\,\text{m}$, the injected intensity per bunch was of the order of 2×10^{10} protons per bunch.

- **IP1**: Two sets of scans performed with the same filling scheme, one bunch crossing. The second set consisted of four scans, two in the horizontal plane and two in the vertical plane in order to check for consistency.
- **IP2**: One set of scans with one bunch crossing.
- **IP5**: Two sets of scans performed with different filling scheme. The first set was done with two bunch crossings and the second set with one bunch crossing. The second set consisted of four scans, two in the horizontal plane and two in the vertical plane in order to check for consistency.
- **IP8**: Two sets of scans performed within the same fill with one bunch crossing. The first scan was performed moving the two beams opposite directions and the second one moving only one beam over a limited range.

Except for the second set in IP8, all the scans consisted of 25 steps of 30 s acquired by moving the two beams in opposite directions. To be noted that the second set of scans in IP1 and IP5 were done during the

same fill. The same bunches collide in IP1 and IP5 which should therefore have the same luminosity. IP2 and IP8 have a large internal crossing angle due to their experimental dipole spectrometer, as shown Chapter 2. This should not affect the measurements precision.

Table 6.3: Nominal beam parameters during the calibration scans.

Energy [GeV]	3500
β^* [m]	2.0
Intensity [10^{10} p/bunch]	2.0
Number of bunch crossing	1-2
Emittance [μm]	3.75
$\sigma_{x,y}$ [μm]	45
Crossing angle [μrad]	0.0 / 150 / 500
β^*/σ_s	26
Beam-Beam Parameter	0.0006
$\mathcal{L}$ per bunch [10^{28}cm^{-2}s^{-1}]	1.76
Events per bunch crossing	0.113

Table 6.3 lists the nominal beam parameters during the calibration scans. The crossing angles of 150 μrad and 500 μrad represent the internal crossing angles for IP2 (vertical) and IP8 (horizontal) respectively. The luminosity per bunch, beam-beam parameter and the number of events per bunch crossing do not take into account the effect of the crossing angle. The beam-beam and hourglass effects are very small and can be neglected.

6.3.2 Beam Profile and Fit Method

Similarly to the RHIC data, non Gaussian tails were systematically observed for all scans which could be fitted with a double Gauss as shown Figure 6.12. We will then recall the expression for the effective beam size presented Chapter 2, in this case:

$$\mathcal{L}_0 = \frac{N_1 N_2 f N_b}{2\pi \sigma_{x\text{eff}} \sigma_{y\text{eff}}}, \tag{6.3}$$

with

$$\sigma_{u\text{eff}} = \frac{A_{au}\sigma_{au} + A_{bu}\sigma_{bu}}{A_{au} + A_{bu}}. \tag{6.4}$$

Since the amplitudes and sizes are highly correlated, we built a fit function in order to get the effective beam size and total amplitude directly from the fit results such that all the correlations are correctly included in the statistical error derived by the fit:

$$F_u(\delta u) = C + A_{au} \exp\left[-\frac{(\delta u - \delta u_0)^2}{2\sigma_{au}^2}\right] + (A_{\text{tot}} - A_{au}) \exp\left[-\frac{(\delta u - \delta u_0)^2}{2\sigma_{bu}^2}\right], \tag{6.5}$$

where

$$\sigma_{bu} = \frac{\sigma_{\text{eff}u} A_{\text{tot}} - A_{au}\sigma_1}{A_{\text{tot}} - A_{au}}, \tag{6.6}$$

where C is a constant to model eventual background or noise, added only if necessary, and A_{tot} is the total amplitude. The constant component has to be removed when calculating the effective beam size, as it is the case in this formulation.

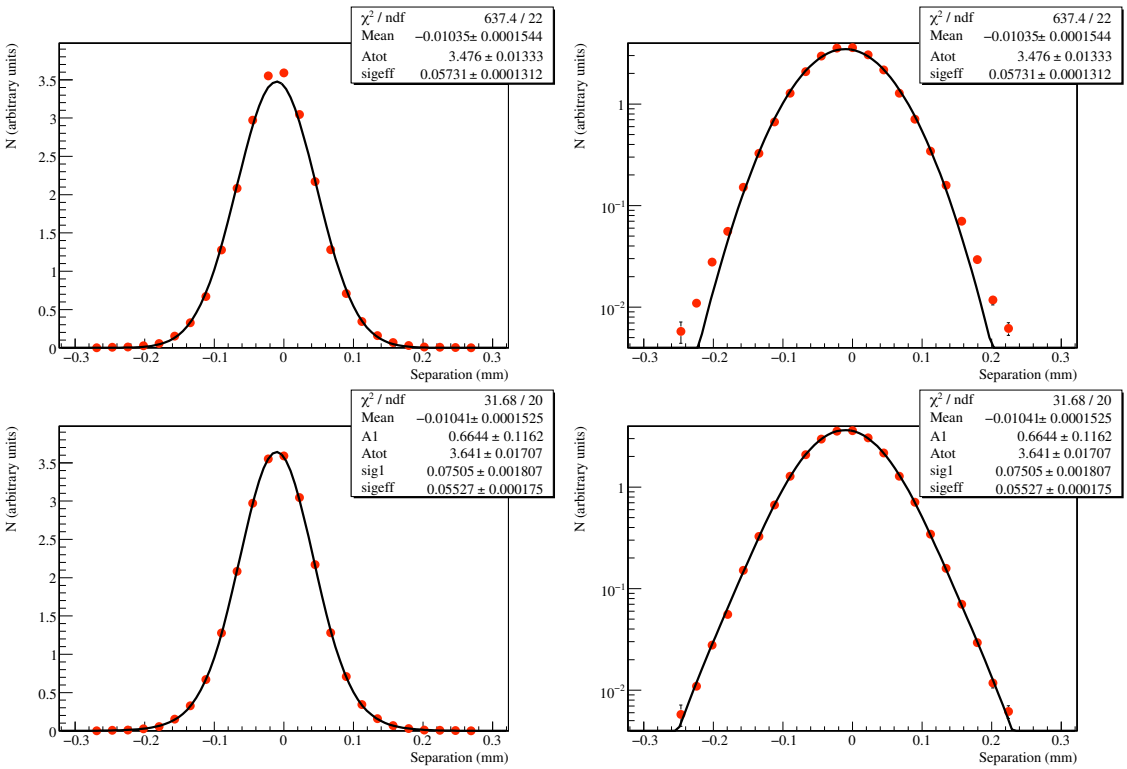

Figure 6.12: Example of a scan performed in CMS in the horizontal plane. A pure Gaussian fit is represented on the top plots and a double Gaussian fit on the bottom ones. Looking at the logarithmic scale plots it is clear that non-Gaussian tails are present and that the double Gaussian fit is more suited for this profile.

In addition to the LHC BRAN, ATLAS provided numerous luminosity signals based on different monitors and algorithms [75] during the calibration scans in IP1. Figure 6.13 displays the effective beam sizes derived from the different signals and shows an excellent consistency from one monitor to the other.

6.3.3 Hysteresis Effects

As shown in Chapter 3, hysteresis effects should in principle be negligible if we restrict ourselves to the MCBC and MCBY magnets to separate the beams and if the scan is performed always in the same direction such that no jump between one hysteresis branch to the other happens during a scan. To validate this and measure the effects of the hysteresis on the effective beam size measurement, consecutive scans were also performed in opposite directions, i.e. on different hysteresis branches. The effect of the hysteresis can then be estimated by the shift of the distribution. This measurement was done for IP1 and IP5. The magnets are the same in the other IPs and we therefore expect effects of the same order of magnitude.

Figure 6.14 shows the example of IP5 in the horizontal plane and IP1 in the vertical plane. An excellent agreement between the forward and backward scans is observed. Table 6.4 summarizes the comparison of the backward and forward scans in IP1 and IP5. The largest shift of the distribution is of the order of 2 μm which corresponds to 0.045 nominal σ. This represents a loss in luminosity at the 0.1 % level. The largest difference in the effective beam size is of the order of 1 % which is comparable to the emittance increase as will be shown in Section 6.3.7. These results confirm the expectations from simulations: the hysteresis has no impact on the beam size measurement and can be considered negligible.

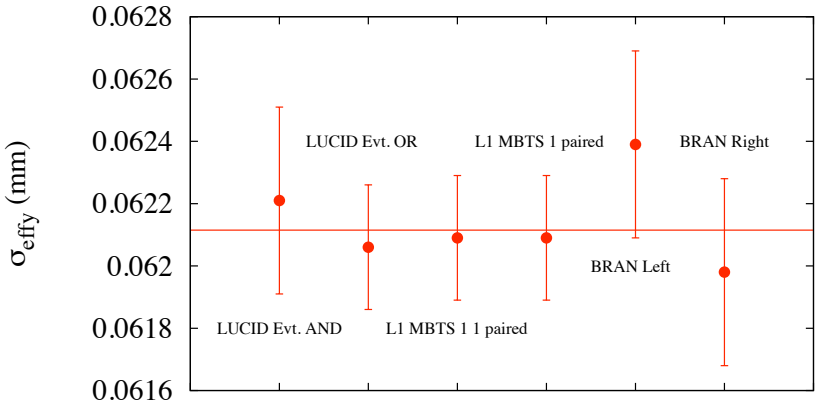

Figure 6.13: Effective beam size derived from different luminosity monitors and algorithm in IP1 [75]. The error bars shown here are the statistical errors derived from the fit.

Table 6.4: Hysteresis checks results in IP1 and IP5.

	Δx_{mean} (mm)	Δy_{mean} (mm)	$\Delta\sigma_x/\sigma_x$	$\Delta\sigma_y/\sigma_y$
IP1	0.002	0.002	0.004	0.006
IP5	0.001	0.002	0.004	0.010

6.3.4 Bump Calibration and Linearity

The absolute knowledge of the beam displacement is essential for the effective beam size measurement as an error on the scale would directly apply to the beam size. As shown in Chapter 3, the closed orbit bumps used to displace the beams at the IP are in principle very well closed. To make sure that the beam displacement was fully understood during the scans a dedicated calibration measurement was performed in all IPs. The method used was to displace both beams in the same direction to move to whole IP transversally. At each scan point the vertex centroid position is provided by the experiements. In addition, the rates were carefully monitored to ensure that the beams remained aligned during the whole procedure. For perfect calibration we would expect the slope of the scatter plot of the bump value versus the vertex position to be equal to 1.

Figure 6.15 illustrates this measurement as performed in IP5. As expected from simulations and measurements presented in Chapter 3, the bump value is in excellent agreement with the vertex position as measured by the experiment. Table 6.5 summarizes the results for IP1, IP2 and IP5. The slopes are consistent with 1 in all IPs and planes, with a resolution of 1 % in the worst case of IP2. At IP8, the bump calibration was done during the scan when only one beam was moved by comparing the bump values with the vertex displacement measurement by the LHCb vertex locator. The results agreed within 1.5 % [78].

Table 6.5: Bump calibration measurements in IP1, IP5 and IP2.

	Horizontal Slope	Vertical Slope
IP1	1.001±0.003	1.001±0.004
IP5	1.000±0.006	0.998±0.006
IP2	0.987±0.009	0.991±0.01

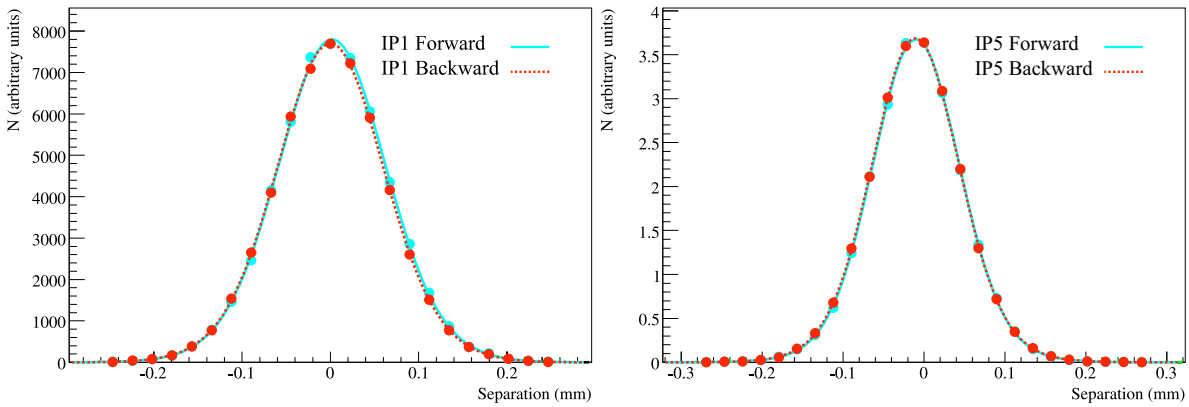

Figure 6.14: Vertical and horizontal scans performed in IP1 and IP5 respectively in opposite directions. An excellent agreement between the forward and backward scans is observed. A comparison between the fit results is shown in Table 6.4.

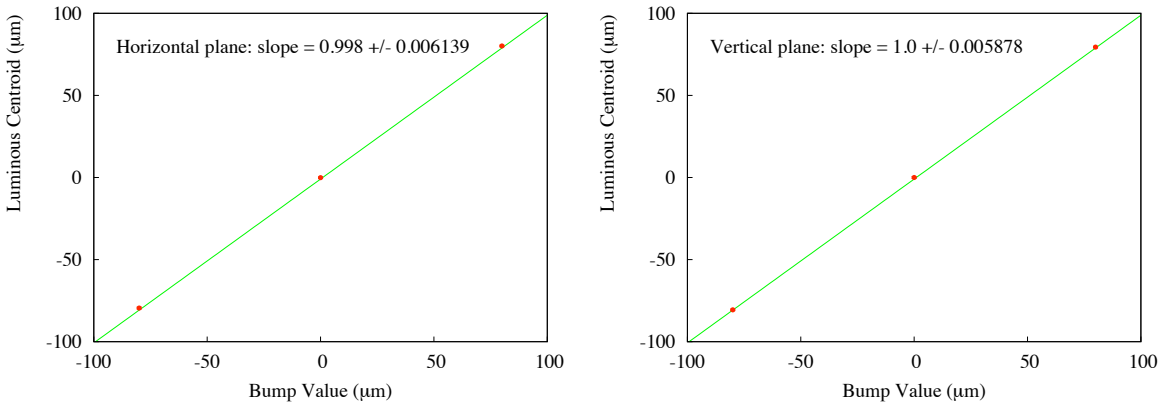

Figure 6.15: Bump calibration measurement done in IP5. Each scan consists of three acquisition points at -100 μm, 0 μm and +100 μm. The bump value is in excellent agreement with the vertex position.

These measurements were performed at low intensity. The time required for the experiments to reconstruct the vertex position was of the order of 5 minutes per point. This explains why the scans were limited to 3 points per plane. It would be good in the future to repeat this measurement with more points to allow for study of the non-linearities.

During the scans the beam positions are also measured with BPMs located in Q1. As a check for linearity, it is possible to look at the correlation of the IP beam position measured by the BPMs and the one calculated from the bump value. Monitoring the displacements in the plane that is not scanned also provides information on coupling.

Figure 6.16 displays the BPM measurements as a function of the bump value. As the scans are performed moving both beams opposite direction we can see a clear slope for the scanned plane for both beams. The orbit in the other plane remains constant in all cases except for IP8. The correlation between the bump value (twice as large as the displacement of one beam, see Table 6.6) and the displacement in the other plane in IP8 is 0.017$\pm$0.004 for beam 2 and -0.017$\pm$0.003 for beam 1. The LHC consists of two separate rings which have therefore different optics errors and coupling properties. Having exactly the same correlation

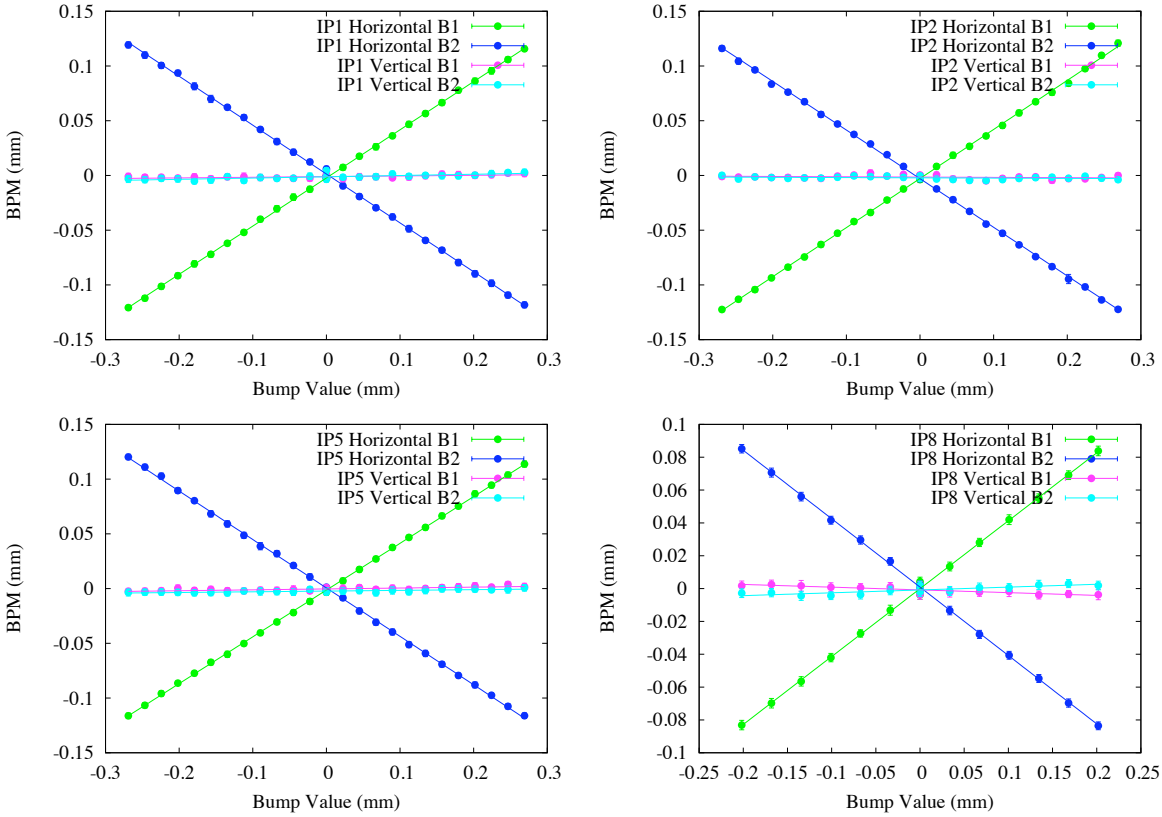

Figure 6.16: IP orbit evolution for beam 1 and beam 2 in both planes as a function of the bump value in all IPs for horizontal scans. The behaviour of the orbit as a function of the bump value is fully linear, no significant coupling is observed except for IP8.

coefficient for beam 1 and beam 2 is therefore very unlikely. The source of the correlation in IP8 is therefore most likely artificial. The BPMSWs located in Q1 is seen by both beams at the same time. A tilt or a drift of one of these monitors could therefore induce such an effect. For each scan, an acquisition at zero separation is taken at the beginning and at the end. These two data points should be equal if there was no drift in the BPM readings. For the example illustrated in Figure 6.16, the maximum drift is of the order of 8 μm over the duration of a scan in the case of IP8 beam 1 and of the order of a few μm for beam 2 and in the other IPs. This drift was later identified as temperature effects observed in all IRs which resulted in large drifts of the BPM readings. The exact source of this correlation in IP8 was not clearly identified, and would require a more detailed analysis. This displacement measuremed by the BPMs is of a few μm for the maximum bump amplitude. This has very little effect on the luminosity (< 0.1 %) and is not anticipated to be an issue if it turns out to be real.

Table 6.6: Slope given by the linear fit of the BPM data versus the bump value.

	Horizontal Beam 1	Horizontal Beam 2	Vertical Beam 1	Vertical Beam 2
IP1	0.44	-0.45	0.44	-0.42
IP2	0.45	-0.44	0.43	-0.43
IP5	0.43	-0.44	0.41	-0.43
IP8	0.41	-0.41	0.40	-0.44

Table 6.6 summarizes the correlation between the beam displacements and the bump values. As the beams are moved in opposite direction these coefficients should be equal to 0.5 for beam 1 and -0.5 for beam 2. It is seen that the BPM calibration factor was systematically underestimated by 10 to 20 %. Evidence of miscalibration and drift of the readings were observed for all BPMSWs. We therefore concluded that these data were not good enough for the purpose of the calibration scans and relied on the bump calibration with the vertex measurement to characterize the beam displacement. The linearity of the BPM response over the duration of a scan should not be affected either by slow drifts or wrong calibration factor. We can still conclude from these measurements that the orbit changes linearly with respect to the bump value.

As a result of the study, a conservative systematic uncertainty of 2 % was assigned to the knowledge of the beam displacement. This uncertainty could be reduced by performing a more detailed cross calibration using vertex data.

6.3.5 Crossing Angle Measurements

The crossing angle is measured by the BPMs situated in Q1 as presented in Chapter 3. At low intensity these BPMs have a resolution of 200 μm. During the fills when the scans were performed temperature effects resulted in drifts with an amplitude of about $\pm$150 μm. Taking into account these two contributions by adding them linearly we get an uncertainty of about 30 μrad on the crossing angle knowledge.

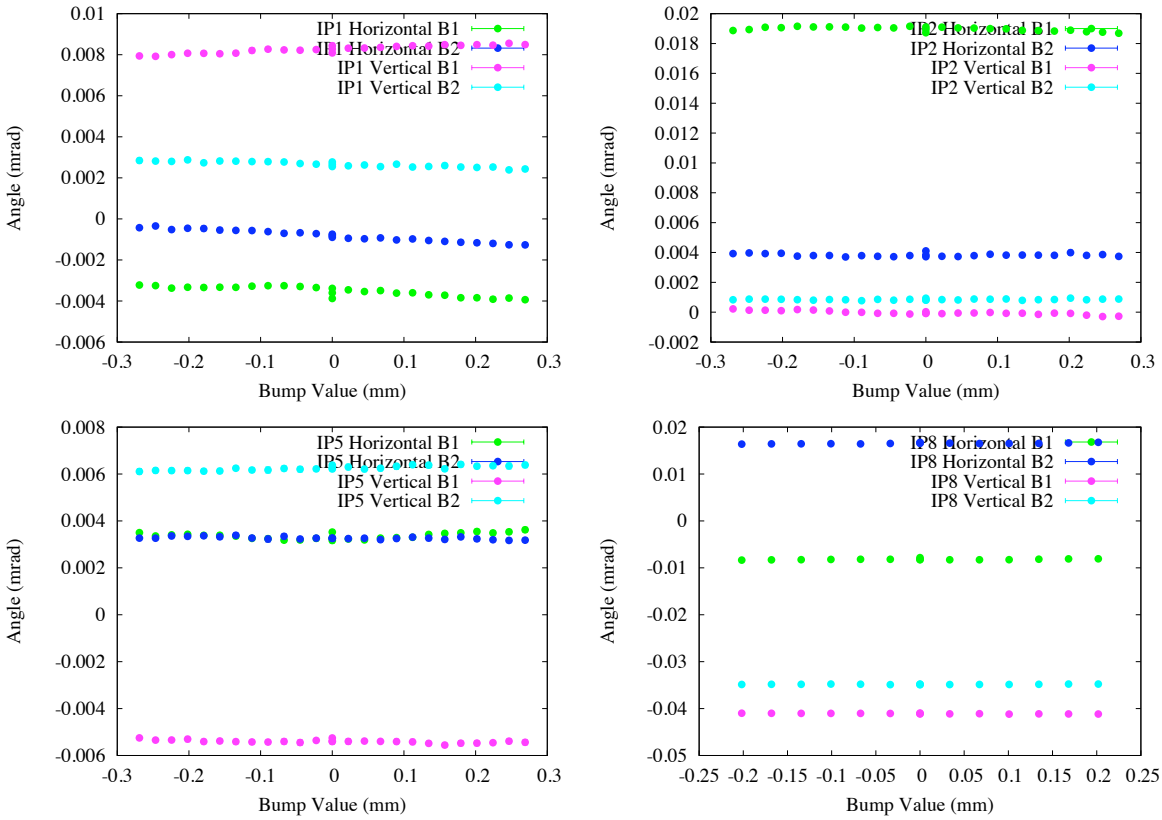

Figure 6.17: IP angle evolution for beam 1 and beam 2 in both planes as a function of the bump value in all IPs for horizontal scans. The variations of the angle over the duration of a scan are of the order of 1 μrad.

Figure 6.17 shows the evolution of the angles during the scans in all IPs. We can see that the angle remains constant within 1 μrad over the duration of a scan. The angles measured in IP2 and IP8 do not

include the internal crossing angle. The crossing angle is derived from the difference between beam 1 and beam 2. Using the derivation of the error due to the crossing angle presented in Chapter 2, we can estimate the uncertainty on the luminosity calibration from the uncertainty in the knowledge of the crossing angle as summarized Table 6.7. The error on the uncertainty was calculated from the BPM resolution. As expected from the results shown in Chapter 2, the uncertainty from the crossing angle is negligible for all scans.

Table 6.7: Crossing angle knowledge (absolute value) and the uncertainty derived on the luminosity calibration. In the case of IP2 and IP8 the nominal values of the internal crossing angle were added, 150 μrad in the vertical plane and 500 μrad in the horizontal plane respectively. The uncertainty on the crossing angle measurement is $\pm 30\,\mu$rad in all cases.

	Fill Number	Horizontal [μrad]	Vertical [μrad]	$(S_x S_y - S)/S$
IP1	1059	4	5	0.0±4e-7
	1089	6	45	0.0±2e-6
IP2	1090	15	151	0.0±2e-5
IP5	1058	0	12	0.0±4e-7
	1089	50	0	0.0±2e-6
IP8	1059	507	56	2e-4±3e-4

6.3.6 Coupling

The tilt angle can de derived from coupling and optics measurements presented in [49] and [79]. A convenient way to quantify the coupling is to determine the normalized coupling matrix $\bar{C}$. The tilt angle of the overlap area and the corresponding uncertainty on the absolute luminosity measurement is then determined by $\bar{C}$, the emittance and the β-function as shown in Appendix B and Chapter 2.

Table 6.8: Tilt angle of the overlap area and associated uncertainty on the absolute luminosity.

	Fill Number	Φ	Uncertainty [%]
IP1	1059	1°	0.0
	1089	17°	0.2
IP2	1090	22°	0.6
IP5	1058	−2°	0.0
	1089	−37°	0.2
IP8	1059	28°	0.1

Table 6.8 summarizes the tilt angles of the overlap area and the resulting uncertainty on the absolute luminosity during the scans. The uncertainty is below 1 % in all case which is negligible with respect to the other systematic uncertainties. These uncertainties on the $\bar{C}$-matrix, the emittance and the β-functions are of the order of 10 %. The tilt angles are therefore subject to very large errors. This table is only intented to show that even with very large tilt angles the uncertainty on the absolute luminosity measurement due to linear coupling is very small with respect to other sources of uncertainty and can be neglected for the first calibration scans in the LHC. It is foreseen to perform scans with at an angle of 45° in addition to the horizontal and vertical ones to confirm these estimates.

6.3.7 Emittance

A change of emittance during the calibration scans would directly affect the effective beam size measurement. In case the changes are large they should be quantified and used to correct the model or included in

the systematic uncertainty. In the case of LHC, the beam conditions at low intensity are relatively stable and the emittance is not foreseen to significantly grow over the duration of a scan. Wire scanner measurements of the transverse emittances were performed before and after each scan during the measurement session of the fill 1089 (IP1 and IP5).

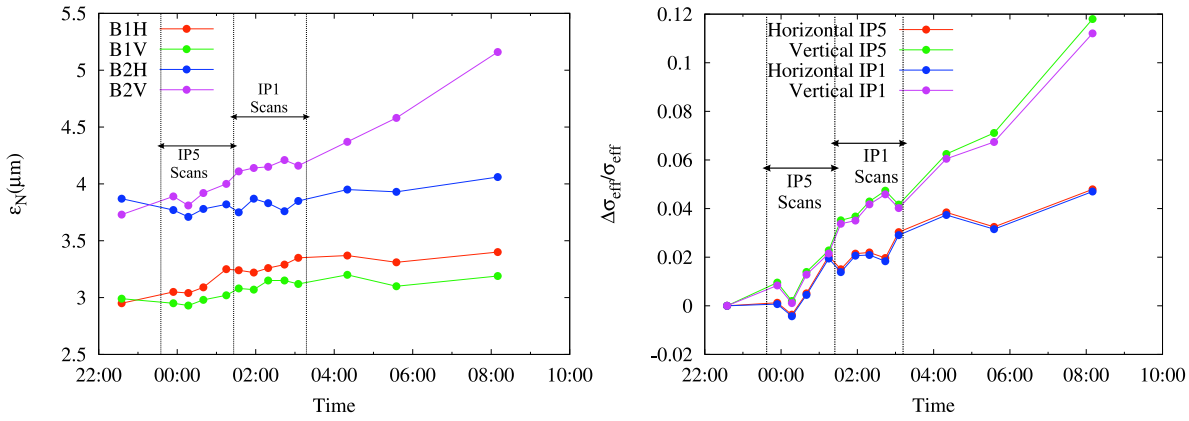

Figure 6.18: Evolution of normalized emittance measured by the wire scanners (left) and the computed effective beam size assuming Gaussian beams during the scans. The difference in effective beam sizes between IP1 and IP5 is explained by the difference of β^*.

Figure 6.18 shows the evolution of the measured normalized emittance and the computed effective beam sizes during the fill 1089. From this measurement we can deduce an emittance increase of 1 % in the worst case of IP5 vertical and significantly lower for all other scans. This confirms the measurements shown in Table 6.4 where the largest difference between two consecutive scans was observed in IP5 vertical at the level of 1 %. The error in the horizontal and vertical plane are combined to compute a systematic uncertainty due to emittance growth during the scans of 1-2 %.

Figure 6.19 shows the evolution of the rates at zero separation in both planes during the scans. Each point consists of a scan data point taken at the beginning, middle or end of a scan. This illustrates the luminosity decay during the scan session in IP5. The dependence is approximately linear on the timescale of the scans. A decrease of 4 % is observed over the duration of the measurements which is consistent with the emittance blow-up displayed in Figure 6.18.

6.3.8 Intensity Measurements

The luminosity is proportional to the product of the intensities of beam 1 and beam 2. Any uncertainty affecting the measurement will therefore directly apply to the absolute luminosity. A special effort was made to improve the accuracy of the measurements for the fills 1058, 1059, 1089 and 1090 where the calibration scans took place. The strategy adopted to correct the bunch-by-bunch intensity measurements by the FBCT can be summarized as follows [80]:

- The FBCT acquisition system consists of windows of 25 ns centered on the circulating bunches. The acquisition timing system should therefore be well synchronized to the revolution frequency such that the total number of charges contained in the bunch is located within a single window. Any timing error would therefore result in a small portion of the bunch intensity appearing in the following or preceding window (not both). This is an instrumental effect and was corrected for by adding to the initially filled bucket the charges present in the neighboring one.

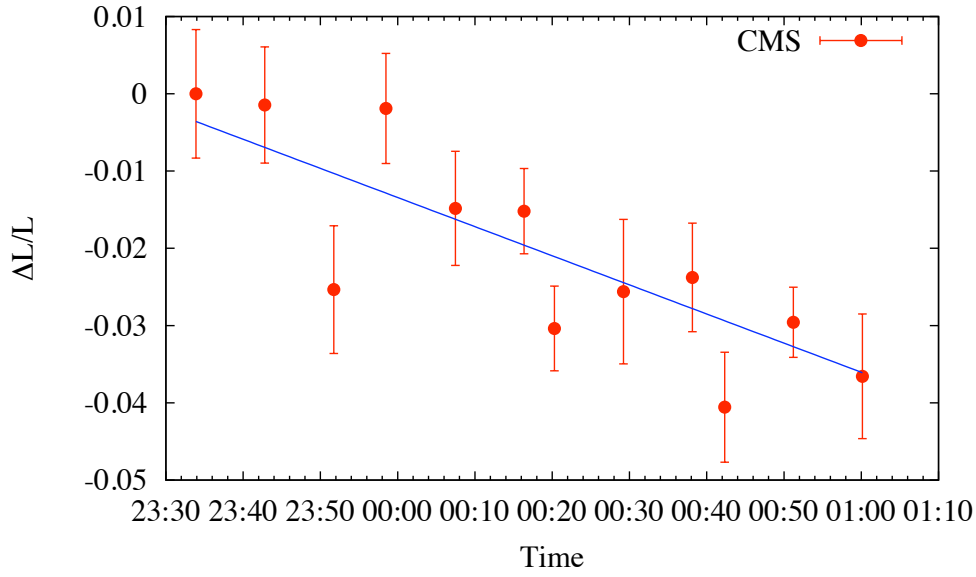

Figure 6.19: Evolution of the rates at zero separation in both planes during the CMS scans.

- The DCCT which measures the total beam intensity is by design easier to calibrate and the absolute value measured by this instrument is in principle more precise than the one measured by the FBCT. At low intensity the signal from the DCCT is subject to high noise level which can be reduced by averaging over time. A cross calibration of the sum of the bunch intensities from the FBCT and the total beam intensity from the DCCT at the end of the ramp, where no unbunched component is present, provides a good calibration of the absolute bunch intensities.

This rescaling of the FBCT data was applied for all scans and resulted in a difference of about 10 % with respect to the raw data.

As mentioned above, the FBCT has an acquisition window of 25 ns, which represents 10 RF buckets. In case of injection mismatch or satellite bunches present in the injectors, particles can be captured in the buckets neighboring the target and would not participate to the luminosity. To characterize the amount of particles present in the buckets surrounding the injected ones, experiments looked at satellite collisions situated at 37.5 cm left or right of the IP. Analysis of the longitudinal vertex distribution showed that less than 0.5 % [81] of the beam was present in the neighboring buckets, which is considered negligible with respect to other sources of uncertainty.

The uncertainty on the rescaled FBCT data is therefore dominated by the ones originating from the DCCT measurement used as a reference for cross calibration. Laboratory measurements show that the DCCT calibration is accurate to better than 2 %. The DCCT suffers from slow drifts that depend on the beam intensity and the temperature. These effects are not yet fully understood and are under study within a dedicated working group [82]. As a result from a general consensus between the instruments experts and representative from the experiments a 10 % uncertainty was assigned to the product of the beam intensities in order to include all these effects.

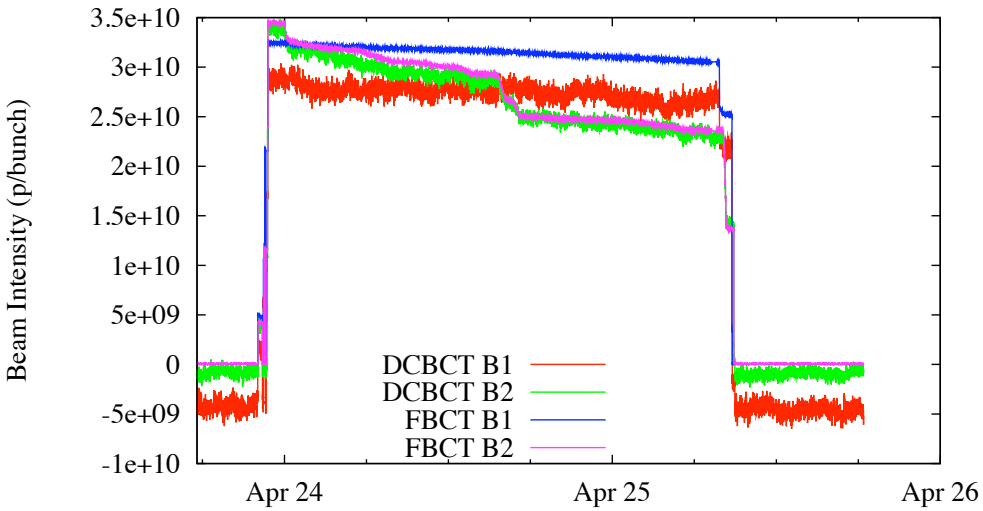

Figure 6.20: BCTs time history plot for the fill 1058 comparing the two systems. The DCCT shows high noise level, which is expected from low intensity and a negative offset that can be corrected for. A small drift can also be observed by comparing the signal before injection and after the dump. The two systems seems to agree on the relative scale.

Figure 6.20 illustrates the intensity measurement acquired during the fill 1058. All the effects mentioned above can be observed in this plot. It is also seen that over the duration of a calibration scan the variations in intensity are at the level of 0.1 %. These variations are very small and no correction was applied to the scan data to compensate for these variations in order to avoid any additional fluctuations.

6.3.9 Comparison with Optics Measurements

The IP beam sizes can be derived from emittance and β^* measurements using Equation 3.4. A comparison with the beam sizes obtained with the Van Der Meer scans can therefore be a useful cross check. The optics measurements were presented in detail in [49] and the emittance was measured with the wire scanner. A detailed set of emittance measurements is available only for the fill 1089 as presented in Section 6.3.7, I will therefore concentrate on this fill where scans were done at IP1 and IP5. The emittance was determined by taking the average value of the measurements before and after the scan.

Table 6.9: Comparison of the effective beam sizes derived from the Van Der Meer method and optics measurements. The two rows for each IP represent the first and the second scan performed in each plane. The errors quoted represent the statistical uncertainty.

	Horizontal Plane [mm]		Vertical Plane [mm]	
	Scan Method	Optics	Scan Method	Optics
IP1	0.0585±0.0002	0.0610±0.0098	0.0622±0.0003	0.0641±0.0038
	0.0587±0.0003	0.0613±0.0098	0.0619±0.0003	0.0640±0.0038
IP5	0.0551±0.0002	0.0604±0.0078	0.0593±0.0002	0.0595±0.0130
	0.0553±0.0002	0.0603±0.0078	0.0598±0.0002	0.0601±0.0132

Table 6.9 shows the comparison between optics measurements and the Van Der Meer method. The large error bars on the beam sizes derived from optics measurements come from the uncertainty on the β^*. Even if the optics measurements seem to over-estimate the beam size the results are consistent within error bars. The differences could come from the fact that the effective beam size calculation from optics and emittance measurements are done using the equation for a Gaussian beam, in addition it was shown that the wire scanner suffered gain issues which resulted in an over-estimation of the emittance. On the relative scale the results are comparable. The same bunches collide in IP1 and IP5. As an additional check we can compare the ratios of the effective overlap areas of IP1 and IP5 measured with the scans and derived from emittance and β^* measurements. We found that they only differ by 1 %.

6.3.10 Fill to Fill Consistency

The luminosity $\mathcal{L}$ for any given process can be expressed as a function of the cross section σ and the event rate $\dot{N}$ as presented in Chapter 1:

$$\mathcal{L} = \frac{\dot{N}}{\sigma}. \tag{6.7}$$

The cross section of a physics process does not depend on the beam conditions. Comparing the scale factors obtained with calibration scans done during different fills, i.e. beam conditions, would therefore give indications on the reproducibility and consistency of the method. Calibration scans were performed with different beam conditions for IP1 and IP5 and differed by 4.8 % (in the worst case) and 5 % respectively as presented in [75] and [76]. This is well within the 10 % uncertainty on the beam intensity measurement. More scans and higher statistics under different conditions will be useful to improve the analysis and provide a better understanding.

6.3.11 Conclusions and Outlook for Future Measurements

Calibration scans were successfully done at the four interaction points. The main sources of systematic uncertainty were identified and characterized based on experimental data.

Table 6.10: List of the relevant uncertainties for the calibration scans.

Source	Systematic uncertainty
Beam Intensities	10 %
Bump Calibration	2 %
Emittance	1-2 %
Fit Error	1 %
Total	11 %

Table 6.10 lists the systematic uncertainties applying to the absolute luminosity determination. The overall uncertainty of 11 % is dominated by the measurement of the beam intensities. Studies are ongoing to further improve the understanding of the intensity measurements and reduce this uncertainty.

For future absolute luminosity measurements one could think of possible improvements in order to reduce the uncertainty:

- **Higher intensities**: would improve the resolution of the DCCT and therefore reduce the uncertainty on the bunch intensity. The few optimization scans with nominal bunch intensities, Section 6.2.5, seem to indicate that the beam-beam effects should not cause any significant blow-up during the scans as was predicted by the experience at RHIC and simulation presented in Chapter 3. Scanning at an

intermediate bunch intensity ($\approx 4 \times 10^{10}$ p/bunch) could therefore significantly reduce the error from intensity while keeping other sources such as beam-beam or pile-up relatively small.

- **Reduce the duration**: increasing the intensity would allow at the same time to reduce the duration of each step. If the emittance is still significantly growing over the duration of the scans, this could reduce the uncertainty due to the blow-up during the scans. At low intensity, the duration of the scans could be reduced by performing the scans in less steps which should not significantly affect the statistical accuracy as demonstrated in Chapter 2.

- **Scan with only one beam**: would allow to reduce the error from the bump calibration as the beam size would be derived from the movement of one beam only. This in return would increase the duration of a scan and should only be considered for very stable emittances.

The first sessions of calibration scans were very successful and already came very close to the original goal of 10 %. The uncertainty could be significantly reduced with a better knowledge of the beam intensities. Other sources of uncertainties are in general very small and could be further improved by optimizing the beam conditions and scan parameters. In these conditions we believe that a precision of 5 % could be reached in future measurements. First observations with high intensities showed no significant issues due to the scans. Scans at nominal bunch intensities should therefore be considered as they would provide very useful information on non-linear effects such as pile-up or beam-beam.

Chapter 7

Towards Higher Precision: The High-β^* Experiments

The high-β^* optics allows to measure the elastically scattered protons down to very small scattering angles. The detectors used for this measurements are movable devices called Roman Pots. The name originates from the CERN-Rome group that developed this technique in the 70's at the ISR [83]. This technique has been used since ISR in a number of machines such as UA4[13] at CERN, the Tevatron [14], RHIC [15] and in HERA [16]. More recently, the TOTEM [17] and the ATLAS [84] experiments proposed to install Roman Pots in the LHC. This chapter will focus on the optics implementation and beam parameters required by these experiments.

7.1 Why High-β^* Optics?

The optical theorem gives a definition of the luminosity $\mathcal{L} = R_{\text{tot}}/\sigma_{\text{tot}}$ as a function of the total interaction rate R_{tot} and the elastic rate R_{el}.

$$\frac{1}{\mathcal{L}} = \frac{1}{16\pi}\frac{\sigma_{tot}^2\,(1+\rho^2)}{dR_{\text{el}}/dt|_{t=0}}, \tag{7.1}$$

where

$$\rho = \left.\frac{Ref_{\text{el}}(t)}{Imf_{\text{el}}(t)}\right|_{t=0}, \tag{7.2}$$

where f_{el} is the scattering amplitude and at small values of t

$$-t = (p\theta)^2. \tag{7.3}$$

Here p is the momentum transfer and θ is the forward scattering angle. In addition, at very small t-values the cross section is sensitive to the Coulomb term. Using this additional constraint both the luminosity and the total cross section can be determined without a measurement of the inelastic rate. This alternative is taken by ATLAS. The determination of the total proton-proton cross section and the luminosity using the Coulomb normalization or the optical theorem requires measurements of small scattering angles of a few micro radians. To understand how this high precision measurement translates into beam parameters and optics constraints we can look back at basic linear optics notions. In general, the transverse trajectory at a

given point away for the IP is given by:

$$\begin{pmatrix} u(s) \\ u'(s) \\ \Delta p/p \end{pmatrix} = \mathbf{M} \begin{pmatrix} u^*(s) \\ u'^*(s) \\ \Delta p^*/p \end{pmatrix}, \tag{7.4}$$

where $u(s)$ represents any transverse coordinate x or y, $u'(s)$ the angle, $\Delta p^*/p$ the momentum loss and $\mathbf{M}$ the transfer matrix from the IP to the observation point as defined in Chapter 1. In the case of elastic scattering the momentum loss and the dispersion can be neglected. The u-component of the scattering angle at the IP θ_u^* can be expressed as a function of the displacement $u(s)$ at the observation point and the particle vertex at the IP:

$$\theta_u^*(s) = \frac{u(s) - \sqrt{\beta_u(s)/\beta^*}(\cos\Delta\mu_u(s) + \alpha^* \sin\Delta\mu_u(s))\, u^*}{\sqrt{\beta_u(s)\,\beta^*}\sin\Delta\mu_u(s)}, \tag{7.5}$$

where $\alpha^* = 0$. The precision of the scattering angle measurement depends on three characteristic parameters:

- The magnification $v_u = \sqrt{\frac{\beta_u(s)}{\beta^*}}\cos\Delta\mu_u(s)$.
- The effective length $L_{eff} = \sqrt{\beta_u(s)\,\beta^*}\sin\Delta\mu_u(s)$.
- The phase advance between the IP and the observation point $\Delta\mu_u(s)$.

The best strategy to design the optics is to minimize the magnification and to maximize the effective length. This would allow for the transverse position at the observation point to be independent from the position at the IP and for the deflection angle to be as large as possible. These conditions are fulfilled for the so-called parallel-to-point focusing and require a phase advance of $\pi/2$ between the observation point and the IP. In addition, keeping $\beta_u(s)$ not too small would help maximizing the effective length. Assuming the parallel-to-point focusing condition the minimum distance d_u of a detector from the beam is proportional to the beam size:

$$d_u \propto \sqrt{\varepsilon\,\beta_u(s)} \tag{7.6}$$

and using 7.5 the smallest detectable angle is proportional to

$$\theta_u^* \propto \sqrt{\frac{\varepsilon}{\beta_u^*}} \tag{7.7}$$

where ε is the beam emittance. The acceptance of the detector can therefore be optimized with a low emittance and a large β^*.

7.2 High-β^* Experiments in the LHC

Two experiments are foreseen to measure the total proton proton cross section using high-β^* optics in the LHC: TOTEM [17] (**TOT**al cross section, **E**lastic scattering and diffractive dissociation **M**easurement at the LHC) experiment situated in IP5 and ATLAS with the ALFA subdetector [84] (**A**bsolute **L**uminosity **F**or **A**TLAS) situated in IP1. The machine layout is similar in these insertions but each experiment has its own design and optics constraints.

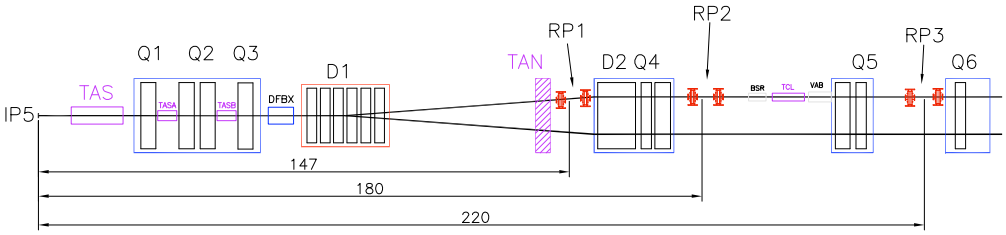

Figure 7.1: Layout of the TOTEM insertion region.

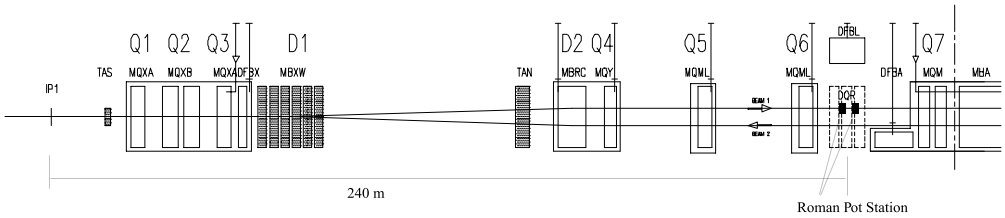

Figure 7.2: Layout of the ALFA insertion region.

Figure 7.1 shows the layout of the TOTEM insertion, three Roman Pot stations composed by two Roman Pots separated by 4 m are installed on each side of the IP at 147 m and 220 m the 180 m station might be installed later.

Figure 7.2 shows the layout of the ALFA insertion, one Roman Pot station composed by two Roman Pots separated by 4 m is installed at 240 m away and on each side of the IP. For both experiments the Roman Pots stations are situated downstream of the IP for both beams. The matching constraints at detector's location therefore only apply on one side of the IP for each beam.

The insertion regions IR1 and IR5 of the LHC have been mainly designed to allow for running at the highest luminosities for the ATLAS and CMS experiments. This will be achieved by running with crossing angles to allow for many bunches at minimum β^*. The strengths of the quadrupoles in the insertions can be individually adjusted. It was always known and taken into account that the strength of each of the quadrupoles will have to remain between the specified minimum and maximum limits. Depending on the quadrupole type, the maximum strength corresponds to about 120 - 220 T/m.

In the LHC we collide particles of the same charge. This makes the insertion optics naturally left/right and beam 1/beam 2 anti-symmetric. In terms of quadrupole strength we have normally kq4.l5b1 = - kq4.r5b1, kq5.l5b1 = - kq5.r5b1 and approximately kq4.l5b1 $\approx$ - kq4.l5b2, kq5.l5b1 $\approx$ - kq5.l5b2 where r5 and l5 stand for the side of the IR where the quadrupole is located and b1 and b2 for the beam it is acting on. This characteristic was assumed to be true for any optics configuration while designing the cabling of the main insertion quadrupole. The present layout consists of a three-lead powering scheme which requires that the currents used to drive any of the quadrupoles from Q4 to Q10 in the insertions do not differ by more than a factor of 2 between beam 1 and beam 2. In the normal approximately anti-symmetric physics optics this is always the case. For the high-β^* optics, the extra asymmetric phase advance constraint breaks anti-symmetric property of these optics and goes against the natural design of these insertions. Hence, it is very difficult to find a converging solution that fulfills the experiments requests as well as the machine's hardware contrains.

The optics studies presented here have been done for the current LHC optics V6.503 starting from previous studies presented in [85, 86, 87] which started in 2004. The aperture checks are done with the latest MAD-X aperture model with a detailed description of the experimental beam pipes. The previous

solutions provided a very good baseline for further investigations but in some cases were incomplete or did not fulfill all the machine constraints. In the following sections a full overview of the high-β^* optics for the LHC as well as new improved solutions and commissioning plans will be presented.

7.3 Analytical Estimates

Before going into the details of individual options we introduce here some general features of the high-β^* optics which are rather different from the normal physics optics. Nominal tune values for physics in the LHC are $Q_x = 64.31$ and $Q_y = 59.32$. Table 7.1 shows the contribution of the arcs and insertions to the total tune. By design, these values are all kept constant during the squeeze. Reducing β^* in one IP will be without effect on the tunes in the rest of the ring.

Table 7.1: Phase advances contributions of the insertions regions and the arcs for nominal LHC physics optics at 7 TeV. IP1 and IP5 $\beta^* = 0.55$ m, IP2 and IP8 $\beta^* = 10$ m.

LHC version V6.503				
	Beam1		Beam2	
arcs	44.1040	40.6890	44.1040	40.6890
IR1	2.6330	2.6490	2.6330	2.6490
IR2	2.9860	2.8086	2.9910	2.8440
IR3	2.2609	1.9054	2.2602	1.9899
IR4	2.0450	1.9414	2.1254	1.9341
IR5	2.6330	2.6490	2.6330	2.6490
IR6	2.0150	1.7800	2.0150	1.7800
IR7	2.4500	1.9236	2.4894	2.0030
IR8	3.1830	2.9740	3.0590	2.7820
tune	64.3100	59.3200	64.3100	59.3200

The effect on the tunes of the squeeze and un-squeeze can be understood by general optics considerations. The betatron phase advance is

$$\mu(s) = \int \frac{1}{\beta(s)}\,\mathrm{d}s. \tag{7.8}$$

We also recall that the phase advance μ and tune are directly related by $Q = \mu/2\pi$.

The β-function in a drift space where s_0 is the position of the interaction point is given by

$$\beta(s) = \beta^* + \frac{(s-s_0)^2}{\beta^*}, \tag{7.9}$$

which is a parabola, see Fig.7.3. For the LHC we use a length of $\ell = 26.15$ m which is the distance between the IP and the center of the first quadrupole (Q1).

The phase advance and tune contribution from the insertion can be obtained analytically by integration from -ℓ to +ℓ. The result is

$$\mu = 2\arctan\left(\frac{\ell}{\beta^*}\right), \qquad Q = \frac{\mu}{2\pi} = \frac{1}{\pi}\arctan\left(\frac{\ell}{\beta^*}\right). \tag{7.10}$$

A low-β insertion with $\beta^* \ll \ell$ contributes with a phase advance of π and tune of 0.5. For very high $\beta^* \gg \ell$ instead, the phase advance and tune contribution drops to zero.

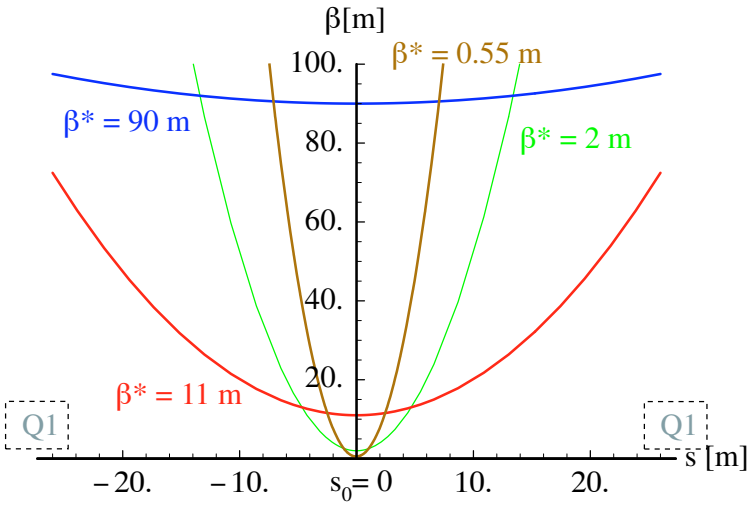

Figure 7.3: β-functions around $s_0 = 0$, for $\beta^* = 0.55, 2, 11$ and 90 m up to ± 26 m as relevant for the LHC.

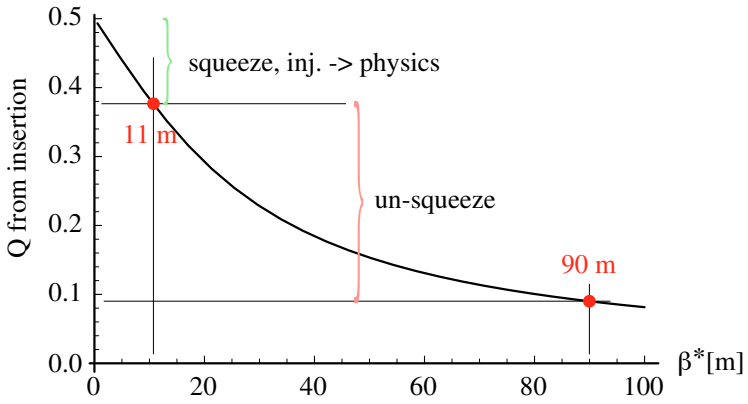

Figure 7.4: Tune contribution from the insertion ± 26 m from the IP as relevant for the LHC.

This is illustrated in Fig.7.4. We see that the local tune change from the IR for the squeeze from 11 m to 0.55 m is approximately +0.1 and about -0.3 for the un-squeeze from 11 m to 90 m. The high-β^* optics have extra constraints on the phase advance on the downstream side from the IP to the Roman Pots close to Q6, which leaves only the upstream side (already contrained by the beam 1 beam 2 strength ratio) for some limited tune compensation. Hence the tune changes in the un-squeeze are too large to be fully compensated internally. A discussion of external tune compensation in the LHC is described in [88]. According to that study, it will be possible for all options discussed here to keep the overall LHC tunes at their standard value and it will not be necessary to lower the integer tunes for high-β operation. Various operation scenarios will be discussed in details in the last section of this chapter.

The requirements of high-β^* operation in terms of luminosity and intensity are rather modest. These optics will be used without crossing angle and the number of bunches will be limited to a maximum of 156 bunches per beam. Bunches will be spaced by 525 ns [89]. The first parasitic bunch encounter is 79 m from the IP, in a region were both beams are already well separated by the separation dipole D1. This makes long range beam-beam effects completely negligible for high-β^* operation. The beam-beam effects from central

collisions does not depend on β^* and will therefore be comparable to normal operation. This can be seen by evaluating the beam-beam tune shift parameter. For round beams and constant normalized emittance ε_N, the beam-beam tune shift parameter can be written as

$$\xi = \frac{N r_p}{4\pi\varepsilon_N}, \tag{7.11}$$

where N is the number of protons per bunch, r_p the classical radius of proton and ε_N the normalized emittance. It only depends on bunch intensity and emittance and not on β^* nor the energy. Numerical values for nominal operation and high-β^* operation are given in Tab. 7.2.

Table 7.2: Linear beam-beam parameters for the high-β^* optics without crossing angle at a single IP.

Optics	Normalized emittance	Intensity	ξ
	[μm]	[10^{10}p/bunch]	
Nominal	3.75	11.5	0.00374
High-β^*	1.0	3.0	0.00366

For high-β^* operation, any reduction in emittance will be accompanied by at least the same reduction in intensity, such that the beam-beam tune shift from central collisions will remain below the value for nominal LHC operation.

7.4 TOTEM 90 m Optics

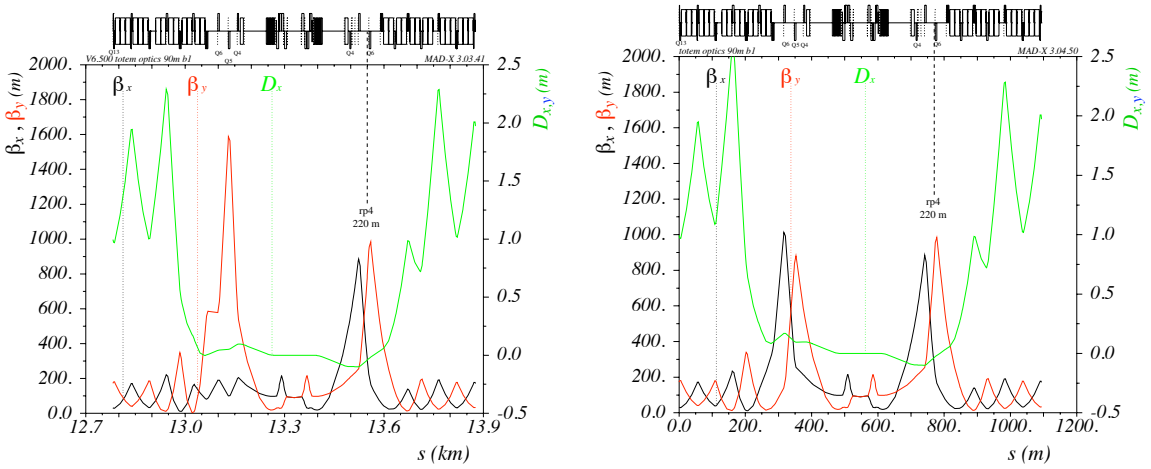

Figure 7.5: 90 m TOTEM optics designed in 2007 (left), and compatible with all known constraints (right), shown is beam 1.

For the earlier LHC operation, TOTEM requires an optics at the intermediate β^* of 90 m with a phase advance of π in the horizontal plane and $\pi/2$ in the vertical plane between the IP and the Roman Pots located 220 m further downstream. Fig. 7.5 left shows the 90 m optics solution, as developed and presented to the CERN experiments committee in 2007.

The optics shown in Fig.7.5 left requires an external tune compensation of about 0.1 in the horizontal plane and 0.03 in the vertical plane. We rematched the 90 m optics to respect the additional limitation on

the strength ratio r between beam 1 and beam 2 of $0.5 < r < 2$ as relevant for the first year of operation. The result is shown in Fig. 7.5 on the right. Beam 2 has the same phase requirements at the roman pots but travels in the opposite direction. Looking from the center of the LHC, we have a roman pot constraint on the right hand side of IP5 for beam 1 and on the left hand side for beam 2. With the extra ratio limit, we loose in flexibility for internal tune compensation. To keep the overall tunes constant, we now require an increase for 0.2 in the horizontal and 0.045 in the vertical plane.

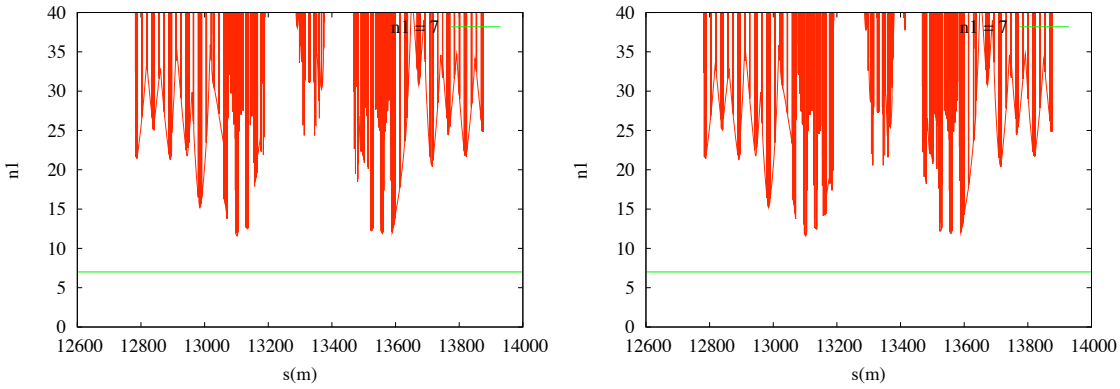

Figure 7.6: 90 m TOTEM optics, 2009 version. Aperture in IR5 at 3.5 TeV, $\varepsilon = 3.75\,\mu$m, without separation (left) and with separation (right).

The 90 m optics is not expected to impose any particular aperture limitations. Even in the least favorable case, at 3.5 TeV and with separation, the minimum $n1$, which defines the MAD-X aperture model, is equal to 11.6 which is above $n_1 = 10.5$, see Fig. 7.6. The limitation of $n1 = 10.5$ comes from the intermediate collimators settings which will used for the first years of operation.

7.5 TOTEM very high-β* Optics

The very high-β* optics for the TOTEM experiment was developed several years ago. To improve the resolution on the polar and azimuthal angle measurement, the parallel to point focusing optics with $\pi/2$ phase advance between the IP and the detector in both planes was required by TOTEM. Our study starts from the high β* optics solution for TOTEM as documented in 2005 in [85]. We briefly review main features of this optics and then discuss modifications required by the additional beam 1 / beam 2 ratio constraint.

7.5.1 Baseline Solution

As a baseline we start from the optics presented in [85]. It has a β* of 1535 m and phase advances of $\mu_x = 0.956 \times \pi/2$ and $\mu_y = \pi/2$ between the IP and the roman pot 220 m downstream of the IP.

The optics parameters for this solution are shown in Figure 7.7 for beam 1. The roman pot is situated for beam 1 on the right hand side of the IP. The left side is used for partial tune compensation. This solution requires an external tune compensation of ΔQ of ≈ 0.5 in the vertical plane. This optics is not compatible with the extra strength ratio constraint and would not be feasible in the LHC as currently installed. The ratio constraint can in principle be removed by adding extra cables. The quadrupoles which are outside the beam 1 / beam 2 strength ratio constraint are listed Table 7.3.

This solution has the Q4 magnet on the downstream side, where the roman pot is installed, switched off. There is a constraint on the minimum allowed current and strength corresponding to about 3% of the

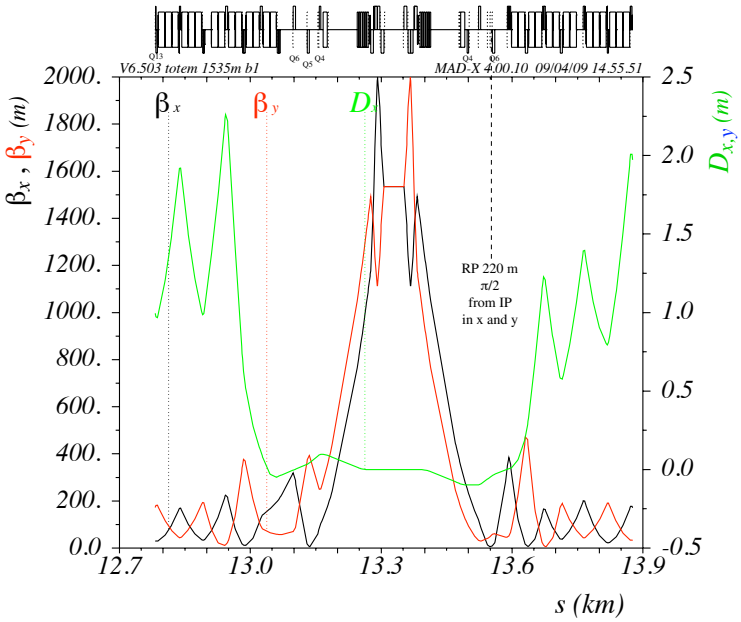

Figure 7.7: Beam 1 optics of the baseline solution.

Table 7.3: Beam 1 / beam 2 strength ratios outside limits.

Magnet	Left side of IP5	Right side
Q4	0	1/0
Q7	26	1/30
Q8	2.1	1/2.1

maximum current and strength when the magnet is on. We cannot turn off Q4 with beam in the LHC and would therefore already have to inject in the LHC with Q4 off which requires a special solution for injection.

7.5.2 Alternative Solution with Q4 On

Keeping Q4 powered as opposed to the baseline solution where it was turned off, would make it potentially feasible to allow to gradually un-squeeze the beams to the nominal β^* of 1535 m from the standard LHC optics. This would be a major advantage from the commissioning point of view. It would require extra cables to remove the beam 1 / beam 2 strength ratio constraint. We discuss here a solution with a β^* of 1535 m that was found with Q4 on at the normal polarity.

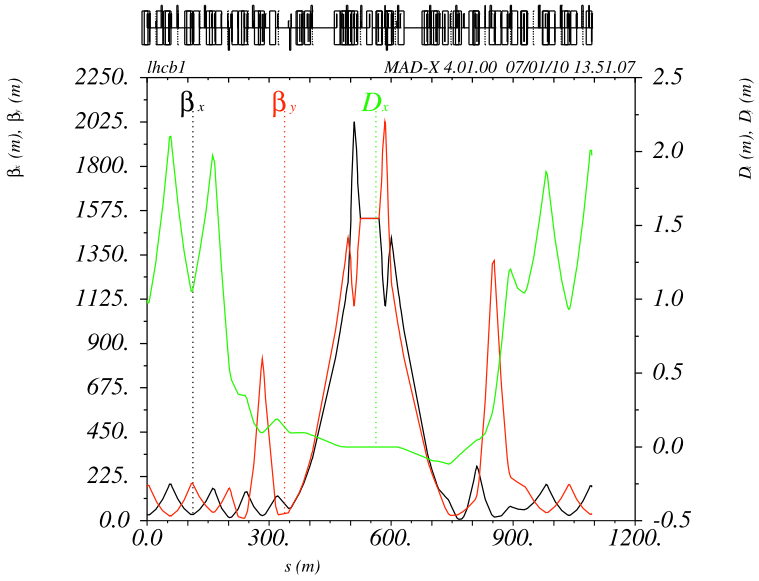

Figure 7.8: Beam 1 optics solutions with Q4 on.

Figure 7.8 shows the solution we found with Q4 on. The tune compensation produces a peak in β_y on the upstream side of the IP where the peak on the downstream side is due to the maximization of the β functions at the Roman Pots which is relevant for the detectors acceptance. The tune contributions for the insertion are $Q_x = 2.36$ and $Q_y = 2.20$. This solution needs additional cables on few insertion quadrupoles (3 in this case). All quadrupole strengths are compatible with the limits coming from the power converters at 7 TeV.

7.5.3 Comparison of the Performance for Physics

The performances of the optics for physics is determined first by its acceptance which depends on the beam divergence D at the IP. D is equal to $\sqrt{\varepsilon/\beta^*}$ and is the same for all the optics presented above. The other relevant parameters for comparison of the performances are the magnification and the effective length which definitions are recalled below.

$$L_{\text{eff}} = \sqrt{\beta_u(s)\,\beta^*}\,\sin\Delta\mu_u(s), \tag{7.12}$$

$$v_u = \sqrt{\frac{\beta_u(s)}{\beta^*}}\,\cos\Delta\mu_u(s), \tag{7.13}$$

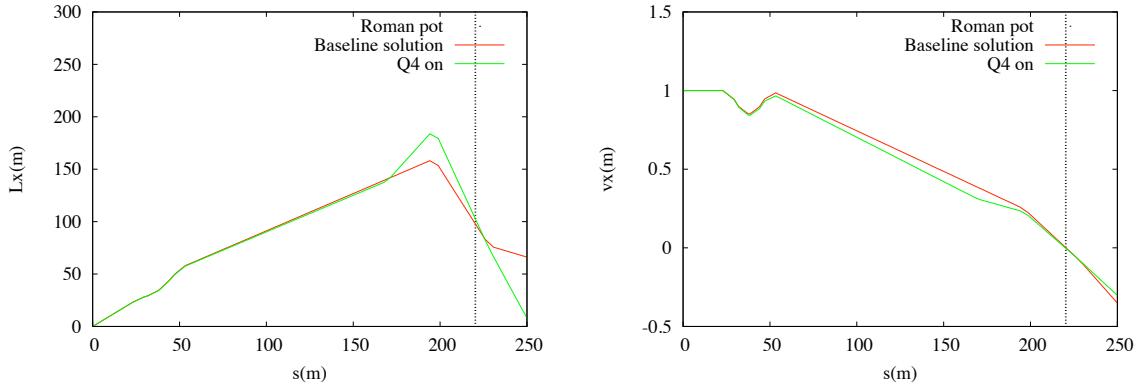

Figure 7.9: Effective length defined in Equation 7.12 (left), magnification defined in Equation 7.13 (right) in the horizontal plane. The performances are similar for both designs.

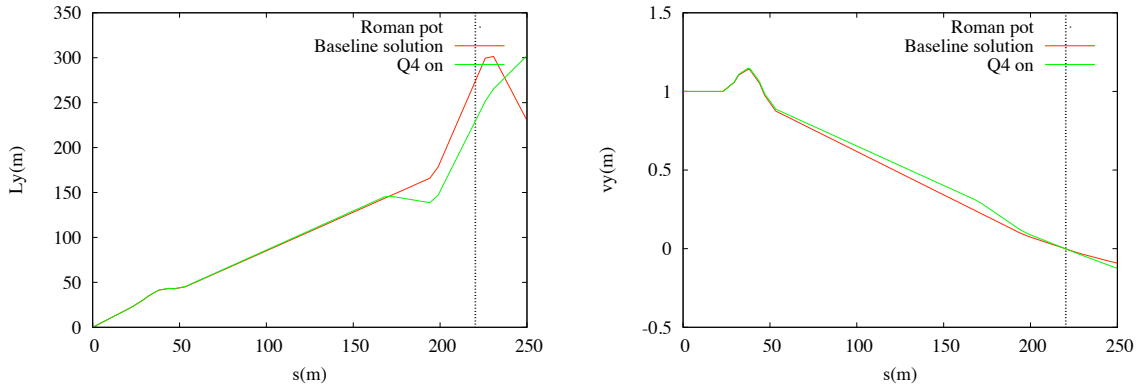

Figure 7.10: Effective length defined in Equation 7.12 (left), magnification defined in Equation 7.13 (right) in the vertical plane. A loss of about 11 % is observed for the effective length with respect to the baseline solution.

Figures 7.9 and 7.10 show a comparison of the effective lengths and magnification on both planes for the baseline solution and the solution with Q4 on. We can see that these parameters are rather similar for all cases except for the effective length in vertical plane were a loss of 11 % is observed with respect to the baseline solution. This loss is explained by the fact that the β-function at the Roman Pot could not be matched to the value of the baseline solution. The beta-beat specification is ≈ 20%, this loss is then a factor 2 lower than the expected optics error.

7.5.4 Aperture

The MAD-X aperture model defines a function $n1$ which is computed via the mechanical aperture and tolerances, the specification is $n1 = 7$. For collision optics at 7 TeV we assume an orbit of 3 mm and a $\Delta p/p$ of 0.00086, the tolerance for the CMS beam pipe where the aperture is critical in the case of high-β* optics was set to 15 mm. The normalized emittance of 1.0 μm was required by the TOTEM experiment. Changing any of these parameters would of course change the results presented here.

It is desirable to do the un-squeeze from the injection to the collision optics with separated beams. We will therefore look at the two cases with and without separation as well as the effect of the emittance on the aperture.

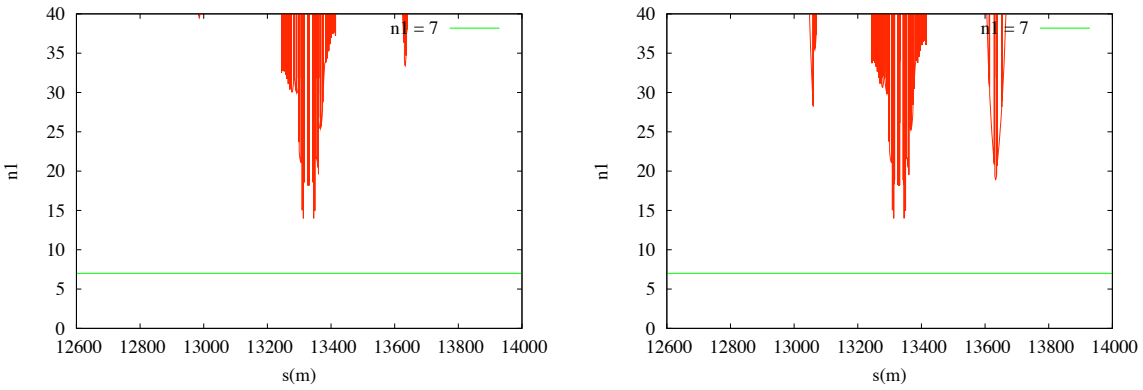

Figure 7.11: Apertures with 1 μm normalized emittance and CMS beam pipe tolerance set to 15 mm for baseline solution (left), Q4 on (right). Minimum n1 = 14 in the CMS beam pipe for both solutions.

Figure 7.11 shows the aperture for the TOTEM optics in collision. All the optics have similar characteristics except for two peaks in Q6L and Q8R due to the tune compensation and optimization of the performances. These optics are compatible with a normalized emittance up the LHC nominal of 3.75 μm without separation as shown Figure 7.13. This is very interesting in the case of the Q4 on option because we could gradually unsqueeze the beams from injection optics without having to reduce the emittance.

Ultimately, when we can achieve a smaller emittance, we could perform a cleaner un-squeeze with separated beams. The collision optics with full separation Figure 7.12 are compatible with an emittance up to 1.5 μm.

7.5.5 Compatibility at 5 TeV

The nominal LHC energy of 7 TeV will not be reached before a few years of operation, for completeness we report on the possibility of running this optics at 5 TeV. The two limiting parameters at lower energy are the minimum strength allowed in the insertion quadrupoles and the aperture.

In order to fullfill the phase advance constraint between the IP and the detector the strength of Q4L had to be set to a value very close to the minimum allowed at 7 TeV (3 % of the nominal strength by design). This

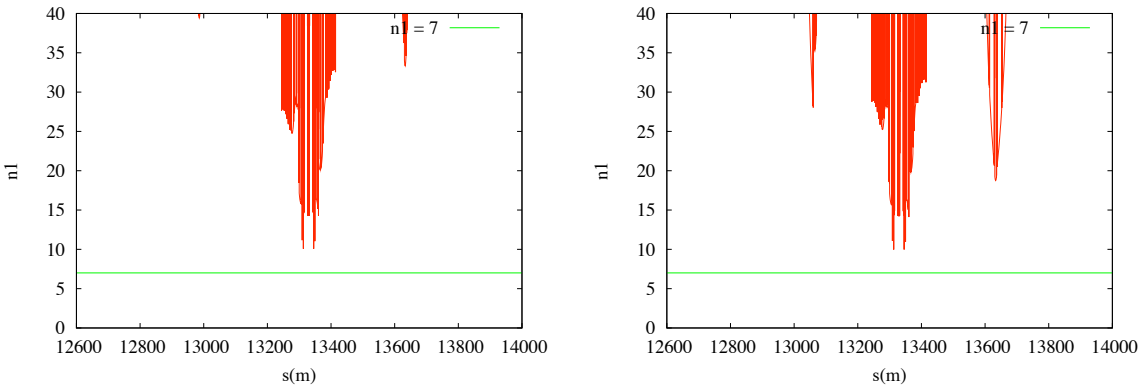

Figure 7.12: Apertures with half-separation of 7 σ at the IP. 1 μm normalized emittance and CMS beam pipe tolerance set to 15 mm for baseline solution (left), Q4 on (right). Minimum n1 = 10 at the CMS beam pipe for both solutions.

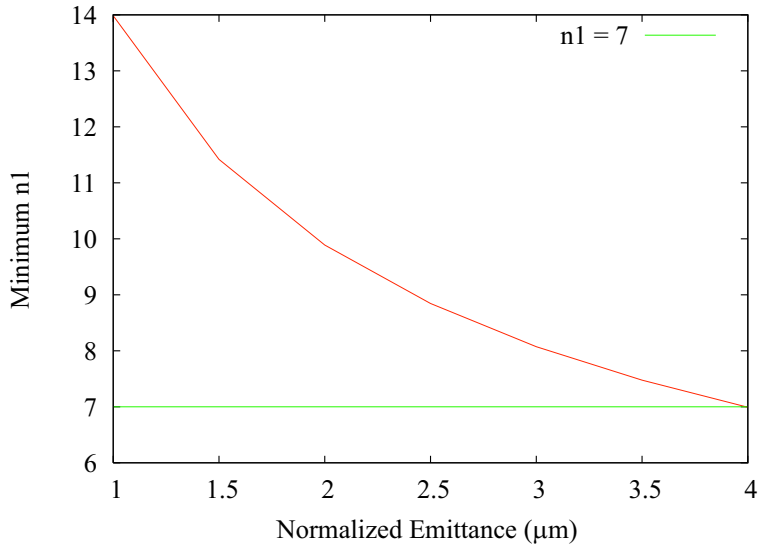

Figure 7.13: Minimum n1 as a function of the normalized emittance for collision optics without separation for the TOTEM optics at 7 TeV.

value remains above the lower strength limit down to an energy of 6.2 TeV. At 5 TeV, the strength in Q4L represent 2.4 % of the nominal which is beyond the minimum. Measurements showed that this limitation could be overcome to allow for a minimum corresponding to 2 % of the nominal, in this case this optics would remain compatible with an energy of 5 TeV.

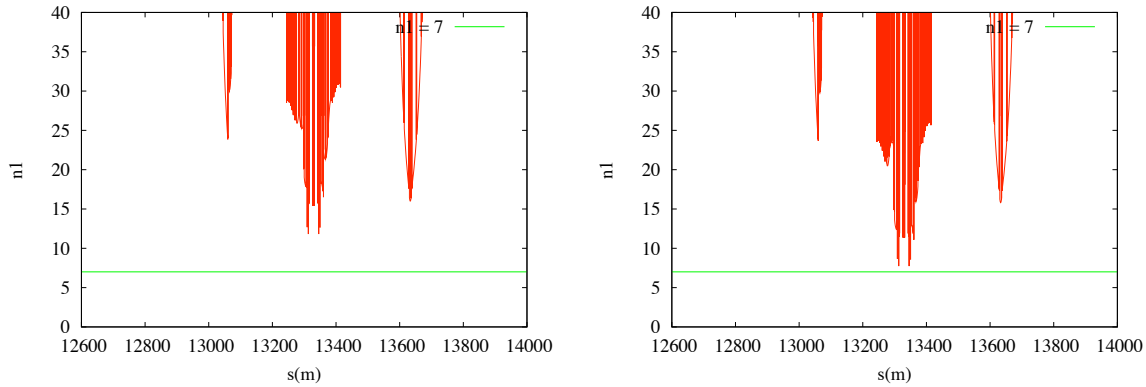

Figure 7.14: Apertures with 1 μm normalized emittance and CMS beam pipe tolerance set to 15 mm without (left) and without (right) separation. Minimum n1 = 12 without separation and 7.7 with separation in the CMS beam pipe.

Figure 7.14 shows the aperture with and without separation for a normalized emittance of 1 μm. The aperture is within specifications for both cases, the un-squeeze could also be performed with separated beams at 5 TeV. The limit is reached for an emittance of 2.7 μm for collision optics as shown Figure 7.15.

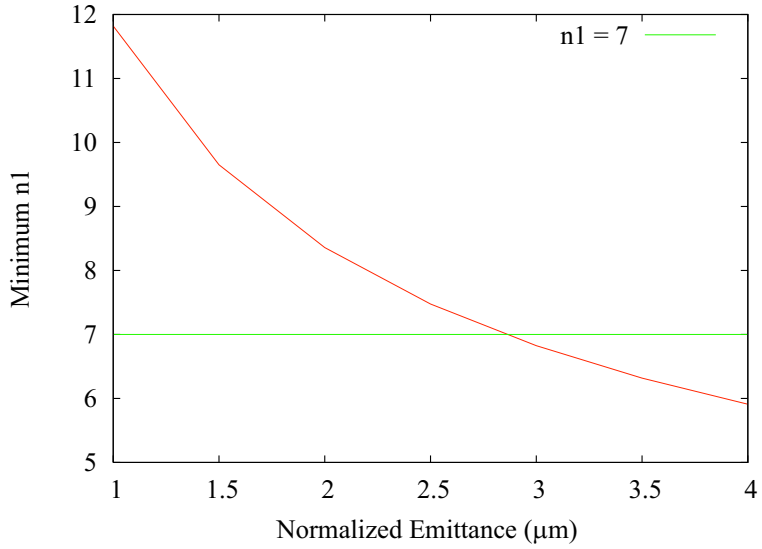

Figure 7.15: Minimum n1 as a function of the normalized emittance for collision optics without separation for the TOTEM Optics at 5 TeV.

For its first two years of operation the LHC will be running at 3.5 TeV, assuming an emittance of 1 μm can be reached in the early operation, $n1$ minimum goes down to 9.8 which is compatible with the nominal collimators settings but not the intermediate settings that will most likely be used during this period. For the nominal emittance of 3.75 μm $n1$ minimum goes down to 5 and is out of specifications. In any case this optics requires a hardware upgrade that can not be performed before the long shutdown in 2012 and

therefore cannot be operated before then.

7.6 ATLAS Very High-β^* Optics

The previous studies for the very high-β^* experiment [87, 86] at IP1 showed that it is possible to find a solution with $\beta^* = 2625$ m and a phase advance of $\pi/2$ in the vertical plane between the interaction point and the Roman Pot. In this case the Roman Pots are situated at 239.6 m away from the interaction point and approach the beams from the top and the bottom, the parallel-to-point conditions is then only relevant in the vertical plane. However the gradients of certain quadrupoles were very close or slightly over the strength limit and a small rematch was necessary to fullfill all the constraints.

7.6.1 Optics for Physics

Starting with those existing studies and keeping $\beta^* = 2625$ m as well as the phase advance between the IP and the Roman Pot it has been possible to find solutions for both beam 1 and beam 2.

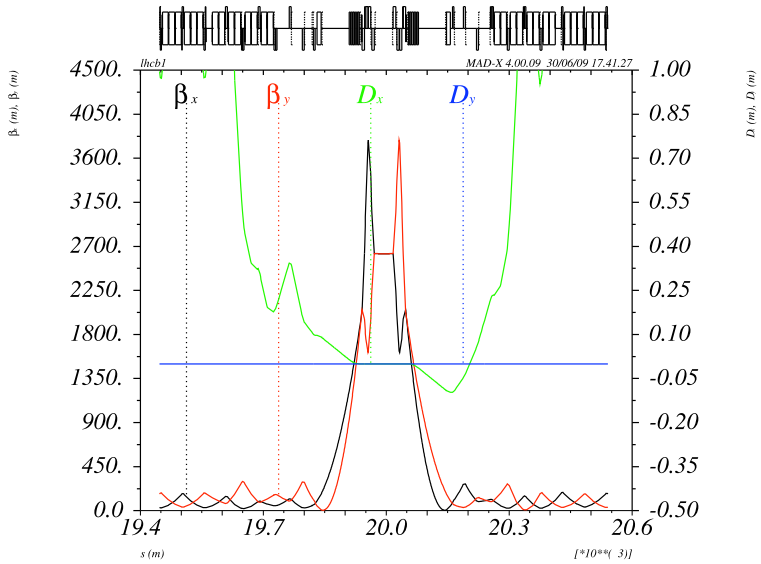

Figure 7.16: Optical functions for β^*=2625 m, beam1 is shown.

Figure 7.16 shows the ATLAS high-β^* optics with $\beta^* = 2625$ m. A detailed description of the matching results was presented in [90]. The tune contributions from the IP1 insertion are $Q_x = 2.44$ and $Q_y = 2.12$. We would then have to compensate for a loss in tune of 0.2 in the horizontal plane and 0.5 in the vertical plane.

7.6.2 Injection Optics with Q4 Inverted

Switching of polarity requires a manual intervention at the power converters. Even if a remote control would be added, it can only be done without beam in the machine. Once the polarity was switched, this will be effective for the whole operation cycle of injection, ramp and un-squeeze. With the inverted $Q4$ polarity it is impossible to match lower values of β^* and beams will have to be injected with β^* well above 100 m.

Figure 7.17 shows the baseline solution for the injection with Q4 inverted on the left. The tune contribution for this optics is $Q_x = 2.40$ and $Q_y = 2.1$ and would require a compensation of 0.24 in the horizontal plane and 0.53 in the vertical plane. The right hand side shows a solution with $\beta^* = 180$ m in which the

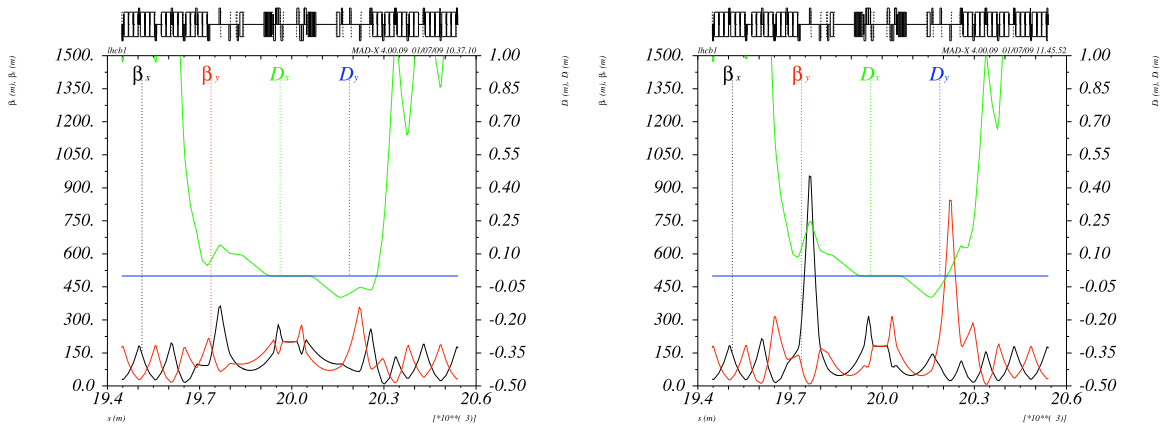

Figure 7.17: Optical functions as designed in 2005 by A. Verdier with $\beta^* = 200$ m requiring a compensation in tune (left), and in 2007 with $\beta^* = 180$ m and standard injection tunes (right).

tunes were kept at their standard injection values. Using the first solution would imply to run the LHC on a different working point as opposed to the second solution.

7.6.3 Aperture

The same aperture study as presented in section 7.5.4 were performed for the ATLAS optics. Few differences apply. The tolerance for the ATLAS beam is tighter and was set to 11 mm. ATLAS requires a dedicated injection optics. The parameters used for the aperture study at injection are are 4 mm orbit and $\Delta p/p = 0.0015$.

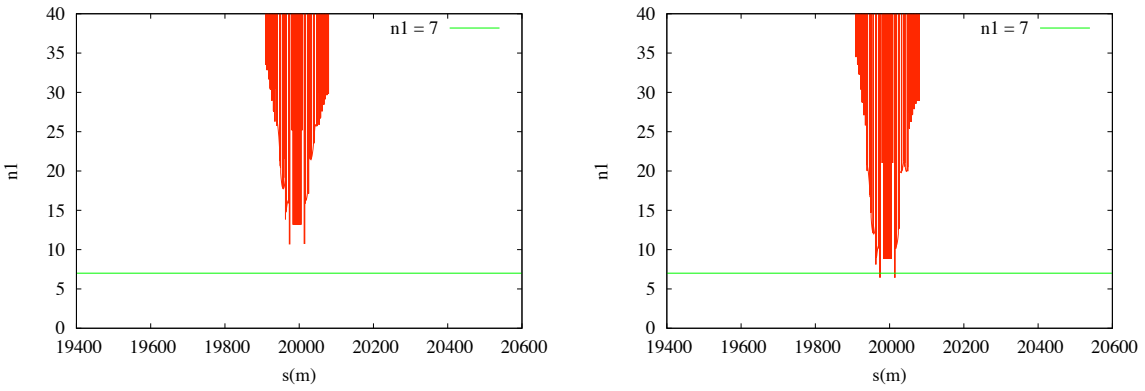

Figure 7.18: Apertures without (left) and with (right) separation of 7 σ at IP1 for collision optics. $\varepsilon = 1\mu$m and ATLAS beam pipe tolerance set to 15 mm. Minimum n1 = 10.8 at the TAS without separation and 6.5 with separation.

Figure 7.18 shows the aperture for the collision optics with and without separation. The specification $n1 = 7$ is not respected for separated beams but a full separation of 14 σ might not be mandatory in the case of the high-β* experiment since the beams will have low intensity and the beam-beam effects are smaller than the ones of nominal LHC. Figure 7.19 shows the aperture for the baseline solution with $\beta^* = 200$ m and the one matched to the nominal LHC tunes. In order to be consistent with the collision optics the separation was set to 4.2 mm which corresponds to 7 σ for a β^* of 2625 m. The nominal tunes optics offers the advantage of running the LHC without changing the working point while keeping the aperture within the

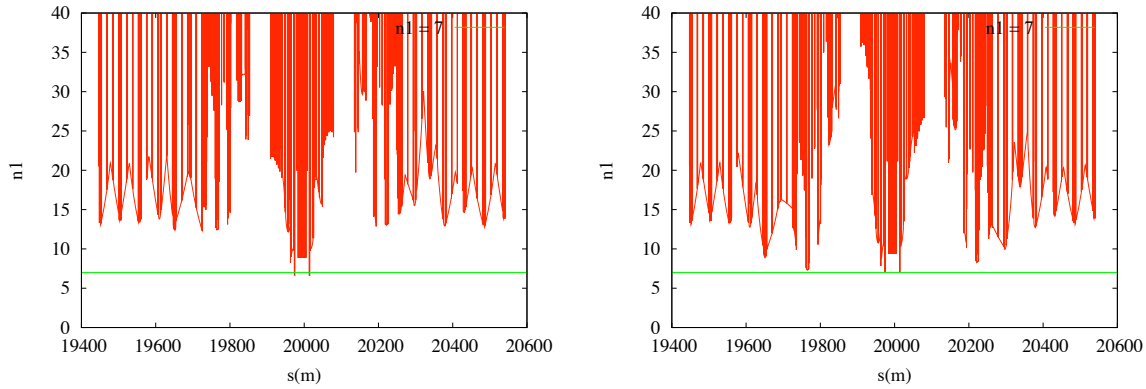

Figure 7.19: Apertures with separation of 4.2 mm at IP1 for injection optics (450 GeV). $\varepsilon = 1\mu$m and ATLAS beam pipe tolerance set to 15 mm. Minimum n1 = 6.6 and 7.1 at the TAS for A. Verdier (left) and nominal tunes optics (right) respectively.

specification. Being so close to the limit in aperture makes it mandatory to run with a normalized emittance of 1 μm unless the separation is reduced.

Reaching the value of 1 μm for the normalized is expected to be very challenging in the LHC. We therefore also determined the lowest emittance compatible with the $n1 = 7$ specification.

As shown in Figure 7.20 the ATLAS high-β* optics would have the potential to run with an emittance of up to 2.3 μm in collision but without margin to separated beams. Squeezing beams in collisions has been successful in other machines including the S$p\bar{p}$S. The main emittance limitation is at injection optics with Q4 inverted in which we really require an emittance of 1 μm. The 200 m injection optics from A. Verdier optics is still compatible with a normalized emittance of 1.5 μm with a separation reduced by a factor 2.

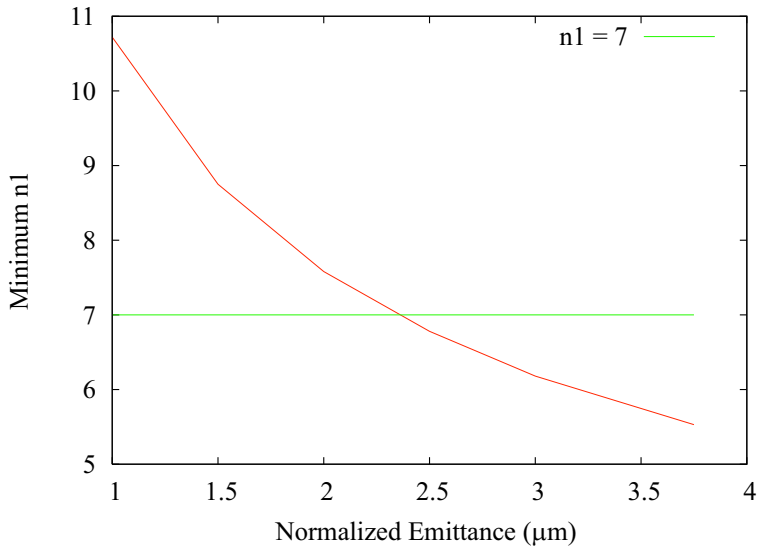

Figure 7.20: Minimum n1 as a function of the normalized emittance for collision optics without separation for the ATLAS Optics.

7.7 Commissioning and Running Scenarios

The commissioning of the very high-β^* optics is expected to be rather challenging in several respects like the need for reduced emittance, tight aperture, external tune compensation and the need for a dedicated injection and ramp for the ATLAS optics. The option with Q4 on normal polarity for TOTEM could potentially be reached without need for an extra injection and ramp. Experience with beams in the LHC and in particular the commissioning of the 90 m TOTEM optics with tune compensation will be very important. The main features and requirements of the various options are summarized below.

7.7.1 Early Running: 3.5 TeV

The only optics compatible with this energy is the 90 m optics. It was initially designed for TOTEM but as IR1 and IR5 have very similar layouts it can also be appplied for for ALFA. This optics requires the commissioning of the un-squeeze at top energy and external tune compensation. At present, it is hard to judge how difficult this would be operationally and how much commissioning time would be required for the 90 m optics. A lot more will be known after first tests in the LHC to un-squeeze beams. The 90 m optics does not require a reduced emittance and should be compatible with normal physics in the other IPs. This may allow to do the un-squeeze from normal physics to 90 m towards the end of a fill.

7.7.2 Very high-β^* Optics

Due to the very tight aperture the very high-β^* optics can only be reached at higher energies. In addition they require a large tune compensation a non standard operation with low emittance and dedicated injection for ALFA. Table 7.4 summarizes the different features of the very high-β^* optics for ALFA and TOTEM with Q4 on.

Table 7.4: Main features of the high-β optics for TOTEM and ALFA.

Beam Parameter	TOTEM	ALFA
β^* [m]	1535	2625
ΔQ_x	0.27	0.19
ΔQ_y	0.45	0.53
E_{min} [GeV]	5000	7000
ε_{min} [μm]	1.5	1.0

The minimum emittances quoted in Table 7.4 assume a nominal separation of 14 σ. Reducing the separation, which should not be an issue while running at lower intensities, would give some margin to increase the emittance. The TOTEM optics is potentially reachable by un-squeeze using the standard injection and ramp and is compatible with nominal emittance in case the un-squeeze is performed with reduced separation. This is very interesting as we could use the end of fills to prove the feasibility of such optics in the LHC. Running the TOTEM optics alone would imply a tune compensation of 0.27 in the horizontal plane and 0.45 in the vertical plane. It was shown in [88] that this could be done using another LHC insertion.

The solution for the ALFA with $\beta^* = 2625$ m the Q4 polarity is inverted and requires a dedicated injection and ramp as the polarity of Q4 can only be inverted manually. This is not compatible with standard LHC operation and will require dedicated runs with low emittance. The ALFA and TOTEM optics have the same requirements in terms of beam parameters and it is foreseen to run the two experiements together once the emittance of 1 μm can be achieved. In this configuration the tune compensation would be 0.36 in the horizontal plane and 0.98 in the vertical plane. A full integer will be difficult to compensate for even using

other insertions, it is therefore foreseen to run the LHC on different working point by reducing the integer part of the tune by one unit in the vertical plane.

Conclusion

The work presented in this thesis significantly contributed to LHC start-up. A first luminosity calibration using the Van Der Meer scan method was provided to the particle physics experiments. The anticipated sources of uncertainty were estimated by simulations and analytical approach which allowed to determine optimum beam conditions and procedures for luminosity calibration measurements. Measurements confirmed that most of them were small and could be well determined. The main contribution to the overall uncertainty comes from the knowledge of the beam intensities. As a result of a very successful collaboration between instrumentation experts, experiments physicists and beam dynamics experts a resolution of 11 % was reached at the very first try. The first observations and a detailed study and characterization of systematic uncertainties indicate that under well controlled and optimized beam conditions a precision of 5 % could be reached in future absolute luminosity measurements.

Measurements were also performed at the RHIC collider. Additional effects such as hourglass and strong beam-beam apply for RHIC and not for the LHC. This triggered a more general study on the implications of these effects on the luminosity calibration using the Van Der Meer method. The impact of the hourglass effect on the measurement of the effective beam size was modeled and measured. The luminosity scans data were also used to compute the beam-beam deflection angle as function of the separation from which the beam-beam parameter could be derived. Even for beam conditions not optimized for a precise luminosity calibration measurement a precision of about 7 % could be reached. The main contribution to this error comes from the intensity measurements ($\approx$3 %) and the determination of the beam displacement. A more detailed orbit analysis combined with a bump calibration as performed in the LHC could further decrease the uncertainty.

As part of this work, analysis and control tools were developed based on the experience acquired at the RHIC collider. They allow for safe and automated luminosity optimization and calibration measurements and are used on a regular basis in the LHC control room. The first observations with nominal bunch intensities are very encouraging as they showed no sign of significant issues directly related to this method for luminosity optimization.

Most of the preliminary studies such as the tracking simulations for the BRAN and beam-beam simulations in the presence of transverse offsets were performed for the LHC design center of mass energy and beam parameters. The results obtained and the tools developed during this thesis should therefore still be valid when the LHC reaches its design energy and could be used as a basis for future measurements and analysis.

Ultimately, the high-β experiments plan to measure the total proton-proton cross section with a precision of a few percents. The requirements in terms of optics and beam conditions to reach this high precision are rather challenging. Optics solutions that fulfill all the constraints from the machine and the experiments were found. The commissioning of intermediate solutions should start in autumn 2010.

Appendix A

Software for Luminosity Optimization and Calibration

As part of the work related to luminosity calibration and optimization, a control software was developed based on the specifications from the technical notes [71] and [91]. The motivations to develop a dedicated software was to allow for fast automated scans and online analysis while storing all the relevant informations for offline analysis to improve operation efficiency.

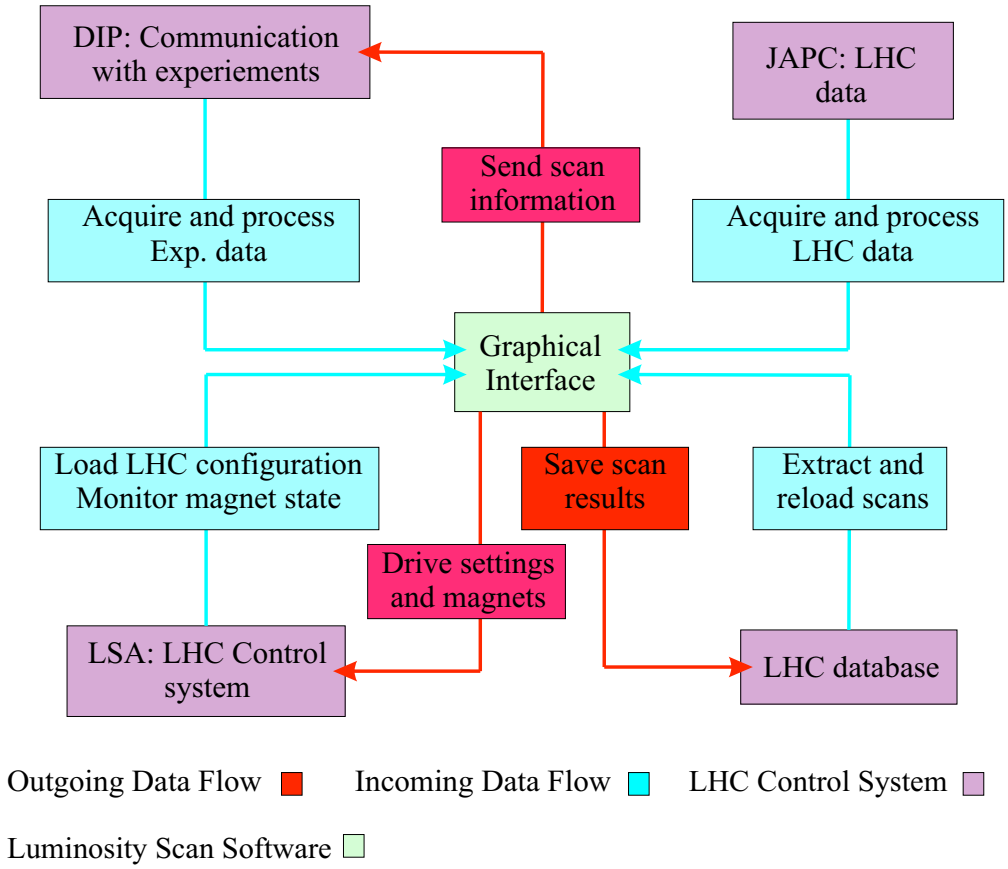

Figure A.1: Data flow chart of the luminosity scan software for the LHC.

Figure A.1 illustrates the data flow and interactions with the different LHC control system components.

The scan data are acquired and processed online from JAPC (Java API for Parameter Control, LHC data) and DIP [70] (Data Interchange Protocol, experiments data). Once the scan is finished the results are saved in the LHC database and in a file. The scans can be reloaded from the database or the files within the software. The drive commands are send to the magnets via LSA (LHC software architecture) [69].

A.1 Synchronization

One of the main challenges that arose while developing the software was the communication in real time and in a synchronous way of the scan progresses, i.e. status of the beams: idle or moving, to the experiments. This is done via DIP and allows the experiments to know exactly when the beams are moving and when they should acquire data. The synchronization is done using a timestamped flag.

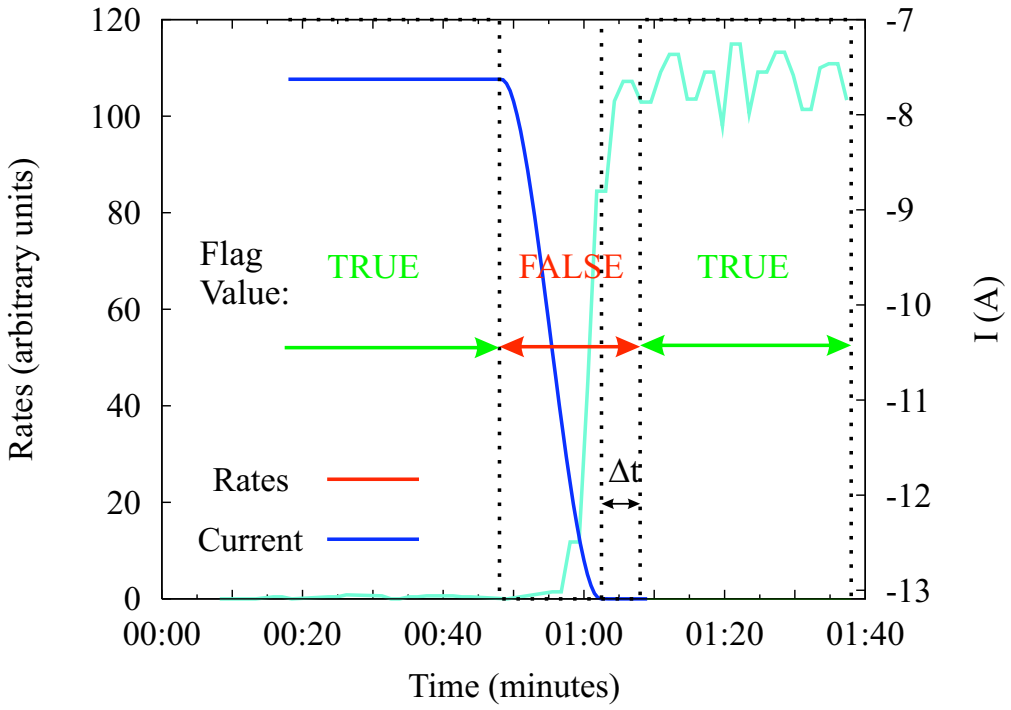

Figure A.2: Synchronization signals over DIP. The flag is used as trigger by the experiments. When the flag is set to TRUE the beams and luminosity monitors are fully idle.

Figure A.2 represents a zoom of a scan step together with the flag value. If we look at the time history from left to right the status starts with the flag equal to TRUE (beams idle) and moves to FALSE when the drive command is sent to the magnets (in practice the status FALSE is sent before the drive command in order to ensure the consistency of the information sent over the network). When the beams have finished moving to the next step the status remains FALSE for a certain time Δt. This time is given by the experiments themselves, still over DIP, and represents the time over which the luminosity is integrated for each update of their publications. One second is added to compensate for network delays. This method ensures that both the magnets and the luminosity monitors are stable when the data are declared as valid.

A.2 Luminosity Calibration Routine

The luminosity calibration scans are performed over large separation range around the peak luminosity in order to fully determine the overlap beam profile. The user inputs are:

- **IP, beam and plane**: the scans can be performed in any IP or plane using beam 1, beam 2 or both. When the two beams are selected they are moved opposite directions.
- **Scan range**: the scan range is set by a minimum and a maximum separation with respect to the initial position. The scan are always performed around a central point which represents the initial position.
- **Number of points**: used to generate the step function by dividing the difference of the maximum and the minimum separation by the number of points.
- **Integration time**: number of seconds per step.

Once all these parameters are filled, the software determines a step function and the scan is performed automatically. During the scan, the RMS, average and number of acquisition is calculated for each step and instrument. The communication with the experiments, the calculation at each step and the drive commands to the magnets are processed on different threads. This insures the real time processing of all information. At the end of the scan the average and bunch-by-bunch data are saved and an automatic fit is performed. The scan can be cancelled at any time, the beams are then brought back to their initial position.

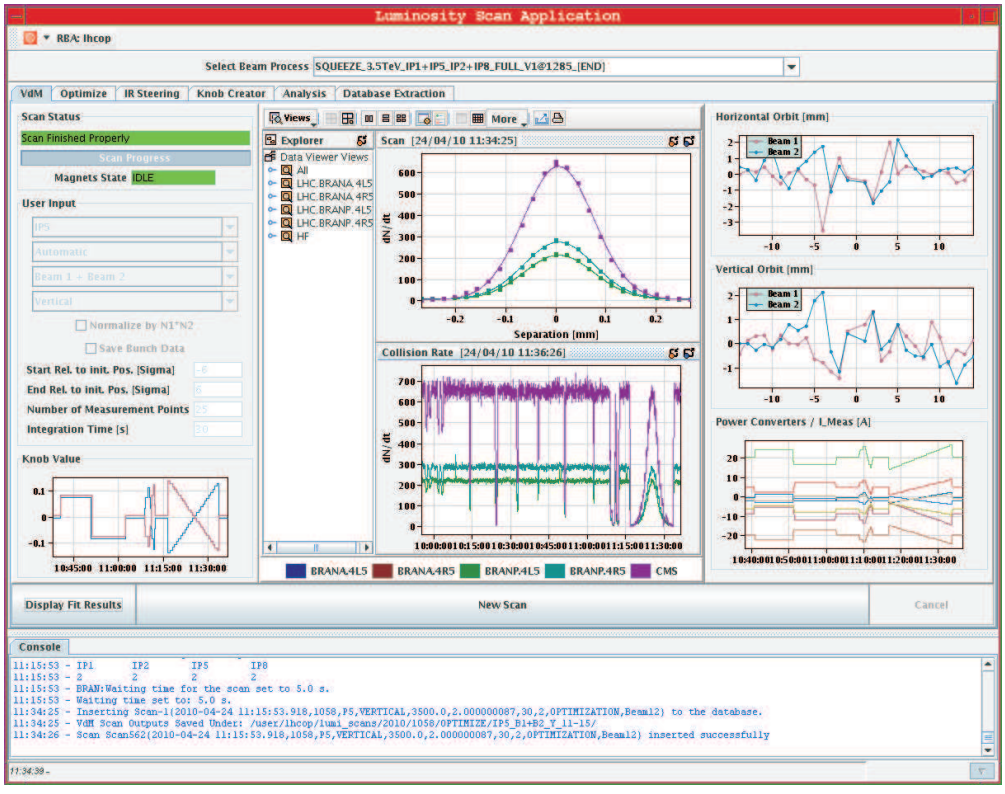

Figure A.3: Panel used for calibration scans. Example of a scan in IP5.

Figure A.3 shows the panel for luminosity calibration. An example of a scan in IP5 is shown. The luminosity signal of the experiment and the BRAN are monitored in real time during the scan. The orbit in the IR, the knob value and the magnet currents are also monitored in real time.

A.3 Luminosity Optimization Routine

Luminosity optimization is usually performed at the beginning of fills when the luminosity lifetime is the worst. The key parameter to develop a routine for luminosity optimization is therefore the efficiency. A simple routine was developed for this purpose which algorithm can be described as follows:

- **1**: take a reference at current location. Integrate the luminosity over n seconds.
- **2**: compute average and RMS at this point.
- **3**: move beam1, beam2 or both by d.
- **4**: integrate over n and Compute average and RMS.
- **5**: compare the two points.
- **6**: step by d if the new point larger than the reference or by -2d if it is smaller.
- **7**: repeat steps 3 to 5 until the new acquisition is smaller than the previous one displacing the beams in the direction set in step 6.
- **8**: compute a parabola (analytically) from the last three points and find the optimum settings.
- **9**: move to the optimum and take a last acquisition to confirm the increase with respect to the reference. This last point requires a confirmation from the operator.

The user inputs for this routine are n which corresponds to the integration time per step and d which corresponds to the step size. d should be large enough to ensure a significant change in rates between to consecutive acquisitions. The operator can also specify the IP beam and plane that requires an optimization and which signal (detector) should be used. This method allows for fast optimization with simple input parameters. It was developed at RHIC [92] and gave excellent results. It was tested for the LHC and is now used on a regular basis in operation.

Figure A.4 shows the panel for luminosity optimization. We can see that the beams are slowly moved to the optimum position and stopped there. In addition to the rates, normalized to the intensity by default, the IP beam coordinates are monitored together with the bump value and the magnet currents. A display of the background is also available which could give information on potential issues. This method stops when the optimum position is found which could be an issue for machine protection if the required corrections are too large, see Chapter 6. To avoid large unwanted corrections a limit is set to the maximum allowed displacement. If this limit is reached during a scan the routine stops. The maximum is computed from a Gaussian fit and the choice is given to the user whether to move to this position or not.

A.4 Steering Routine

The two methods presented above require that the beams are colliding. If the beams are separated by a large amount and there are no collisions the automated methods cannot be used. It is therefore convenient to have a simple steering routine that allows the operator to move the beams at the IP manually.

Figure A.5 shows the steering panel. The initial selection of the IP, beam and plane are similar to the automated method. This method allows to correct the beam position or angle at the IP. Two types of trim are correction. An absolute correction which will drive the beam to the postion or angle input by the operator or a relative correction which will add the input value to the previous one. The knob value, the magnet current, the IP beam coordinates, the beam intensities and the rates of the selected IP are monitored in real time.

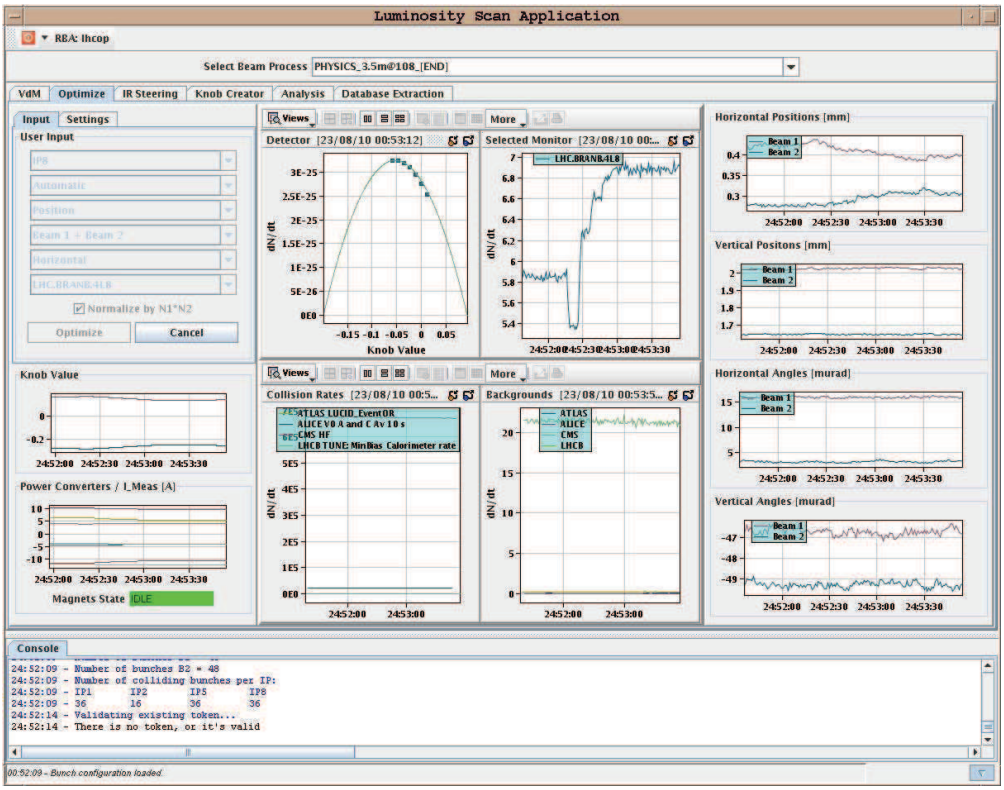

Figure A.4: Panel used for luminosity optimization. Example of a scan in IP8.

A.5 Online Analysis

The package used for the online analysis is MINUIT [22]. The default automatic fit is a pure Gaussian added to a constant component. As seen in the LHC and RHIC data, Chapter 6 and 5, this fit function is not always appropriate. Within the software an analysis tool was developed which allows to perform a more detailed analysis. It offers the possibility to fit a scatter plot of any variables (bump value, rates, BPM, BCT). The fit functions available are pure Gauss, Gauss plus constant, Gauss plus first order polynomial, double Gauss, parabolic and linear. This tool is intended as giving a fast online diagnosis of the quality of the data and estimates of the beam sizes and absolute luminosity.

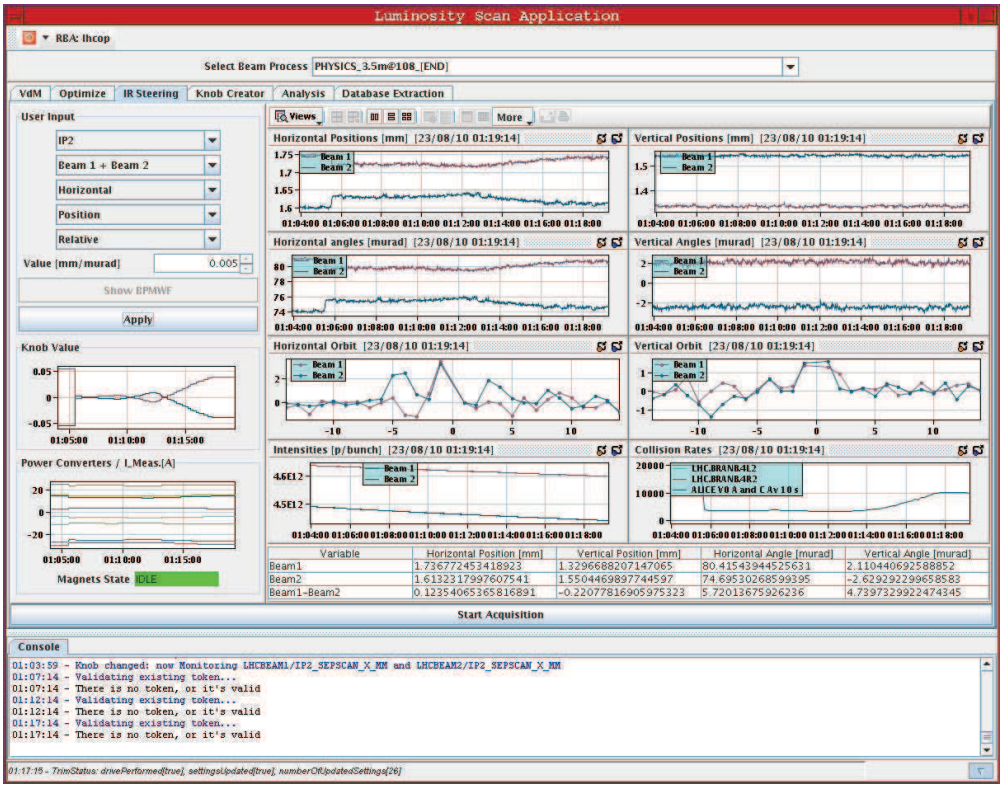

Figure A.5: Steering panel.

Appendix B

Coupling Angle Calculation

General expressions of the transverse beam sizes and quasi-emittances for linearly coupled lattices were derived in [93] from which an expression of the tilt angle due to coupling can be determined. In the laboratory frame system, the beam size matrix Σ is:

$$\Sigma = \begin{pmatrix} \sigma_{xx} & \sigma_{xx'} & \sigma_{xy} & \sigma_{xy'} \\ \sigma_{x'x} & \sigma_{x'x'} & \sigma_{x'y} & \sigma_{x'y'} \\ \sigma_{yx} & \sigma_{yx'} & \sigma_{yy} & \sigma_{yy'} \\ \sigma_{y'x} & \sigma_{y'x'} & \sigma_{y'y} & \sigma_{y'y'} \end{pmatrix}, \tag{B.1}$$

for which the tilt angle in the $x-y$ plane is expressed as:

$$\tan 2\phi = \frac{2\sigma_{xy}}{\sigma_{xx} - \sigma_{yy}}. \tag{B.2}$$

For Gaussian distributions, the beam size matrix Σ_N in the normalized uncoupled coordinate system is:

$$\Sigma = \begin{pmatrix} \varepsilon_I & 0 & 0 & 0 \\ 0 & \varepsilon_I & 0 & 0 \\ 0 & 0 & \varepsilon_{II} & 0 \\ 0 & 0 & 0 & \varepsilon_{II} \end{pmatrix}. \tag{B.3}$$

For 2D coupled transverse motion, two uncoupled eigenmodes (I and II) will contribute to the single particles motion. The motion of a single particle in the laboratory coordinate system is in this case:

$$\mathbf{X} = \begin{pmatrix} x \\ x' \\ y \\ y' \end{pmatrix} = \mathbf{P} \begin{pmatrix} \sqrt{\varepsilon_I}\cos\Phi_I \\ -\sqrt{\varepsilon_I}\sin\Phi_I \\ \sqrt{\varepsilon_{II}}\cos\Phi_{II} \\ -\sqrt{\varepsilon_{II}}\sin\Phi_{II} \end{pmatrix}, \tag{B.4}$$

where Φ_I and Φ_{II} are the phases of the two eigenmodes. It was shown in [94] that the two-dimensional phase space (x, x', y, y') one-turn matrix $\mathbf{T}$ can be expressed as:

$$\mathbf{T} = \mathbf{V}\mathbf{U}\mathbf{V}^{-1} \tag{B.5}$$

where

$$\mathbf{U} = \begin{pmatrix} \mathbf{G}_I & 0 \\ 0 & \mathbf{G}_{II} \end{pmatrix} \begin{pmatrix} \mathbf{R}(\Phi_I) & 0 \\ 0 & \mathbf{R}(\Phi_{II}) \end{pmatrix} \begin{pmatrix} \mathbf{G}_I^{-1} & 0 \\ 0 & \mathbf{G}_{II}^{-1} \end{pmatrix}, \tag{B.6}$$

where

$$\mathbf{G}_{I,II} = \begin{pmatrix} \sqrt{\beta_{I,II}} & 0 \\ \frac{-\alpha_{I,II}}{\sqrt{\beta_{I,II}}} & \frac{1}{\sqrt{\beta_{I,II}}} \end{pmatrix}, \tag{B.7}$$

and $\mathbf{R}(\Phi_{I,II})$ are 2×2 rotation matrices. $\mathbf{V}$ is written in the form:

$$\mathbf{V} = \begin{pmatrix} \gamma\mathbf{I} & \mathbf{C} \\ -\mathbf{C}^{+} & \gamma\mathbf{I} \end{pmatrix}, \tag{B.8}$$

where the symplectic conjugate $\mathbf{C}^{+}$ is:

$$\mathbf{C}^{+} = \begin{pmatrix} C_{22} & -C_{12} \\ -C_{21} & C_{11} \end{pmatrix}, \tag{B.9}$$

and

$$\gamma^2 = 1 - |\mathbf{C}|. \tag{B.10}$$

A this point, it is convenient to normalize out the β dependence in $\mathbf{C}$ via $\mathbf{N} = \mathbf{G}^{-1}$ as shown in [95]. We can expressed $\mathbf{T}$ in terms of normalized matrices:

$$\mathbf{T} = \mathbf{N}^{-1}\bar{\mathbf{V}}\bar{\mathbf{U}}\bar{\mathbf{V}}^{-1}\mathbf{N}, \tag{B.11}$$

where

$$\bar{\mathbf{U}} = \mathbf{N}\mathbf{U}\mathbf{N}^{-1} = \mathbf{R}, \tag{B.12}$$

and

$$\bar{\mathbf{V}} = \mathbf{N}\mathbf{V}\mathbf{N}^{-1} = \begin{pmatrix} \gamma\mathbf{I} & \bar{\mathbf{C}} \\ -\bar{\mathbf{C}}^{+} & \gamma\mathbf{I} \end{pmatrix}. \tag{B.13}$$

Comparing the expression of $\mathbf{T}$ in Equation B.11 with the expression of the uncoupled one-turn matrix $\mathbf{U}$ in Equation B.6, we can conclude that $\mathbf{P} = \mathbf{N}^{-1}\bar{\mathbf{V}} = \mathbf{G}\bar{\mathbf{V}}$ which can be expressed in terms of Twiss parameters:

$$\mathbf{P} = \begin{pmatrix} \gamma\sqrt{\beta_I} & 0 & \bar{C}_{11}\sqrt{\beta_I} & \bar{C}_{12}\sqrt{\beta_I} \\ \frac{-\alpha_I\gamma}{\sqrt{\beta_I}} & \frac{\gamma}{\sqrt{\beta_I}} & \frac{-\alpha_I\bar{C}_{11}}{\sqrt{\beta_I}} + \frac{\bar{C}_{21}}{\sqrt{\beta_I}} & \frac{-\alpha_I\bar{C}_{12}}{\sqrt{\beta_I}} + \frac{\bar{C}_{22}}{\sqrt{\beta_I}} \\ -\bar{C}_{22}\sqrt{\beta_{II}} & \bar{C}_{12}\sqrt{\beta_{II}} & \gamma\sqrt{\beta_{II}} & 0 \\ \frac{\alpha_{II}\bar{C}_{22}}{\sqrt{\beta_{II}}} + \frac{\bar{C}_{21}}{\sqrt{\beta_{II}}} & \frac{-\alpha_{II}\bar{C}_{12}}{\sqrt{\beta_{II}}} + \frac{-\bar{C}_{11}}{\sqrt{\beta_{II}}} & \frac{-\alpha_{II}\gamma}{\sqrt{\beta_{II}}} & \frac{\gamma}{\sqrt{\beta_{II}}} \end{pmatrix}. \tag{B.14}$$

Finally, the beam size matrix in laboratory system can be expressed as:

$$\Sigma = \mathbf{P}\Sigma_N\mathbf{P}^T, \tag{B.15}$$

from which we derive:

$$\sigma_{xx} = \gamma^2\beta_I\varepsilon_I + \beta_I(\bar{C}_{11}^2 + \bar{C}_{12}^2)\varepsilon_{II},$$

$$\sigma_{yy} = \gamma^2\beta_{II}\varepsilon_{II} + \beta_{II}(\bar{C}_{22}^2 + \bar{C}_{12}^2)\varepsilon_I,$$

$$\sigma_{xy} = \gamma \sqrt{\beta_I \beta_{II}} \, (\bar{C}_{11} \, \varepsilon_{II} - \bar{C}_{22} \, \varepsilon_I). \tag{B.16}$$

The tilt angle in the $x-y$ plane is:

$$\tan 2\phi = \frac{\gamma \sqrt{\beta_I \beta_{II}} \, (\bar{C}_{11} \, \varepsilon_I - \bar{C}_{22} \, \varepsilon_I)}{\gamma^2 \, \beta_I \, \varepsilon_I + \beta_I \, (\bar{C}_{11}^2 + \bar{C}_{12}^2) \, \varepsilon_{II} - \gamma^2 \, \beta_{II} \, \varepsilon_{II} - \beta_{II} \, (\bar{C}_{22}^2 + \bar{C}_{12}^2) \, \varepsilon_I}. \tag{B.17}$$

Bibliography

[1] S. Van der Meer. Calibration of the Effective Beam Height in the ISR. *CERN-ISR-PO-68-31*, 1968.

[2] W.Herr. Beam-Beam Interaction. *Yellow Report*, (CERN 2006-002), 2006.

[3] J. E. Augustin. Effet Faisceau-Faisceau. *36-69 JEA-LN*, 1969.

[4] M. Bassetti and G. A. Erskine. Closed expression for the electrical field of a 2-dimensional Gaussian charge. *CERN-ISR-TH/80-06*, 1980.

[5] A. G. Ruggiero. The Luminosity from the Collisions of Two Unequal and Not-Round Beams. *FN-271*, 1974.

[6] W.Herr and B.Muratori. Concept of Luminosity. *Yellow Report*, (CERN 2006-002), 2006.

[7] C. Moller and K. Danske. *Vidensk. Selk. Mat.-Fys. Medd.*, 1945.

[8] W. Grobner and N. Hofreiter. Integraltafel, Springer-Verlag. *II Teil - Bestimmte Integrale*, 1950.

[9] T. Suzuki. General Formulae of Luminosity for Various Types of Colliding Beam Machines. *KEK-76-3*, 1976.

[10] M. A. Furman. Hourglass Effects for Asymmetric Colliders. *PAC 1991 Proceedings*, 1991.

[11] Y. Cai. Luminosity of Asymmetric e+e- Collider with Coupling Lattices. *EPAC Proceedings*, 2000.

[12] M. Dittmar et al. Towards a Precise Parton Luminosity Determination at the CERN LHC. *Phys. Rev. D 56*, 1997.

[13] UA4 Collaboration. The Real Part of the Forward Proton AntiProton Elastic Scattering Amplitude Measurement at the Center of Mass Energy of 546 GeV. *Phy. Lett. B 198*, 1987.

[14] F. Abe et al. Measurement of small angle antiproton-proton elastic scattering at $\sqrt{s} = 546 and 1800 GeV$. *Phy. Rev. D 50*, 1994.

[15] PP2PP Collaboration. The PP2PP experiment at RHIC: silicon detectors installed in Roman Pots for forward proton detection close to the beam. *Nucl. Instrum. and Meth. A 535*, 2004.

[16] P. Van Esch et al. The H1 forward proton spectrometer at HERA. *Nucl. Instrum. and Meth. A 446*, 2000.

[17] G. Anellli et al. The TOTEM Experiment at the CERN Large Hadron Collider. *JINST 3 S082007*, 2008.

[18] H. Burkhardt and P. Grafstrom. Absolute Luminosity from Machine parameters. *LHC Project Report 1019*, 2007.

[19] M. Ferro-Luzzi. Proposal for an Absolute Luminosity Determination in Colliding Beam Experiments Using Vertex Detection of Beam-gas Events. *Nucl. Instr. and Meth. A 553*, 2005.

[20] M. Seidel. The proton collimation system of HERA. *Ph.D. thesis, Hamburg University, DESY 94-103*, 1994.

[21] S. M. White, R. Alemany Fernandez, H. Burkhardt, and M. Lamont. Luminosity Optimization and Calibration in the LHC. *PAC Proceedings*, 2009.

[22] F. James. MINUIT - Function Minimization and Error Analysis. *CERN Program Library -D506*, 1998.

[23] N. Sammut, S.M. White, H. Burkhardt, C. Giloux, and W. Venturini Delsolaro. Measurement and Effects of the Magnetic Hysteresis on the LHC Crossing Angle and Separation Bumps. *EPAC Proceedings*, 2008.

[24] W. Kozanecki et al. Interaction-Point Phase-Space Characterization using Single-Beam and Luminous-Region Measurements at PEP-II. *SLAC-PUB-13383*, 2008.

[25] C. Fischer and R. Schmidt. On the Measurements of the Beam Current, Lifetime and Decay Rate in the LHC Rings. *LHC-BCT-ES001*, 2005.

[26] A. Drees et al. Results from Vernier Scans During the RHIC During 2008 PP run. *PAC Proceedings*, 2009.

[27] G. Aad et al. The ATLAS Experiment at the CERN Large Hadron Collider. *JINST 3 S08003*, 2008.

[28] K. Aamodt et al. The ALICE Experiment at the CERN Large Hadron Collider. *JINST 3 S08002*, 2008.

[29] S. Chatrchyan et al. The CMS Experiment at the CERN Large Hadron Collider. *JINST 3 S08004*, 2008.

[30] A. Augusto Alves Jr. et al. The LHCb Experiment at the CERN Large Hadron Collider. *JINST 3 S08005*, 2008.

[31] O. Adriani et al. The LHCf Experiment at the CERN Large Hadron Collider. *JINST 3 S08006*, 2008.

[32] O. Bruning, P. Collier, P. Lebrun, S. Myers, R. Ostojic, J. Poole, and P. Proudlock. LHC Technical Design Report Vol.I - The Main Ring. *CERN-2004-003*, 2004.

[33] O. Bruning, W. Herr, and R. Ostojic. A Beam Separation and Collision Scheme for IP1 and IP5 at the LHC for Optics Version 6.1. *LHC Project Report 315*, 1999.

[34] O. Bruning, W. Herr, and R. Ostojic. A Beam Separation and Collision Scheme for IP2 and IP8 at the LHC for Optics Version 6.1. *LHC Project Report 367*, 1999.

[35] R. Bailey and P. Collier. Standard Filling Schemes for Various LHC Operation Modes. *LHC Project Note 323*, 2003.

[36] N. Sammut, C. Giloux, M. Lamont, W. Venturini Delsolaro, and S. M. White. Hysteresis Effects of MCBX Magnets on the LHC Operation in Collision. *PAC Proceedings*, 2009.

[37] N. Sammut, L. Bottura, and J. Micallef. A Mathematical Formulation to Predict the Harmonics of the Superconducting LHC Magnets. *Phys. Revs ST - Accel. Beams, Vol 9 No 1*, 2006.

[38] H. Grote and W. Herr et al. Contributions of the SL Division to the Workshop on Beam-beam Effects at Fermilab. *LHC Project Report 502*, 2001.

[39] BE-BI. First Results from LHC Beam Instrumentation Systems. *LHC Performance Note 006*, 2009.

[40] J. P. Koutchouk. Measurement of the Beam Position in the LHC Main Rings. *LHC-BPM-ES-004*, 2002.

[41] S. M. White, H. Burkhardt, S. D. Fartoukh, and T. Pieloni. Optimization of the LHC Separation Bumps Including Beam-Beam Effects. *PAC Proceedings*, 2009.

[42] H. Grote and F. Schmidt et al. http://mad.web.cern.ch.

[43] T. Pieloni, W. Herr, and Ji Qiang. Emittance Growth due to Beam-Beam Effects with a Static Offset in Collision in the LHC. *PAC Proceedings*, 2009.

[44] B. Muratori. Study of Offset Collisions and Beam Adjustment in the LHC Using a Strong-Strong Simulation Model Horizontal Offset. *LHC Project Report 593*, 2002.

[45] Burkhardt and R. Schmidt. Intensity and Luminosity after Beam Scraping. *CERN-AB-2004-032*, 2004.

[46] K. Yokoya et al. Tune Shift of Coherent Beam-beam Oscillations. *Part. Acc. 27*, 1990.

[47] K. Cornelis, M. Meddahi, and R. Schmidt. The Beam-beam Effect in the SPS Proton Antiproton Collider for Beams with Unequal Emittances. *CERN-SL/90-73*, 1990.

[48] S. M. White, R. Tomas, W. Venturini Delsolaro, and G. Vanbavinckhove. Construction and Performance of IP Optics Tunig Knobs in the LHC. *IPAC Proceedings*, 2010.

[49] R. Tomas et al. LHC Optics Model, Measurements and Corrections. *IPAC Proceedings*, 2010.

[50] J.B. Jeanneret and R. Ostojic. Geometrical Acceptance in LHC version 5.0. 1997.

[51] C. Fischer et al. Desing and Test of a New Rest Gas Ionization Profile Monitor Installed in the SPS as a Prototype for the LHC. *CERN-AB-2004-031*, 2004.

[52] T. Lefevre et al. First Beam Measurements with the LHC Synchrotron Light Monitors. *IPAC Proceedings*, 2010.

[53] E. Bravin et al. Collision Rate Monitors for the LHC. *PAC Proceedings*, 2007.

[54] W.C. Turner et al. Development of a detector for bunch by bunch measurement and optimization of luminosity in the LHC. *Nuclear Instruments and Methods in Physics Research A 461*, 2001.

[55] R . Assmann et al. On the Measurement of the Relative Luminosity at the LHC. *LHC-B-ES-0007*, 2004.

[56] S. M. White and E. Bravin. Fluka Simulations and SPS Measurements for the LHC BRAN. *PAC Proceedings*, 2009.

[57] A. Ferrari, A. Fasso P.R. Sala, and J. Ranft. FLUKA: a multi-particle transport code. *CERN 2005-10, INFN/TC-05/11*, 2005.

[58] H. Burkhardt, D. Macina, V. Talanov, and E. Tsesmelis. Numerical study of the very forward background from the proton-proton collisions in the experimental insertions of the LHC. *PAC Proceedings*, 2007.

[59] R. Miyamoto, H. S. Matis, A. Ratti, J. Stiller, W. C. Turner, and S. M. White. Simulation of the BRAN Luminosity Monitor for High Luminosity Interaction Regions. *IPAC Proceedings*, 2010.

[60] A. Ratti et al. Test Results of the Luminosity Monitors for the LHC. *PAC Proceedings*, 2009.

[61] P. Datte et al. Initial Test Results of an Ionization Chamber Shower Detector for a LHC Luminosity Monitor. 2007.

[62] A. Drees et al. Results from Vernier Scans at RHIC During the PP run 2001-2002. *PAC Proceedings*, 2003.

[63] M. Bai et al. First Polarized Proton Collisions at a Beam Energy of 250 GeV in RHIC. *PAC Proceedings*, 2009.

[64] T. Hallmann, T. Kirk, T. Roser, and R. G. Milner. RHIC II/eRHIC White Paper. 2003.

[65] A. Drees and S. M. White. Vernier Scan Results from the First RHIC Polarized Proton Run at 250 GeV. *IPAC Proceedings*, 2010.

[66] P. Cameron et al. RHIC Beam Position Monitor Characterization. *PAC Proceedings*, 1995.

[67] M. Venturini and W. Kozanecki. The Hourglass Effect and the Measurement of the Transverse Size of Colliding Beams by Luminosity Scans. *PAC Proceedings*, 2001.

[68] C. Bovet, M. D. Hildreth, M. Lamont, and J. Wenninger. Luminosity Optimization Using Beam-beam Deflections at LEP. *PAC Proceedings*, 1996.

[69] G. Kruk, S. Dehaye, M. Lamont, M. Misiowiec, and W. Slinwinski. LHC Software Architecture [LSA] - Evolution Toward LHC Beam Commissioning. *ICALEPCS Proceedings*, 2007.

[70] W. Salter. LHC Data Interchange Protocol Description. *EDMS-457113*, 2004.

[71] R. Alemany-Fernandez, Mike Lamont, and S. M. White. Separation Scan Application Requirements. *EDMS/894460*, 2008.

[72] S. M. White and H. Burkhardt. Luminosity Optimization. *LHC Commissioning Workshop*, 2010.

[73] Courtesy of R. Jacobsson.

[74] S. M. White, R. Alemany-Fernandez, H. Burkhardt, and M. Lamont. First LUminosity Scans in the LHC. *IPAC Proceedings*, 2010.

[75] The ATLAS Collaboration. Luminosity Determination Using the ATLAS Detector. *ATL-ATLAS-CONF-2010-060*, 2010.

[76] The CMS Collaboration. Measurement of CMS Luminosity. *CMS PAS EWK-10-004*, 2010.

[77] R. Aaij et al The LHCb Collaboration. Measurement of sigma(pp -¿ b anti-b X) at $\sqrt{s} = 7$ TeV in the forward region. *Submitted to Phys. Lett. B.*, 2010.

[78] Personnal communication with V. Balagura.

[79] G. Vanbavinckhove et al. Coupling and Vertical Dispersion Studies for the LHC Using Skew Quadrupoles and Vertical Orbit Bumps. *IPAC*, 2010.

[80] Personnal communication with J. J. Gras.

[81] Presentations from the BCNWG. *http://indico.cern.ch/conferenceDisplay.py?confId=100586*.

[82] Bunch Current Normalization Working Group. *http://indico.cern.ch/conferenceDisplay.py?confId=98860*.

[83] CERN-Rome Collaboration. The Real Part of the Forward Proton Proton Scattering Amplitude Measurement at the CERN Intersecting Storage Rings. *Phy. Lett. 66 B*, 1977.

[84] ATLAS Collaboration. ATLAS Forward Detectors for Measurement of Elastic Scattering and Luminosity (TDR). *CERN-LHCC-2008-004*, 2008.

[85] A. Verdier. TOTEM optics for LHC V6.5. *LHC-Project-Note-369*, 2005.

[86] A.Faus-Golfe and A.Verdier. High-beta and very high-beta optics studies for LHC. *EPAC'04 Proceedings*, 2004.

[87] A.Faus-Golfe and A.Verdier. High-beta and very high-beta optics studies for LHC. *LHC-Project-Note-357*, 2004.

[88] M. Aiba, H. Burkhardt, S. Fartoukh, M. Giovanozzi, and S. M. White. Optics Flexibility in the LHC at Top Energy. *EPAC'09 Proceedings*, 2008.

[89] R. Bailey and P. Collier. Standard Filling Schemes for Various LHC Operation Modes. *LHC-Project-Note-323*, 2003.

[90] H. Burkhardt, S. Cavalier, M. Heller, P. Puzo, and S. M. White. Overall Optics Solutions for very high-beta in ATLAS. *EPAC'08 Proceedings*, 2008.

[91] S. M. White, R. Alemany-Fernandez, and M. Lamont. Luminosity Scans Data Storage Requirements. *EDMS/970037*, 2008.

[92] A. Drees and T. D'Ottavio. Luminosity Optimization Using Automated IR Steering at RHIC. *EPAC*, 2004.

[93] Y. Luo. Transverse Beam sizes and Quasi Emittances for Linearly Coupled Optics. *NIM, A562*, 2006.

[94] D. Edwards and L. Teng. Parametrization of Linear Coupled Motion in Periodic Systems. *IEEE Trans. Nucl. Sci. NS-30*, 1973.

[95] D. Sagan and D. Rubin. Linear Analysis of Coupled Lattices. *PRST-AB 2 074001*, 1999.

Acknowledgments

It is an honor for me to have spent these three years working at CERN under the supervision of Helmut Burkhardt. During these three years, he has always been available to help me with his advices and knowledge throughout the different studies I presented in this thesis. He also gave me enough space and freedom to express my opinions and take initiatives. I am very proud to have worked with him and would like to express my gratitude to Helmut for making this experience at CERN even more exciting and enriching.

I would like to thank Patrick Puzo for introducing me to the world of accelerators physics and having directed my PhD thesis for the University of Paris 11. Despite the distance he has always been of good advices and provided help and support when I needed them.

I am thankful to Wolfram Fischer, Valerie Halyo, Olivier Napoly and Guy Wormser (President of the Jury) for accepting to be part of the Jury and having taken the time to carefully read the manuscript. Their comments were very useful and really helped me in the process of producing this thesis.

I am grateful to Oliver Brüning and Massimo Giovannozzi for their warm welcome and having hosted me into their teams. A special thank goes to Mike Lamont for his trust and confidence. He always supported me while I was developping the software and gave me beam time time when I needed it. He also allowed me to collide the beams for the first time in the LHC which made me very proud and represents a great achievement for a PhD student.

In 2009, I had the chance to spend a few week at BNL in Upton, New York to work on luminosity calibration at the RHIC collider. At the time, it was not sure the LHC would restart in time for me to work on real data and it was great relief for me to be able to apply the work I had done on the RHIC data. I would like to thank Angelika Drees for supervising me during this stay, Wolfram Fischer for hosting within his group and Rama Calaga for showing me around and making this stay more pleasant.

This work is the result of an excellent collaboration with the four main LHC experiments. I would the like to acknowledge the following people for their support and contributions on various subjects and level: Nadia Adam, Vladik Balagura, Davide Caforio, Antonello Di Maurio, Massimiliano Ferro-Luzzi, Valérie Halyo, Richard Jacobsson, Witold Kozanecki, Atonello Sbrizzi, Jeremy Werner.

Several people contributed to the various studies presented here on different subjects and in different ways: Reyes Alemany Fernandez, Enrico Bravin, Stéphane Fartoukh, Werner Herr, Tatiana Pieloni, N. Sammut, R. Tomàs, Glenn Vanbavinckhove, Walter Venturini Delsolaro.

A special thanks goes to Benoit Salvant, Giovanni Rumolo, Rogelio Tomàs, Rama Calaga, Giulia Papotti, Giulia Bellodi, Yngve Levinsen, Nicolas Mounet, Tatiana Pieloni, Glenn Vanbavinchove for the coffees lunch and good times inside and outside of CERN.

Finally I would to thank my parents, Richard and Josiane White, and my brother Pierre White for all their love and support all of this would not have been possible without them.

You all made this a great experience. Thanks to all of you and to all the ones I forgot.

Résumé

Les paramètres les plus importants décrivant les performances d'un collisionneur de particules sont l'énergie et la luminosité. Les hautes énergies permettent aux expériences de physique des particules d'étudier de nouveaux effets. La luminosité décrit la capacité du collisionneur à produire le nombre requis d'interactions utiles ou événements. Le Large Hadron Collider (Grand Collisionneur de Hadron) ou LHC a été conçu pour produire des collisions proton proton à une énergie dans le centre de masse de 14 TeV. Cette énergie est la plus haute jamais atteinte jusqu'alors dans un accélérateur de particules. Les connaissances et la compréhension de la physique des particules à de telles énergies sont basées sur des simulations et des prédictions théoriques. Contrairement aux collisionneurs électron positron pour lesquels la section efficace de diffusion de Bhabba peut être précisément calculée et utilisée pour calibrer la luminosité, il n'existe pas de processus ayant une section efficace bien connu et un taux de production suffisant pour être utilise afin de calibrer la luminosité durant les premières années d'opération du LHC. La luminosité peut aussi être exprimée en fonction du nombre de charges par faisceau et leur taille au point d'interaction. Il est donc possible d'utiliser cette propriété afin de déterminer la luminosité a partir des paramètres machine. La détermination de la luminosité absolue a partir des paramètres machine est une méthode alternative a celle utilisant les sections efficaces et offre des informations complémentaires au modèle de fragmentation. Pour le LHC, il a été proposé d'utiliser la méthode développée par S. Van Der Meer à ISR afin d'offrir une calibration de la luminosité aux expériences de physique des particules durant les premières années d'opération. Cette thèse décrit comment cette méthode a été implémentée et utilisée pour la première fois au LHC afin d'optimiser et de calibrer la luminosité. Des études complémentaires d'optique linéaire et de dynamique faisceau ainsi que des mesures faites pour le collisionneur RHIC sont aussi décrites.

Cette étude commence par un chapitre introductif qui reprend les notions de physique des accélérateurs nécessaire à la compréhension des chapitres suivants. Les équations décrivant les mouvements des particules dans un accélérateur circulaire sont rappelées ainsi que les principes de base d'optique linéaire. Des grandeurs caractéristiques du faisceau et de la machine telles que l'émittance ou le tune sont définies. Une brève introduction aux effets faisceau-faisceau est aussi présentée ces derniers étant inhérent aux collisionneurs de particules. Une description plus détaillée du concept de luminosité est donnée. Les équations générales de luminosité en présence d'effets tel qu'un angle de croisement sont dérivées. Enfin différentes méthodes permettant de déterminer la luminosité absolue sont présentées et le choix de la méthode de Van Der Meer pour les premières années d'opérations du LHC est expliqué.

Le second chapitre se concentre sur la méthode de Van Der Meer. Le principe développé par S. Van Der Meer est décrit et plus particulièrement comment cette méthode offre une mesure directe de l'intégrale de recouvrement, décrivant la région d'interaction des deux faisceaux, sans avoir besoin de connaître les distributions initiales des faisceaux. L'impact des différents effets présentés dans le chapitre1 sur la précision de la mesure sont étudiés analytiquement afin de déterminer les paramètres faisceau optimaux pour une mesure de la luminosité absolue. Enfin une estimation de l'erreur sur la détermination de la luminosité basée sur des études numériques et les spécifications des instruments utilisés durant cette mesure est donnée.

Le chapitre 3 présente le LHC et comment les principaux paramètres faisceau ont été choisis afin de délivrer une luminosité de $10^{34}\mathrm{cm}^{-2}\mathrm{s}^{-1}$ aux expériences ATLAS et CMS. Quelques dates clé de la mise

en route du LHC sont rappelées afin de justifier l'orientation de certaines études présentées dans cette thèse et comment il a été nécessaire de s'adapter au changement de programme de mise en marche du LHC. Les différentes étapes permettant d'accélérer et de mettre les faisceaux en collision à partir de l'injection sont brièvement décrites. Dans le cadre de cette thèse des études concernant plus particulièrement la mise en collision des faisceaux dans le LHC. Des simulations de l'impact sur l'orbite des effets d'hystérésis présents dans les aimants permettant de déplacer les faisceaux au point d'interaction ainsi que la manière dont ceux-ci sont utilisés pour générer l'angle de croisement, la séparation ou l'optimisation des collisions sont décrites. Lors de la mise en collision des faisceaux de nombreux effets liés à la dynamique faisceau et plus particulièrement aux effets faisceau-faisceau entrent en jeux. Des simulations permettant de modéliser ces effets et de comprendre leur impact sur l'émittance ont été réalisées et seront aussi décrites dans ce chapitre.

Le chapitre 4 donne une description des divers instruments utilisés lors de l'analyse des données permettant de déterminer la luminosité absolue. En principe, seules les mesures de courant sont nécessaires pour déterminer la luminosité. Des informations complémentaires et qui se sont révélées très utiles par la suite ont été données par d'autre instruments tel que les wire-scanner permettant de mesurer l'émittance ou les BPM permettant déterminer la trajectoire des faisceaux le long de l'anneau. Ces instruments sont donc aussi décrits dans ce chapitre. Enfin, le LHC est équipé de moniteurs de luminosité donc le but est de fournir des signaux robustes grâce auxquels il est possible d'optimiser la luminosité. Ce chapitre se termine donc sur une description détaillée de ces moniteur de luminosité et les simulations qui été faites a l'aide du logiciel FLUKA afin de déterminer les performances et l'efficacité de ces moniteurs à haute énergie.

Le chapitre 5 présente les résultats des mesures effectuées sur le collisionneur RHIC (relativistic ion collider). Ces mesures ont été effectuées en 2009 alors que le LHC était stoppé suite à l'incident de Septembre 2008. RHIC présente certaines caractéristiques communes au LHC et représente donc un excellent test pour les futures mesures au LHC. La calibration de la luminosité par la méthode de Van Der Meer est aussi utilisé à RHIC, une collaboration avec ce laboratoire a donc été mise en place afin de profiter de l'expérience acquises par le passé dans ce laboratoire. Malgré certains paramètres faisceaux non optimisées pour une mesure de précision de la luminosité absolue il a été possible de déterminer celle-ci avec une précision de 7% dominée par l'erreur sur les mesures de courant et la détermination du déplacement des faisceaux. Une étude détaillée des différentes sources d'erreur ainsi que des propositions pour les réduire lors de futures mesures sont présentées. Les faisceaux du collisionneur RHIC ont un courant élevé ce qui n'est pas optimal pour la détermination de la luminosité absolue mais a permis d'observer certains effets faisceau-faisceau qui n'avaient pas été observé par le passé à RHIC et présentent donc un résultat très intéressant de ce chapitre.

Le chapitre 7 présente les résultats obtenus en 2010 au LHC. L'année 2010 a été une année de beaucoup de premières pour le LHC auxquelles j'ai eu la chance de participer. J'ai notamment été impliqué dans l'établissement des premières collisions, les premières optimisations de luminosité. Ces trois contributions sont décrites dans ce chapitre ainsi que les outils développés afin de réaliser ces mesures et plus particulièrement le logiciel d'optimisation et de calibration de la luminosité qui est décrit plus en détail dans les annexes. Enfin l'année 2010 a aussi vu la première calibration de la luminosité utilisant la méthode de Van Der Meer à 3.5TeV. Le protocole de la méthode est présenté ainsi qu'une étude détaillée des erreurs systématiques associées a cette méthode. Ces premières mesures ont permis de déterminer la luminosité avec une précision de 11% largement dominée par les mesures de courant des faisceaux. Pour terminer, des propositions pour améliorer la précision des futures mesures sont présentées.

Le dernier chapitre de cette thèse présente des travaux effectués sur les optiques de beta élevés. Ces optiques ont été développées pour les expériences TOTEM et ATLAS et permettront de mesurer précisément les angles de diffusion élastiques des interactions proton-proton et ainsi déterminer leur section efficace. Cette méthode présente un alternative a la méthode de Van Der Meer et devrait en principe donner une mesure de section efficace avec une précision de quelques pour cents. Ces optiques étant très difficiles ils ne pourront pas être mis en place avant que le LHC atteigne son énergie nominale de 7TeV par faisceau.

Des optiques intermédiaires ont donc aussi été développées et sont présentée brièvement dans ce dernier chapitre.